HOKKAIDO UNIVERSITY

Title	Study on modulation of flow transition by microbubble injection
Author(s)	渡村, 友昭
Degree Grantor	北海道大学
Degree Name	博士(工学)
Dissertation Number	甲第11449号
Issue Date	2014-03-25
DOI	https://doi.org/10.14943/doctoral.k11449
Doc URL	https://hdl.handle.net/2115/58197
Type	doctoral thesis
File Information	Tomoaki_Watamura.pdf

Hokkaido University Collection of Scholarly and Academic Papers : HUSCAP

Study on modulation of flow transition by microbubble injection

Tomoaki WATAMURA

Laboratory for Flow Control,
Graduate School of Engineering,
Hokkaido University

Supervised by
Prof. Dr. Y. Murai

February 20th, 2014

Copyright © 2014 Tomoaki WATAMURA
Laboratory for Flow Control
Hokkaido University
All right reserved

Study on modulation of flow transition by microbubble injection

Thesis for Ph.D. (Engineering) at Hokkaido University
Submitted at February 20th, 2014

Advisory Committee
Prof. Dr.-Eng. Yuichi Murai, Hokkaido University, Chair / Chief examiner
Prof. Dr.-Eng. Nobuyuki Oshima, Hokkaido University, Co-examiner
Prof. Dr.-Eng. Masao Watanabe, Hokkaido University, Co-examiner
Assoc. Prof. Dr.-Sci. Susumu Goto, Osaka Universiy, Co-examiner
Assoc. Prof. Ph.D. (Eng.) Yuji Tasaka, Hokkaido University, Co-examiner

Acknowledgement

I wish to express my gratitude to my supervisor Prof. Dr. Yuichi Murai for giving me the opportunity to accomplish this work and for his helpful advices. His extensive perspective on the studies of fluid engineering has made me being broad interested in the field of engineering and has made me free from established interests in my laboratory life.

I would like to thank Assoc. Prof. Dr. Yuji Tasaka for giving me chances to discuss various subjects on fluid dynamics. His way of thinking has encouraged me to address many issues of interests in the world.

I also would like to thank Assist. Prof. Yoshihiko Oishi for giving me chances to taking discussion on many things. His personal view of thinking for living has accelerated me to take off and to fly away.

I wish thank Technician Mr. Toshiyuki Sampo for supporting my research by his excellent techniques. His kindnesses and illustrious sense of fabrications have grown my perception of engineering.

I would like to express my gratitude to Prof. Dr. Nobuyuki Oshima, Prof. Dr. Masao Watanabe, and Assoc. Prof. Dr. Susumu Goto for their insightful comments on this thesis.

I would like to thank Prof. Dr. Dr. Yasuhi Takeda, Assoc. Prof. Dr. Ichiro Kumagai, Dr. Kazuyasu Sugiyama, Assoc. Prof. Dr. Atsuhide Kitagawa, Assoc. Prof. Dr. Shusaku Harada, Prof. Dr. Shigeo Hosokawa, Dr. Shizuo Yoshida, and Dr. Takao Suzuki for giving me essential comments on my research. I couldn’t do this work without them.

Finally, I would like to thank my family, best friends, and personal supporters.

Tomoaki Watamura

Sapporo

February, 2014

Table of Contents

Chapter 1

Introduction 1

1.1 Preface 1

1.2 Background & literature survey 2

1.3 Objective 6

1.4 Outline 7

Chapter 2

Development of PTV utilizing particle color information 11

2.1 Introduction 12

2.2 Algorithms for identifying particle color 17

2.3 Evaluation of the algorithm performances for color information processing ... 24

2.3.1 Setup 24

2.3.2 Evaluating the performance of the algorithms 25

2.4 Application 1: LCD-projector-based 3D color PIV 27

2.4.1 Multi-cycle color illumination for higher spatial resolution 27

2.4.2 Experimental setup and configuration 29

2.4.3 Particle trajectory and velocity vector as a qualitative visualization 30

2.4.4 Evaluating accuracy of single and multiple-cycle color techniques 31

2.4.5 Measurement of instantaneous flow quantities 33

2.5 Application 2: particle discrimination in multiphase flow 35

2.5.1 Experimental setup and configuration 35

2.5.2 Algorithms for particle identification 37

2.5.3 Particle hue distribution 37

2.6 Conclusions 39

Chapter 3

Wave modifications in a microbubble Taylor–Couette flow 52

3.1 Introduction 53

3.2 Experimental Systems 58

3.2.1 Experimental setup and definitions 58
3.2.2 Measurement techniques 60
3.3 Determination of the critical Reynolds number 64
3.4 Modification of flow structures by microbubbles 67
3.4.1 Modification of wave power in MWVF 67
3.4.2 Prevention of appearance and growth of waves 68
3.4.3 Statistic quantities of secondary flow 70
3.4.4 Bubble distribution in Taylor vortex tubes 72
3.4.5 Reduction of azimuthal shear 75
3.5 Conclusion 79

Chapter 4

PIV and DNS combined hybrid analysis of Taylor–Couette flow 94
4.1 Introduction 95
4.2 Experimental setup 97
4.3 Hybrid algorithm 99
4.4 Result and discussion 102
4.4.1 Experiment 102
4.4.2 Direct numerical simulation 103
4.4.3 Flow field obtained by hybrid simulation 103
4.4.4 Wall shear stress and torque 105
4.4.5 Contribution of weight function 106
4.4.6 Remark from findings 107
4.4.7 Candidate for improvement 108
4.5 Conclusion 110

Chapter 5

Spatial development of microbubble clouds near a vertical plane wall 118
5.1 Introduction 119
5.2 Experimental setup 122
5.3 Characteristic of microbubble cloud 125
5.3.1 Flow visualization 125

5.3.2 Statistic of local velocity and void fraction 125
5.3.3 Characteristics of velocity profile 127
5.3.4 Time interval of cloud transit 129
5.4 Conclusion 133

Chapter 6
Spectra modification of a mixing layer by introducing microbubbles 146
6.1 Introduction 147
6.2 Experimental system 149
6.2.1 Experimental setup 149
6.2.2 Measurement system 151
6.3 Modification of developing mixing layer 153
6.3.1 Enlargement of vortex layer 153
6.3.2 Modification of Reynolds shear stress 154
6.3.3 Modification of instantaneous velocity field 158
6.4 Conclusion 162

Chapter 7
Conclusion 171
7.1 Review of chapters 171
7.2 Organizing parameters 174

Appendix 1:
Estimation of hydrogen microbubble generation rate 179

Appendix 2:
Kinematic viscosity of silicone oil, KF96-10cs 180

Appendix 3:
Definition of variable locations in collocated and staggered grid arrangement ... 182

Appendix 4:

Derivation of the Kolmogorov length scale in a Taylor-Couette flow 184

Appendix 5:

Oscillation frequency of a deformable bubble 186

Appendix 6:

Validation of PIV/PTV performance 188

References 193

Publication & Presentation 206

Curriculum Vitae 208

Chapter 1
Introduction

1.1 Preface

The potential impact of flow controls is known to be tremendous for many industrial applications. For example, in worldwide, ocean shipping consumes about 300 million tons of oil per year; the airline industry consumes about 200 million tons of jet fuel per year; trucking industry consumes 170 million tons of total amounts of petrol and diesel oil per year [1] [2]. The reduction of the fluid resistance could help save earth's limited natural resources. Furthermore, the drag reduction by flow controls enables to increase fuel efficiency, endurance, range, and speed. Many studies on flow controls have conducted probably since ancient times in which human beings created the stuffs such as streamlined spears. Flow control methods are well categorized and their historical background are highlighted by Gad-el-Hak (1996) [3]. The review articles are already available, e.g. general turbulence control [4], natural life forms [5], heat transfer [6], combustion [7], free shear flow [8], jets [9], bluff body [10], wall bounded flow [11], using surfactant [12], using micro electro mechanical system (MEMS) [13], and using bubbles [14].

Use of bubbles as a way for skin frictional drag reduction in shear flows has been focused for an engineering application in flow controls, especially for large vessels [14]. The drag reduction using bubbles has been investigated in terms of physical theories, experiments and numerical models since its first report by McCormick & Bhattacharyya (1973) [15]. The performance rate of drag reduction reaches nearly-100 % of drag reduction, i.e. no drag, at the maximum case [16] [17]. The drag reduction obeys the bulk void fraction in turbulent flow with high Reynolds number independent with the size of the microbubbles with diameter [18]. The performance, however, shows large scattering of data as a function of the bulk void fraction [14]. With the addition of bubbles in diameter smaller than $O(100\ \mu m)$ in the actual laboratory scale, the significant drag reduction rate of $O(10^{-1})$ were enabled to be achieved even with the dilute void fraction of $O(10^{-4})$ [19] [20] [21] [22] [23] [24]. These tremendous drag reduction rates against the void fraction pointed out a

considerable gap for which theoretical studies could be conducted. Careful investigations are required to reveal the drag reduction mechanism in two-phase flows.

1.2 Background & literature survey

As a fundamental approach for understanding the drag reduction mechanisms, modification of the liquid medium properties in bulk of fluids have been considered as a function of the void fraction so far. The modification on the bulk density of continuous phase is given as

$$\rho = (1-\alpha)\rho_C + \alpha\rho_D , \tag{1-1}$$

where ρ_C and ρ_D are the original density of the continuous and dispersed phase. In bubbly flows, the density of bubbles (actually density of gas, dispersed phase) is much smaller than that of the liquids (continuous phase) and is regarded as zero, therefore Eq. (1-1) yields as $\rho = (1 - \alpha)\,\rho_C$. The decrease in the medium's density with increasing void fraction provides the primary mechanism for drag reduction with decreasing the bulk density of the medium in turbulence [25].

In contrast, the effective (bulk) viscosity of the fluid in simple laminar shear flows is estimated by Taylor's formula [26] [27],

$$\mu = \left[1+\alpha\left(\frac{\mu_C+\frac{5}{2}\mu_D}{\mu_C+\mu_D}\right)\right]\mu_C , \tag{1-2}$$

where μ_C and μ_D are the viscosity of the continuous and dispersed phase. For a suspension of rigid particles the effective viscosity is greater than the viscosity of the continuous phase by a fraction of $5\alpha/2$, while for suspension of gas bubbles the effective viscosity is greater than the viscosity of the continuous phase by a fraction of α. This modification of viscosity for suspension yields the opposite relationship, i.e., an increase in the shear stress with increasing the void fraction. An increase in the void fraction decreases the frictional drag by decreasing the Reynolds shear stress with decreasing the medium density, as described in Eq. (1-1), and increases the frictional drag by increasing the effective viscosity at the moment, according to Eq. (1-2). The linear theory of two-fluid description of turbulent flows that resolves this contradiction states that the modification on the properties of fluids with uniformly dispersed bubbles is of the same order as the void fraction [28]. The effect of modifications in density and

effective viscosity would be of the same order as the void fraction, α, and would be negligible in dilute two-phase flows in void fraction of $\alpha < O(10^{-4})$.

Nevertheless, the drag reduction rate in previous experimental investigations of dilute microbubbly flows take significantly high values in drag reduction of $O(10^{-2})$, because the non-linear interactions occur between microbubbles and flow structures in turbulent flows [28]. The earlier studies on drag reduction using microbubbles are highlighted in TABLE 1-1, which respect to the diameter of bubble, D, void fraction, α, drag reduction rate (DRR), Reynolds number, Re, and configuration for the investigations. " ? " indicate that the value in the table has not been investigated in the literature. The diameter of bubbles used in the literatures was small as O(100 μm) at anytime. So that the drag is enable to be reduced in any configuration with microbubble injections. FIG. 1-1 shows the skin frictional drag coefficient in (a) pipe flows [29], (b) channel flows [30], and (c) flows on parallel flat wall [29], respectively. The Reynolds numbers in the investigations of drag reduction shown in TABLE 1-1 are larger than that at laminar-transition flow regime or at the early phase of turbulent flows in any configurations. Ferrante & Elghbashi (2004) [31] (2005) [32] have numerically investigated the modification of the velocity profile near a parallel flat wall. They imposed already developed turbulent velocity profiles at the inlet of the computational domain [33]. In the range of Reynolds number at which the presence of microbubble reduced the skin frictional drag, the coherent turbulent vortical structures are generated and lie above the viscous sub-layer. The influence of the addition of microbubbles on the near-wall coherent structures of flows has been commonly thought to be the key factor in the mechanism of modification of the velocity field and the wall shear stress.

McCormick & Bhattacharyya (1973) [15] measured the drag acting on the hull model from the angle of strut suspending the model. Madavan, *et al*. (1985) [34] measured the local wall shear stress from the velocity gradient of temporally averaged vertical velocity profiles obtained from a hot film probe and a laser-Doppler anemometer which traversing in the wall normal direction. Kodama, *et al*. (2000) [35], Murai, *et al*. (2005) [19], Sanders, *et al*. (2006) [16], Elbing, *et al*. (2008) [17], Shen, *et al*. (2006) [18], and Hara, *et al*. (2011) [23] measured the local skin frictional shear stress using a shear transducer. Hassan, *et al*. (2005) [20] and Serizawa, *et al*. (2005) [36] measured the spatially averaged frictional drag from the pressure drop between two

measurement points placed with the distance between 100 times of the pipe diameter. Ferrante & Elghbashi (2004) [31] (2005) [32] also calculated the area averaged frictional drag from the velocity gradient in the whole of the calculation domain. Ortiz-Villafurte & Hassan, (2006) [22] and Jacob, *et al.*, (2010) [24], measured the local wall shear stress from the velocity gradient of vertical velocity profiles obtained by particle image velocimetry. The most of previous studies, therefore, measured the averaged value of velocity or shear stress. Some of the investigations in pipe flow, channel flows, and flow on a parallel plat wall show that the viscous sub-layer is expended by the injection of microbubbles. Hara, *et al.*, (2011) [23] also measured the local shear stress from the Reynolds shear stress distribution across the channel from the spatially and temporally resolved velocity profiles obtained by particle image velocimetry. So that the one of the mechanism on the modification in velocity distributions are suggested as the modification of the near-wall coherent vortical structures in shear flows due to the dispersed microbubbles. Despite the importance of understanding the flow field on drag reduction, the modifications of the flow field leading the skin frictional drag reduction are still unveiled yet.

TABLE 1-1 Drag reduction rate (DRR) reported by literatures of study on drag reduction by injecting microbubble in flows

References	D_b [μm]	α	DRR [%]	Re	Configuration
McCormic & Bhattacharyya, 1973 [15]	?	?	70	5×10^3	Hull model (Exp.)
Madavan, *et al.*, 1985 [34]	?	4×10^{-1}	80	1×10^6	Channel (Exp.)
Kodama, *et al.*, 2000 [35]	?	8×10^{-2}	25	8×10^4	Channel (Exp.)
Ferrante & Elghbashi, 2004 [32]	62	2×10^{-2}	20	8×10^5	Flat plate (Sim.)
Ferrante & Elghbashi, 2005 [33]	40	3×10^{-4}	19	2×10^6	Flat plate (Sim.)
Serizawa, *et al.*, 2005 [36]	37	5×10^{-3}	60	5×10^3	Pipe (Exp.)
Murai, *et al.*, 2005 [19]	30	2×10^{-4}	20	2×10^4	Channel (Exp.)
Hassan, *et al*. 2005 [20]	30	5×10^{-2}	38	5×10^3	Channel (Exp.)
Ortiz-Villafurte & Hassan, 2006 [22]	30	6×10^{-2}	39	3×10^3	Channel (Exp.)
Shen, *et al.*, 2006 [18]	480	2×10^{-1}	2×10^{-1}	4×10^6	Channel (Exp.)
	320	2×10^{-1}	2×10^{-1}		
	250	2×10^{-1}	2×10^{-1}		
	44	1×10^{-2}	5×10^{-2}		
Sanders, *et al.*, 2006 [16]	250	1×10^{-1}	90	1×10^8	Flat plate (Exp.)
Elbing, *et al*, 2008 [17]	100	5×10^{-2}	90	5×10^7	Flat plate (Exp.)
Jacob, *et al.*, 2010 [24]	150	6×10^{-4}	9	2×10^6	Flat plate (Exp.)
Hara, *et al.*, 2011 [23]	60	3×10^{-4}	16	5×10^3	Channel (Exp.)

1.3 Objective

The object of this study is to elucidate the dynamic interaction between microbubbles and coherent vortical structures in time dependent flows. In order to investigate the bubble behavior in flows, the simultaneous measurement system for velocity fields of liquid phase and microbubbles whose diameter is almost same as tracer particles is developed at the beginning. To simplify the flow for investigating the influence of microbubbles on flow structures, three different flows are examined as platforms to extract the essentials in interactions between the presence of microbubbles and coherent vortical structures. (i) Vertically arranged Taylor–Couette flow that is the flow generated in concentric double cylinders was adopted for a model of fully developed streak in turbulent flows for elucidating *wave modifications by injecting microbubblss*. (ii) Motion of microbubbles rising near a vertical plane wall is investigated as a platform for understanding *generations and spatial evolutions of microbubble clouds* in which microbubbles generate locally high void fraction region. Finally, (iii) the horizontal mixing layer in free shear flow is adopted as a platform for the investigating of *modifications of developing flows and the generation of preferential concentration of microbubbles* in flows with velocity fluctuations. In order to study the mechanisms in the generation of preferential concentration of microbubbles, called as microbubble clouds, and the modification of flow field by the preferentially distributed and rising microbubbles, we deploy the Reynolds number and Froude number as below

$$\frac{\partial \boldsymbol{u}}{\partial t} + \boldsymbol{u}\left(\nabla \cdot \boldsymbol{u}\right) = -\nabla p + \frac{1}{Re}\nabla^2 \boldsymbol{u} + \frac{1}{Fr^2}, \tag{1-3}$$

$$Re = \frac{UL}{\nu}, \tag{1-4}$$

$$Fr = \frac{U}{\sqrt{\alpha L |\boldsymbol{g}|}}. \tag{1-5}$$

The author attempts to organize the integrations between the motion of liquid phase and microbubble cloud as a function of the Reynolds number and Froude number.

1.4 Outline

This thesis consists of five chapters for individual investigations. As each chapter excluding introduction and conclusion has individually accepted to be published for various journals or international conferences, they have Abstract, Introduction and Conclusion part. Contents of the chapters are summarized as follows.

In Chapter 2, the measurement systems for the high-dimensional velocity profiling utilizing color information in an image captured by a single color imaging camera have developed; three-dimensional (3D) three-component (3C) particle tracking velocimetry (PTV), and two-phase simultaneous PTV. Color information in a particle image have remarked from the founding period of particle image velocimetry (PIV). Utilizing color information in PIV is old-fashion techniques for experiments in fluid flows. No one, however, has presented the quantitative velocity field applying color information in the human history because of large ambiguity in the definition of particle representing color and large error in experimental systems. The algorithm called Saturation weighted averaged hue in polar coordinate (SWAH-P) was developed for providing averaged color of a particle. SWAH-P yielded the standard deviations for determination of particle information, 1.4 % in hue and 2.0 % in position estimated from the hue. Particles can be categorized into 30 classes or be discriminated 25 depth positions from those color information. As applications of color information on particles, the 3D-3C velocity vector fields (a) in helical rotating flow and that (b) behind the rotating impeller were obtained. Furthermore, when the tracer particles containing a laser induced fluorescent dye are illuminated by a laser light, the microbubbles and tracer particles in two-phase flows are discriminated from their color information: scattering light from gas-liquid interface, or fluorescent light differ from the incident laser light.

In Chapter 3, the influence of the presence of microbubbles in vertical Taylor–Couette flow which is a flow between two concentric rotating cylinders driven by their rotation has been experimentally investigated. The average diameter of microbubbles is 60 μm, which is smaller than the length scale of Taylor vortices appearing in the fluid layer of ~ 10 mm and Kolmogolv length scale of ~ 0.2 mm. The void fraction was 1.2×10^{-4} at the maximum case. The velocity field of the flow containing microbubbles was measured by particle tracking velocimetry (PTV) applying

laser induced fluorescence (LIF), ultrasonic Doppler profiling (UVP), and laser Doppler velocimeter (LDV) depending on their suitability in various measurements of velocity components. As the result of measurement using PTV applying LIF, the microbubbles in Taylor vortices are visualized and exhibit the preferential distribution and motion in waves superimposing on Taylor vortices. Velocity fluctuations of liquid phase acquired by PTV and UVP indicated that the power of the basic wave propagating in the azimuthal direction is enhanced. Its modulation, however, is decreased by addition of microbubbles in the flow regime corresponding to modulated wavy vortex flow. Further, the measurement results using LDV show that the gradient of azimuthal velocity decreased by 10 %. The modified velocity distribution by adding microbubbles was comparable to that obtained with 20 % lower Reynolds number. The microbubbles generating preferential distribution in coherent vortex structure in Taylor Couette flow modified the flow filed as a pseudo-decrease in the effective Reynolds number even with dilute void fraction.

In Chapter 4, the drag reduction due to the modification of waves in Taylor Couette flow was investigated by the hybrid simulation combining direct numerical simulation (DNS) and particle tracking velocimetry (PTV) that satisfies the Navier-Storks equation and the equation for continuity of incompressible flows. Three-dimensional velocity vector fields showing the azimuthal waves of Taylor-Couette flow were reconstructed with feeding two-dimensional velocity field on the meridional plane obtained from PTV. The hybrid simulation represented flow phenomena. The modulation waves were captured in the single phase condition, and diminishment of modulation waves were also reconstructed in the two-phase condition. The torque acting on the axis was equivalent to that of empirical value in the single phase flow, while the torque was decreased by 3 % in two-phase condition. This attributed that the modification of the secondary flow by the addition of microbubbles with void fraction of $O(10^{-4})$ can achieve to reduce the skin frictional drag by $O(10^{-2})$ in bulk of the system.

In Chapter 5, the ascending motions of microbubbles generating number density distributions near a vertical plane wall were experimentally investigated. The microbubbles in flows generate inhomogeneous distribution patterns of local void fraction, called microbubble cloud, whose length scale is much greater than diameter of

the bubbles. The average diameter of microbubbles is 40 μm. The bubbles were generated by water electrolysis and dispersed from the bottom of the fluid layer of vertically long aspect ratio of 10. The local rising velocity of microbubbles and the void fraction were simultaneously measured by UVP and image analysis. The relationship between the fluctuations of velocity and void fraction shows the time lag between them in spite of the positive cross-correlation vale. The void fraction increases first, then the vertical velocity increases. The wavelet coefficient of the fluctuations of the vertical velocity profiles displayed non periodic motion of ascending microbubble cloud as a frequency modulation. The transit interval of microbubble cloud was evaluated from the modulus maxima of wavelet coefficient, and its probability distributions showed development of the mode of transit interval. The growth of the cloud structure was enhanced by the pulsatile injection of microbubbles with the amplitude of 5 %.

In Chapter 6, the influence of the presence of microbubbles in developing mixing layer of free shear flows was experimentally investigated. The averaged diameter of microbubbles was 40 μm, and the maximum void fraction estimated by input power of water electrolysis was 1.8×10^{-4}. The horizontal mixing layer consisted of ~ 50 mm/s in upper layer and ~ 10 mm/s in the lower layer. The back ground disturbance in the inlet flows was controlled as straightened or turbulent flows by honeycombs placed upstream of the measurement section. The velocity distribution of liquid phase was obtained from PTV applying LIF and UVP, while the local void fraction was obtained by PTV applying LIF. The vortex layer thickness was enlarged by addition of microbubbles in turbulent flows. The distribution pattern of microbubbles obtained from correlations of velocity fluctuation and local void fraction showed the preferential distribution in the mixing layer. The power of the horizontal velocity fluctuation induced by the shear of flows was locally reduced by addition of microbubbles. The length scale in which the flow field modified was comparable to the initial vortex layer thickness. The preferential concentration of microbubbles enhanced the development of the flow.

In chapter 7, the author summarizes the results and knowledge obtained above chapters and concludes this thesis.

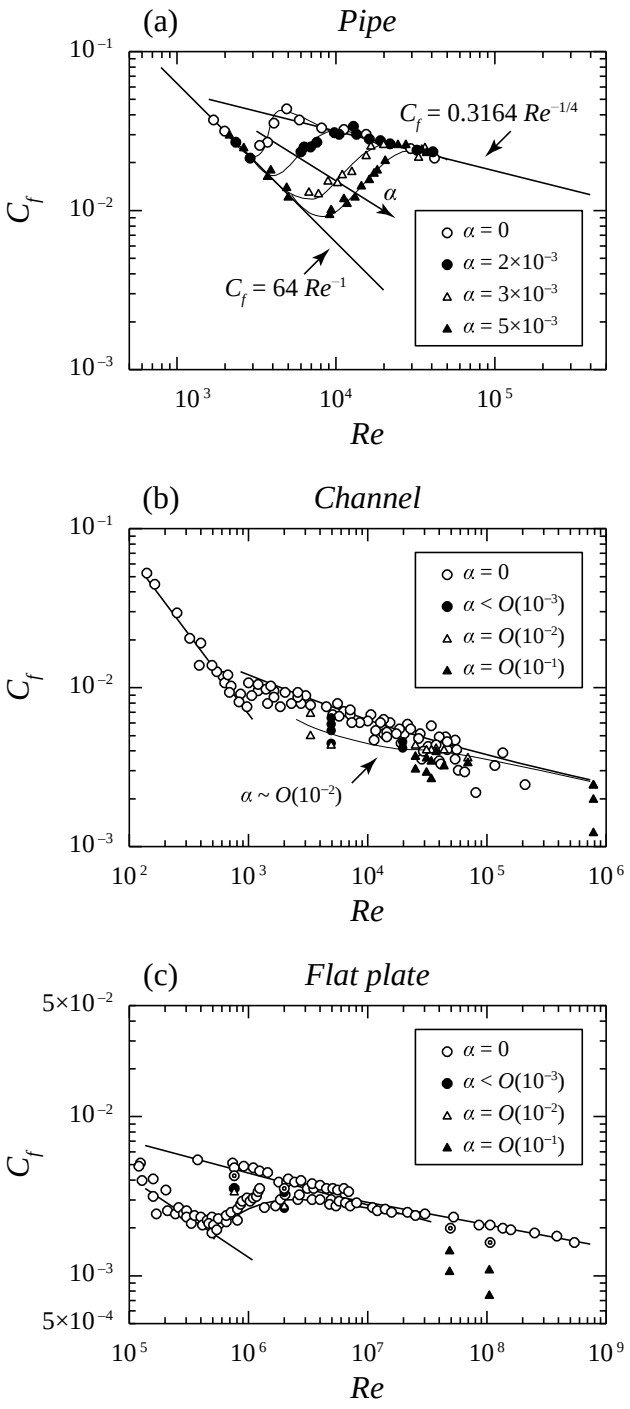


FIG. 1-1 Frictional drag coefficient for (a) pipe flows [36], (b) channel flows, and (c) flows on parallel flat wall, where the symbols for single phase flows are values obtained from literatures [29] [30]

Chapter 2
Development of PTV utilizing particle color information

Abstract

To minimize the uncertainties in identifying the representative color of particles, we propose new color identifying algorithms that average hue in polar rather than linear coordinates. The proposed algorithm, a saturation-weighted-averaged hue in polar coordinates, yields smaller standard deviations than conventional algorithms: 2.8 % in hue and 4.0 % in classification of particle of 95 % confidence level. Two different flow field measurements are demonstrated as applications of PTV utilizing color information. Color-based three-dimensional (3D) particle tracking velocimetry (PTV) using a single camera and an liquid crystal display (LCD) projector, which can measure the out-of-plane velocity component from particle color information, is improved for practical use in 3D velocimetry without losing the original simplicity on the optical configuration of planner 2D PTV. The position and velocity of the out-of plane component are estimated from the linear mapping of the hue-position relationship. Use of a multiple color-cycle gradation light for volumetric illumination of the fluid layers also improves the resolution of the position and velocity measurements in the depth direction. The proposed measurement technique can display the flow patterns of an axisymmetric rotating flow from instantaneous 3D–3C velocity vector fields, as well as the vortex structure of an unsteady flow represented as iso-surfaces of vorticity and enstrophy density. The discrimination of dispersed phases and tracer particles was demonstrated in two different systems consist of a laser and tracer particle containing laser induced fluorescent (LIF) dye. Two apparent peaks appeared in probability distribution of particle hue. Color in an image can provide adequate information for high-order PTV even in a much simple configurations using a single camera.

2.1 Introduction

Particle Image Velocimetry (PIV), including Particle Tracking Velocimetry (PTV) allows instantaneous velocity vector fields to be measured in a two-dimensional (2D) planar domain from time-sequential images of particles seeded in fluids. PIV/PTV has been used in experimental fluid dynamics studies [37], and commercial PIV systems have been widely applied in both academia and industry. However, original PIV system could not process higher-dimensional information such as three-dimensional three-component (3D–3C) velocity vector fields, and their handling of systems were rather complicated, limiting their applicability [38]. PIV, therefore, has been adapted to resolve 3D and/or 3C velocity vector, and a number of sophisticated PIV techniques are established since now. These include 3D PTV [39] [40] [41], stereo PIV [42], scanning PIV [43], stereo-scanning PIV [44], holographic PIV [45], defocused PTV [46] [47], micro PTV (μ-PTV) [48], tomographic PIV [49] or scanning tomographic PIV [50]. However, all these techniques for 3D and/or 3C velocimetry require multiple cameras [39] [40] [41] [42] [49] or complex optical configurations [43] [45] [46] [47] [48]. TABLE 2-1 shows the measurable number of dimensional space, velocity components, and essential number of cameras in each category of PIV resolving 3D and/or 3C velocity vector field.

For the experimental investigations of flows in multiphase flows, PIV has been also used because of its advantages; PIV can resolve spatio-temporal velocities of phases, positions of dispersed phase, and boundary between phases [22] [81] [82] [83] [84] [85] [86] [87] [88] [89] [90] [91] [92] [93] [94]. Some of the PIV leverages the intensity, or/and size of the objects, shadow in images, in order to identify the dispersed phases and tracer particles in the carrier phases [22] [83] [88] [90] [91]. This method for the identifications is applicable for the flow containing at least 10 times larger size of dispersed phase comparing with that of tracer particle [90] and 5 times larger bubbles are distinguished at the smallest case [22]. Intensity of the refection light from the boundary between dispersed and continuous phase increases and inhibits the identification of tracer particles around the dispersed phase, when the size of dispersed phase comparing to the racer particle increases. To overcome the difficulty in measurements, backlighting being different color of light from one for the illumination of tracer particles is concomitantly used for shadow imaging of dispersed phases [81]

[82] [84] [85] [86] [87] [89]. This technique for dispersed multiphase flow requires complex optical configurations consisting from multiple cameras, optical filters, and two different light sources for backlight and sheet illumination, and requires usage of fluorescent tracer particle: called PIV utilizing shadow imaging technique (SIT) and laser induced fluorescence (LIF)). As a simpler method for discrimination of dispersed particles, Kitagawa, *et al.* [94] used the intensity ratio of RBG color information of scattering and fluorescent light from particles for the phase discrimination. Despite the developing of PIV for multiphase flow mentioned above, the identification of dispersed phase with being same size of tracer particle is the challenging subject to be established. Furthermore, the PIV techniques for measurement of neither 3D–3C velocity nor multiphase flow address the remaining problem of simplicity.

Utilization of color information has been tried by PIV developers since 1980s, as a method for obtaining additional information from a single image. One of the applications utilizing color information is color-based 3D PTV (e.g., [50] [52] [53] [54] [55] [56] [57] [58] [59] [60] [61]) which can produce 3D velocity vector fields via simple configurations using commonly available optical equipment, such as a single color-imaging camera and a liquid-crystal display (LCD) projector for color illumination. The color-imaging cameras record the images from the colored light of scattered particles in the measurement volume illuminated by a gradational-colored light. Then, the ‘depth position’ (i.e., position in camera view direction) of particles is estimated from the color of the scattered light, in principle. Furthermore, this concept of idea using color information on particle images is applicable for identifying particles in multiphase flow. For example, in multiphase medium, fluorescent tracer particles are identified from the color of their fluorescent light, that differ from the color of scattering light from bubbles or solid particles. These PTVs utilizing color information require no 3D optic–geometric calibration prior to doing experiments. The simplicity and easy implementation of this system are the greatest advantages of this approach over conventional techniques [39] [40] [41] [42] [43] [44] [45] [46] [47] [48] [49] [50]. Color PTV, however, remains underdeveloped because of large uncertainties in identifying the representative colors of particles. For example, Ido *et al.* [56] tracked ten consecutive positions of individual particles by spline-curve approximation. Although this approach minimizes the random error in color information, it restricts particle

matching in the image sequence. Previous studies incorporating color information cannot use the whole color range of hues, which ranges from 0 to 360 degrees (Munsell [62] [63]), but are limited to 240 degrees of hues at most [52] [56]. Classification of color-painted particles is also subject to difficulties and ambiguities regarding the color information [64] [65]. A neural network approach such as that adopted by Bendickes *et al*. [65] satisfactorily tackles the particle classification problem, but provides no clear definition of the color of the particles. Thus, accurate color identification remains an ongoing problem.

This study proposes new algorithms that minimize the uncertainties in identifying the colors of individual particles under PTV. In addition, the algorithms enhance the color range over which PTV can operate *whole color range* and *multicycle color range*. The algorithms are tested on (i) measurements of particle positions on the basis of particle color information for 3D PTV and (ii) identification of fluorescent particles in bubbly flows. Algorithm performance is evaluated and compared with that of conventional algorithms. To investigate the applicability of the algorithms, measurements of a 3D–3C velocity vector field in a rotating flow using a single camera and multiple-cycle color gradation light are performed. Finally, the system performance is verified by measurements of an unsteady non-axisymmetric flow generated by a rotating impeller, in which the iso-surfaces of physical values exhibiting vortex structures formed in the unsteady flow are calculated from obtained 3D–3C velocity vector fields.

TABLE 2-1 Categories of PIV resolving three-dimensional and/or three-component velocity vector field

Categories	Dimensional space	Velocity component	Number of camera	Special equipment
3D PTV [39] [40] [41]	3	3	3	· Volumetric illumination
Stereo PIV [42]	2	3	2	· Planimetric illumination
				· Optical offset les
Scanning PIV [43]	3	2	1	· Planimetric illumination
				· Galvano mirror
Stereo scanning PIV [44]	3	3	2	· Planimetric illumination
				· Galvano mirror
				· Optical offset les
Holographic PIV [45]	3	3	1	· Laser volumetric illumination
				· Hologram plane screen
Defocused PTV [46] [47]	3	3	1	· Volumetric illumination
				· 3 pinhole mask
Micro PTV [48]	3	3	1	· Volumetric illumination
				· Microscope
Tomographic PIV [49]	3	3	4	· Volumetric illumination
Scanning tomographic PIV [50]	3	3	4	· Volumetric illumination
				· Galvano mirror

TABLE 2-2 PIV in bubbly flows reported in literature

Authors	Type of flow	Dispersed phase diameter [mm]	Tracer particle diameter [μm]	Diamter ratio	Number of camera	Phase separation method
Khalitov & Longmire, 2002 [83]	GS	0.025 - 0.075	1	25 - 75	1	Size, Intensity
Ortiz-Villafuerte & Hassan, 2005 [22]	LG	0.03	6	5	1	Size, Intensity
Tanaka & Eaton, 2010 [88]	GS	0.25, 0.5	0.3	800 - 1700	1	Size
Cheng, *et al.*, 2010 [90]	LS	~ 0.1	8 - 12	~ 10	1	Size, Intensity
Jacob, *et al.*, 2010 [91]	LG	0.15	5	30	1	Size
Bröder & Sommerfeld, 2002 [81]	LG	0.5 - 4	50	10 - 100	2	LIF, OF
Lindken & merzkirch, 2002 [82]	LG	3 - 6	10	300 - 600	1	LIF, OF, SIT
Fujiwara, *et al.*, 2004 [84]	LG	2 - 6	1 - 10	200 - 6000	3	LIF, OF
Kitagawa, *et al.*, 2005 [85]	LG	0.5	1 - 10	50 - 500	2	LIF, OF, SIT
Kitagawa, *et al.*, 2007 [86]	LL	4 - 5	60	70 - 80	1	LIF, SIT
Kitagawa, *et al.*, 2008 [87]	LG	0.4 - 0.8	60	7 - 13	1	LIF, SIT
Sathe, *et al.*, 2010 [89]	LG	0.3 - 15, 52	?	?	2	LIF, OF, SIT
Ishikawa, 2013 [92]	LG	~ 3	60	~ 50	1	LIF, OF, SIT
Hosokawa & Tomiyama, 2013 [93]	LG	2 - 4	N/A	N/A	2	SIT, OF
Kitagawa, *et al.*, 2013 [94]	LGS	0.01 - 0.05 0.05 - 0.14 0.03 - 0.16	N/A	4 (G vs. S)	1	Color intensity

L, G, and S indicate liquid; gas, and solid, respectively. Diameter ratio represents the dispersed phase diameter normalized by tracer particle diameter. LIF, OF, and SIT represent laser induced fluorescence, optical filter, and shadow image technique, respectively.

2.2 Algorithms for identifying particle color

Illumination patterns for color-based PIV techniques are broadly categorized as, discrete layers [54] [60] [61], continuous color-gradation [50] [52] [53] [55] [56] [57] [58] [59], and laser light sheet for LIF [86] [87]. Advantages and disadvantages of the illumination methods have been highlighted by Ruck [61]. While discrete layering provides a clear threshold value for classifying the particle scattering color, the construction of thinner layers is much difficult in the setup for measurements than a coarse resolution in depth using this pattern. At present, discrete layering has achieved a maximum of 11 layers [61]. Particles that locate at the gaps between layers indicate mixed false color resulting in positional estimation errors. Further, the velocity resolution of out-of-plane component depends on the number of layers in this way. Pick & Lehmann [60] adopted a stereo technique to obtain of out-of-plane velocity for this reason. By contrast, continuous gradation in the depth of illumination light is equivalent to seamless color layering. While taking measurements, liquid-crystal display (LCD) projectors can provide color gradation illuminations whose patterns change both spatially and temporally. An image given by an LCD projector consists of a pixilated pattern of red, green, and blue (RGB) dots, and numerous gaps are created between dots on the focused plane. Defocusing the projection light overcomes this disadvantage without modifying the gradation pattern of color illumination. The advantages and disadvantages of different illumination methods are summarized in TABLE 2-3. According to Mie-scattering theory, the scattered light provides demixing of a composed color, depending on the difference between light projection and viewing angle. This demixing also introduces effective error, when the diameter of a tracer particle is smaller than $O(10\ \mu m)$ [61]. Unlike PIV, PTV requires low particle concentration and large particle areas on a pixelated image because of the need to identify each particle. Further, targets for the color-based 3D PTV in the present study are on centimeter rather than micrometer scale. Hence, 100 μm is assumed an appropriate diameter for the flow tracer [60] [61]. Moreover, images on a focal plane display optical aberrations, including chromatic aberration, when light passes the lens of a camera. Consequently, the particle shape on an image is distorted, and the color at the particle edge differs from the actual color. CCD/CMOS sensors in digital imaging devices contain non-reactive areas, excluded from micro-lenses on photodiode arrays,

which also create false colors [57]. Furthermore, color information processed in commonly available digital color-imaging devices comprises the RGB primary colors corresponding to human trichromatism, whereas color variation comprises continuous spectrum of wavelengths in nature. This discrepancy creates additional challenge for accurate particle color identification using these devices. The resulting recorded color information contains uncertainties when the color of a particle is represented as the color at the centre of the pixels representing the particle. The above-mentioned uncertainties and the sites of their occurrences are summarized in FIG. 2-1. The uncertainties depends on the categories of particle illumination for 3D-3C PTV or particle classification in multiphase flow measurement, most of the uncertainties, however, arise as general problems in commonly used equipments, lens or CCD/CMOS in a camera.

To reduce the uncertainties introduced by these multiple factors and by random noise at any time, averaged hue in linear coordinates (hereafter AH-L) has been conventionally adopted [56] [59]. Hue [66], H, lies within the range $H \in [0, 360]$ degrees, and is defined as

$$H = \begin{cases} 60 \times \dfrac{G-B}{\max(R,G,B) - \min(R,G,B)} & (\text{if } \max(R,G,B) = R) \\ 60 \times \dfrac{B-R}{\max(R,G,B) - \min(R,G,B)} + 120 & (\text{if } \max(R,G,B) = G) \\ 60 \times \dfrac{R-G}{\max(R,G,B) - \min(R,G,B)} + 240 & (\text{if } \max(R,G,B) = B) \\ \text{undefined} & (\text{if } R = G = B) \end{cases}, \quad (2\text{-}1)$$

where variables R, G, and B represent the intensity of red, green, and blue, defined over $R \in [0, 1]$, $G \in [0, 1]$, and $B \in [0, 1]$, respectively. When the result of the first equation in Eqs. (2-1) is negative (e.g., −30 degrees), it is replace with its corresponding positive value in the 0 to 360 degree range (e.g. −30 degrees becomes 330 (= 360−30) degrees). This coordinate system is discontinuous at ‘red’ (where hue equals both zero and 360 degrees), although the hue changes continuously (i.e., is differentiable) at around this point. The particle color distributions in linear coordinates are illustrated in FIG. 2-2 (a). The white and gray bars indicate, hue-saturation [67] or hue-chroma [68] distribution of pixels within individual particles. Because of the discontinuity in the

linear coordinate, the arithmetic hue average of pixels with scattered light centering on red (gray bars) is falsely estimated as cyan. To calculate a more accurate value of hue, we here adopt the principle of circular mean [69] [70], in which a particle's representative color is given as the averaged hue in polar coordinates (hereafter AH-P). FIG. 2-2 (b) shows hue-saturation or hue-chroma plane in polar coordinate. The white and gray circles indicate, respectively, hue-saturation or hue-chroma distribution of pixels within individual particles. Since polar coordinates are free of discontinuities, the averaged hue in polar coordinate provides a more appropriate descriptive color than that obtained in linear coordinates. The averaging equations of AH-P are defined as

$$\begin{cases} C_1 = \dfrac{1}{n}\sum_{i=1}^{n}\cos\left(H_i\right) \\ C_2 = \dfrac{1}{n}\sum_{i=1}^{n}\sin\left(H_i\right), \\ \bar{H} = \tan^{-1}\left(\dfrac{C_2}{C_1}\right) \end{cases} \tag{2-2}$$

where H_i is the hue value of the i-th pixel in an area where a particle was projected on, C_1 and C_2 are the axes in Cartesian coordinates on the plane. The positions, C_1 and C_2, are calculated first, and then the averaged hue of the particle, $\bar{H}$, is determined from Eq. (2-2). The arctangent domain is restricted from −90 to 90 degrees, and the value of H is adjusted depending on the signs of C_1 and C_2, which admit values of $\bar{H}$ between 0 and 360 degrees inclusive in the calculation of $\tan^{-1}$ value. McGregor *et al.* [59] used a weighting function to reduce the influences of the measurement noise. In this way, whiteness pixels of higher intensity make larger contributions to the averaging. The hue of averaged RGB (HARGB) in an area, where a particle was projected on, is a one of simple averaging algorithms. During the averaging process of HARGB, however, the intensity of the pixel makes contribution of weighting factor. By contrast, we posit that saturation and chroma are more suitable weight function factor for particle color representation. Saturation and chroma lie within the range of $S \in [0, 1]$, $C \in [0, 1]$, and are defined as follows;

$$S = \frac{\max\left(R,G,B\right) - \min\left(R,G,B\right)}{\max\left(R,G,B\right)}, \tag{2-3}$$

$$C = \sqrt{\frac{3}{2}}\sqrt{\frac{R^2+G^2+B^2}{\left(R+G+B\right)^2}-\frac{1}{3}}. \tag{2-4}$$

The weighted averages of C_1, C_2 and H in the polar coordinates are defined as

$$\begin{cases} C_1 = \dfrac{\sum_{i=1}^{n} f_{\mathrm{w},i}\cos\left(H_i\right)}{\sum_{i=1}^{n} f_{\mathrm{w},i}} \\ C_2 = \dfrac{\sum_{i=1}^{n} f_{\mathrm{w},i}\sin\left(H_i\right)}{\sum_{i=1}^{n} f_{\mathrm{w},i}}, \\ \bar{H} = \tan^{-1}\left(\dfrac{C_2}{C_1}\right) \end{cases} \tag{2-5}$$

where $f_{\mathrm{w},i}$ is a weighting function that overplays saturation, S, or chroma, C. The range of chroma depends on the hue. For instance, the maximum value of chroma at hue of 60 degrees is 0.5, not 1. It seems that saturation yields a fairer weight function than chroma, because the maximum value of saturation is 1 at all hue angles. Particles in an image are identified by the threshold value of their 'value', denoted by V, on each pixel and searching eight surrounding pixels. Value [66], V, lies within the range of $V \in [0, 1]$, and is defined as

$$V = \max\left(R,G,B\right). \tag{2-6}$$

Imposing the threshold ensures that low-value particles with ambiguous hue are excluded from the averaging process. After averaging, positions on the image plane are defined as the center of the particle area.

Seven algorithms were proposed, whose performances are examined in the next section. These algorithms are as follows: center of a particle (CP, in which hue is extracted from the center of the particle area); the AH-L; the chroma-weighted-averaged hue in the linear coordinate (CWAH-L); the saturation-weighted-averaged hue in the linear coordinate (SWAH-L); the AH-P, the chroma-weighted-averaged hue in the polar coordinate (CWAH-P); and the saturation-weighted-averaged hue in the polar coordinate (SWAH-P). For illustrative purpose, three colors in a representative particle are listed in TABLE 2-3. FIG. 2-2 (c) shows how these colors appear on pixels, while

the white circles in FIG. 2-2 (d) show the positions of the colors in the hue-saturation plane. The hues assigned to the particles by the seven algorithms, in addition to HARGB as a reference case, are listed in TABLE 2-4, and highlighted by arrows in FIG. 2-2 (d). Because CP was unable to define the hue of Pixel 2, which locates at the center of the three particles, this pixel is excluded from the averaging algorithms.

The idealized quantization number of the hue depends on the bit depth of the color components. For example, 8 bit RGB color provides N_H (= 6 × 2^8) = 1536 hues, when saturation is at maximum value. The idealized resolution of the hue is then ΔH (= 360 / N_H) = 0.23 degrees, in principle.

Table 2-3 Pixel color decomposition of a particle composed of three particle

Variables	Pixel 1	Pixel 2	Pixel 3
R	1	1	0.5
G	0.5	1	0
B	0.5	1	1
H	0 degrees	Undefined	270 degrees
S	0.5	0	1
C	0.25	0	0.58
V	1	1	1

Table 2-4 Hue calculated by various algorithms

Algorithms	Hue [degrees]
CP	Undefined
HARGB	300
AH-L	135
CWAH-L	188
SWAH-L	180
AH-P	315
CWAH-P	293
SWAH-P	296

TABLE 2-5 Categories of color information supplied to various PIV applications.

Categories	Advantages	Disadvantages	Applications
Lasers	· Discrete wavelength (layered method)	· Low resolutions	· 2 layered stereo PIV [54]
		· Gaps	· 3D positional detection [61]
	· Continuous hue (gradation method)	· Low resolutions	· 3D–3C PTV
		· Mie-scattering	(Principle) [50] [52] [53],
			(3D visualization) [55]
Prism	· Continuous wavelength	· Divergence	· Out-of-plane velocimetry [57]
		· Mie-scattering	· 3D visualization [52] [58]
			· 3D positional detection [59]
Filtered color light	· Discrete hue	· Low resolutions	· 6 layered stereo PIV [60]
		· Gaps	
		· Divergence	
		· Mie-scattering	
LCD projector	· Continuous hue	· Mie-scattering	· 3D particle trajectories [56]
	· Changeable and adjustable color pattern	· Divergence	· *Present chapter*
	· Easy setup	· Dot pattern	
Colored particle	· Increase in number of particle matching	· Ambiguities in classification	· Particle classification [64] [65]
Multiphase flow	· Single camera setup	· Mie-scattering	· Phase discrimination [94]
	· Discrimination in same size of particles		· *Present chapter*

2.3 Evaluation of the algorithm performances for color information processing

2.3.1 Setup

A schematic outline of the experimental apparatus and configuration for evaluating the performance of the proposed algorithms is shown in FIG. 2-3. The experiments were conducted using a transparent, rectangular open tank made of Plexiglas (where the ends of the tank are of area 150 × 150 mm^2). Tap water containing porous resin particles (HP20SS, Mitsubishi Chemical Co., specific gravity 1.02 and mean diameter 100 μm) was poured into the tank to a depth of 100 mm. The color gradation light varying in color in the vertical direction, x, was generated by an LCD projector (TH-LB10NT, Panasonic Co., 220 W, 2000 lm), and the thickness of the color-gradated light sheet, δz, was 10 mm (see FIG. 2-3). The hue of the gradated color code linearly changes from zero (at $X = 0$) to 360 degrees (at $X = 1$) along the X ($= x / x_{cycle}$) axis, and completes a further cycle from $X = 1$ to $X = 2$, following the relationship given as

$$H = \begin{cases} 360X & (\text{if } 0 \le X \le 1) \\ 360(X-1) & (\text{if } 1 \le X \le 2) \end{cases}. \tag{2-7}$$

Saturation (Eq. (2-3)) and value (Eq. (2-4)) are constant in the cylindrical HSV color space [71]. The particle images obtained from the colored scattered light were recorded by a digital camera (D700, Nikon Co., 36.0 × 23.9 mm RGB Bayer CMOS, 4256 × 2832 pixels) with a lens (focal length, 200 mm; aperture, F8; Tamron Co.) in a direction perpendicular to the projection direction of the illuminated light sheet. The size of the test section is 50 mm × 13 mm and the corresponding pixel number was 1900 × 500 pixels at spatial resolution of 20 μm/pixel. FIG. 2-4 shows an idealized artificial synthetic image (AI), an experimental image (Exp.) captured by a digital camera, and the particle positions identified from the experimental image. The brightness of a particle in the artificial image is represented by a Gaussian function with random noise, and the S/N ratio is 3 (4.8 dB). The hue of particles in the artificial image changes linearly with the particle position. Because the hue of the gradational color code projected by the LCD projector yields identically to that of the artificial image, the experimental images are expected to show the same gradation lines as a function of the particle position.

2.3.2 Evaluating the performance of the algorithms

FIG. 2-5 plots the distribution of particle color determined from the algorithms developed here, (a) CP (hue extracted at the center of the particle area), (b) AH-L (averaged hue in linear coordinates) and (c) AH-P (averaged hue in polar coordinates) for the various X, positions. The figures in the left panels display results from the experimental data (FIG. 2-4 (b)), while the right panels represent those from the idealized artificial synthetic image (FIG. 2-4 (a)). All of the algorithms distorted the hue variations in the experimental data, while the artificial images preserve the original linear relationship between hue and position. The distortion in the experimental data arises from the characteristics of the devices used, i.e., the LCD projector and/or the digital camera. The local resolution of positional estimation by particle color is determined from the inverse gradient, $\partial X/\partial H$. The distortion can be improved by adjusting the color balance of the projector or the programming code for the projection light source. One potential solution is to adopt a feedback mechanism that adjusts for aberrant light source and/or color distortion in captured images (see in FIG. 2-1). This study focuses on the performance of the algorithms for particle color identification. The deviations in the distributions of the hues (H) obtained by both AH-L and AH-P are smaller than that from CP. The AH-L, however, produces large deviations at $X \sim 0$, 1, and 2, where the linear coordinates become discontinuous and create false colors. By contrast, the AH-P shows a smaller variance in this color region.

To quantitatively evaluate the performance of the algorithms, the standard deviation for the hue, σ_H and position, σ_X, were calculated. Particle position, X, estimated from the representative color of particles was calibrated as a spline-curve connecting the average of the hue at 72 sections in the X direction. Because the conclusive performance of the color-position or color-class conversion depends on the curvature of the calibration curve and the deviation of each particle color from the calibration curve, σ_H and σ_X were defined as the deviation from the spline curve. Furthermore, since the color identification may depend strongly on exposure time, three different exposure times were examined for each of the seven algorithms (CP, AH-L, CWAH-L, SWAH-L, AH-P, CWAH-P, and SWAH-P). The σ_H and σ_X for each algorithm and the exposure time are shown in FIG. 2-6. The exposure time which is controlled by the shutter speed (SS) of the camera reaches its local minimum standard deviation at SS

= 1/50 s for the all algorithms; similar optimal exposure conditions for color identification have been also reported by McGregor *et al*. [59]. This may be ascribed to the fact that hue depends on the gradation of the RGB value of a pixel; therefore loss of the RGB tone during over/under exposure causes the standard deviation to increases. In the case of SS = 1/50 s at 360 degrees of hue, the algorithms processed in linear coordinates (AH-L, CWAH-L, SWAH-L) yield an uncertainty in the color determination three times larger than that of CP, because of the false color around red, at $H = 0$. The algorithms utilizing polar coordinates (AH-P, CWAH-P, SWAH-P) achieve 30 % lower standard deviation than that with CP. As expected, using a limited hue domain that excludes the discontinuity, $30 < H < 330$ (300 degrees), provides a significantly smaller standard deviation even with the linear coordinates. The polar coordinate systems provide superior results across the entire range of hues. The effort of using chroma or saturation in the weighting function for the averaging was also investigated. The hue distribution of CWAH-P was somewhat more distorted into RGB original color than that of SWAH-P because of the inhomogeneous definition of chroma (Eq. (2-4)) across the hue range. Comparing SWAH-P to AH-P or CWAH-P, the deviations in particle position from the spline-curve are improved by 7 % at most. It can be concluded that, in minimizing the uncertainties in particle color identification, the most important factors are the selection of the coordinates for averaging and enrichment of the gradation (RGB tone) of particle color.

In the present evaluation, SWAH-P yields minimum errors of 1.4 % in the particle hue and 2.0 % in the position, X, estimated from the hue. According to the linear relationship between hue, H, and position, X, given as Eq. (2-7), the relationship between resolutions of hue, ΔH, and position, ΔX, is given as

$$\Delta H = 360 \Delta X \ . \tag{2-8}$$

Thereby, the resolutions of hue, ΔH, and position, ΔX, should be identical in principle. In practice, the standard deviation in the depth position is slightly greater than in the hue from which the depth is transformed, because the hue-position function is distorted (as discussed above and illustrated in FIG. 2-5). However, because of the one-on-one correspondence between position and hue, the nonlinear effects caused by distortion exert no significant effect on the estimation of the particle position.

2.4 Application 1: LCD-projector-based 3D color PIV

2.4.1 Multi-cycle color illumination for higher spatial resolution

Particle tracking velocimetry provides two-dimensional two-component velocity vectors from the displacement of the particle positions from two consecutive images in general principle. The resolution of velocity depends on the image resolution. Sub-pixel estimation of particle position provides 1/10 accuracy in pixel [71]. Using color gradation light does not provide a linear relation but one-by-one correspondence between hue and position (see SECT. 2.3), particle positions in the depth (viewing direction), z, are available from the color information. In the setup of the volumetric illumination, hue, H, of the gradation is given as a function of the depth position, z, as

$$H = cz\,, \tag{2-9}$$

where c is a constant (but is also a function of z in feedback adjustment (see in FIG. 2-1)), in degrees/mm. Since the particle position in the depth is directly calculated from its hue only in cases in which the c is constant, the resolution of the depth position, Δz, is of the same order as the resolution of the hue, ΔH, as

$$\Delta z = \frac{1}{c}\Delta H\,. \tag{2-10}$$

According to the above estimations, the depth position can, in principle, be divided into 1536 partitions for a one color-cycle from red to red via green and blue, when an image is consisted from 8 bit RGB information. The scattering plots of hue, H, and position, X, show nonlinear curvature, i.e. distortion from a line, in experiments (see in FIG. 2-5). Standard deviation hue depends on the ambiguities of color in a particle. While, standard deviation of a particle position estimated from a particle color depends on nonlinearity of H-X relation in addition to the ambiguities in particle color estimation. The estimations of the hue of particle and particle position from its hue also yield the standard deviation in the estimation of particle hue of σ_H / H = 1.4 % and standard deviation in the positional estimation of particle from its hue of σ_X / X = 2.0 %, respectively, from saturation-weighted-averaged hue in the polar coordinate (SWAH-P) providing the lowest values (SECT. 2.3). These standard deviations give errors in hue of E_H (= $2\sigma_H$ / H) = 2.8 % and positions of E_X (= $2\sigma_X$ / X) = 4.0 % for the confidence interval of 95 % (2σ). In other words, the depth was divided into 25 partitions (N_z = 1 / ($2\sigma_z$ / z) = 1 / ($2\sigma_X$ / X)) in the experiments conducted here. Another important and

remarkable aspect of 3D PTV that ensure its accuracy is the resolution of the velocity component in the depth direction. Velocity vectors, $\boldsymbol{u}$, are derived from the displacement of a particle position in two consecutive images, and are given as,

$$u = \alpha \frac{\boldsymbol{x}_2 - \boldsymbol{x}_1}{\Delta t}, \tag{2-11}$$

where, α, $\boldsymbol{x}_1$, $\boldsymbol{x}_2$, and Δt are unit conversion factors from pixel to mm, position of the particle at 1st, 2nd, and time interval, respectively. Position errors, $E_{\boldsymbol{x}}$ (= $2\sigma_X$), propagate with the velocity errors, $E_{\boldsymbol{u}}$, defined as

$$E_u = \alpha \frac{\sqrt{2}E_x}{\Delta t}. \tag{2-12}$$

The errors in the velocity, therefore, is $E_{\boldsymbol{u}}$ = 5.7 %, in the experiments conducted here. This uncertainty, which defines the relative resolution in the measurement depth direction, is larger than that of μ-PTV, using a single camera and the geometry of astigmatic-defocused images of 2.24 % [48]. Indeed, the error obtained here is acceptably small for general flow measurements, and can be further reduced by adjusting the color code of the projection light (FIG. 2-1), as mentioned above.

Despite the improvements in particle color determination imparted by our algorithm utilizing average in polar coordinates, the resolution and accuracy in the depth direction determined from color information of the particles remain much larger than those in the imaging plane. To overcome this disadvantage in color-based 3D–3C PTV, without compromising simplicity, our proposed technique was extended to multi-cycle color illumination. The principle of multi-cycle color PTV is shown in FIG. 2-7. FIG. 2-7 (a) shows general single-cycle color profile for the volumetric illumination whose color profile changes in depth direction, *z*, on the other hands, (b) and (c) shows the two and four-cycle color gradation of illumination light, respectively. A coarse estimate of the particle position is obtained using a single-cycle color profile with one-on-one correspondence between hue and depth position, even in the case using multi-cycle color gradation. Following the presentation of the second image, the resolution in the depth position of the particle is attained by the projection of multi-cycle color gradation. Sequential changes in LCD projector images can be achieved in 1/30 second steps in general, with corresponding color gradation changes in consecutive measurements. Much greater latitude and control of illuminations are

offered by LCD projectors than by lasers [50] [53] [54] [55] [61] or by prisms [52] [57] [58] [59]. Particle positions can be estimated during each color cycle ($\boldsymbol{x}_{2,1}$, $\boldsymbol{x}_{2,2}$ ...), and are tracked from an original position (estimated in the single cycle condition) by four-time-steps PTV. In the PTV scheme, a ghost particle may be tracked when the particle displacement between two images exceeds half of the color gradation thickness (x_{cycle} / 2). The measurable magnitude of the velocity vector is constrained by

$$u_{\max} = \frac{x_{\mathrm{cycle}}}{2\Delta t}. \tag{2-13}$$

In FIG. 2-7 (b), the correct particle position at each time step is given as the trajectory [$\boldsymbol{x}_1$, $\boldsymbol{x}_{2,1}$, $\boldsymbol{x}_{3,1}$, $\boldsymbol{x}_{4,1}$]. Even when inequality of Eq. (2-10) is satisfied, the PTV scheme may provide incorrect particle positions, for example, the trajectory [$\boldsymbol{x}_1$, $\boldsymbol{x}_{2,2}$, $\boldsymbol{x}_{3,2}$, $\boldsymbol{x}_{4,1}$] might be estimated as the most likely. Erroneous vectors due to incorrect particle positions can, however, be eliminated by comparison with surrounding vectors. The resolution in the depth direction can be improved by (I) estimating the maximum velocity and (II) setting the number of color cycle of gradational illuminations prior to conducting an experiment.

2.4.2 Experimental setup and configuration

To assess the performance and applicability of the developed algorithms in color identification of particles for color-based 3D–3C PTV, the algorithms were applied to a well-known 3D helical rotating flow driven by a rotating disk [29]. Although this rotating flow has a simple forced vortex structure, the 3D–3C velocity vector fields are difficult to measure unless axial symmetry is assumed, which allows validation of the out-of-plane velocity component obtained in the imaging plane. The experimental setup and general configuration of the test are shown in FIG. 2-8. A disk of radius in 30 mm was rotated at rotation frequency of 30 rpm in a cylindrical container made of Plexiglas (radius, 80 mm). The container was set in a transparent water jacket with 200 mm cubic. The rotating disk was concentric with the outer cylindrical container. Tap water seeded with resin particles (as described in Sect. 3) was used as the working fluid. The central vertical plane of the cylinder was illuminated by a gradational-colored light sheet of thickness, 50 mm, and the color changed with the camera view direction, z, relative to the LCD projector. The gradational-colored light was characterized by single (360

degrees) of hue. The center of the light sheet was located at the axis of the rotating disk. The observation volume, delineated by the dashed cube FIG. 2-8, was 50 × 50 × 50 mm. Images containing 1300 × 1300 pixels were recorded by a digital camera. Over a single color gradation cycle, the spatial resolutions of the camera were 38 μm/pixel in both *x* and *y* directions, and 2.5 mm/arbitrary scale in the *z* direction. Temporal resolution was 0.125 sec/frame.

2.4.3 Particle trajectory and velocity vector as a qualitative visualization

FIG. 2-9 (a) shows the trajectories of particle positions from 15 sequential images (corresponding to 2 seconds) inside the measurement volume. The gray scale indicates the depth position estimated from the particle color determined by SWAH-P. These particle trajectories qualitatively express the rotating flow. Direction of the rotation is revealed by the velocity vector distribution obtained under four-time-steps PTV [41] (FIG. 2-9 (b)). The color of arrows in the figure indicates the magnitude of the out-of-plane velocity component, u_z. For the correct evaluation of the measurement accuracy, the velocity vectors were not interpolated or smoothed.

The tracer concentration in the fluid layer was increased for the investigation of the number of tracer particles detectable by the present technique. The instantaneous numbers of detected particles and velocity vectors obtained in each PTV procedure are listed in TABLE 2-6. In these tests, the measurement volume was adjusted to 45 × 78 × 30 mm, with corresponding image size 1800 × 3120 pixels. Nearly 700 instantaneous 3D–3C velocity vectors were obtained by the PTV. Following the elimination of erroneous vectors (EEV) by comparison with surrounding vectors [71], 500 velocity vectors remained, equating to about 30 % of the particles identified in the single shot image. The number of velocity vector from PTV depends on camera resolution, frame rate, particle-tracking algorithm, and flow pattern in the measurement volume, as has been widely emphasized in previous literature to date. This quantity of vectors is sufficient to represent the flow structure of rotating flow.

Table 2-6 Number of particles and velocity vectors per image

Quantities	Number	Number density [cm^{-3}]
Particles	1562	14.8
Vectors	685	6.5
Vectors after EEV*	503	4.8

*EEV = elimination of erroneous vectors

2.4.4 Evaluating accuracy of single and multiple-cycle color techniques

The measurement accuracy can also be further assessed by a scattering plot and statistical analysis assuming an axisymmetric flow pattern. Generally, rotating flows are conveniently expressed by converting polar coordinates to Cartesian coordinates u_x and u_z as follows:

$$\begin{cases} u_x = -u_\theta \sin\theta + u_r \cos\theta \\ u_z = +u_\theta \cos\theta + u_r \sin\theta \end{cases}, \tag{2-14}$$

where u_θ and u_r are the circumferential and radial velocities, respectively. The flow structure is a forced vortex ($u_\theta = ar$, where a is a constant), giving a radial velocity component outside of the boundary layer is minor effect, since the magnitude of the radial velocity component is less than 1/10 comparing to that of the circumferential velocity [29]. Under these conditions, Eq. (2-11) is reduces to

$$\begin{cases} u_x = -az \\ u_z = +az \end{cases}. \tag{2-15}$$

The mean velocity and the standard deviation of the velocity components along the x or z directions in the x-z plane obtained by the proposed PTV arrangement are shown in FIG. 2-10 and FIG. 2-11. The light sheet projected onto the fluid layer was subjected to various color cycles: one ((a) and (d)), two ((b) and (e)), and four ((c) and (f)) in both FIG. 2-10 and FIG. 2-11. FIG. 2-10 shows that the velocity components in the figures increase or decrease linearly in the directions as specified by Eq. (2-12). The u_z component of the two-cycle color code is more smoothly distributed than that of one or four cycles of color gradation. FIG. 2-11 shows that the standard deviation of the x velocity component σ_{ux} increases at four-cycle comparing to one and two-cycle: standard deviation of the z velocity component σ_{ux} monotonically decreases with

increasing the number of gradation color cycle. The velocity distributions along the x and z directions and their approximate least-square linear fits are shown in FIG. 2-12. The best fit gradient of the approximate line, a, and standard deviation of the velocity around the approximate line, σ_u, are detailed in TABLE 2-7. The minimum standard deviation of velocity, σ_{uz}, estimated from the propagation of errors estimated from Eq. (2-9) is 11.3 mm/s. Color illumination scheme of one and two cycles provide similar values for a (~ 1.7 s^{-1}). However, the velocity component in the depth direction (expressed by σ_{uz}) is better resolved under two-cycle color gradation. Four color-cycles illumination generates somewhat larger deviation of a, and increases σ_{uz}, because of an increased number of incorrectly tracked particles. In four-time-steps PTV, if the radius to search particles in the next time step, R_{search}, [41], is set to larger than half size of the color gradation cycle, x_{cycle}, a ghost particle near the first particle position is tracked in the PTV procedure as the most likely trajectory (see FIG. 2-7). And thus this increases erroneous vectors. In the present measurements, a constant R_{search}, was used for every cycle of the color illumination, such that the corresponding radius of R_{search} / x_{cycle} were 0.15, 0.30 and 0.61 (larger than 0.5) for one, two, and four cycles, respectively. This shows that the resolution of the position and velocity component in the depth direction is improved, when R_{search} is set to be smaller than the half size of x_{cycle}, following the manor given as Eq. (2-10).

Table 2-7 Gradient and standard deviation of velocities in an axisymmetric rotating flow test

	R_{search} / x_{cycle} [-]	a_x [1/s]	a_z [1/s]	σ_{ux} [mm/s]	σ_{uz} [mm/s]
Theory	-	-	-	4.7	11.3
1 cycle	0.15	1.7	1.8	5.5	14.0
2 cycles	0.30	1.6	1.7	5.6	9.7
4 cycles	0.61	1.5	1.9	9.1	8.5

2.4.5 Measurement of instantaneous flow quantities

To exam the applicability of the new averaging algorithm in color-based 3D PTV, a global flow structure of non-axisymmetric unsteady turbulent flows were measured. To create such a flow using the same configuration as for the accurate validation (FIG. 2-8), an impeller (height, 20 mm; thickness, 1 mm) was attached on the rotating lid of radius in 30 mm as shown in FIG. 2-13. The schema of experimental configuration is illustrated in FIG. 2-14 (a). The disk rotates at 15 rpm in the cylindrical container made of transparent Plexiglass (radius, 160 mm; height, 160 mm) and the measurement volume, delineated by the cube in FIG. 2-14 (a), is 90 × 60 × 60 mm, corresponding to the width, height, and depth. The spatial and temporal resolutions are the same as those used in the previous section. The unsteady non-axisymetric mixing phenomenon within the cylindrical container was measured using two cycles of color code. The color-coded illumination light was projected from the right-hand side of the apparatus (see FIG. 2-8), enabling visualization of the wake structure induced by the impeller called as s trailing vortex, a significant component of flow mixing [72] [73], when the impeller is positioned at $z > 0$. In addition, it must be noted that the viewing angle and measurement volume are restricted by the moving objects in the multi-camera set-up for the 3D–3C velocity vector measurements.

FIG. 2-14 (b) shows the raw data of the instantaneous velocity vector field obtained by four-times-steps PTV and the post-processing data (following grid point relocation of velocity vectors, interpolation (BER) and correction (VCP) of the vectors [74]) in (c) entire of the flow field and (d) whole of the measurement volume. The region behind the impeller is dominated by a large upward flow, as shown in FIG. 2-14 (a), and an adjoining downward flow region; both of these regions have large circumferential velocities. The depiction confirms the generating and trailing of a vortex by a rotating impeller blade [75] [76]. FIG. 2-14 (e) shows the stream line [77] representing disturbed flow behind the impeller as well as the global flow structure of the rotating flow. Three physical scalar values were calculated from two instantaneous 3D velocity vector fields for quantitative visualization of the vortex structure. The vortex structure are frequently represented in term of vorticity, $\boldsymbol{\omega}$, enstrophy density [78], s, given by

$$s = \frac{1}{2}|\boldsymbol{\omega}|, \quad \boldsymbol{\omega} = \nabla \times \boldsymbol{u}, \tag{2-16}$$

and the Laplacian of pressure [79] [80], Δp,

$$\Delta p = \nabla \cdot \left(-\rho \frac{D\boldsymbol{u}}{Dt} + \mu \Delta \boldsymbol{u} \right), \tag{2-17}$$

Iso-surfaces of axial and circumferential vorticity component, ω_z, ω_θ, enstrophy density, s, and Laplacian of pressure, Δp, are shown in FIGs. 2-14 (f) (g) and (h), respectively. The iso-surface of the axial vorticity component, ω_z, and circumferential one, ω_θ, are exhibited as white and blue iso-surface in FIG. 2-14 (f), respectively. The iso-surface of ω_z and s represent the tilting of the rotating flow, furthermore ω_θ and s represent the trailing vortex behind the tip of the impeller. The iso-surface of Δp is less evenly distributed than s, because the BER interpolation scheme used in the post processing of the raw velocity vector field supports up to second-order continuities in the velocity distribution, while Δp requires a third-order differential to determine the velocity distribution (Eq. (2-14)). Consequently, the iso-surface of Δp used to display localized strong vortex tubes, i.e., vertical structures accompanied by large deformation of flow elements, may not be clearly depicted on this iso-surface (FIG. 2-14 (h)). Although the Δp iso-surface is ineffective at representing the vortex structure investigated here, it remains of use in detecting localized strong vortex tubes. Here we emphasize that color-based 3D PTV can provide such differential values of velocity fields with quality comparable to that of CFD.

As mentioned above, the stream lines, the vorticity, and the enstrophy density calculated from the instantaneous 3D–3C velocity distribution provide good qualitative representations of the global flow structure, even if the resolution in the depth direction remains inferior to that in the imaging plane.

2.5 Application 2: particle discrimination in multiphase flow

2.5.1 Experimental setup and configuration

In order to identify tracer particles, bubbles or solid particles, the intensity on pixels or/and the size of object area on images are used as conventional method in dispersed multiphase flow highlighted in TABLE 2-2. The diameter ratio, the bubble normalized by the one of the tracer particle, were greater than $O(10)$, and the minimum diameter ratio identified so far was 5 (Ortiz-Villafuerte & Hassan, 2005 [22]) in the literatures. These method, however, are not applicable for the measurement of multiphase flows which contain seeded tracer particles in diameter of the same order as that of dispersed phase, like a microbubbly flow. Good performance of particle color identification with standard deviation of 1.4 % (SECT. 2-3) suggests us use of color information for discrimination of tracer particles and bubbles without information of intensity or area of particles on an image. The color information of fluorescent light from tracer particles containing laser fluorescent dye differ from scattering light from the gas-liquid interface of dispersed phase in a single shot color-image, when the particles and bubbles are illuminated by laser light. Hence, in principle, color information of particles would enable the discrimination of tracer particles and dispersed phase in diameter of as same order as that of tracer particle.

Schematic outline of the configuration in two different systems are illustrated in FIG. 2-15. Tap water containing microbubbles is used as investigation for the identification of the tracer particles and dispersed phase. Hydrogen bubbles with 60 μm in mean diameter were generated by water electrolysis. Two different systems for illumination light and tracer particle containing LIF dye are installed and their performances are investigated. A green laser with orange tracer particles, hereafter GL-OT system (FIG. 2-15 (a)), uses a green laser (MGL-532, Changchun New Industries (CNI) Optoelectronics Technology Co., Ltd., 1000 mW, wavelength: 532 nm) and tracer particles (FLUOSTAR, EBM Co., mean diameter: 15 μm, Specific gravity: 1.1, absorption wavelength: 550 nm, emission wavelength: 580 nm). A blue laser with green tracer particles, hereafter BL-GT system (FIG. 2-15 (b)), uses a green laser (MGL-473, CNI Optoelectronics Technology Co., Ltd., 140 mW, wavelength: 473 nm) and tracer particles (Fluo-MAX, Thermo Co., mean diameter: 50 μm, Specific gravity: 1.1, absorption wavelength: 468 nm, emission wavelength: 505 nm). Specification of

the lasers and tracer particles are listed in TABLE 2-8. Thickness of the laser light sheet was 2 mm in both GL-OT and BL-GT systems. The particle images with color light were recorded by a high speed video-camera (Fastcam MAX 120KC, Photron Co., RGB bayer type CMOS) in the measurement section of 10 × 40 mm whose corresponding size is 256 × 1024 pixels, where the spatial resolution is 39 μm/pixel.

TABLE 2-8 Specifications of properties for particle discrimination in multiphase flow measurement utilizing LIF tracer particle

Title	Name / values (GL-OT system)	Name / values (BL-GT system)
Laser		
Product name	MGL-532	MBL-473
Manufacture	Changchun New Industries (CNI) Optoelectronics Technology Co., Ltd.	Changchun New Industries (CNI) Optoelectronics Technology Co., Ltd.
Power	1000 mW	140 mW
Wavelength	532 nm	473 nm
Tracer particle		
Product name	FLUOSTAR	Fluo-MAX
Manufacture	EBM Co.	Thermo Co.
Mean diameter	15 μm	50 μm
Specific gravity	1.1	1.1
Absorption wavelength	550 nm	468 nm
Emission wavelength	580 nm	505 nm
Diameter ratio	4	1.2

GL-OT is Green laser with orange tracer particle, and BL-GT is blue laser with green tracer particle, respectively.

2.5.2 Algorithms for particle identification

Particles in an image are identified by two different methods, (1) labeling: extraction of the particle position as the center of object area which is identified on the image with the threshold value of their 'value', denoted by *V*, on each pixel and then is searched from eight surrounding pixels, and (2) particle mask correlation (PMC) [95]: extraction of the particle position as the local maxima of the cross correlation between the Gaussian shape mask and brightness pattern of the image. Hue of a particle is calculated by saturation-weighted-averaged hue in polar coordinates (SWAH-P) of pixels which constitute a particle in labeling method. On the other hand hue of a particle is calculated by SWAH-P of pixels whose *V* is greater than the mean *V* in the mask area in PMC method. Rich gradation in hue on pixels could be allowed for calculation of averaging in the labeling method, number of the particle identified by labeling is inferior to one by PMC due to the disadvantage of labeling well elaborated by Takehara & Etoh [95].

Particle identifications using labeling and PMC methods were conducted in GL-OT and BL-GT systems. FIG. 2-16 shows the original color images size of 128 × 128 pixels ((a) and (e)), binalized images of particles identified by labeling ((b) and (f)) and PMC ((c) and (g)), respectively. Upper panels represent the results in GL-OT system, while lower panels represent the results in BL-GT system. Colors in binalized images ((b), (c), (f) and (g)) represent reconstructed particle color in which hues take obtained SWAH-P and values take 1 for good visibility. Numbers of particle identified from PMC is greater than ones from labeling, as expected. Color of particles successfully corresponds to the color in original image despite of the differences between the particle identification methods. Particle positions identified by labeling or PMC are displayed at the same panel shown in FIG. 2-16 (d) and (h). Closed symbol indicates the particle position identified by labeling, and open symbol indicates one by PMC, respectively. Particle positions identified by both labeling and PMC are in good agreement in each other. These qualitative findings led us the advantages of PMC for particle identification even in the color imaging processing.

2.5.3 Particle hue distribution

FIG. 2-17 shows the probability of hue determined from (a) labeling and (b) PMC in GL-OT system, and from (c) labeling and (d) PMC in BL-GT system. Samples are

acquired from 5000 of 8 bit RGB color images. Number of samples is greater than 10^5 in all conditions. In BL-OT system ((a) and (b)), the local maxima around 30 and 120 degree represent orange fluorescent light from tracer particles and green scattering light from the gas-liquid interface of microbubbles, respectively. Further, in BL-GT system ((c) and (d)), the local maxima around 150, 130 and 240 degree represent green fluorescent light from tracer particles and blue scattering light from the gas-liquid interface of microbubbles as well. The difference in the maxima position of hue in particle identification method (labeling or PMC) arises from the lack in richness of the hue on low brightness pixels. Probability distribution of hue depends on the methods for particle identification, two maxima, however, appear in the both methods. Thus, colors representing tracer particles and bubbles in the images can be distinguished using the criteria determined by a multilevel threshold method [96] based on Otsu method [97]. In FIG. 2-17, the vertical lines indicate the criteria of hue discriminating tracer particles or microbubbles. Consequently, this conclude that the color averaging technique provides simultaneous PTV for dispersed phases in diameter of same as tracer particles, using a single camera instead of using two cameras with optical filters.

2.6 Conclusions

This chapter reports improved color-information-utilized in PTV achieved by (1) 3D–3C PTV with a single camera and an LCD projector enabling use in practical applications, and by (2) discrimination of tracer particles in bubbly flow with LIF. The hue measure is used to convert RGB color information of a tracer particle to depth position (position in the out-of-plane direction of the imaging plane). Thus, the identification of the particle color is the crucial factor in the accuracy of the measurements. To minimize the uncertainties in identifying representative scattered colors of tracer particles illuminated by color-coded light, we proposed the saturation(or chroma)-weighted-averaged hue in polar coordinates (SWAH-P or CWAH-P) algorithm. The performance of the algorithms was evaluated by determining the uncertainties in unique position identification experiments. The uncertainties were successfully reduced to well below other conventional algorithms. SWAH-P yielded the smallest uncertainties among the tested algorithms: 2.8 % in hue and 4.0 % in the position estimated from the hue of 95 % confidence. Averaging in the polar coordinates circumvents the discontinuity that occurs in the linear coordinate at the red, hue, so we can detect these hues accurately. To achieve further improvements in the measurement accuracy in the depth direction, a gradation code with multiple color cycles was designed, and measurement principles for applying the code to PTV were proposed.

The 3D velocity vector field obtained by color-based 3D PTV using the proposed algorithm was validated in both a steady axisymmetric and an unsteady non-axisymmetric rotating flow. The measurements revealed that:

(1) A 3D helical rotating flow structure is adequately represented by the particle trajectories. The velocity component in the depth (camera view) direction can be determined from the particle color. The 3D–3C velocity vector field can be captured using a single digital camera and projection of a light source enabling volumetric color gradation.

(2) The accuracy in accuracy of particle position and velocity resolutions in the depth direction are improved by using multiple cycling of the color gradation code. The velocity measurement is limited by the length ratio (the search radius for particle tracking to the thickness of the gradation light sheet per color-cycle, as defined by

Eq. (2-10)).

(3) To evaluate the applicability of the color-based 3D PTV in turbulent flow measurements, a global rotating flow induced by an impeller blade attached to a rotating disk was investigated. Details of the flow field and the trailing vortex behind the blade were visualized as instantaneous velocity vector fields. Stream lines, vorticity, enstrophy density, and Lapracian of pressure calculated from the 3D velocity vector fields were shown to accurately represent the vortex structures in the vessel.

The discrimination of dispersed microbubbles in diameter of same as that of tracer particle for flow visualization was conducted as an application of color information for multiphase flow measurements. The measurement reveals that:

(4) To investigate the applicability of laser induced fluorescent tracer particles in microbubbly flows, particle identification was conducted in two different systems; utilizing (i) a green laser light sheet and orange fluorescent particles, and (ii) a blue laser light sheet and green fluorescent particles. Commonly used particle identification methods, binarization and particle mask correlation, are demonstrated in averaging process of particle hue. Probability distribution of hue weakly depends on the identification method. The local maxima of hue, representing the fluorescent light from tracer particles and the scattering light from gas-liquid interface of microbubbles, appear in results from both identification methods.

Finally, in this chapter, I would like to emphasize that all of the improvements demonstrated here were achieved with simple measurement apparatus. That is, sufficiently accurate measurements can be obtained with a single camera and an LCD projector / a laser light. This simplicity offers the greatest advantage of the technique over other techniques for higher-dimensional velocity measurements utilizing multiple cameras or complex special optical equipments.

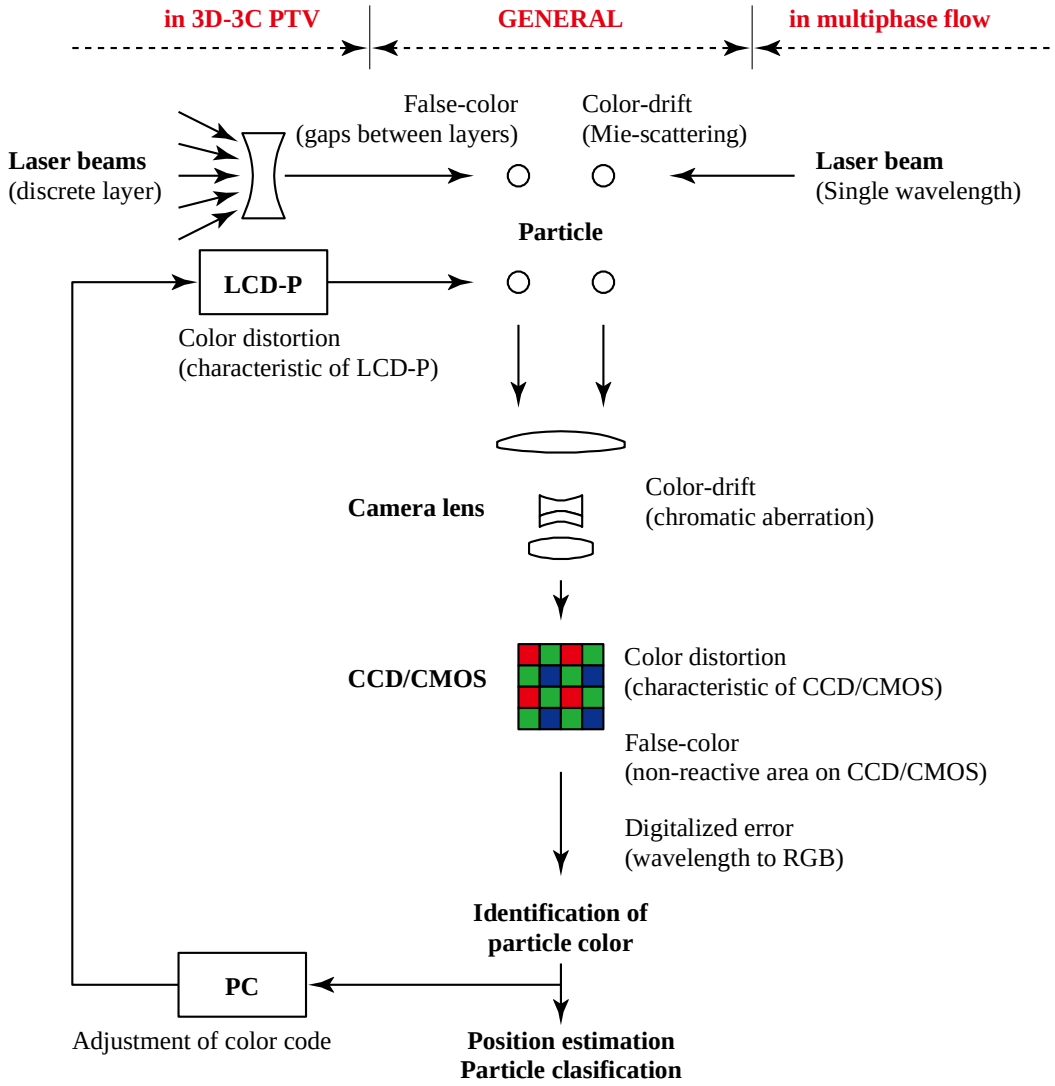


FIG. 2-1 Schematic chart of measurement uncertainties leading to color identification error of a particle, and their occurrence sites

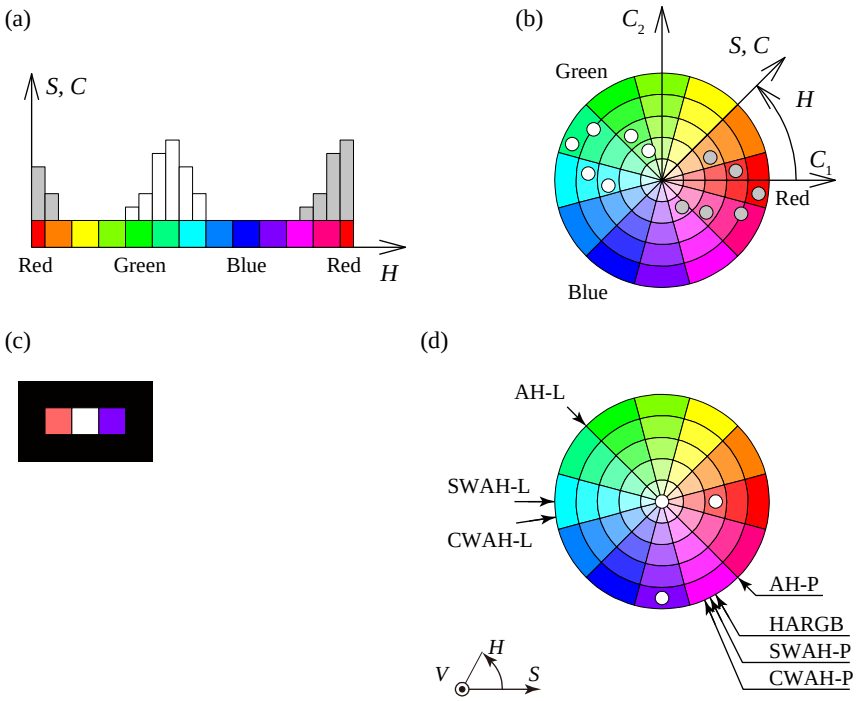


FIG. 2-2 Color space of (a) linear and (b) polar coordinates, (c) pixels of different colors corresponding to a single particle, and (d) particle colors on the hue-saturation plane, where H, S, C, and V donate the hue, saturation, chroma, and value, respectively; C1 and C2 are temporal Cartesian coordinates in polar coordinates. White and gray bars in (a) indicate the hue-saturation and hue-chroma distribution of pixels, respectively, within individual particle. White circles in (b) and (d) indicate particle colors on the coordinate plane; arrows in (d) indicate hue determined seven algorithms; center of particle (CP), hue of averaged RGB (HARGB), averaged hue in linear coordinates (AH-L), chroma-weighted-averaged hue in linear coordinates (CWAH-L), saturation-weighted-averaged hue in linear coordinates (SWAH-L), averaged hue in polar coordinates (AH-P), chroma-weighted-averaged hue in polar coordinates (CWAH-P), saturation-weighted-averaged hue in polar coordinates (SWAH-P).

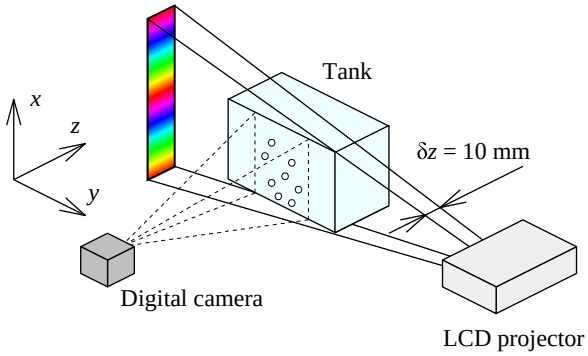


FIG. 2-3 Schematic outline of the experimental setup used to evaluate the algorithm for particle color identification

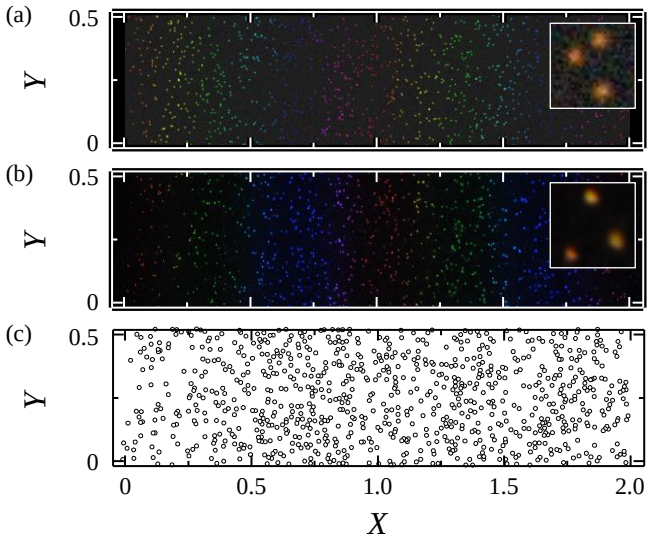


FIG. 2-4 Color-illuminated particle images: (a) idealized artificial synthetic image, (b) experimental image captured by a digital camera, (c) particle position determined from the experimental image

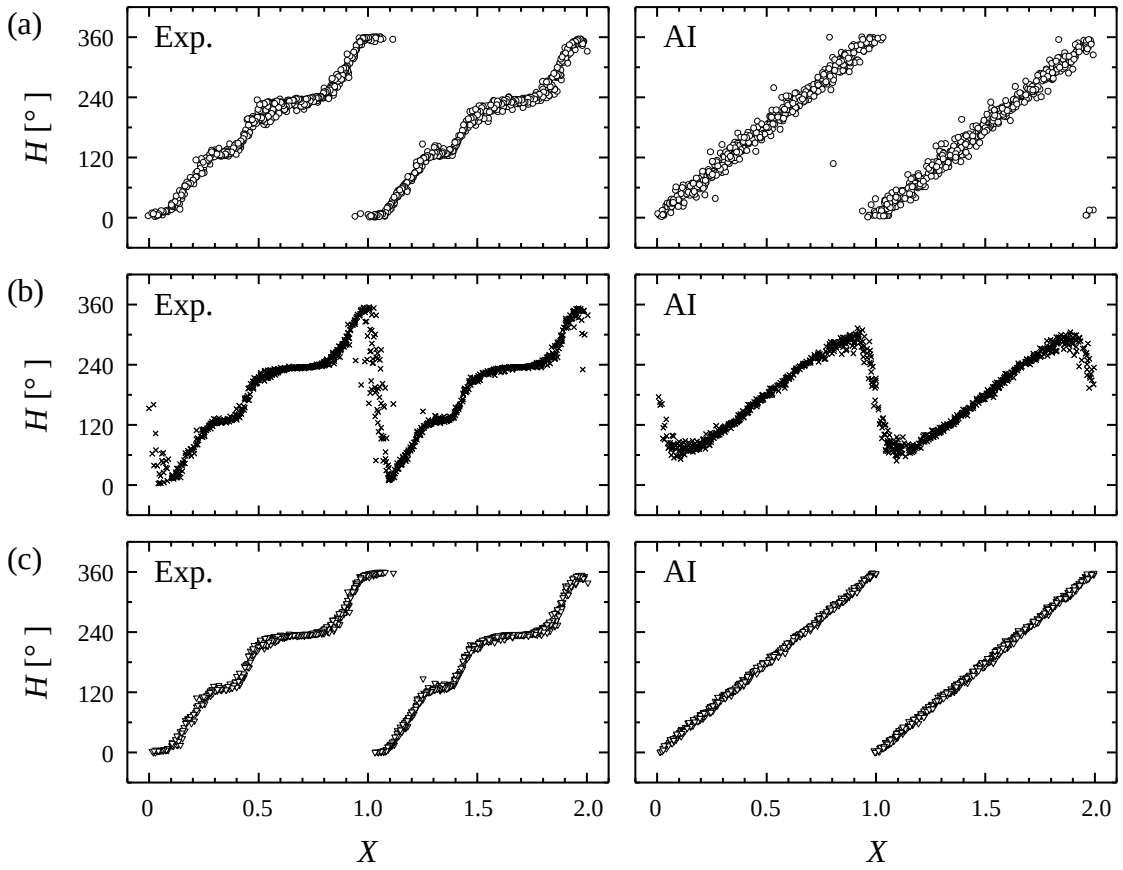


FIG. 2-5 Hue distribution as a function of particle position, determined by following algorithms: (a) hue at center of particle (CP), (b) averaged hue in linear coordinates (AH-L), and (c) averaged hue in polar coordinates (AH-P). The left panels display results from experimental data (Exp.), while the right panels represent those from an idealized artificial synthetic image (AI)

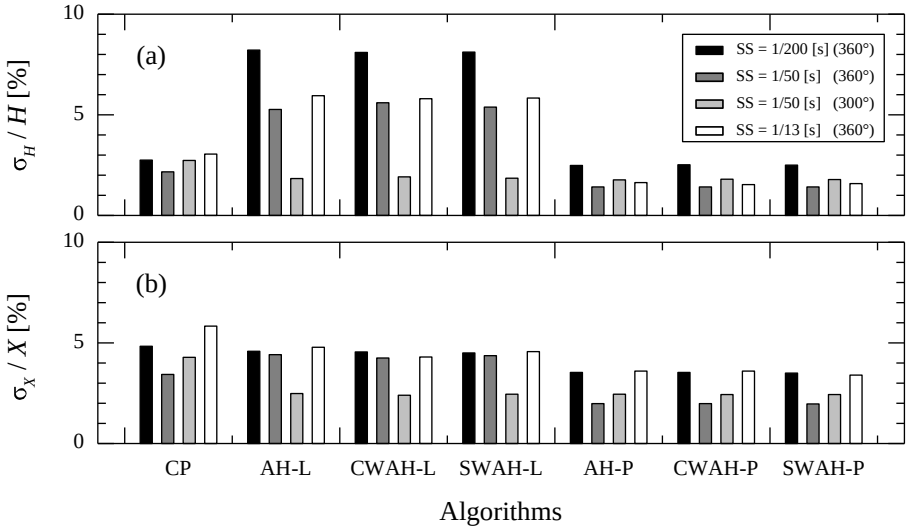


FIG. 2-6 Standard deviation of (a) hue and (b) position for seven algorithms at different exposure times controlled by shutter speed (SS); hue at center of particle (CP), averaged hue in linear coordinates (AH-L), chroma-weighted-averaged hue in linear coordinates (CWAH-L), saturation-weighted-averaged hue in linear coordinates (SWAH-L), averaged hue in polar coordinates (AH-P), chroma-weighted-averaged hue in polar coordinates (CWAH-P), saturation-weighted-averaged hue in polar coordinates (SWAH-P)

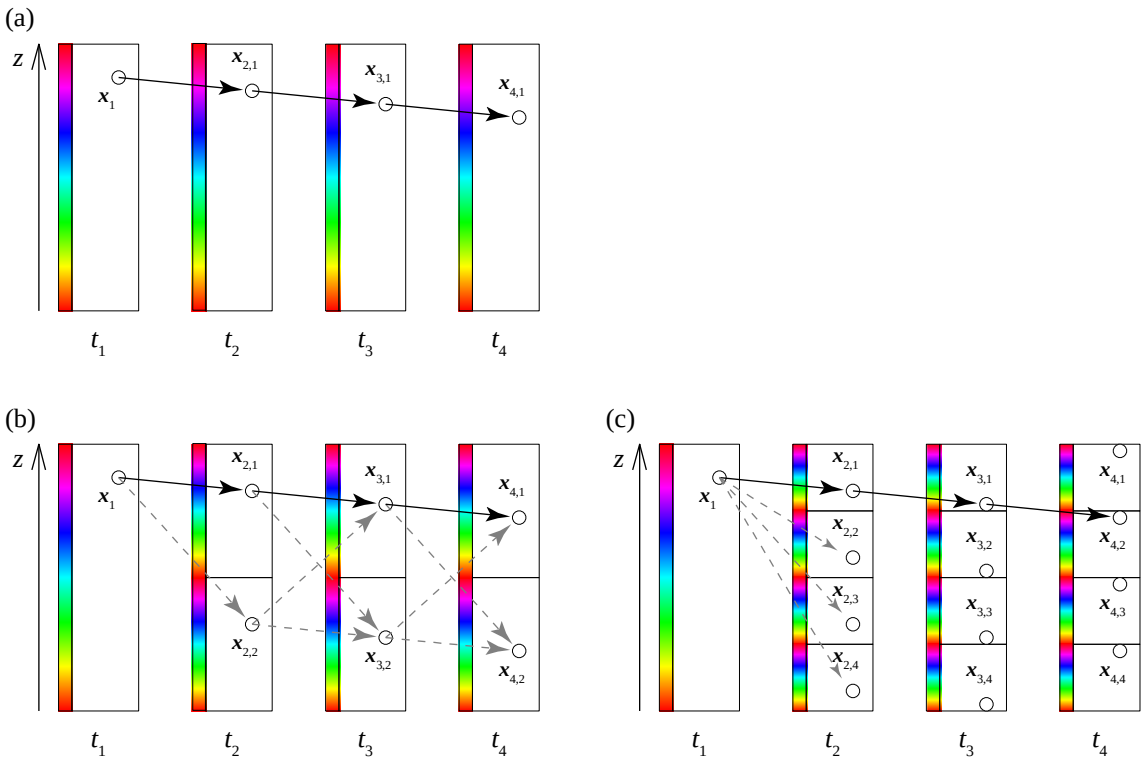


FIG. 2-7 Principle of multi-cycle color PTV: (a) single-cycle, (b) two-cycles, and (c) four-cycles of color gradation

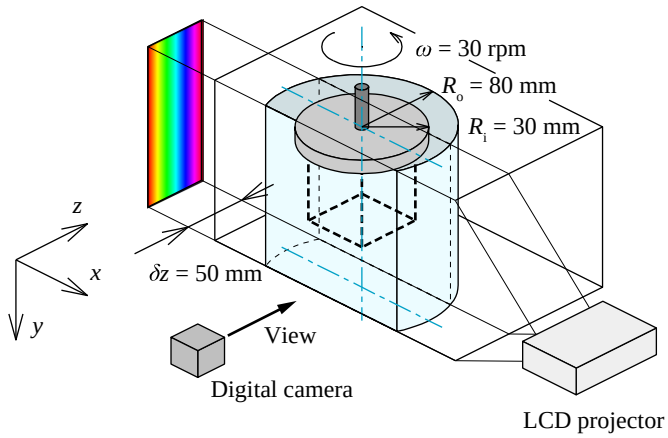


FIG. 2-8 Schematic outline of the experimental setup for the rotating flow test

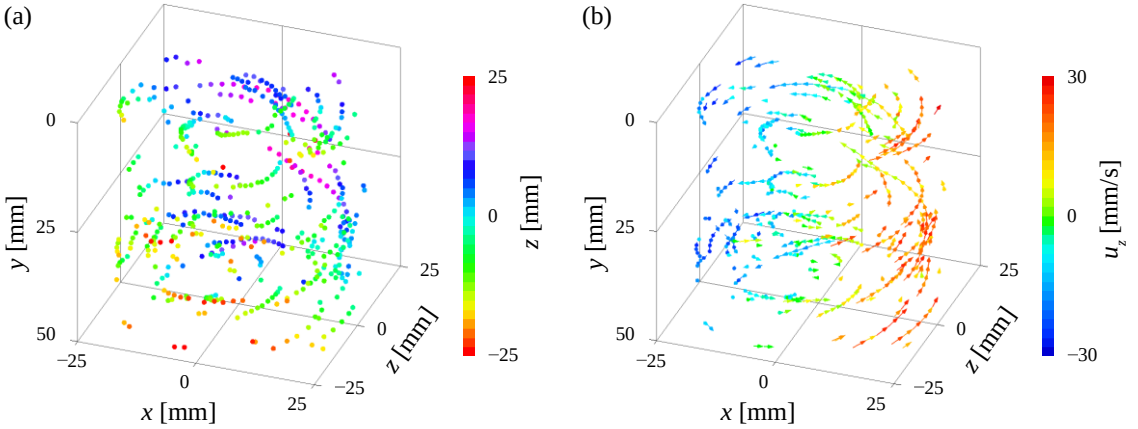


FIG. 2-9 Overall view of (a) particle positions and (b) the 3D–3C velocity vector field of the rotating flow

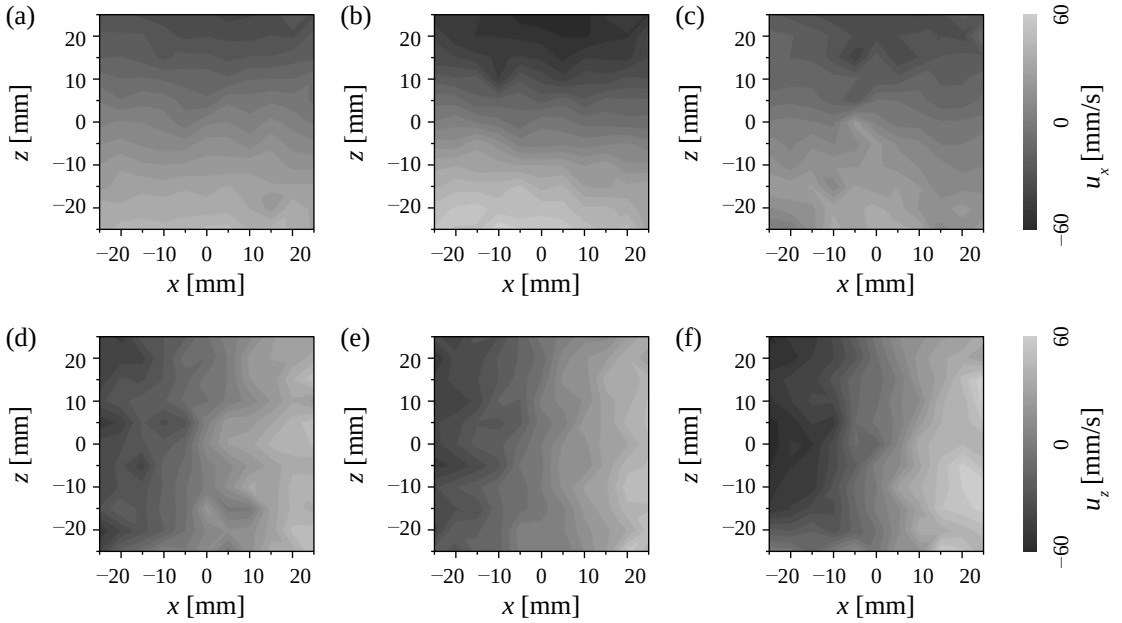


FIG. 2-10 Averaged velocity components: (a) u_x and (d) u_z using one color cycle; (b) u_x and (e) u_z using two color cycles; and (c) u_x and (f) u_z using four color cycles

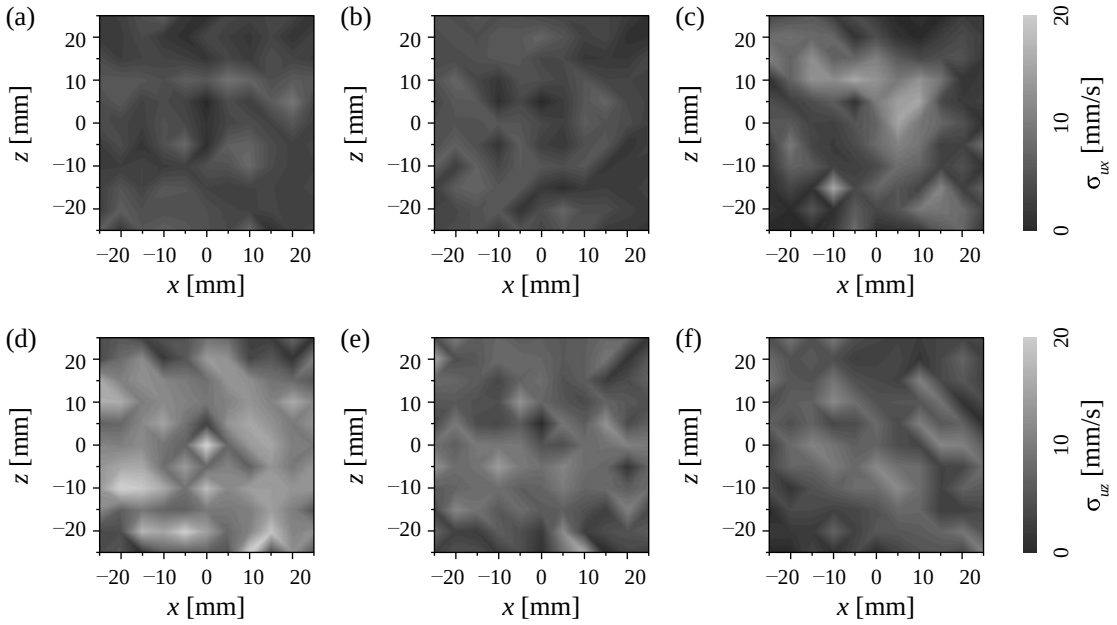


FIG. 2-11 Standard deviation of the velocity components: (a) σ_{ux} and (d) σ_{uz} using one color cycle; (b) σ_{ux} and (e) σ_{uz} using two color cycles; and (c) σ_{ux} and (f) σ_{uz} using four color cycles

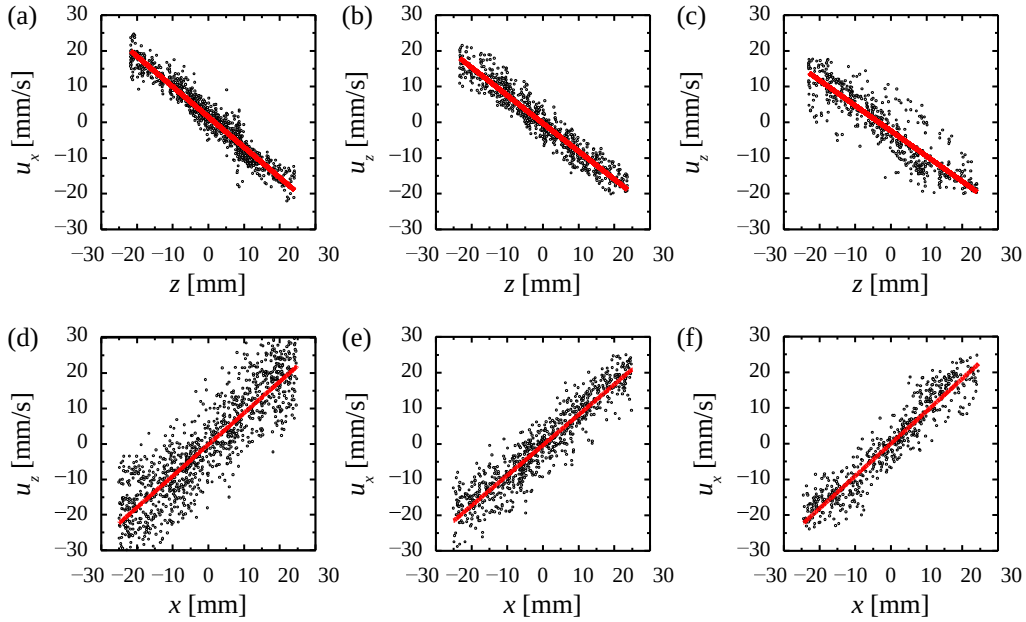


FIG. 2-12 Velocity distribution along the x and z directions: (a) u_x and (d) u_z using one color cycle; (b) u_x and (e) u_z using two color cycles; and (c) u_x and (f) u_z using four color cycles, lines represent the least square approximations

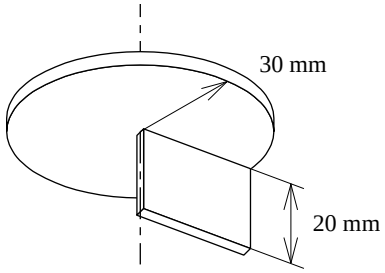


FIG. 2-13 Schematic representation of the rotating disk with impeller

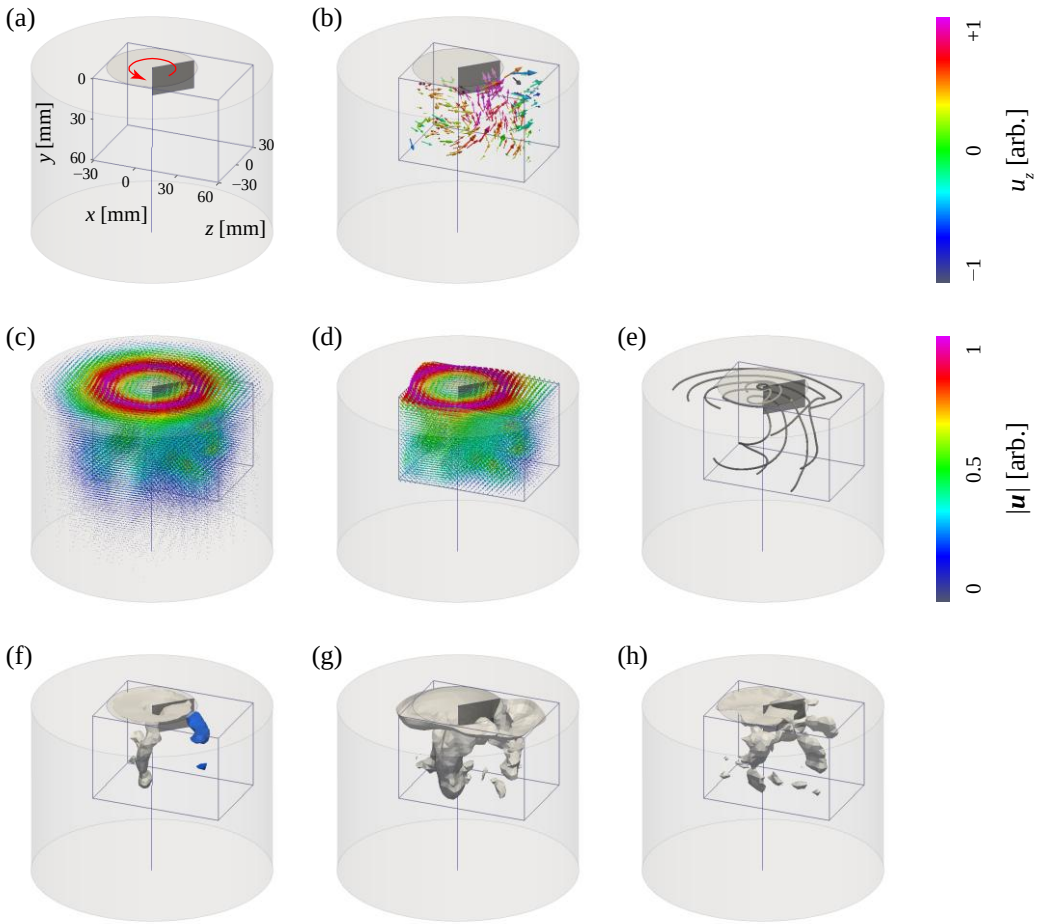


FIG. 2-14 (a) Configuration of visualized volume in a flow induced by the rotating impeller on the disk; (b) Instantaneous 3D–3C velocity distribution obtained by two-cycle color PTV, after grid point relocation, BER interpolation, and VCP correction of (c) entire system and (d) volume in visualized; (e) Instantaneous snapshot of streamlines; Instantaneous snapshot of the vortex structure shown as iso-surfaces of (f) axial vorticity, ω_z, (white) and tangential vorticity, ω_θ (blue), (g) enstrophy, s, and (h) Laplacian of pressure, Δp

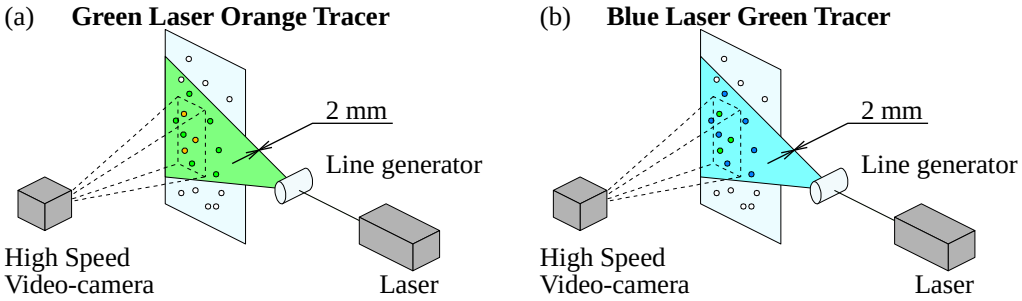


FIG. 2-15 Schematic of the experimental setup for particle discrimination of tracer particle and microbubble in (a) green laser orange tracer (GL-OT) and (b) blue laser green tracer (BL-GT) system

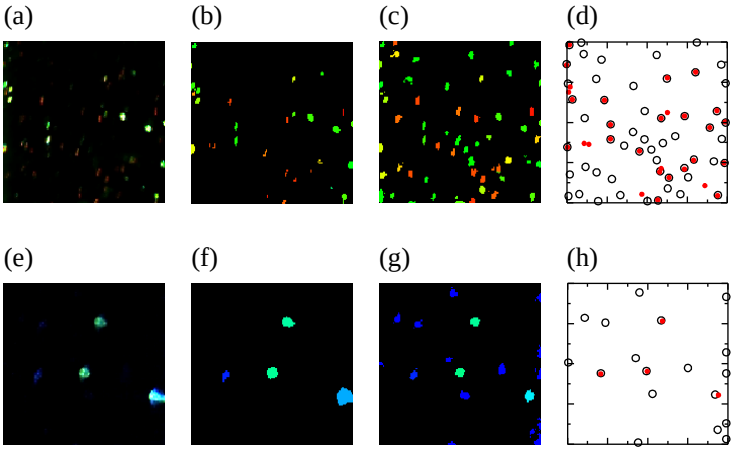


FIG. 2-16 Particle image display of LIF tracer particles and microbubbles: original image in (a) GL-OT and (e) BL-GT system; Binarized image thresholding intensity in (b) GL-OT and (f) BL-GT system; Binarized image thresholding cross correlation value of Gaussian matching (PMC) in (c) GL-OT and (g) BL-GT system; Particle positions identified from thresholding intensity (closed symbols) and cross correlation (open symbols) value in (d) GL-OT and (h) BL-GT system

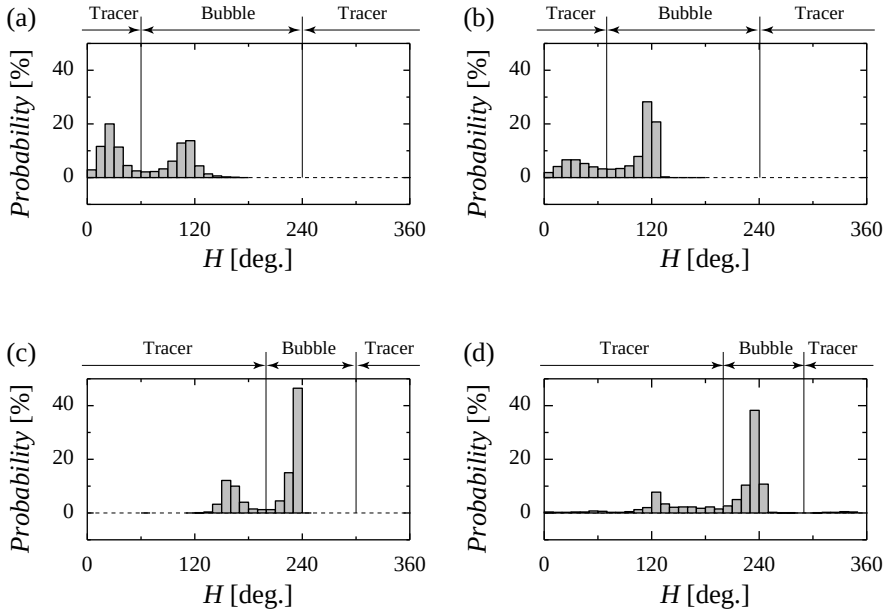


FIG. 2-17 Probability distributions for hue of particles identified from labeling in (a) GL-OT and (c) BL-GT system, and PMC in (c) GL-OT and (d) BL-GT system

Chapter 3
Wave modifications in a microbubble Taylor–Couette flow

Abstract

The effect of the presence of microbubbles on a flow state is experimentally investigated in a Taylor–Couette flow with azimuthal waves, in order to examine the interaction mechanism of bubbles and flows that result in drag reduction. The average diameter of the bubbles is 60 μm, which is smaller than the Kolmogorov length scale, and the maximum void fraction is 1.2×10^{-4}. The modifications of the fluid properties, bulk density, effective viscosity, and the extra energy input caused by the addition of microbubbles are expected to have a small effect on modifying flow states. The power of the basic wave propagating in the azimuthal direction is enhanced; its modulation, however, is decreased by adding microbubbles in the flow regime corresponding to modulated Taylor vortex flow. Moreover, the gradient of the azimuthal velocity near the walls, source of the wall shear stress, decreases by 10 %. The modified velocity distribution by adding microbubbles is comparable to that obtained with a 20 % lower Reynolds number. Microbubbles in the coherent structure of the wavy Taylor vortices are visualized and exhibit a preferential distribution and motion at the crests and troughs of the waviness. The roles of the inhomogeneously distributed microbubbles in wavy vortical structures are discussed in view of our findings.

3.1 Introduction

Injecting bubbles as a way for skin frictional drag reduction in shear flows has been considered for engineering applications, particularly for large vessels [14]. Drag reduction by the injection of $O(10\ \mu m)$ diameter bubbles (hereafter termed as "microbubbles") into turbulent boundary layers has been a subject of intensive research since the first experimental investigation [15] because of its high efficiency, i.e., drag reduction rate versus the input void fraction. The performance of the drag reduction rate has been experimentally investigated in turbulent channel flows [20] [19] [21] [22] [23] or in turbulent boundary layers on a flat wall [24], and reaches around 40 % at the maximum. The remarkable feature of drag reduction by microbubbles is that $O(10\ \%)$ of the drag reductions are achieved by low void fractions of $\alpha \sim O(10^{-4})$.

As a fundamental approach for understanding the drag reduction mechanisms, modifications of the liquid medium property in bulk have been considered as the function of the void fraction so far. The modification on the bulk density of liquids is given as

$$\rho = (1-\alpha)\rho_0, \tag{3-1}$$

where ρ_0 is the original density of the liquids. The air density of bubbles is much smaller than that of the liquids and is regarded as zero. The decrease in the medium's density with increasing void fraction provides the primary mechanism for drag reduction with decreasing the bulk density of the medium in turbulence [25]. In contrast, the effective (bulk) viscosity of the fluid in simple laminar shear flows is estimated by Taylor's formula [26] [27],

$$\mu = (1+\alpha)\mu_0, \tag{3-2}$$

where μ_0 is the viscosity of the liquids, and it yields the opposite relationship, i.e., an increase in the shear stress. An increase in the void fraction decreases the frictional drag by decreasing the Reynolds shear stress with decreasing the medium density, as described in Eq. (3-1), and also increases it by increasing the effective viscosity at the moment, according to Eq. (3-2). The linear theory that resolves this contradiction states that the modification on the properties of fluids with uniformly dispersed bubbles is of the same order as the void fraction [28]. Further, the energy relationship for systems containing bubbles in an isentropic process is given as

$$\left\langle \overline{E} \right\rangle = \left\langle \overline{\varepsilon} \right\rangle - \left\langle \overline{\boldsymbol{f}_{\text{bubble}} \cdot \boldsymbol{u}} \right\rangle, \tag{3-3}$$

where E, ε, and $\boldsymbol{f}_{\text{bubble}}$ are the energy input rate, energy dissipation rate, and extra energy input to the system due to the momentum transfer of bubbles, respectively. The angle brackets, < >, and overline, $\bar{}$, indicate spatial and time averages, respectively. Assuming that changes in the energy relationship are caused by the sum of the buoyant forces acting on each microbubble dispersed in the liquid phase

$$\left\langle \overline{\boldsymbol{f}_{\text{bubble}} \cdot \boldsymbol{u}} \right\rangle \approx -\alpha \mathbf{g} \cdot \left\langle \overline{\boldsymbol{u}_{\text{bubble}}} \right\rangle, \tag{3-4}$$

and the microbubbles should modify the momentum transfer very little or not at all [98], if the mean void fraction is as small as $O(0.1\ \%)$. The effects of the modification in density, effective viscosity and extra energy input would be of the same order as the void fraction, and would be negligible in dilute two-phase flows, i.e., $\alpha \leq O(10^{-4})$. The drag reduction rate in previous experimental investigations of dilute two-phase flows containing microbubbles [19] [23] [24], in contrast, takes significantly high values by $O(10\ \%)$ since nonlinear interactions occur between microbubbles and flow structures in turbulent flows, as mentioned by L'vov, *et al*. [28] Investigations of flow fields in the liquid phase indicate that the drag reduction mechanisms can now be attributed to a decrease in the coherence of near wall structure (the source of Reynolds shear stress), which arises from interactions between microbubbles and coherent structures of turbulent flows [21] [22] [23] [24]. Numerical works as well as experiments exhibited that the decrease in the Reynolds shear stress near the wall, due to the displacement of the near-wall structures, which is so called streamwise vortices generating ‘sweep’ and ‘ejection’, away from the wall and reducing the frictional drag [31] [32] [99].

The influence of the addition of microbubbles on the coherent fluid structure has been commonly thought to be the key factor in the modification of the velocity fields and the wall shear stress. Nevertheless, uniformly dispersed microbubbles cannot modify the structure very well, as shown by our estimation above. It is necessary to investigate the two-way interactions between the microbubbles and flow structures, and further, the clustering of bubbles in coherent structures in turbulence. The detailed distribution and motion of microbubbles, however, have not been discussed because of difficulties in the simultaneous measurement for both microbubble motion and the

velocity field of the surrounding liquid phase. Furthermore, the measurement of the turbulent structures itself is still a challenging problem because of the complex three-dimensional characteristics of the flows.

To simplify the flow structure in order to investigate the effect of the addition of microbubbles on the coherent flow structure, Taylor–Couette flows [100] [101] that are flows between two concentric cylinders driven by their rotation have been adopted as platforms for experimental investigations. The major advantages of using Taylor–Couette flows for the evaluation are: (a) the system is closed, unlike those spatial-developing flows, for example, channel, pipe flows and boundary layers on flat plates, (b) the flow modes and transitions in the system can be controlled well by the Reynolds number based on the rotation speed of cylinders, and (c) the system provides rich knowledge of single phase flows as in literatures, e.g. [102] [103]. Because of these advantages, so far, Taylor–Couette flows containing bubbles have been both experimentally and numerically investigated [98] [104] [105] [106] [107] [108] [109] [110] [111] [112]. van Gils, *et al.*, (2013) [112] have highlighted the advantage in the use of a Taylor–Couette flow and also the drag reduction mechanisms by bubble injection in Taylor–Couette flow that unveiled so far are . The flow regime, the mean bubble diameter, and the drag reduction rate (DRR) are also summarized in TABLE 3-1. Relatively large bubbles with O(1 mm) in diameter reduce the frictional drag by 20 % by modifying the boundary layer in Taylor–Couette flows when bubbles are deformable [107] [109] [112]. Bubble deformability or compressibility is also one of the factors in drag reduction as in spatially developing channel flows [113] [114]. Non-deformable bubbles with O(100 μm) in diameter, however, yield a drag reduction of 20 % at most [110] even in a direct numerical simulation adopting a point-force coupling model [98]. This phenomenon has been attributed to modifications of vortical structures; the axial elongation of the Taylor vortices by a localized buoyant force generated by preferentially accumulated bubbles [110], or global changes in the coherent Taylor vortex structure that reduce the Reynolds stress [98] or switch the flow regime from the toroidal to the spiral vortices [111].

This study aims to elucidate how the flow structure in a Taylor–Couette flow can be influenced by the addition of microbubbles with tiny volume concentrations (less than 0.1 %, i.e., a typical dilute two-phase condition). Modifications of the fluid

properties in bulk, i.e., the density, viscosity, and extra energy, are of the same order as the void fraction, which are expected to be negligible. Countable numbers of basic flow elements, i.e., the basic shear flow (circular Couette flow), vortex array (Taylor vortices), and waves (azimuthally propagating waves), appear as flow instabilities in the laminar-transition flow regime in so called time-dependent flows. The number of flow elements increases in sequence of increasing the Reynolds number, and the variations in their magnitude can be described by the weakly non-linear theory. The effects of the presence of microbubbles on the flow elements would be amplified in the periodic flow structure of the closed Taylor–Couette system and are easily observed. We carefully investigate the modification of the flow elements in the Taylor–Couette system by using appropriate measurement equipment. The distribution of microbubbles on a cross section of the vortices is measured to evaluate the dynamic interaction of bubbles with coherent flow structures. Finally, we mention the effect of microbubbles on the flow transitions of the system, namely a pseudo-decrease in the Reynolds number. The flow state subjected in this study is the beginning of the transition to turbulence and is not the fully developed turbulence considered in the frictional drag reduction problems. However, elucidating the interaction between microbubbles and the fundamental flow elements should provide important insights for understanding the drag reduction mechanisms.

TABLE 3-1 Flow regime and bubble diameter reported by literatures of study on Taylor–Couette flow containing bubbles

Literature	*Re*	α_{max}	D_b [mm]	d [mm]	D_b / d	DRR [%]
Shiomi, *et al.*, 1993 [104]	1×10^4 - 8×10^4 Turbulent	N/A	1	10	0.1	N/A
Djeridi, *et al.*, 2004 [105]	350 - 750 WVF - MWVF	0.17	0.1 - 0.7	5	0.02 - 0.14	N/A
Mehel, *et al.*, 2007 [106]	590 - 1700 WVF - MWVF	7.5×10^{-3}	0.8 - 3.6	20	0.04 - 0.18	N/A
Climent, *et al.*, 2007 [108]	130 - 170 TVF - WVF	NULL	0.1	5	0.02	N/A
van den Berg, *et al.*, 2005 [107]	7×10^4 - 1×10^6 Turbulent	0.1	0.5 - 2	60	0.008 - 0.03	20 ($\alpha = 4 \times 10^{-2}$, $Re = 9 \times 10^5$)
van den Berg, *et al.*, 2007 [109]	1×10^5 - 4×10^5 Turbulent	0.08	0.5 - 2	60	0.008 - 0.03	25 ($\alpha = 8 \times 10^{-2}$, $Re = 3 \times 10^5$)
Murai, *et al.*, 2008 [110]	600 - 4500	0.3	0.6	12	0.08	35
Yoshida, *et al.*, 2009 [111]	WVF - CWVF					($\alpha = 5 \times 10^{-2}$, $Re = 6 \times 10^2$)
Sugiyama, *et al.*, 2008 [98]	600 - 2500 WVF - chaotic	0.007	0.6	12	0.08	20 ($\alpha = 1 \times 10^{-3}$, $Re = 6 \times 10^2$)
van Gils, *et al.*, 2013 [112]	5×10^5 - 2×10^6 Turbulent	4×10^{-2}	1.5	79.4	0.02	40 ($\alpha = 4 \times 10^{-2}$, $Re = 2 \times 10^6$)
Present	270 - 1200 WVF - MWVF	1.2×10^{-4}	0.06	10	0.006	10 ($\alpha = 1 \times 10^{-4}$, $Re = 1 \times 10^3$)

WVF, MWVF, and CWVF represent wavy vortex flow, modulated wavy vortex flow, and chaotic wavy vortex flow, respectively.

3.2 Experimental Systems

3.2.1 Experimental setup and definitions

The experiments were conducted in the vertical Taylor–Couette system shown in FIG. 3-1. The rotating inner cylinder with 95.1 ± 0.1 mm in radius (R_i) was made of carbon fiber reinforced plastic (CFRP); its surface was painted black, and it was driven by a stepper motor with 500 steps per revolution. The stationary outer cylinder with 105 ± 0.1 mm in inner radius (R_o) was made of transparent Plexiglas to allow the visualization of the flows generated in the gap between the concentric cylinders. The cylinders were held by Plexiglas end plates and were set in a rectangular transparent water jacket for visualization and to maintain the temperature of the test fluid at 20 ± 0.5 °C. The gap distance between the cylinders, d, and their height, h, were 9.9 mm and 197 ± 0.5 mm, respectively. The corresponding radius ratio of the cylinders, η (= R_i / R_o), and the aspect ratio of the fluid layer, Γ (= h / d), are 0.906 and 19.9, respectively. The Reynolds number of the flow is defined as

$$Re = \frac{U_{wall} d}{\nu} = \frac{2\pi\Omega R_i (R_o - R_i)}{\nu}, \tag{3-5}$$

where U_{wall}, Ω and ν are the inner wall velocity (U_{wall} = $2\pi\Omega R_i$), rotation frequency and kinematic viscosity of water used as test fluid, respectively. The reduced Reynolds number, Re^* (= Re / Re_c), is adjusted to $2 \leq Re^* \leq 9$ (i.e., $269 \leq Re \leq 1210$), where Re_c is the critical Reynolds number for the onset of the primary instability from the circular Couette flow (CCF) to Taylor vortex flow (TVF). Estimated value of Re_c in this experimental system is Re_c = 134.0, which agrees rather well with the published values [115] [116] [117]. The details of the estimation of Re_c are described in SECT. 3. In this range of the Reynolds number, the flow regimes correspond to wavy vortex flow (WVF, azimuthal waves superimposed on the Taylor vortices) and modulated wavy vortex flow (MWVF, in which the wave modulation appears on the azimuthal waves) [102]. Two independent flow modes coexist in MWVF [118]: GS mode (Gorman & Swinney, (1979) [119]) and ZS mode (Zhang & Swinney, (1985) [120]). The GS mode extends over the roll of the azimuthal wave and is a wave component for a modulation, leading to a periodic flattering of the out-flow boundary of the vortices. The ZS mode appears near the out-flow region with (about twice) higher phase velocity increasing the appearance of a ripple on the roll. The modulation waves of both GS and ZS modes

have the multiplicity in the number of azimuthal wave and the traveling velocity which are independent with those of the basic wave. Counlin &Marcus (1992) [118] [119] elaborated on the characteristics of GS and ZS mode in MWVF. FIG. 3-2 shows the schematic of the flow elements which appear in each flow mode; CCF, TVF, WVF, and MWVF in Taylor–Couette flows. The circular flow, Taylor vortices, single azimuthal wave superimposed on the Taylor vortices, and its modulations sequentially appear with increasing the Reynolds number, *Re*. In these experiments, first the rotation velocity of the inner cylinder was set at a value corresponding to the highest *Re* with a fixed acceleration rate. Then, the velocity was decreased to smaller values to avoid the excitation of unstable flow modes while varying the *Re* [123]. The eigenvalues of the flow (the axial wavelength of the Taylor vortices, frequency of waves, number of azimuthal waves, and traveling velocity of waves) occurred within a certain range throughout all of the experiments.

Hydrogen bubbles with *O*(10 μm) in diameter were generated by water electrolysis from a platinum wire with 100 μm in diameter mounted at the bottom of the fluid layer (i.e., on the surface of the bottom end plate) and are dispersed into the fluid layer. The bubble diameter was measured by image analysis. Bubbles in an image are identified by giving a threshold value of their intensity. The object diameter of the bubbles is measured, and then, their probability density function (PDF) is calculated. The PDF of the bubble diameter is shown in FIG. 3-3. The mean bubble diameter was 64 μm, which is 0.2 of the Kolmogorov length scale in the minimum *Re* case of the two-phase condition and 0.3 of the Kolmogorov scale in the maximum *Re* case. Here, based on the relation of the empirical torque [124] and energy dissipation rate [98], the Kolmogorov length scale, ℓ_d, is given as

$$\ell_d = \left\{ \frac{\pi \nu \left(R_o^{\,2} - R_i^{\,2} \right)}{1.45 U_{wall}} \frac{(1-\eta)^{\frac{7}{4}}}{(Re\,\eta)^{\frac{3}{2}}} \right\}^{\frac{1}{4}}, \tag{3-6}$$

where ν, R_i, R_o, η, and U_{wall} are the kinematic viscosity of the test fluid, inner and outer cylinder radii, radius ratio of the cylinders, and inner cylinder wall velocity, respectively (see also the APPENDIX 4 for the detailed derivation). The gas flow rate in the microbubble generation, *Q*, is theoretically estimated from Faraday's low and gas state equation that given as

$$Q = \frac{RTI}{2P}, \tag{3-7}$$

where R, T, I, and P are gas constant, temperature, electric current for water electrolysis, and pressure, respectively. Stokes rising velocity of microbubble is given as

$$U_{St} = \frac{\rho g D_b^{\,2}}{12\mu}, \tag{3-8}$$

where ρ, μ, g, and D_b are the density and viscosity of the test fluid, gravitational acceleration, and mean bubble diameter, respectively. The time averaged bulk void fraction, α, was estimated using the input gas flow rate, Q, Stokes terminal velocity of rising microbubble, U_{St}, and cross sectional area, π ($R_o^{\,2} - R_i^{\,2}$), is given as

$$\alpha = \frac{Q}{U_{St}\pi\left(R_o^{\,2} - R_i^{\,2}\right)}. \tag{3-9}$$

The estimated maximum value of α was smaller than 1.2×10^{-4}. The experimental conditions are listed in TABLE 3-1.

3.2.2 Measurement techniques

Particle Tracking Velocimetry (PTV), Ultrasonic Velocity Profiling (UVP), and Laser Doppler Anemometer (LDA) were used selectively for measurements depending on their suitability for various purposes in experiments.

The velocity distributions of the liquid phase and velocity vectors of the dispersed microbubbles on the radial-axial cross section were measured by image analysis consisting of PTV applying Laser Induced Fluorescence (LIF) using a single color-imaging video camera. This measurement method provides time series of the velocity vector field of the liquid phase flow, i.e., instantaneous velocity vectors and position vectors of the microbubbles at moments, namely $\boldsymbol{u}$ [u_r (r, z, t), u_z (r, z, t)], $\boldsymbol{u}_{\mathrm{bubble}}$ [$u_{r\ bubble\ (j\ (t))}$, $u_{z\ bubble\ (j\ (t))}$], and $\boldsymbol{x}_{\mathrm{bubble}}$ [$r_{\ bubble\ (j\ (t))}$, $z_{\ bubble\ (j\ (t))}$], where j (t) denotes the jth bubble at time t. The number density of the velocity vectors for microbubbles, N_{bubble}, indicates the instantaneous local void fraction at a moment. Information on the color of the scattering light from the gas-liquid interface or of fluorescent light from tracer particles containing laser induced fluorescent dye in response to an incident laser sheet was used for the criteria to distinguish tracer particles and microbubbles. The details of the technique are described in CHAPTER 2. The measurement section, i.e.,

the *r*-*z* cross section of the fluid layer in the middle of the axial direction, was illuminated by a laser sheet (2 W, 532 nm) with 2 mm in thickness. Resin particles with 15 μm in diameter containing LIF dye (EBM Co., Fluostar, specific gravity: 1.1, absorption wavelength: 550 nm, emission wavelength: 580 nm) were seeded as tracer particles that follow the flow. The Stokes number that represents the relative response time of the particles in the flow for a typical velocity fluctuation of the wave frequency, *f*, is defined as

$$St = \frac{\left(2\rho_{\mathrm{p}} + \rho\right) D_{\mathrm{p}}{}^{2} f}{24\mu}, \tag{3-10}$$

where ρ_{p}, ρ, D_{p}, and μ are the density of the particles, density of the test fluid, particle diameter, and viscosity of the test fluid, respectively. The Stokes number of the tracer particles was $St \sim O(10^{-4})$ and the volume concentration was 1×10^{-5}. Particles with color information were acquired by a color-imaging high-speed video camera (Photron Co., Fastcam MAX 120 KC) in a spatial range of z = 80 mm to 120 mm (i.e., z^* (= $z - h/2$) = $-2d$ to $2d$, where d is the gap distance of the fluid layer) with a spatial resolution corresponding to 39 μm/pixel. The temporal resolution was 8 ms, and the velocity resolution was 0.78 mm/s, respectively. Grid point relocation of the velocity vectors and interpolation for lacking velocity vectors at grid points were conducted to obtain the velocity vector distribution of the liquid phase [74]. Then the stream function of the flow field, ψ, was calculated to determine the global motion of the oscillating Taylor vortex array appearing in the fluid layer [101] [111] as,

$$\psi\left(r,z\right) = -\int_{wall}^{r,z} r' u_z(r',z)\, dr' . \tag{3-11}$$

The velocity distributions of the axial component were also measured by Ultrasonic velocity profiling (UVP [125]) as well as image analysis to measure the power of the axial velocity fluctuations and to determine the flow mode of the Taylor–Couette flow. UVP can record instantaneous velocity profile information for much longer than PTV can do thanks to real-time data acquisition in UVP. It has, therefore, a great advantage for obtaining the temporal statistics of velocity fluctuations. Resin particles with 60 μm in mean diameter were seeded as tracer particles in a volume concentration of 5×10^{-4}, where $St \sim O(10^{-3})$. The oscillation frequencies of bubbles in diameter of 60 μm are estimated to smaller than 0.1 MHz, the UVP, therefore, do not

affect on the motion/behavior of bubbles in measurement system (see also the APPENDIX 5 for the detailed estimation). An ultrasonic transducer (US-TDX, for both emitting ultrasonic burst of 4 MHz in frequency and receiving ultrasonic echo from seeded tracer particles) was mounted on the top end wall near the rotating inner cylinder (see FIG. 3-1), being parallel to the rotational axis. A time series of instantaneous velocity profile at $(r - R_i)/d = 0.25$ was measured as a function of the axial position and time, namely u_z (z, t) along the inner cylinder. The measurement volume of each point had the shape of a disk with 5 mm in diameter (for the radial and tangential directions) and 0.70 mm in thickness (for the axial direction). The sampling period was 72 ms, and the velocity resolution was 0.39 mm/s, respectively. The velocity profiles were measured from z = 50 mm to 150 mm (i.e., $z^* = -5d$ to $5d$) to eliminate the end wall effect as much as possible.

The mean tangential velocity component, i.e., the main flow in a Taylor–Couette system, was measured by the LDA using a 5 mW diode laser. Because PTV and UVP are not suitable for measuring the tangential velocity component in this configuration, LDA measurement was adopted as a practical, conventional, and noninvasive method of measuring the velocity component in the narrow fluid layer. The measurement point was scanned on a meridional plane using a three-axis traverse system with a positioning accuracy of 0.1 mm. The measurements were conducted from z = 70 mm to 130 mm, i.e., $z^* = -3d$ to $3d$, at 4 mm intervals. The LDA measurements yielded a time series of the tangential velocity u_θ (r, z, t) measured spatially at each point. The resin particles used for UVP measurement were also seeded as the flow tracers with the same concentration as that for UVP. The size of the measurement volume was 450 μm in the radial direction and 60 μm in the tangential and axial directions, respectively. The sampling period was 100 ms, and the maximum velocity resolution was 2.3 mm/s, respectively. To minimize uncertainties due to the curvature of the outer cylinder, the position and beam angle were carefully calibrated.

TABLE 3-2 Experimental conditions

Contents	Symbols	Values
Inner cylinder radius	R_i	95.1 ± 0.1 mm
Outer cylinder radius	R_o	105 ± 0.1 mm
Gap distance	$d = R_o - R_i$	10 mm
Radius ratio	$\eta = R_i / R_o$	0.905
Cylinder height	h	197 ± 0.5 mm
Aspect ratio	$\Gamma = h / d$	19.9
Kinematic viscosity	ν	1.0×10^{-6} m^2/s
Density of test fluid	ρ	999.9 kg/m^3
Mean void fraction	α	0 to 1.2×10^{-4}

3.3 Determination of the critical Reynolds number

Since Couette's [100] and Taylor's [101] studies, the flow modes in supercritical Taylor–Couette flows have been well investigated and were categorized as a function of the Reynolds number on the basis of the rotational speed of the cylinders [102]. For the determination of the critical Reynolds number for the onset of the primary instability for CCF to TVF, spatio-temporal velocity distribution near the inner cylinder were measured by UVP in the various rotational speed of the inner cylinder. The experiments were conducted in horizontally arranged Taylor–Couette apparatus. Silicone oil in kinematic viscosity of 11.31×10^{-6} m^2/s (Shin-etsu chemical co., KF96-10cs, specific gravity: 0.922) was used as the test fluid at temperature of 16.1 °C (measurement detail of kinematic viscosity is described in APPENDIX 2). Resin particles with diameter of 180 μm (Sumitomo seika co., FLO-BEADS, specific gravity: 0.919) were seeded as tracer particles.

Spatio-temporal distributions of axial velocity component u_z UVP (e.g., Takeda, *et al.* [123] [125] [127]) in various *Re* are shown in FIG. 3-4. Panels in the left column represent the measurement results in the experiment of 1st run, while ones in the right column represent that in the experiment of 2nd run, respectively. Horizontal stripes in figures indicate the velocity fluctuation due to the motion of Taylor vortices in fluid layer. Number of Taylor vortex differs in both experimental run 1 and 2. Amplitude of spatial velocity fluctuation increases with increasing the Reynolds number. Temporal fluctuations in the velocity distribution appear at $Re \geq 175$ ((g) - (n)) as the second instability of a Taylor–Couette flow. FIG. 3-5 shows the (a) temporally averaged power spectra of the spatial velocity fluctuation $\overline{u_z^2}$ and (b) spatially averaged power spectra of the temporal velocity fluctuation, $\langle u_z^2 \rangle$. The overline '¯', angle blacket '< >', hat '^', and tilde '~' indicate the time average, spatial average, power of spatial velocity fluctuation, and power of temporal velocity fluctuation, respectively. The peak values of both $\overline{u_z^2}$ and $\langle u_z^2 \rangle$ increase with increasing *Re*. The peak wavenumber, *k*, and frequency, *f*, correspond the axial wavelength of Taylor vortices, k_v, and the frequency of axially-oscillating azimuthally-propagating basic wave, f_w, respectively. The growth of $\overline{u_z^2}(k_v)$ and $\langle u_z^2 \rangle(f_w)$ are shown in FIG. 3-6 as a function of *Re*. Open and closed symbols represent the experiments of lst and and 2nd run, respectively. According to the theory of weakly non-linear growth of perturbations [128] [129], the

amplitude of grown perturbation, u and u, increases proportionally to the square root of Reynolds number as

$$u = C_t \sqrt{Re - Re_{\text{critial}}}, \tag{3-12}$$

$$u = C_s \sqrt{Re - Re_{\text{critial}}}, \tag{3-13}$$

where Re_{critical}, C_t, and C_s are the critical Reynolds number for the appearance of instability, and growth rate of the temporal and spatial fluctuation power, respectively. Consequently, the fluctuation power of the wave, u_z^2 and u_z^2, increases as a linear function of the Reynolds number, Re. The lines in FIG. 3-6 are least square approximation lines following the power of $\overline{u_z^2}(k_v)$ and $\langle u_z^2 \rangle (f_w)$. The critical Reynolds number from CCF to WVF, Re_c, is determined as the cross points between the lines and the Re-axis. The critical Reynolds number is Re_c = 134.0, which is determined as the average of the values obtained in two experimental runs. This value of Re_c agrees rather well with the values obtained from experiments in similar radius ratio, η (= R_i / R_o), (Di Prima & Swinney [115]) and from empirical relations by Dutcher & Muller [116] given as

$$Re_c = \frac{10.81264}{\eta} + \frac{41.45025}{(1-\eta)^{1/2}} - 11.67578, \tag{3-14}$$

or Esser & Grossmann [117] given as

$$Re_c = 41.3029 \frac{(1+\eta)^2}{2\eta\{(1-\eta)(3+\eta)\}^{1/2}}. \tag{3-15}$$

The critical Reynolds number obtained in this experiment and ones in literatures are listed in TABLE 3-2. The critical Reynolds number from TVF to WVF, Re_w, is also determined from the cross point between the approximation line and Re-axis, and takes Re_w = 1747.8. The reduced critical Reynolds number Re^*_w (= Re_w / Re_c) = 1.31 is also in good agreement with literature [102].

TABLE 3-3 Critical Reynolds number for the onset of the primary instability obtained from the experiments and published literatures

Reference	Re_c
1st run (η = 0.906)	134.9
2nd run (η = 0.906)	133.1
Average of 1st & 2nd run (η = 0.906)	**134.0**
Di Prima & Swinney [115] (η = 0.9)	135.2
Di Prima & Swinney [115] (η = 0.925)	132.9
Di Prima & Swinney [115] (η = 0.906 (interpolated))	**134.6**
Dutcher & Muller [116]	135.1
Esser & Grossmann [117]	136.3

3.4 Modification of flow structures by microbubbles

3.4.1 Modification of wave power in MWVF

FIG. 3-7 shows spatio-temporal distributions of axial velocity component in various normalized Reynolds numbers Re^* = 3 to 9 (WVF to MWVF). The figures on the left panel represent the single-phase condition, and those on the right panel represent the two-phase condition with $\alpha = 6 \times 10^{-5}$. Amplitude of the velocity fluctuations increases in two-phase conditions, number of the Taylor vortices, however, is unchanged in two-phase conditions comparing to that in single phase conditions. Fine rising diagonal strokes from bottom left to top right shown as red stripes in the figures indicate bubble or bubbles rising up in the vortex tubes appearing in the fluid layer. These strokes appear in the relatively high-velocity region of the upward flow in all figures. Thus, the axial velocity distributions show that bubbles preferentially rise up at the crest of the oscillating Taylor vortex tubes.

FIG. 3-8 shows spatially averaged power spectra of the axial velocity fluctuation $\left\langle u_z^{\tilde{}\,2} \right\rangle$ obtained by UVP for various Re^* values, where angle brackets, < >, and tilde, $\tilde{}$, indicate the spatial average from 5d to 15d, and Fourier transform of the temporal fluctuations. The figures on the left panel represent the single-phase condition, and those on the right panel represent the two-phase condition, $\alpha = 6 \times 10^{-5}$. The frequency of the basic wave, f_w, and its modulation, f_m, are unchanged by the addition of microbubbles under these experimental conditions. The power of the basic wave fluctuation increases with adding microbubbles, whereas that of the modulation wave decreases in the MWVF (FIG. 3-8 (b) and (c)). In any case, peak frequencies in the spectra can be described as linear combinations of f_w and f_m, hence, these results conclude that the addition of microbubbles does not create any additional frequency components of the oscillating flows.

Variations in the powers of the components of MWVF, f_w and f_m, with various void fractions, α, are presented in FIG. 3-9, where the background component (BG) represents the minimum power between the frequency components of f_w and f_m. Open symbols in the figure represent UVP data, and solid symbols represent PTV data, $\left\langle u_z^{\tilde{}\,2} \right\rangle$ at $(r - R_i)/d = 0.25$, respectively. The error bars indicate the magnitudes of the standard deviation of the ensemble average in several runs of experiments. The powers of waves are determined by Fourier transform of the axial velocity fluctuation with a finite

measurement time length, which depends on the measurement equipment. Owing to this experimental limitation of the measurement time (mentioned in SECT. 3.2.2), the magnitudes of the powers of the waves obtained from PTV and UVP differ in FIG. 3-9 (b). The modifications of the powers of the basic and modulation waves show the same tendency of the variation. The power of the basic wave increases with increasing α for all Re^*. In contrast, the power of the modulation wave decreases with increasing α. Further, the peak representing the modulation component is buried in the background components, particularly for $\alpha > 3 \times 10^{-5}$ at $Re^* = 7$. These results suggest that the addition of microbubbles enhances the basic wave and reduces the modulation wave. Axially aligned Taylor vortices oscillate in the axial direction, and the oscillation (waviness of the vortex tube) propagates in the azimuthal direction with the basic frequency of the wavy vortex flow (WVF) mode. With increasing Reynolds number, the modulation wave appears as an additional azimuthal wave in modulated wavy vortex flow (MWVF). The increase of Re provides growth of the modulation component and decay of the basic wave in MWVF. In other words, the power of basic wave does not increase any more, while one of modulation wave increases. The power of basic wave is redistributed in linear components of f_w and f_m. The addition of microbubbles, however, prevents the flow transition in the variations of the oscillating wave power. In each graph in FIG. 3-9, unstable changes appeared at a very low void fraction of microbubbles, less than $\alpha < 2 \times 10^{-5}$. One of the considerable reasons is that the number of microbubbles is very few in this range of the void fraction. Hence, they can not be distributed equally to arranged Taylor vortices. This is an inevitable but common effect of dilute dispersive multiphase flows being discussed like a continuum.

3.4.2 Prevention of appearance and growth of waves

For quantitative understanding of modification of wave powers in the two-phase states, the flow modes in both the single phase and two-phase conditions are determined in this experimental system. The power of the velocity fluctuation of the basic wave, $\langle u_z^2 \rangle (f_w)$, or the modulation wave, $\langle u_z^2 \rangle (f_m)$, obtained from a power spectrum of the spatio-temporal distribution of the axial velocity component, are shown in FIG. 3-10 as a function of Re^* (= Re / Re_c). The error bars in the figure show the magnitude of the standard deviations of the ensemble average in several runs of experiments. Re^*_w (=

Re_w / Re_c) and Re^*_m (= Re_m / Re_c) are the normalized critical Reynolds number for the onset of transition from TVF to WVF, Re_w, and from WVF to MWVF, Re_m, where Re_c is the critical Reynolds number for the onset of the primary instability from CCF to TVF. The power of the basic wave increases until $Re^* \sim 5$. The modulation wave, GS mode [119], appears for $Re^* > 5$, and its power increases. Because of the appearance of the modulation wave, the power of the basic wave decreases and is decentralized into linear combination components. The waviness, i.e., the axial oscillation of the Taylor vortex array propagating in the azimuthal direction, in a Taylor–Couette system is related to the growth of dynamic instabilities [130] [131] [122] [132]. The power of basic and modulation waves also increases proportionally to the square root of Reynolds number as following the theory of weakly non-linear growth of perturbations [128] [129] given by Eq. (3-9). The lines in FIG. 3-10 are least square approximation lines following the power of $\langle u_z^2 \rangle (f_w)$ and $\langle u_z^2 \rangle (f_m)$. The critical Reynolds numbers for WVF, Re_w, and MWVF, Re_m, are determined as the cross points between the lines and the Re-axis. The growth rate as a function of the Reynolds number in the basic wave, C_w, and modulation wave, C_m, are determined from the gradient of the lines in FIG. 3-10. The critical Reynolds numbers and growth rates are listed in TABLE 3-3. The critical points for the onset of each mode are delayed by the addition of microbubbles. The growth rate of the wave amplitudes are also modified by the addition of the microbubbles: The growth rate of the basic wave amplitude, C_w, is increased and that of the modulation wave amplitude, C_m, is decreased with increasing the void fraction, α.

In FIG. 3-10, the values of the power $\langle u_z^2 \rangle$ for the basic wave, f_w, and the modulation component, f_m, in a two-phase condition, $\alpha = 1.2 \times 10^{-4}$, at $Re^* = 8$ are comparable with those in the single phase condition at $Re^* = 6.5$, i.e., the modification of waves equivalent to a 20 % decrease of the relative Reynolds number. The microbubbles seem to have little effect on the wave power at $Re^* = 9$ in FIG. 7 (c) and FIG. 3-8 (c) compared to that at $Re^* = 8$ in FIG. 3-7 (b) and FIG. 3-8 (b). The maximum influence on the intensification of the basic wave power appears at $Re^* = 5$ in FIG. 3-3. These phenomena suggest that the influence of microbubbles on the waviness in flow is selective but would produce the optimum conditions for preventing the flow transition. The axial length of the Taylor vortex tubes arranged in the fluid layer is maintained even in the two-phase conditions (see spatio-temporal velocity distribution shown in FIG.

3-4). The waviness of the vortex tube, however, is significantly modified by the addition of microbubbles conforming to the basic wave, inferred from the motion of microbubbles from UVP investigation (mentioned in SECT. 3.4.1). Bubbles in this Taylor–Couette flow are expected to be preferentially distributed at the crest of the basic wave in the azimuthal direction, and the distribution may play a key role in the enhancement of the basic wave. Thus, the basic wave enhancement has the greatest effect at $Re^* = 5$, which is just below the onset of wave modulation.

TABLE 3-4 Critical Reynolds numbers and growth rates of wave powers; Re_w, and Re_m are the critical Reynolds number from TVF to WVF, and WVF to MWVF, respectively. C_w and C_m are the growth rates of the basic and modulation wave, respectively, as a function of the Re^*, where Re_c is the critical Reynolds number for the onset of instability from CCF to TVF.

α	Re^*_w (= Re_w/Re_c)	C_w^2	Re^*_m (= Re_m/Re_c)	C_m^2
0	1.26	0.879	5.83	3.83×10^{-2}
3×10^{-5}	1.87	1.58	6.27	2.62×10^{-2}
6×10^{-5}	1.89	2.63	6.46	2.00×10^{-2}
9×10^{-5}	N/A	N/A	6.92	1.93×10^{-2}

3.4.3 Statistic quantities of secondary flow

FIG. 3-11 shows time averaged quantities in the r-z cross section of the fluid layer at $Re^* = 8$ obtained from PTV; (a) velocity vector field, (b) radial velocity component, (c) axial velocity component, (d) rms value of the radial velocity component, (e) rms value of axial velocity component, (f) stream function indicating a pair of the Taylor vortices, and (g) tangential component of the voricity, respectively. The out-flow region, in which a radial jet extends from near the inner cylinder to the outer one between a pair of the vortices, locates at $(z - h / 2) / d = 0$. The axial wavelength of the Taylor vortex, i.e. length between successive out-flow region, was λ (= 1 / k_v) = 2.75d in this results.

Through the experiments, the axial wavelength λ took values 2.22d to 2.86 d depending on the number of Taylor vortex pairs in the finite length of the fluid layer. Addition of microbubbles did not modify λ as mentioned in SECT. 3.4.1. The maximum values of the time averaged radial and axial velocity are $\bar{u}_{r,\max} / U_{\text{wall}} = 0.17$ and $\bar{u}_{z,\max} / U_{\text{wall}} = 0.13$, where U_{wall} is the inner cylinder wall velocity, U_{wall} (= $2\pi\Omega R_{\text{i}}$). The spatial averaged rms values of radial and axial velocity fluctuation are $\langle u_{r,rms} \rangle / U_{\text{wall}} = 0.03$ and $\langle u_{z,rms} \rangle / U_{\text{wall}} = 0.05$, respectively. Stream function and vorticity exhibit the vortex structure in r-z cross section. Those signs represent the rotational direction, positive (reddish) and negative (bluish) indicate clockwise (CW) and counter clockwise (CCW) direction. The magnitude of the maximum and minimum value of vorticity yields the characteristic time for the rotation of the Taylor vortex τ / Ω (= $4\pi / \bar{\omega}_{\theta,\max,\min}$) = 18.

The most of the energy in the Taylor–Couette flow is supplied from the motion of the Taylor vortices, the largest organized-structures. The length scale of energy containing eddies are estimated from a model, empirical correlation or integral length based on the autocorrelation in general turbulent flows [133] [134], Taylor vortex tubes remains its torus structure even at Re^* = 1000 flow region so called turbulent flow. The energy-containing length scale ℓ_{e}, therefore, would be interpreted as the time averaged length, λ, or wavenumber, k_{v}, of the Taylor vortices given as

$$\ell_{\text{e}} \left(= \frac{1}{2k_{\text{v}}} \right) = \frac{\lambda}{2}. \tag{3-16}$$

The ratio of the mean bubble diameter D_{b} to the turbulent length scale ℓ_{e} is $D_{\text{b}} / \ell_{\text{e}} \sim 5 \times 10^{-3}$. On the other hands, the ratio of the bubble diameter to the Kolmogorov length scale, ℓ_{d}, is $D_{\text{b}} / \ell_{\text{d}} \sim 0.3$ at the maximum. This means that the diameter of microbubbles is smaller than length scale of the Kolmogorov length scale as well as the size of the energy supplying vortex scale. The normalized length scale is used as criteria for the modification of turbulent intensity in *turbulence* [133]. The turbulent intensity is increased at $D_{\text{b}} / \ell_{\text{d}} > 0.7$, or is decreased at $D_{\text{b}} / \ell_{\text{d}} < 0.7$. Therefore, in the flows, the presence of microbubbles is expected to reduce the turbulent intensity. Any RMS values in secondary flow are not modified in two-phase conditions, the powers of the azimuthal waves, however, shows significant modifications in those spectra.

3.4.4 Bubble distribution in Taylor vortex tubes

An instantaneous distribution of microbubbles in an *r*-*z* cross section of the wavy Taylor vortex structure is shown in FIG. 3-12, where the reduced Reynolds number, $Re^* = 8$ (MWVF) and the void fraction, $\alpha = 6 \times 10^{-5}$. The panels at the bottom left ((b) – (d)) and bottom right ((e) – (g)) show the results obtained at the crest and trough of the azimuthal wave on the vortices illustrated in FIG. 3-12 (a), respectively. The figures in each panel represent the velocity vector field of the liquid phase ((b) and (e)), corresponding stream function ((c) and (f)), and velocity vectors of microbubbles ((d) and (g)), respectively. At the crest (left panel), microbubbles are accumulated in the axial flow that connects adjacent vortices. In contrast, microbubbles do not show any typical pattern of ascent at the trough (right panel). Taylor vortex structures are represented by stream function, ψ, in FIGS. 3-12 (c) and (f). The colors indicate the rotation direction; reddish and bluish colors correspond to clockwise (CW) and counter clockwise (CCW) rotation, respectively. The axial size of the Taylor vortices (axial wavelength) is unchanged by the addition of microbubbles relative to that in the single phase state. In FIG. 3-13, the time series of the stream function at the center line of the fluid layer, $(r - R_i)/d = 0.5$, shows a pair of axially oscillating torus vortices. Elongation in the axial direction, the advection of the vortex tube upward, or changes in the flow mode (torus/spiral) do not appear with the addition of bubbles, unlike the results of previous studies in which larger bubbles with 1 mm [105] or 600 μm [110] [111] in mean diameter (so called milli-bubbles or sub-milli-bubbles) were added. Other eigenvalues of the Taylor–Couette flow, i.e., the frequency of the basic azimuthal waves, f_w, its modulation frequency, f_m, the wavenumber of the basic azimuthal wave, and the traveling velocity of the waves, were also unchanged. The presence of bubbles has no effect on the basic flow structure qualitatively (also mentioned by Murai, *et al.* [19] and Xu, *et al.* [99]). This could be expected, since the variations in the properties of the fluids containing a dispersed phase, i.e., the density and viscosity in bulk, are of the same order as the void fraction, which is negligible in this experimental condition, $\alpha < 1.2 \times 10^{-4}$.

FIG. 3-14 shows (a) the positions of the vortex cores, defined as the position at which ψ takes the maximum or minimum value, $z|_{\psi_{max,min}}$, where blue circles indicate the core positions of counter clockwise (CCW) rotating vortices and red circles indicate the

core positions of clock wise (CW) rotating vortices, the spatially averaged (b) radial and (c) axial velocity of tracer and bubbles obtained by PTV on the measurement plane ($<u_r>$ and $<u_z>$), and (d) fluctuation of the number density of bubbles N normalized by temporal averaged value $\overline{N}$ in the measurement plane. The spatio-temporal average of the rising velocity of bubbles decreases with increasing the Reynolds number, Re; $\left\langle \overline{u_{z\ \mathrm{bubble}}} \right\rangle / U_{\mathrm{St}} = 1.1$ at $Re^* = 3$ and $\left\langle \overline{u_{z\ \mathrm{bubble}}} \right\rangle / U_{\mathrm{St}} = 0.79$ at $Re^* = 9$, where the overline, '¯', indicates the time average, and U_{St} is the Stokes rising velocity given by Eq. (3-6). The spatially averaged axial velocity shows the significant fluctuation whose amplitude is larger than that of radial velocity, because of the mean flow generated formed by the azimuthal wave of Taylor–Couette flows. Microbubbles in flow rises up due to the slip between bubbles and liquid phase, the time series of spatially averaged axial velocity of microbubbles indicates larger upward velocity than that of tracer particle at the anywhere in the wave (in FIG 3-14 (c)). The dashed line in FIG 3-14 (c) indicates the spatio-temporal averaged value, $\left\langle \overline{u_{z\ \mathrm{bubble}}} \right\rangle / U_{\mathrm{St}} = 0.98$ at $Re^* = 8$. The ratio of mean (spatio-temporal averaged) bubble velocity to the maximum mean secondary velocity, $\left\langle \overline{u_{z\ \mathrm{bubble}}} \right\rangle / \overline{u}_{r,\max}$, and the RMS value of the axial velocity fluctuation, $\left\langle \overline{u_{z\ \mathrm{bubble}}} \right\rangle / \left\langle u_{z,rms} \right\rangle$, are 1.0 an 0.6, respectively. The individual bubble motion also is smaller than the secondary velocity component and its fluctuation, as well as the diameter comparing to the length scale of the flow. The eddy viscosity ratio defined as

$$\phi\left(=\frac{\nu_{\mathrm{b}}}{\nu_{\mathrm{e}}}\right)=\frac{\left\langle \overline{u_{z\,\mathrm{bubble}}} \right\rangle}{\left\langle u_{z,rms} \right\rangle}\frac{D_{\mathrm{b}}}{\ell_{\mathrm{e}}} \tag{3-17}$$

by Hosokawa & Tomiyama [134] takes 3×10^{-3} in this condition. Following the knowledge, the presence and motion of individual microbubbles are expected not to be enough minor effect on the flow.

FIG 3-12 shows that bubbles rise upward globally at the crests and descend at the troughs of the azimuthal wave. At the moment, the fluctuation of number density of bubbles is larger than that of tracer particle shown in FIG 3-14 (d). The cross-correlation between the temporal fluctuation of spatial averaged upward velocity and number of tracer particle obtained from PTV (shown in FIG 3-14), takes 0.08, on the other hand, that of microbubble takes 0.5, respectively. This indicates that bubbles form an organized fluctuation of the void fraction, i.e., a voidage wave, in the azimuthal wave of

the Taylor–Couette flow. The cross-correlation between the axial position of the vortex core and the number of detected bubbles that shows the relationship between the axial oscillation of the azimuthal wave and the voidage wave is 0.91. Thus, it can be said that the microbubbly voidage waves that are highly synchronized with the azimuthal wave are generated in the flow field. This would be caused by a global (fluid layer scale) effect appearing as the result of mutual interaction between the bubble distribution and flow structure of the surrounding liquid phase. Moreover, the fluctuation amplitude of the Taylor vortex tube in the axial direction, $\tilde{z}|_{\psi_{\max,\min}}$, is greater in the two-phase conditions (TABLE 3-3). The oscillation amplitude of the vortex tubes generally decreases with increasing Reynolds number [135]. The resulting effect shows that the addition of microbubbles to the flows enhances the basic wave oscillation of the Taylor vortex tubes and modifies the flow state into that obtained with lower Reynolds number.

The fluctuations of the values at the center of the oscillating Taylor vortices, i.e., the maximum or minimum values of the stream function, $\tilde{\psi}^2{}_{\max,\min}$, in the single phase and two-phase cases are shown in FIG. 3-15. The frequencies of the fluctuations are also unchanged; the fluctuation powers, however, indicate an increase at the basic frequency, f_w, and a decrease at twice the basic frequency, $2f_w$ (TABLE 3-3). The fluctuation power corresponding to $2f_w$ increases with the non-linear development of the waviness with increasing *Re*. This is the selective intensification of the vortex strength at the crest of the wave by preferentially rising bubbles (FIGS. 3-12 and 3-14), which also appears in the velocity profiles (FIGS. 3-7 and 3-8).

Shiomi, *et al.* [104], Djeridi, *et al.* [105], and Murai, *et al.* [110] have experimentally investigated the distribution of bubbles in a vertical Taylor–Couette system. Murai, *et al.* [110] concluded that the bubble motions captured in the vortical structure are governed by the Froude number, i.e., the centrifugal acceleration relative to the gravity/buoyancy, defined as

$$Fr = \frac{U_{\text{wall}}}{\sqrt{gR_i}}, \tag{3-18}$$

where U_{wall}, g and R_i are the inner wall velocity ($U_{\text{wall}} = 2\pi\Omega R_i$), gravity acceleration, and radius of the inner cylinder, respectively. Bubbles in the Taylor–Couette flows are trapped into the core of the Taylor vortices when *Fr* is greater than 0.6. Under our experimental conditions, the maximum Froude number *Fr* is 0.1, and bubbles would not

be trapped into the vortical structure. Because of the considerable slip velocity between the bubbles and the liquid phase flows, bubbles with *O*(1 mm) in diameter are captured in the cores of the vortices at the crests and troughs alternately, which are the local minima of the pressure, in the relatively weak wavy Taylor vortex flow [108]. The bubbles, however, migrate and rise in the axial flow when they are ejected from the core of the Taylor vortices in the relatively strong wavy flow mode [108]. Our observation agrees well with this expectation based on the governing relation of the force balance, *Fr*. The organized azimuthal distributions of bubbles that resemble those in FIG. 3-6 have also been observed in the previous studies by Murai, *et al.* [110] and Yoshida, *et al.* [111], which used relatively small bubbles with *O*(100 μm) in diameter. The mechanisms that generate the organized inhomogeneous bubble distribution, however, have not been discussed and are still unknown. Fluid particles experience periodic accelerations and pressure fluctuations in the waviness of WVF [136] in the Lagrangian-frame. The voidage wave, i.e., the fluctuation in the number density of microbubbles, in the azimuthal direction might be related to the integration of the drift due to the small but unignorable slip velocity in the periodically accelerated wavy flow. Because the rising velocity of microbubbles is relatively small compared to the mean azimuthal velocity of the fluid, about 40 % of the inner wall velocity [137], microbubbles form a preferential concentration pattern in the long-time scale of travel in the azimuthal wavy flow patterns.

3.4.5 Reduction of azimuthal shear

The time-averaged distribution of the azimuthal velocity component is shown as contours in FIG. 3-10 for (a) single phase and (b) two-phase conditions with a void fraction of $\alpha = 1.2 \times 10^{-4}$. Whiteness and blackness represent high and low velocities, respectively. An out-flow region in which the azimuthal jet carries the high azimuthal momentum outward exists around $z^* = 0$ in both the single and two-phase conditions. The mean azimuthal flow structure remained in the two-phase case, because the mean rising velocity of microbubbles is smaller compared to the inner wall velocity (see FIG. 3-6 (b)). The high-velocity regions are expanded at the upper region of the out-flow region and are reduced at the lower region of the out-flow region. The azimuthal flow structure was made asymmetrically distorted about the out-flow region in the

axial/gravitational direction by the addition of microbubbles (FIG. 3-10 (b)). FIG. 3-11 (a) shows the axial and temporally averaged azimuthal velocity profiles along the radial direction. The velocity gradient decreases monotonically in the radial direction in the two-phase condition. The laminar profile (circular Couette flow (CCF), dashed line), which is given by the geometry of system following as

$$u_\theta = U_{\mathrm{wall}}\left(-\frac{R_\mathrm{i}}{R_\mathrm{o}^{\,2}-R_\mathrm{i}^{\,2}}r+\frac{R_\mathrm{o}^{\,2}R_\mathrm{i}}{R_\mathrm{o}^{\,2}-R_\mathrm{i}^{\,2}}r^{-1}\right),\ U_{\mathrm{wall}}=2\pi\Omega R_\mathrm{i}, \tag{3-19}$$

is displayed as references. The numerical profile obtained from Direct Numerical Simulation (DNS) for a single phase flow that authors calculated by our own code (dashed-dotted line) shows the feature of the distortion in the azimuthal velocity profile. The azimuthal velocity distribution is distorted from the CCF and becomes a stepper shape, which agrees well with that in a similar experimental configuration [137]. The gradient of the azimuthal velocity profile, $-\frac{\partial}{\partial r}\langle\overline{u_\theta}\rangle$, near the inner and outer walls can be obtained from the velocity difference between the wall velocity and measurement data, and is shown in FIGS. 3-11 (b) and (c). In the figures, the lines connecting the wall and symbols indicate the velocity gradient. The velocity gradient near the walls that provides the wall shear stress, $\tau_{\mathrm{wall}}\left(=-\mu\frac{\partial}{\partial r}\langle\overline{u_\theta}\rangle\Big|_{\mathrm{wall}}\right)$, decreases by approximately 10 % near both the inner and outer cylinder walls in the two-phase condition (TABLE 3-3). These decreases of the mean azimuthal velocity gradient near the walls by the addition of microbubbles are equivalent to decreasing the Reynolds number at the flow regime below the turbulent Taylor vortex flow [137].

Momentum transfer in supercritical Taylor–Couette flows is conducted mainly by radial flows due to the appearance of Taylor vortices: The out-flow carries high-speed azimuthal flows from near the inner cylinder to the outer cylinder and the low-speed azimuthal flows are carried by the radial counter flows, and vice versa. The Taylor vortex tube array exhibits the axial oscillation propagating in the azimuthal direction, owing to the instabilities of the out flow jet [128] or shear instabilities of the azimuthal velocity in the axial direction [131] [122] [132]. The general mechanism of the appearance of the azimuthal wave is still an open problem. The roots of the waviness, however, are definitely linked to the hydrodynamic instability of the velocity gradient in the out-flow region. Wave modulations appear as the result of the non-linear development of the waves at high Reynolds number regimes. These results suggest that

the reduction in the wave modulation (see SECT. 3-4) is due to the decrease in the instabilities related with the spatial velocity gradient in the out-flow regions. FIGS. 3-12 (a) and (b) show schematic outlines of the microbubble distribution in the wavy vortex structure on the rotating frame and the momentum transfer in the fluid layer under bubbly conditions, respectively. The momentum exchange is enhanced by the preferential distribution and migration of microbubbles swarming near the out-flow region and near the inner cylinder, which supply the momentum into the fluid. The fluctuation of the azimuthal velocity of the basic power, $\langle u_\theta \rangle (f_w)$, is also decreased (see TABLE 3-3), because migration of bubble swarms shifts the direction of the high-speed azimuthal flows to the axial direction. The flow elements naturally appear owing to the hydrodynamic instabilities with the increase in the Reynolds number in Taylor–Couette flows. The external forcing from oscillating cylinders modifies the onset of the appearance of the primal instability [138] or energy concentration [139] of a flow mode. The modifications of flow elements shown in TABLE 3-3, i.e., intensification/attenuation of waviness and relaxation of the velocity gradient, represent energy conversions within flow modes. The spatial distribution pattern of the buoyant force due to the inhomogeneously distributed microbubbles is generated by the interaction from the spatially and temporally periodic flow pattern of the surrounding liquid phase. This non-uniform external forcing of microbubbles has modified the liquid phase flow as oscillating cylinders do [138] [139].

TABLE 3-5 Variations in typical quantities of flow elements in Taylor–Couette flow at two void fractions

	$\alpha = 6 \times 10^{-5}$	$\alpha = 1.2 \times 10^{-4}$	Measurement instruments
$\left\langle u_z^{\,2} \right\rangle (f_\mathrm{w})$	+ 94 %	+ 122 %	UVP, PTV
$\left\langle u_z^{\,2} \right\rangle (f_\mathrm{m})$	− 72 %	− 78 %	UVP, PTV
$\tilde{z}\big\vert_{\psi_{\max,\min}} (f_\mathrm{w})$	+ 7 %	+ 51 %	PTV
$\tilde{\psi}_{\max,\,\min} (f_\mathrm{w})$	+ 13 %	+ 55 %	PTV
$\tilde{\psi}_{\max,\,\min} (2f_\mathrm{w})$	− 5 %	− 13 %	PTV
$-\dfrac{\partial}{\partial r}\left\langle \overline{u_\theta} \right\rangle\Big\vert_{r=R_\mathrm{i}}$	N/A	− 8 %	LDA
$-\dfrac{\partial}{\partial r}\left\langle \overline{u_\theta} \right\rangle\Big\vert_{r=R_\mathrm{o}}$	N/A	− 11 %	LDA
$\left\langle u_\theta \right\rangle (f_\mathrm{w})$	N/A	− 52 %	LDA

3.5 Conclusion

The effects of the presence of microbubbles with $O(10\ \mu m)$ in the mean diameter on the coherent vortical structures and the flow transition were investigated in a vertical Taylor–Couette system in laminar-transition regions corresponding to wavy/modulated-wavy Taylor vortex flow regimes. The addition of uniformly dispersed microbubbles was not expected to modify any fluid phenomena, since the variations in the fluid characteristics, i.e., the density and viscosity of the bulk, and the external energy input by the bubbles forcing are small enough even at the case of the maximum void fraction, $\alpha = 1.2 \times 10^{-4}$. However, our experimental results indicated considerable modifications of the flows, particularly at the flow transition of the system.

The first finding is that microbubbles form voidage waves in the azimuthally traveling waviness; the number density of the microbubbles increases at the crest of the waves and decreases at the trough. Further, highly concentrated microbubbles migrate in the axial streams that connect successive counter-rotating Taylor vortices. In contrast with other studies [104] [105] [110] [111], the presence of microbubbles in our experiments does not modify the flow into new flow states as expected, because of the smaller diameter and lower void fractions. The axial wavelength of the Taylor vortices, frequency of waves, number of azimuthal waves, and traveling velocity of waves were unchanged in two-phase conditions compared to the single phase state. However, the voidage wave, whose structure conforms to the basic azimuthal wave, affected on the waviness. The power of the basic wave fluctuation is enhanced by the addition of microbubbles. On the other hand, the modulation on the basic wave is reduced. Heavy solid particles also show organized distributions of number concentrations in flows [140] [141]. Bosse, *et al.* [140] presented the heavy particle motion simulated by a point-force coupling model with an Eulerian–Lagrangian LES in an isotropic homogeneous turbulence: The particle concentration distribution is formed by the vortical structure, and thus highly concentrated heavy particles preferentially settle down in the downward flow region of the continuous phase. Further, in settling, the preferentially dispersed particles selectively modify the flow structure, as represented in the power spectra of the spatial velocity fluctuation. The flow regime where we conducted experiments is generally not a turbulent flow but a primal time-dependent flow in the so called transition regime. The frequency components of the power spectra

for the velocity fluctuation, however, are also selectively modified by the organized microbubble distribution in our experiments. Intensification and attenuation of wave components by the addition of microbubbles obey a simple law, i.e., the dominant wave represented by the strongest power in the spectra is enhanced, and other weaker waves are diminished. The detailed mechanisms for generating voidage waves conforming to the azimuthal wave are not fully understood yet and require further investigation.

The second finding is that microbubbles modify not only the flow structure in the buoyant direction, but also that in the direction perpendicular to the buoyant direction. The spatial gradient of the tangential velocity distribution is decreased by the addition of microbubbles. Typically, the gradient in the radial direction is reduced by 10 % near both the inner and outer cylinder walls in the two-phase condition. This suggests that the wall shear stress may be reduced 10 % by the addition of microbubbles even at a very small void fraction, $\alpha = 1.2 \times 10^{-4}$. Bubbles in the horizontal channels accumulate in the region so-called ‘sweep’ or ‘ejection’ region; they modify the role of the momentum exchange described as the Reynolds shear stress [21] [23] [31] and displace the streamwise vortical structures away from the wall because of the gravity force [31]. The reduction of the wall shear stress as the gradient in the streamwise velocity is thought to be resulted from the modification of flow structure in the direction of gravity [32]. Gravitational force did not displace the flow structures in the vertical Taylor–Couette system, unlike the case in horizontal channel flows. The secondary wavy structure, however, is vertically modified by the basic oscillation whose power is intensified in the direction of gravity. The momentum exchange in supercritical Taylor–Couette flows is conducted mainly by Taylor vortices: the secondary flow (the radial out-flow jet) carries high-speed fluids from near the inner cylinder to the outer cylinder. Microbubble migration in the axial flow is proposed to shift the flow direction of the fluid having high azimuthal velocity to the gravitational / axial direction. The axial oscillation of the basic wave is simultaneously enhanced. Further, the modulation wave resulting from the instability due to large velocity gradients is reduced because the gradient of the azimuthal velocity is relaxed by this increase in the mixing effect with the addition of microbubbles. The modification of the secondary wavy structure reaches a global shear state, even when the direction of gravity direction is perpendicular to the direction of the main flow, ‘sweep’ or ‘ejection’. In channel flow, drag reduction can be

achieved by controlling secondary flow with the wall normal velocity (blowing/suction at a wall surface) or spanwise velocity (corresponding to the axial velocity in a Taylor–Couette flow) (artificial slip at a wall surface). The modification of main flow and wall shear stress at a wall surface could be also achieved as well as velocity control in channel.

To summarize, the present experiments demonstrated several modifications of flows with the addition of microbubbles; intensification of the basic azimuthal wave, attenuation of the wave modulation, and a decrease in the spatial gradient of the azimuthal velocity. These modifications induce a pseudo-decrease in the effective Reynolds number with a tiny void fraction. Similar modifications of the global flow field, such as a decrease in the effective Reynolds number or a delay in the flow transitions, have also been reported [19] [22] [24] [36]. A coherent flow structure near the wall, the source of global momentum transfer, also still exists at the flow regime on which those studies focused. In shear flows containing microbubbles including open systems such as channel flows, the interaction between organized distributions of microbubbles and the coherent secondary wavy structures would result in modifications of the global flow state like those in our investigations.

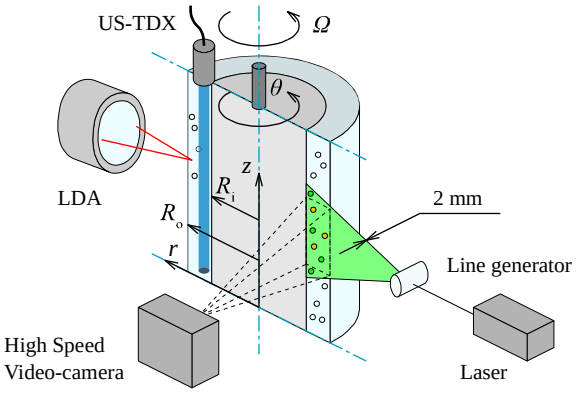


FIG. 3-1 Schematic outline of experimental setup

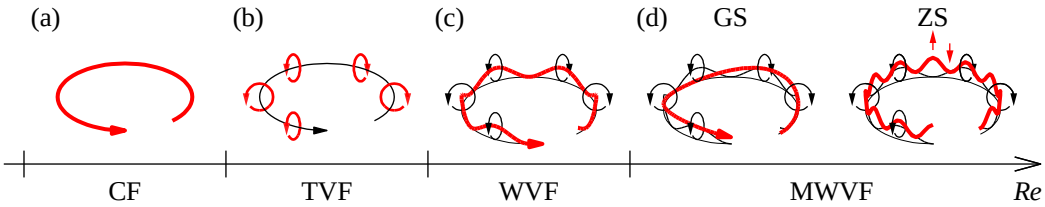


FIG. 3-2 Schema of the appearing flow elements in each flow mode of Taylor-Couette flows; (a) circular flow in circular Couette flow (CF), (b) Taylor-vortex in Taylor-vortex flow (TVF), (c) basic wavy motion in wavy-vortex flow (WVF), and GS and ZS mode of modulated wavy motion in modulated wavy vortex flow (MWVF), respectively

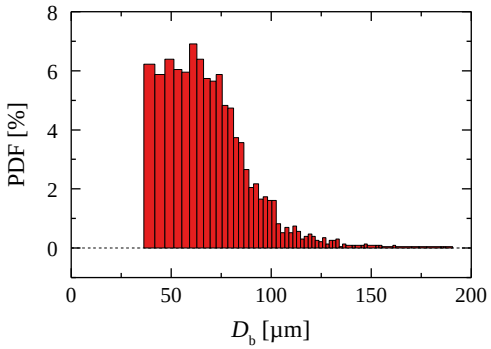


FIG. 3-3 Distribution of microbubble diameter

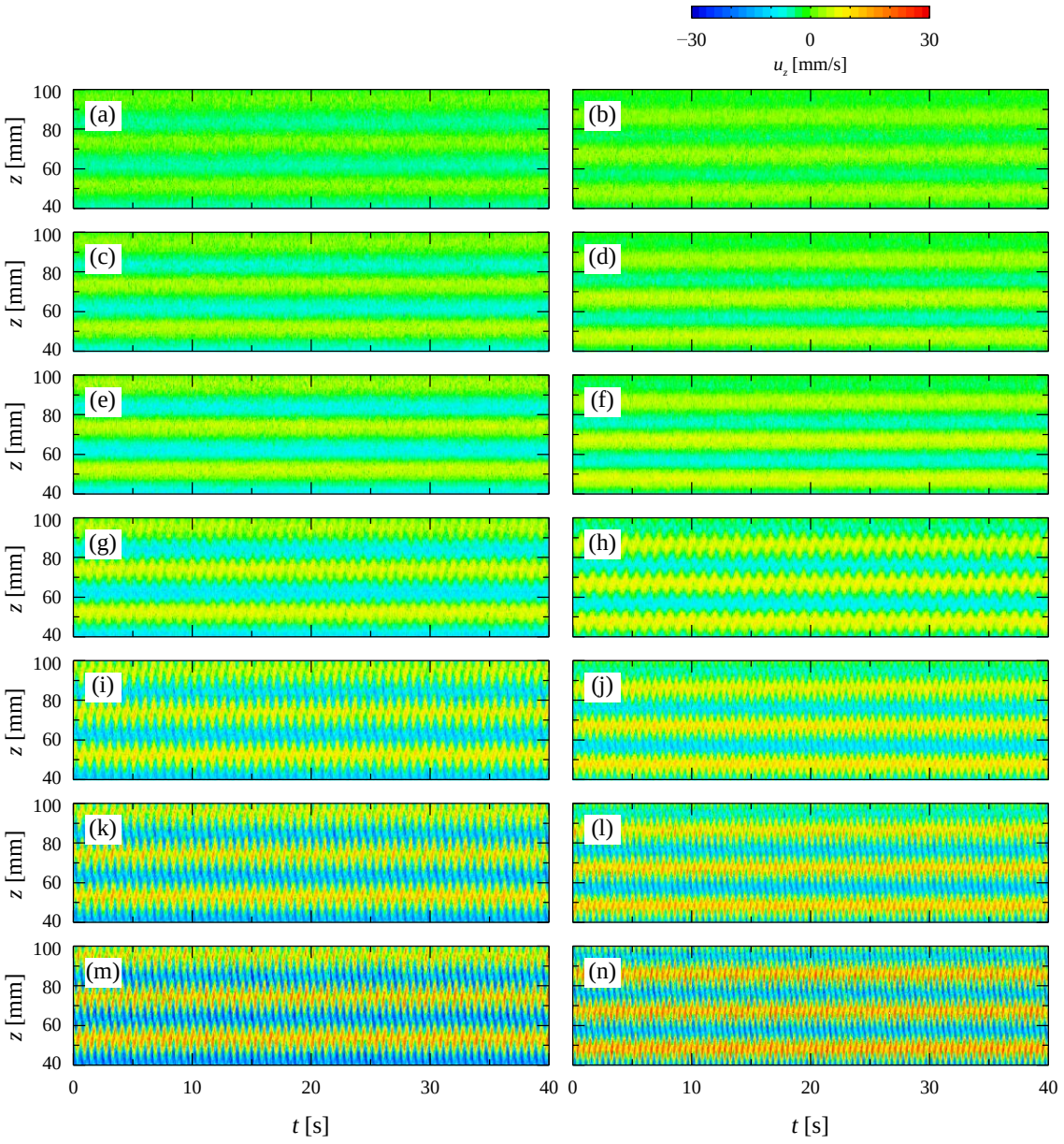


FIG. 3-4 Spatio-temporal velocity distribution of axial velocity component at *Re* = 140 ((a) and (b)), *Re* =150 ((c) and (d)), *Re* = 160 ((e) and (f)), *Re* = 175 ((g) and (h)), *Re* = 200 ((i) and (j)), *Re* = 225 ((k) and (l)), and *Re* = 250 ((m) and (n)), respectively. Left panels display velocity profiles at experimental run 1, while right panels display velocity profiles at experimental run 2.

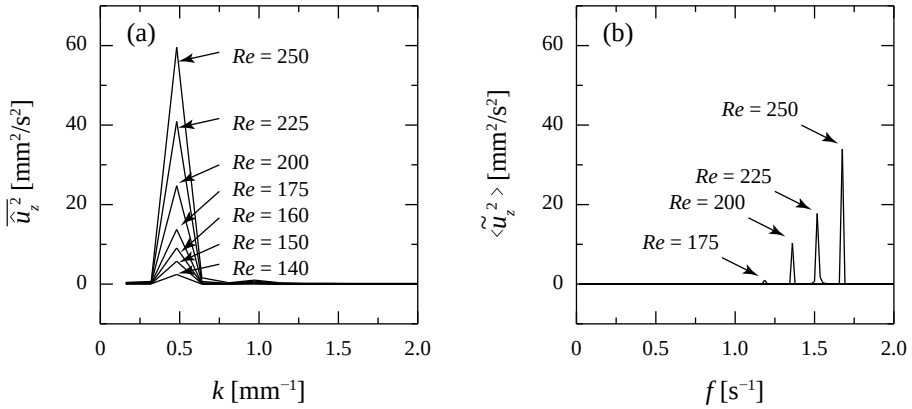


FIG. 3-5 (a) Temporally averaged power spectra of the spatial velocity fluctuation and (b) spatially averaged power spectra of the temporal velocity fluctuation for various *Re*

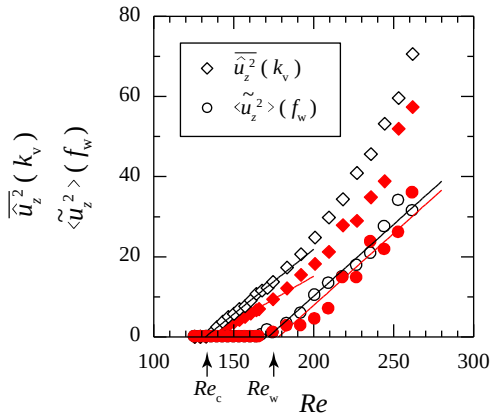


FIG. 3-6 Power of Taylor vortices as spatial velocity fluctuation, $\overline{u_z^2}(k_v)$, (diamond) and azimuthal basic wave as temporal velocity fluctuation, $\langle u_z^2 \rangle (f_w)$, (circle) versus Reynolds number, where open and closed symbols represent different run of experiments.

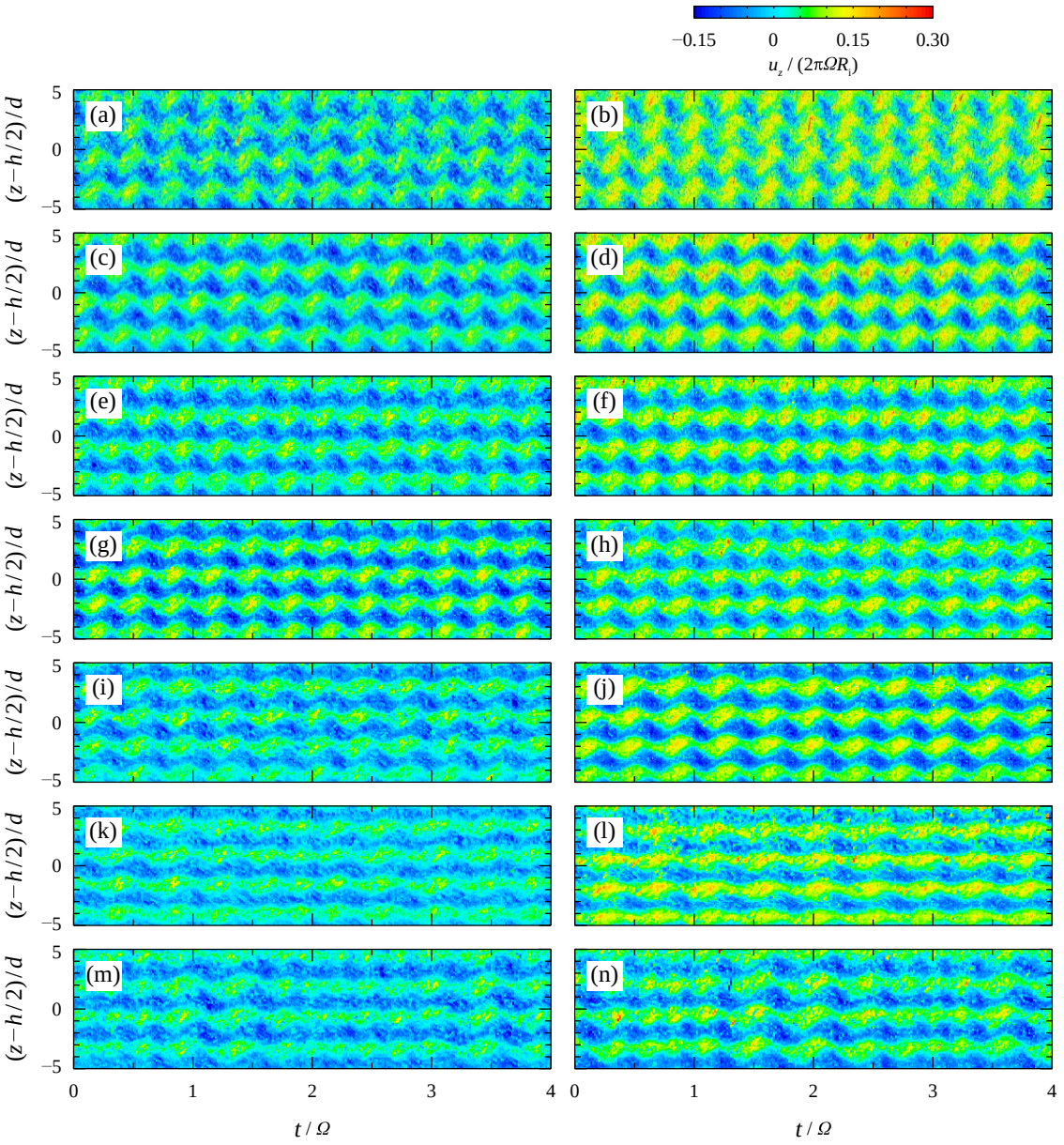


FIG. 3-7 Spatio-temporal velocity distribution of axial velocity component at Re^* = 3 ((a) and (b)), Re^* = 4 ((c) and (d)), Re^* = 5 ((e) and (f)), Re^* = 6 ((g) and (h)), Re^* = 7 ((i) and (j)), Re^* = 8 ((k) and (l)), and Re^* = 9 ((m) and (n)), respectively. Left panels display velocity profiles in single phase flow conditions, while right panels display velocity profiles in two-phase flow ($\alpha = 6 \times 10^{-5}$).

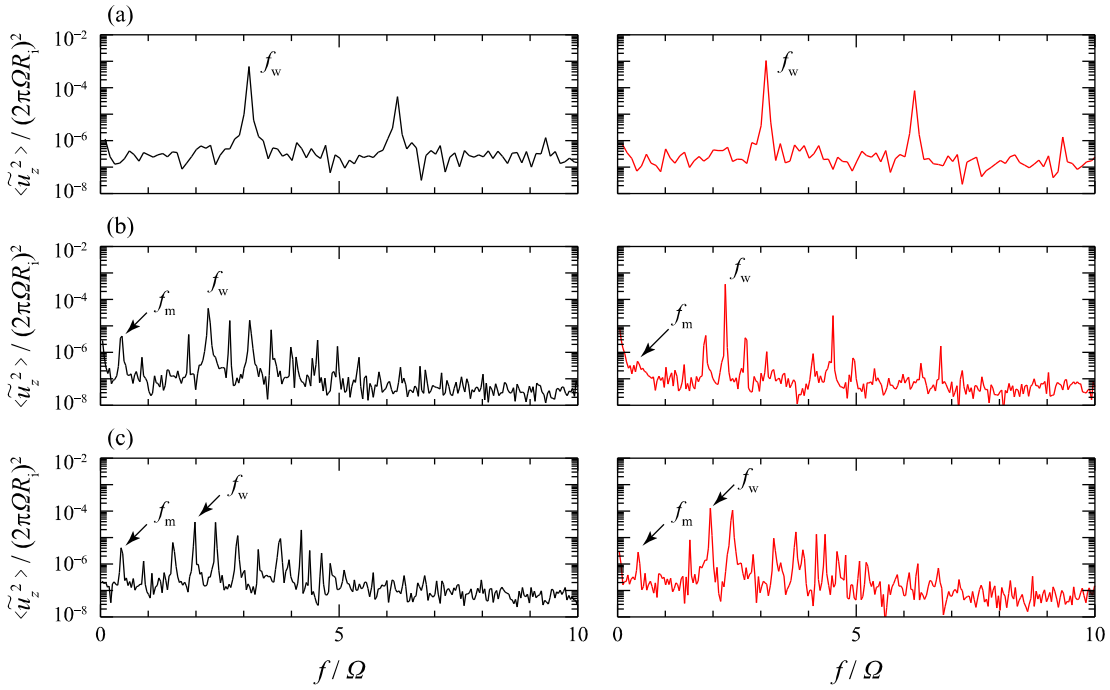


FIG. 3-8 Comparison of power spectra of the axial velocity fluctuation, $\langle u_z^2 \rangle$, normalized by the inner cylinder wall velocity, $2\pi\Omega R_i$, at (a) $Re^* = 3$, (b) $Re^* = 8$, and (c) $Re^* = 9$. Spectra on the left panels are for single phase flow, whereas spectra on the right panels are for two-phase flow ($\alpha = 6 \times 10^{-5}$); f_w and f_m represent the basic and modulation frequencies, respectively.

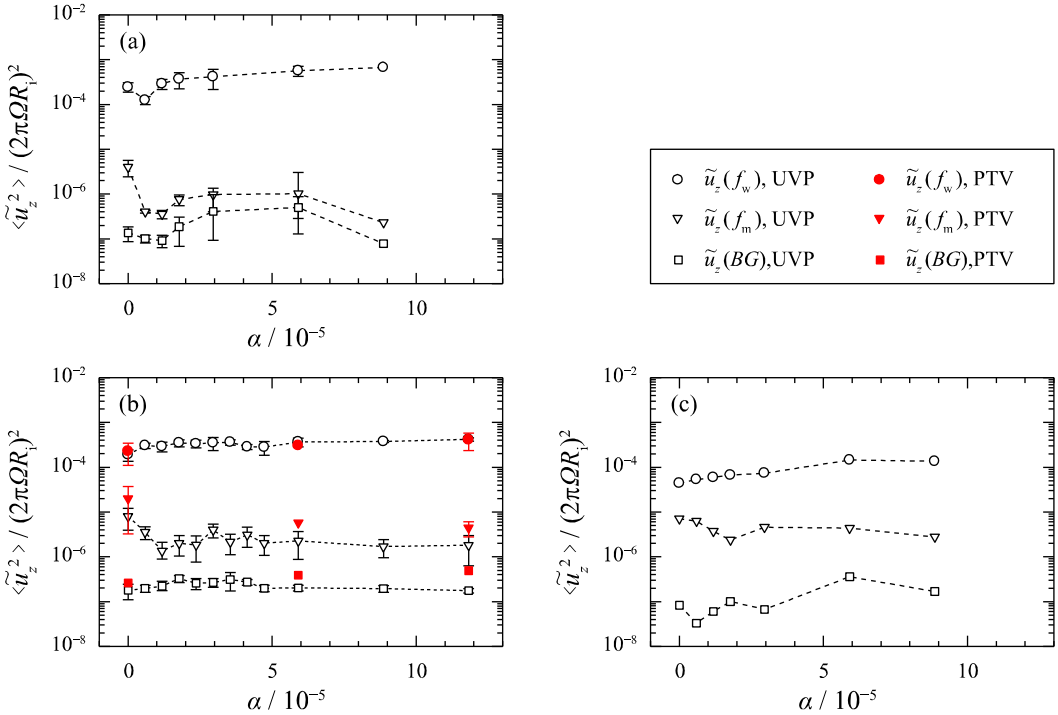


FIG. 3-9 Power of the basic wave, $\langle u_z \rangle (f_w)$, modulation wave, $\langle u_z \rangle (f_m)$, and background component, $\langle u_z \rangle (BG)$, at $(r - R_i)/d = 0.25$ versus the void fraction, α, obtained by UVP (open symbols) and PTV (solid symbols): (a) $Re^* = 7$, (b) $Re^* = 8$, and (c) $Re^* = 9$. The error bars indicate the magnitude of the standard deviation of ensemble average in runs of experiments.

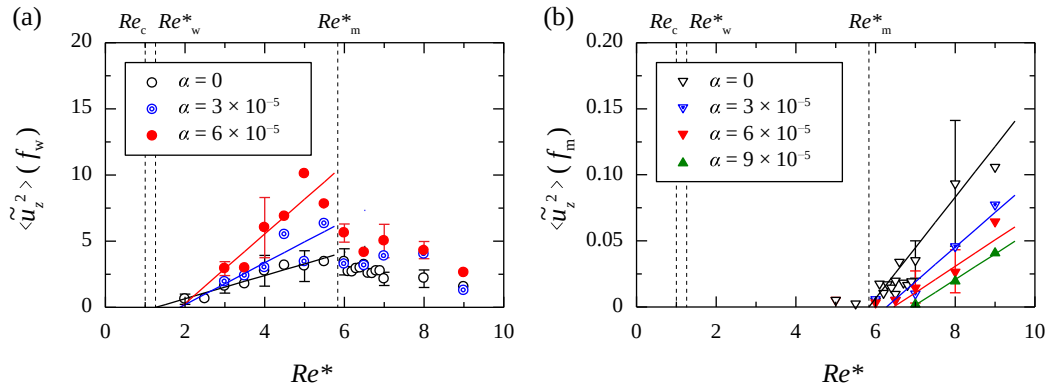


FIG. 3-10 Power of axial velocity fluctuations of (a) basic wave $\langle u_z^{\sim 2} \rangle (f_w)$ and (b) modulation wave $\langle u_z^{\sim 2} \rangle (f_m)$ versus normalized Reynolds number *Re** in single phase and two-phase conditions (α = 3 × 10^{-5}, 6 × 10^{-5}, and 9 × 10^{-5}). The solid lines represent the least square approximation lines following the basic and modulation powers, and the error bars indicate the magnitude of the standard deviations of ensemble average in runs of experiments. The vertical dotted lines indicate the critical Reynolds number for the flow transition from CCF to TVF, Re_c; and normalized critical Reynolds number from TVF to WVF, Re^*_w (= Re_w / Re_c); and WVF to MWVF, Re^*_m (= Re_m / Re_c) of the single phase flow, respectively.

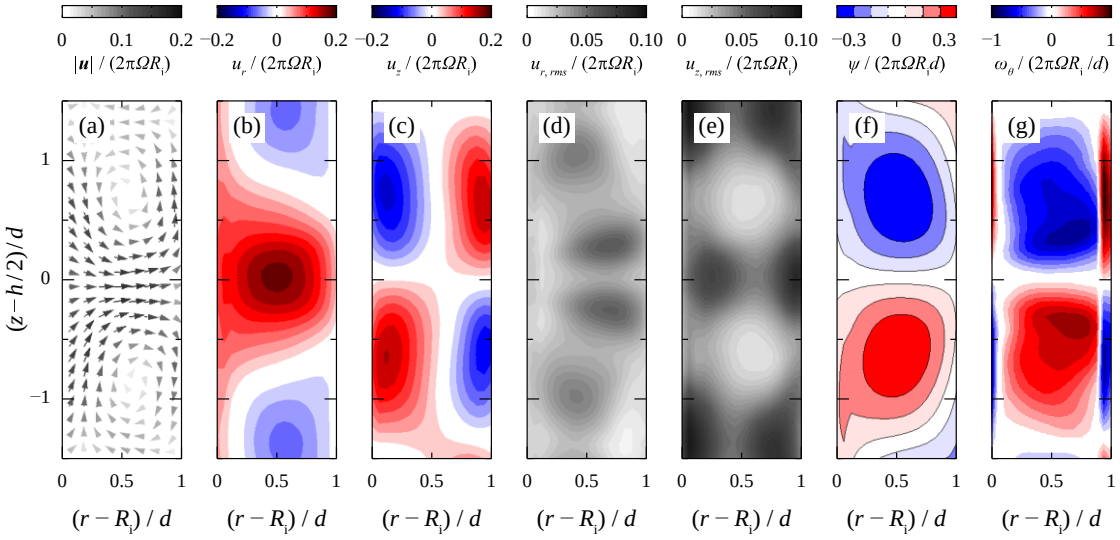


FIG. 3-11 Time averaged distribution of (a) velocity vector, (b) radial velocity, (c) axial velocity, (d) RMS value of radial velocity fluctuation, (e) RMS value of axial velocity fluctuation, (f) stream function, and (g) tangential vorticity

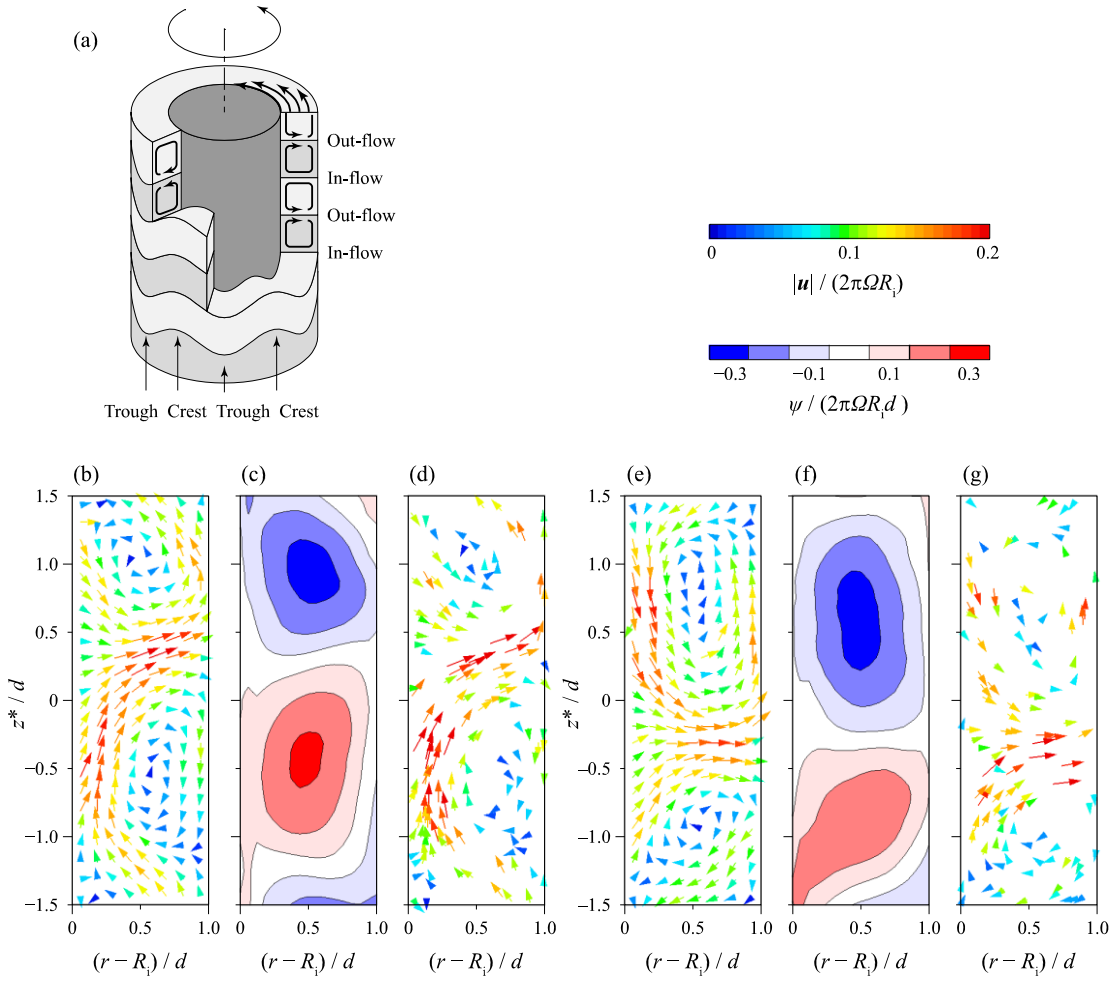


FIG. 3-12 (a) Axially oscillating Taylor vortices appearing in the fluid layer, (b) and (e) velocity vector field of liquid phase, (c) and (f) corresponding stream function, and (d) and (g) velocity vector of microbubbles at Re^* = 8, where (b) (c) (d) and (e) (f) (g) indicate the results obtained at the crest and trough of the wavy motion, respectively

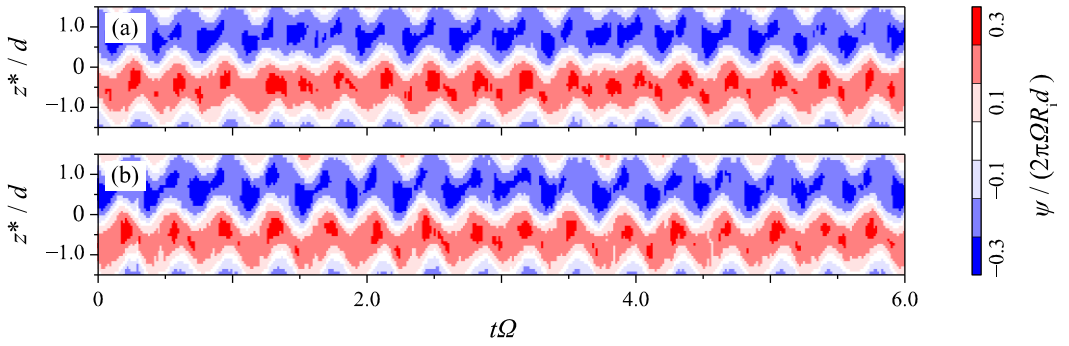


FIG. 3-13 Time series of stream function at the center of the fluid layer, $(r - R_i)/d$ = 0.5, obtained at Re^* = 8: (a) single phase flow and (b) two-phase flow ($\alpha = 6 \times 10^{-5}$)

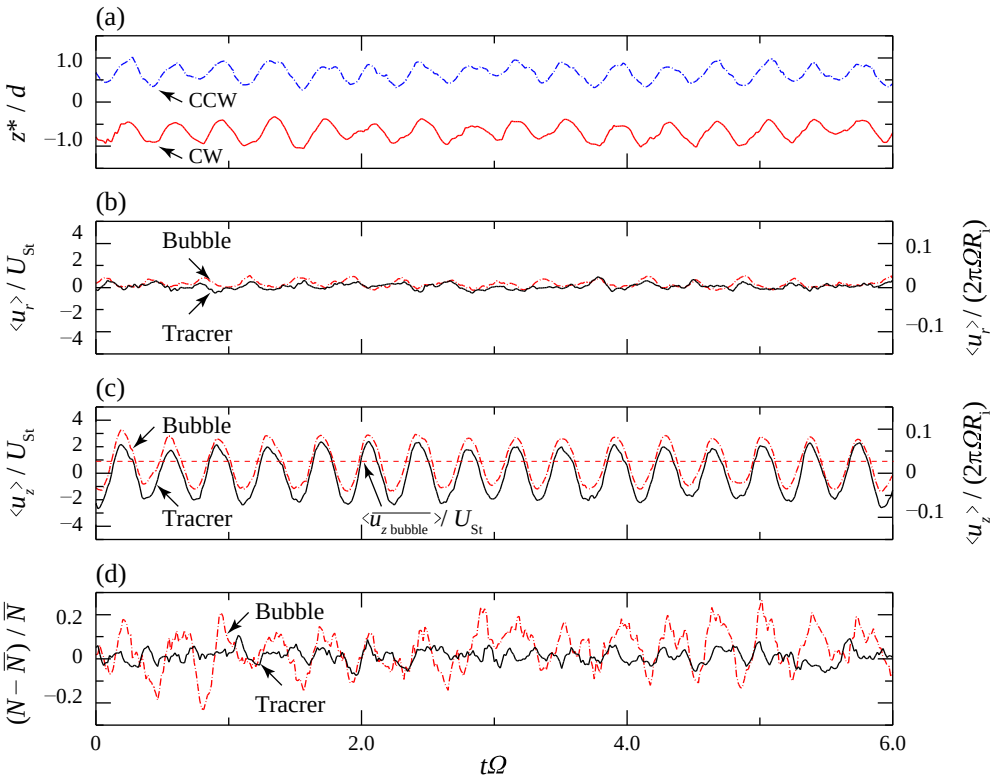


FIG. 3-14 Time series of (a) axial position of vortex core, where blue and red lines indicate counter clock wise (CCW) and clock wise (CW) rotation vortices, respectively, spatially averaged (b) radial and (c) axial velocity of tracer and microbubbles normalized by Stokes rising velocity of the microbubble, U_{St}, and the inner cylinder wall velocity, $2\pi\Omega R_i$, and (d) temporal fluctuation of number of tracer and microbubbles

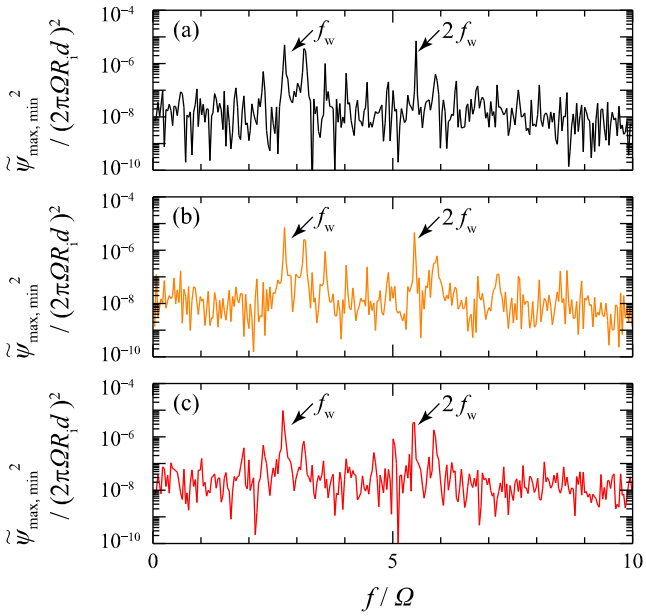


FIG. 3-15 Power spectra of the fluctuation in the stream function at the center of the vortices, $\tilde{\psi}_{\,\mathrm{max,\,min}}{}^{2}$, at Re^* = 8: (a) single phase flow, (b) two-phase flow at $\alpha = 6 \times 10^{-5}$, and (c) at $\alpha = 1.2 \times 10^{-4}$, respectively

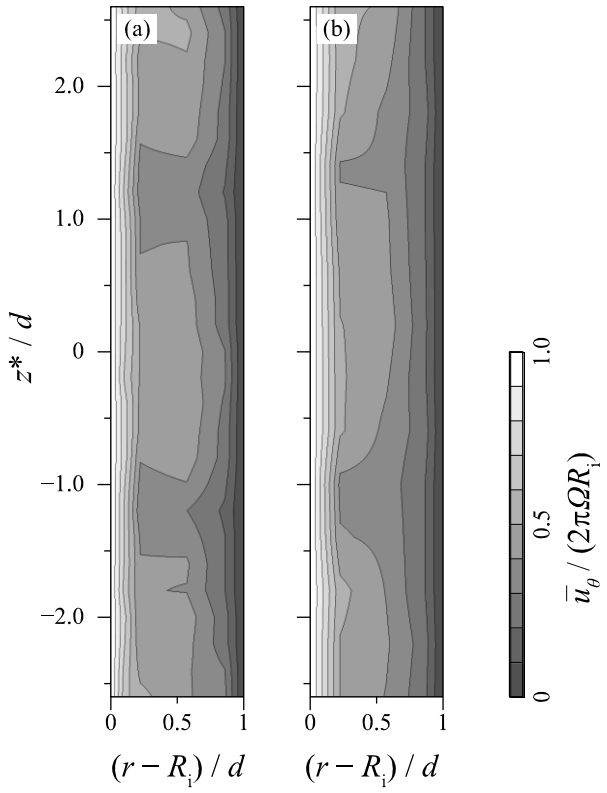


FIG. 3-16 Time-averaged azimuthal velocity components for (a) single phase and (b) two-phase flow (α = 1.2 × 10^{-4}) at Re^* = 8

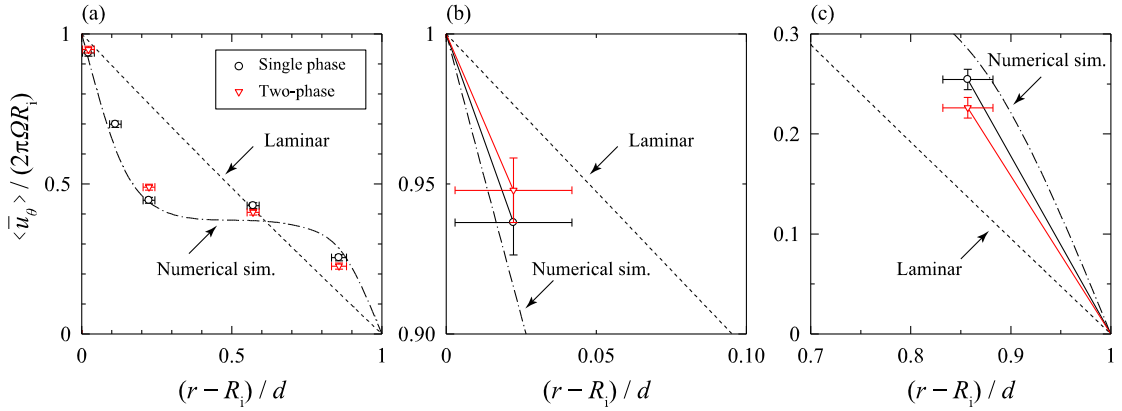


FIG. 3-17 Comparison of time-averaged azimuthal velocity data at Re^* = 8: (a) whole of the fluid layer, near the (b) inner and (c) outer cylinder. Symbols indicate single phase flow (circles) and two-phase flow (triangles, α = 1.2 × 10^{-4}), and lines indicate the velocity profiles of numerical simulation (DNS) and the laminar flow (i.e., analytical solution for circular Couette flow, CCF, short dashed line). Error bars indicate the spatial (horizontal bar) and velocity resolution (vertical bar).

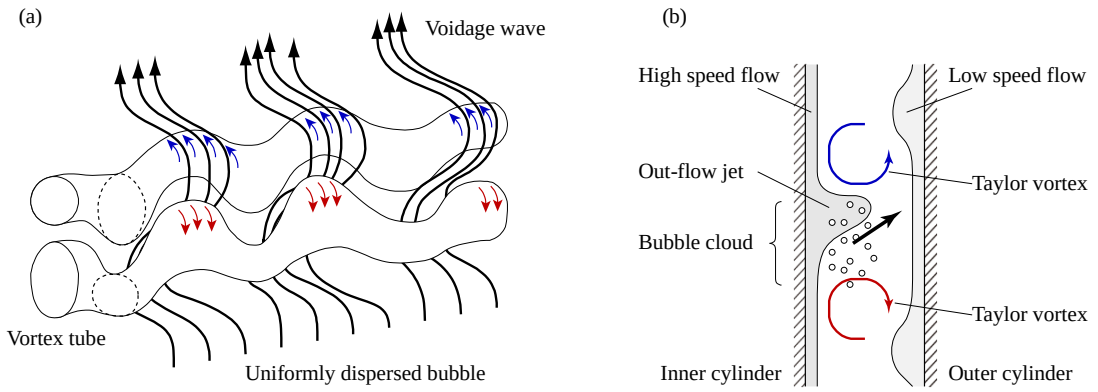


FIG. 3-18 Schematic outline of (a) microbubble distribution in wavy Taylor vortex tube. Red and blue arrows indicate rotational direction of vortices; black arrows indicate the motion of microbubbles. (b) Rising motion of microbubble cloud in the cross section of Taylor vortices.

Chapter 4
PIV and DNS combined hybrid analysis of Taylor–Couette flow

Abstract

Effects of flow structure modifications due to addition of microbubbles with 60 μm in mean diameter to a vertical Taylor–Couette flow are analyzed by hybrid simulations, where experimentally obtained velocity fields and velocity fields estimated by DNS are coupled to enrich the flow information to be discussed. A spatio-temporal structure of azimuthally propagating waves is reconstructed from the experimentally obtained planner velocity field. Doubly-periodic modulation waves are captured in the single phase condition, and diminishment of the wave modulation is also captured in a two-phase flow condition. Velocity gradient, Reynolds shear stress, and torque acting on the axis are decreased by $O(10^{-2})$ in the two-phase condition, comparing to the single phase flow. This attributed that the modification of the secondary flow by the addition of microbubbles at a void fraction $O(10^{-4})$ can achieve to reduce the skin frictional drag by $O(10^{-2})$ in bulk of the system.

4.1 Introduction

Drag reduction technique using microbubbles with tens of micrometer in mean diameter provides significant high efficiency on the reduction. For instance, the reduction ratio in skin frictional drag reaches up to $O(10^{-1})$ with tiny amount of volume fractions smaller than $O(10^{-3})$ [36] [19] [23] [24]. The previous experimental studies on turbulent boundary layers in the horizontal channel flows containing microbubbles suggest that the interaction between distributions of microbubbles and turbulent coherent structures is an important factor for the drag reduction [19] [22] [23] [24]. The scopes of previous studies were limited to present statistics of the velocity field, namely, averages and correlations (including Reynolds shear stress), due to the limitation of measurements on basis image analyses. The quantitative understanding of the modifications of the coherent streak structure generating, such as displacement of ‘sweep’ and ‘ejection’ reported by numerical works [31] [32], is still challenging problem in experiment. Spatially developing flows also provide difficulties on investigations of the mechanism of drag reduction. The vortical structures are modified due to the non-linearity of the flow in advection to the downstream.

In contrast, Taylor–Couette flows have been adopted as an experimental platform for investigating the interaction between coherent vortical structures and bubble distribution patterns [98] [144]. As mentioned in CHAPTER 3, the azimuthal wave structures of a vertical Taylor–Couette system are modified by the addition of microbubbles at cases in which the void fraction is smaller than $O(10^{-4})$; Power of the primary wave increases, on the other hand, that of the modulation wave decreases. The modulation waves naturally appear owing to hydrodynamic instabilities and grow with the Reynolds number. Thus, this can conclude that the modification of the waves by the addition of microbubbles prevent the flow transition and induces the pseudo-decrease of the effective Reynolds number. Velocity fluctuations of the secondary flow representing the wavy structures conduct the main role of the momentum exchange in supercritical Taylor-Couette flows. The mean azimuthal velocity profile measured by laser Doppler velocimeter showed that the shear stress in the two-phase condition, therefore, is reduced by the reduction of the effective Reynolds number due to the modification in the flow structure by the addition of microbubbles.

For investigating the shear stress profiles, that consist of viscous and Reynolds

shear terms, a time series of azimuthal and redial velocity profile in the fluid layer, namely, u_θ and u_r as functions of time and positions, are numerically acquired in this chapter. The careful measurement must be conducted for suppressing measurement noises and obtaining highly resolved velocity data in the determination process of Reynolds shear stress in experiments. Numerical simulations can provides high resolved unsteady three-dimensional velocity fields excluding noises and errors in measurement resolutions. Because of non-linear nature of Navier-Stokes equations, there are non-unique states in numbers of Taylor vortices and azimuthal waves [144] [145]. This is called as multiplicity of the solution. Generally, the flow states extracted from experiments are required to be fed as initial velocity disturbances for the generation of the particular flow state in numerical simulations. Nevertheless, the difficulties for capturing the transition point of flow state or modulation of velocity fluctuations still lie in numerical simulations. Numerical simulations of two-phase flows, unfortunately, have further difficulty in the modeling of the flow which basis on the physical lows, i.e. equation of continuity, momentum conservations in each phase and the between phases. Many approaches have been developed in order to resolve the multiphase flow dynamics and are well highlighted by Elgohbashi [146] and Balachandar & Eaton [147]. In spite of these efforts, the numerical simulations have still in progress for reconstruction the actual flow phenomena, e.g. simulation of flow mode transition [98] [110] or multiplicity of flow state [144] [145].

Hybrid simulations combining velocity fields obtained by experiments and numerical simulations overcome one of those disadvantages in pure numerical simulations. It can produce the low-noise level velocity fields from the experimental data [148], and can reconstruct the non-periodic flow phenomenon [149]. In this study, the hybrid simulation for a transition/time-dependent flow regime of a Taylor–Couette flow is performed, in order to investigate the contribution of wave modification on the azimuthal shear profiles. The share stress distributions and torque acting on the rotation axis are analyzed from the provided velocity field by the hybrid simulation. Then, the drag reduction performance owing to the addition of microbubbles is evaluated.

4.2 Experimental setup

The experiments were conducted in a vertical Taylor–Couette system shown in FIG. 4-1 (same as one in CHAPTER 3). The coaxial rotating system has a rotating inner cylinder, 95 mm in radius (R_i), and a fixed outer cylinder, 105 mm in radius (R_o). The gap distance between the cylinders, d (= $R_o - R_i$), and their height, h, are 10 mm and 200 mm, respectively. The radius ratio of the cylinders, η (= R_i / R_o), and the aspect ratio of fluid layer, Γ (= d / h), are 0.905 and 20, respectively. The Reynolds number of the flow is defined as

$$Re = \frac{U_{Wall} d}{\nu} = \frac{2\pi \Omega R_i d}{\nu}, \tag{4-1}$$

where U_{wall}, Ω and ν are the inner wall velocity ($U_{wall} = 2\pi\Omega R_i$), rotating frequency of the inner cylinder, and kinematic viscosity of water which is used as the test fluid, respectively. The Reynolds number is fixed at Re = 1080 (Re / Re_c = 8), where Re_c (= 134.6) (see CHAPTER 3) is the critical Reynolds number for the onset of the primary instability. The flow mode corresponding to this condition is modulated wavy vortex flow that has an azimuthal modulation wave superimposed on Taylor vortices and primary azimuthal wave. Hydrogen bubbles, 60 μm in mean diameter, were generated by water electrolysis from a platinum wire with a diameter of 100 μm mounted at the bottom of fluid layer and are dispersed into the fluid layer. The void fraction, α, was estimated by the input power for electrolysis as $\alpha = 1.2 \times 10^{-4}$. The measurement for the single phase flow was conducted at first, then, one for the two-phase flow was conducted.

Particle image velocimetry (PIV) and Laser Doppler Velocimetry (LDV) were used in velocity measurements. The velocity distributions of liquid phase (namely, radial, u_r, and axial velocity, u_z) and number density of microbubbles on the r-z cross section were simultaneously measured by PIV applying LIF technique, where a spatial, temporal, and velocity resolutions corresponding to 39 μm/pixel, 8 ms, and 0.78 mm/s, respectively. The measurement section of r-z cross section of the fluid layer in the middle of the axial direction was illuminated by the laser sheet (1 W, wavelength: 532 nm) with 2 mm in thickness. Particles containing laser fluorescent dye with 15 μm in diameter were used as tracer particles for PIV. To distinguish the tracer particles and microbubbles in an image, information on color of the scattering light from gas-liquid

interfaces of microbubbles and fluorescent light from the tracer particles was utilized for the criteria to distinguish tracer particles and microbubbles as following the method already mentioned in CHAPTER 2. Particle images with color information were acquired by a color-imaging high-speed video camera at a spatial range from $z = -2d$ to $2d$, in the middle of the fluid layer. The azimuthal velocity, u_θ, was measured by LDV with a velocity and spatial resolution corresponding to 4.3 mm/s, and 450 μm in the radial direction and 60 μm in the tangential and axial directions, respectively. The measurement point was scanned on the r-z plane using a traverse system. The measurements were conducted at a spatial range from $z = -3d$ to $3d$ with 4 mm interval in the axial direction.

4.3 Hybrid algorithm

The original hybrid algorithm combine velocity fields obtained by particle tracking velocimetry (PTV) and direct numerical simulations (DNS), and solve Navier-Stokes equation and equation of continuity of two-dimensional unsteady flows around an airfoil at $Re \leq 10^4$ in order to obtain two-dimensional velocity vector field $\boldsymbol{u}$ [u_x (x, y, t), u_y (x, y, t)] and pressure field p(x, y, t) as a function of space: x, y, and time, t. By contrast, in this study, the time series of radial and axial velocity components, (i.e., u_r^{PTV} (r, z, t) and u_z^{PTV} (r, z, t)), measured by PTV on the r-z cross section are coupled with three-dimensional velocity vector field obtained from DNS $\boldsymbol{u}$ [u_r^{DNS} (r, z, θ, t), u_z^{DNS} (r, z, θ, t), u_θ^{DNS} (r, z, θ, t)], for the reconstruction of flow field obtained in the experiment.

The time series profile of two-dimensional velocity vector field obtained from PTV is converted into rotating three-dimensional velocity dataset as a function of time. The experimentally obtained velocity data from PTV were relocated on the 17 × 65 of Cartesian grid points on the r-z cross section. The lacking velocity vectors on the grid points were interpolated based on the biquadratic-ellipsoidal equation [74]. We refer the experimentally obtained velocity data rearranged on the grid points instead of raw velocity vectors from PTV adopted in the original algorithm [148] [149]. The time series of PTV velocity data was rearranged in the cylindrical coordinate, namely, r, z, θ, using Taylor's frozen hypothesis [150] as

$$\theta = -c_t \tau \,, \tag{4-2}$$

where c_t and τ are the azimuthal traveling velocity of primary wave and period corresponds to the wave travelling around a cylinder, respectively. The traveling velocity c_t was determined from the frequency of primary wave, f_w, obtained by Fourier transform of axial velocity fluctuations and number of azimuthal basic wave, m, obtained by flow visualization as

$$c_t = f_w / m \,. \tag{4-3}$$

The experimentally obtained velocity components rearranged on the grid points of cylindrical coordinate were shifted and were periodically rotated in the tangential domain with the velocity, c_t, to represent the azimutally propagating wavy structures. The relation of the tangential position, θ, and the time, t, are given as

$$\theta = -c_t \left(\tau - t \right) . \tag{4-4}$$

We note that θ is adjusted in the range between 0 to 2π by adding or subtracting 2π

times integer. In this study, the experimentally obtained velocity for a single period, τ, was used as the velocity dataset for the hybrid combination. By employing Eq. (4-5) the experimentally obtained velocity vector dataset $\boldsymbol{u}^{PIV}(r, z, \theta, t)$ gives rotating dataset $\boldsymbol{u}^{PIV}(r, z, -c_t(\tau - t), t)$.

In physics, the equation of momentum conservation of liquid phase is given as

$$\frac{\partial \boldsymbol{u}}{\partial t} + (\boldsymbol{u}\cdot\nabla)\boldsymbol{u} = -\frac{1}{\rho}\nabla p + \frac{\mu}{\rho}\nabla^2\boldsymbol{u} + \boldsymbol{F}_b, \tag{4-5}$$

where $\boldsymbol{F}_b$ is the force from bubbles. In single phase flow, the force from bubbles takes $\boldsymbol{F}_b = 0$, Eq. (4-5) yield Navier-Stokes equation. $\boldsymbol{F}_b$ *is unknown*, because $\boldsymbol{F}_b$ can not measured in the experiment. Therefore, in this study, the experimentally obtained velocity data superimposed on the numerically obtained velocity dataset helps to correct velocity distribution in two-phase flow without giving $\boldsymbol{F}_b$. In addition, the experimental data provides the vortex size in axial direction, the number of waves in azimuthal direction and modulation mode in waves. The hybrid method also helps the flow field to develop into that obtained in the experiment even in the single phase flow.

In order to superimpose the experimental data on DNS data, the radial and axial velocity components were obtained by PIV, and were combined with DNS. The azimuthal velocity component, on the other hands, was calculated from DNS, because the azimuthal velocity components were not simultaneously obtained from the experiment. The hybrid velocity field is given by immersing experimental data in numerical data asthe following linear combination:

$$\begin{pmatrix} u_r \\ u_z \\ u_\theta \end{pmatrix}^{Hybrid} = \begin{pmatrix} 1-\omega f(z,t) \\ 1-\omega f(z,t) \\ 1 \end{pmatrix} \cdot \begin{pmatrix} u_r \\ u_z \\ u_\theta \end{pmatrix}^{DNS} + \begin{pmatrix} \omega f(z,t) \\ \omega f(z,t) \\ 0 \end{pmatrix} \cdot \begin{pmatrix} u_r \\ u_z \\ u_\theta \end{pmatrix}^{PIV}, \tag{4-6}$$

where the supersctipts '*DNS*' and '*PIV*' denote the velocity field calculated by DNS and one obtained by PIV. The weight function on the combination ω is a constant in time and space domain. The patch function, f, is the function of time and space. It gradually increase from 0 (at $t\Omega = 0$) to 1 (at $t\Omega = 1$), in order to reduce an abrupt impact of velocity obtained by PIV on the hybrid velocity field in the time developing region. It also takes 1 at the center of the camera window and gradually decreases to 0, to reduce the uncertainties of measurements. The shape of $f(z)$ is shown in FIG. 4-2.

By synchronizing the computational time step and with the frame rate of high

speed video camera, the hybrid velocity field is combined those updated from DNS and those obtained by PIV (FIG. 4-3). Hence, the ratio of computational time step and one of PIV, $\Delta t^{PIV} / \Delta t^{DNS}$, must to be set in an integer. In order to investigate the contribution of PTV data on the hybrid velocity fields, the hybrid simulations were performed in various value of weight function, ω, and ratio of $\Delta t^{PIV} / \Delta t^{DNS}$. The DNS domain is set at 2λ (= $5.5d$) in the axial direction, where λ is the axial wavelength of Taylor vortices obtained by the experiments (see CHAPTER 3). Periodic boundary condition in axial direction was used, for simplicity. The regular grid was used for the computational mesh, where 16 × 88 × 154 grids are distributed in the radial, axial and azimuthal directions, respectively. In DNS, the unsteady incompressible Navier-Stokes equations in the 3D cylindrical coordinate were solved by HSMAC (SOLA) scheme [151], where the TVD scheme using the van Leer limiter [152] is adopted for the convection term. For other spatial derivatives, the second order central-differencing scheme was used. For the times stepping scheme, forward Euler scheme was used. The fractional time step method is composed of the following two step time-marching schemes:

$$\frac{\hat{\boldsymbol{u}}-\boldsymbol{u}_n}{\Delta t} = -\left(\boldsymbol{u}_n \cdot \nabla\right)\boldsymbol{u}_n + \nabla p_n + \frac{1}{Re}\nabla^2 \boldsymbol{u}_n, \tag{4-7}$$

$$\frac{\boldsymbol{u}_{n+1}-\hat{\boldsymbol{u}}}{\Delta t} = -\nabla \phi_{n+1}, \tag{4-8}$$

where subscript n denotes the time generation, and ϕ is given by the Poisson equation as follows:

$$\nabla^2 \phi_{n+1} = \frac{1}{\Delta t}\nabla \cdot \hat{\boldsymbol{u}}. \tag{4-9}$$

The updated velocity field $\boldsymbol{u}_{n+1}$ is guaranteed to satisfy the divergence-free condition. The Poisson equation (Eq. (4-9)) is solved with a parallel successive over relaxation (SOR) red-black scheme. The flow chart of the above noted hybrid simulation is shown in FIG. 4-4. The velocity $\boldsymbol{u}_n$ is replaced by the linear combination of PIV and DNS data given by Eq. (4-6). The most of the numerical part follows the HSMAC method and the hybrid algorithm is enabled to be simply installed before the calculation of the Navier-Stokes equation.

4.4 Result and discussion

4.4.1 Experiment

FIG. 4-5 shows that the wavy motion of a pair of the Taylor vortices can be represented by iso-surface of the stream factions in (a) single phase and (b) two-phase flow. The red and blue colors of iso-surfaces represent clockwise and counter clockwise rotation directions of vortices, respectively. The gray iso-surface represents a locally high void fraction region. The azimuthal position, θ, is converted from the time, t, by using Eq. (4-2) and Eq. (4-3).

A regular wavy pattern of axially oscillating Taylor vortices can be observed in FIG. 4-5. The wavy iso-surfaces are locally modified due to the appearance of modulation wave appearing as seen around $\theta = \pi$ in the single phase condition (FIG. 4-5 (a)). The modulation wave, however, cannot be recognized by naked eyes in the two-phase condition in FIG. 4-5 (b). The disappearance of modulation wave has quantitatively estimated by the velocity fluctuation of axial component in the frequency domain (see CHAPTER 3). The modulation waves appear due to the hydrodynamic instabilities with increase of the Reynolds number in Taylor-Couette flows. As well discussed in CHAPTER 3, the diminishment of modulation wave by the addition of microbubbles may be induced by pseudo-decrease of the effective Reynolds number that is evaluated form the flow stats.

Again, in FIG. 4-5 (b), the iso-surface display of the void fraction shows the spatially organized pattern in the wavy Taylor vortices. Microbubbles experience the periodic accelerations from the surrounding liquid phase flow in the Lagrangian-frame. Then these make an organized distribution in Taylor vortices and rise up due to the small but unignorable slip velocity between a bubble and surrounding liquid phase (see CHAPTER 3). The Stokes rising velocity of bubbles, u_{St}, against the RMS value of axial velocity component, $u_{z,\,RMS}$, takes a value of $u_{St} / u_{z,\,RMS} = 0.6$, that means the rising velocity is smaller than the magnitude of axial velocity fluctuation. The mean diameter of microbubbles is small enough compared to the flow structure. The modification of wavy structure would be arisen from the collective and organized motion of microbubbles.

4.4.2 Direct numerical simulation

The hybrid simulation presented in Eq. (4-5) is equivalent DNS for single phase flows, when the weight on the experimental data in linear combination ω takes $\omega = 0$. The multiplicity of the flows sates (i.e. number of Taylor ans azimuthal wave) was investigated in DNS, before the evaluation of flow modification by the hybrid simulation. The axial length of the simulation domain is fixed as the twice of the axial wavelength of successive Taylor vortex pair, i.e. 4 vortices exist in the simulation domain. As mentioned in CHAPTER 3, the number of azimuthal wave (m-state) takes 5, 6, and 7 in this experimental system. Taylor vortex like velocity disturbances are added as the initial velocity distribution and develop to wavy Taylor vortex tubes. FIG. 4-6 shows instantaneous snap shots of the radial velocity distribution in the θ-z plane at $(r - R_i) / d = 0.5$ obtained by DNS, where m is the number of the azimuthal wave called m-state. The obvious wavy pattern of the velocity distribution is vanished for $m = 4$, so that the wave for $m = 4$ could not exist stably in this fixed axial length of calculation domain. The velocity distributions show the wavy pattern of velocity fluctuation for $5 \leq m \leq 9$. These wavy pattern for $5 \leq m \leq 9$ provided by "pure" DNS qualitatively agree with the experimental results. The modulation waves of GS mode which is observed in the experiment (as shown in FIG. 4-5(a)), however, does not appear in any m-sate. The reconstructions of the modulation wave are most surely laid as the difficulty in DNS as mentioned in SECT. 4.1.

4.4.3 Flow field obtained by hybrid simulation

The Spatio-temporal axial velocity distributions at $(r - R_i) / d = 0.25$ are shown in FIG. 4-7 for the single phase flow and in FIG. 4-8 for the two-phase flow. In the hybrid simulation, the velocity obtained by PIV (FIG. 4-7 (a) and FIG. 4-8 (a)) fed hybrid simulation (FIG. 4-7 (b) and FIG. 4-8 (b)), where the weight on the velocity obtained by PIV, ω, and the time interval for the hybrid combining, $\Delta t^{PIV} / \Delta t^{DNS}$, are 2×10^{-4} and 16, respectively. The high-speed video-camera can record fluid motion in a finite domain of the fluid layer. Therefore, the domains of velocity distributions obtained by PIV are limited from $-2d$ to $2d$ in FIG. 4-7 (a) and FIG. 4-8 (a).

The hybrid velocity fields were calculated from the laminar state as the initial condition and with feeding experimental data. The wavy patterns of axially oscillating

azimuthal waves appear in the both single and two-phase conditions at $t\Omega > 4$, after the Taylor vortices are developed. Further, doubly-periodic wave modulations appear at around $t\Omega = 6$ and 9 in the flow reconstructed by the hybrid simulation of the single phase flow condition shown in FIG. 4-7 (b). The wave pattern of modulation wave, however, does not appear at $t\Omega = 14$. The disturbed wave by the modulation, which has small amplitude of the axial oscillation and small azimuthal wavelength, is merged into the larger wave structure at around $t\Omega = 11$. Therefore, unstable wave pattern of the azimuthal wave is generated and propagates in the azimuthal direction. The modulated waves have never appeared after the merging of waves. In contrast with the single phase flow, the significant wave modulations are not appeared in the velocity distribution obtained by the hybrid simulation in the two-phase flow case. The azimuthal waves are reconstructed and are stably existed after the appearance of wavy structures at $t\Omega > 4$.

Time series of instantaneous distributions of the radial velocity component at $(r - R_i) / d = 0.5$ are shown in FIG. 4-9 for single phase flow and in FIG. 4-10 for two-phase flow, where the both distributions obtained by (a) PIV and (b) hybrid simulation are displayed. The waves containing an irregular fluctuation are shown in the velocity field obtained by PIV at the single phase condition as shown in FIG. 4-9 (a). The number of waves in the azimuthal direction, called *m*-state, is 6 or 7. This modulated wavy pattern is reconstructed by the hybrid simulation and is shown in FIG. 4-9 (b). Arrows in the figures indicate the modulation wave appearing among the regularly oscillating basic wave. The modulation wave is identified at $t\Omega = 4$ at first, then it disappear because of the merge with neighboring waves around $t\Omega = 12$. In the two-phase flow, on the other hand, the radial velocity fluctuation shows much regular fluctuation pattern in the FIG. 4-10 (b).

Within the algorithm of hybrid simulation, the time interval and weight on PIV data are the same for the both single and two-phase conditions. The resulting flow structures, however, show significant difference and well agreement with those obtained by PIV. This can conclude that the reconstruction of azimuthal wavy pattern depends on the feeding velocity distribution in the hybrid simulations. In the view of the flow visualization of the wave patterns in a flow, the hybrid simulation has successfully reconstructed the wave and its modulation.

4.4.4 Wall shear stress and torque

In the hybrid simulation, the azimuthal velocity distribution, that is unable to be measured by the planar PIV on *r-z* cross section, is obtained simultaneous with the radial and axial velocity component. FIG. 4-11 shows (a) the mean azimuthal velocity distribution and (b) mean Reynolds shear stress component. The bracket "< >" and overline " ¯ " indicate the spatial and time averages. It is noted that these statistical quantities are calculated after the system reaches statistically steady condition, $6 < t\Omega < 10$, here after. The mean azimuthal velocity profile does not show significant modifications by the addition of microbubbles. The Reynolds shear stress, however, decreases in two-phase case. The shape and value of mean azimuthal velocity and the Reynolds shear stress component are consistent with those in the similar radius ratio of the configuration and the Reynolds number [98]. The wall shear stress acting on the both inner and outer cylinders are given as

$$\tau\big|_{r=R_i} = -\mu\left(\left.\frac{\partial\langle\bar{u}_\theta\rangle}{\partial r}\right|_{r=R_i} - 2\pi\Omega\right), \tag{4-10}$$

$$\tau\big|_{r=R_o} = -\mu\left.\frac{\partial\langle\bar{u}_\theta\rangle}{\partial r}\right|_{r=R_o}, \tag{4-11}$$

where μ and Ω are the viscosity of test fluid and rotation frequency of the inner cylinder, respectively. The modification of viscosity by the existence of dispersed microbubbles is not counted. Magnitude of the modifications on the wall shear stress estimated under each hybrid simulation parameter is summarized in TABLE 4-1. The subscript '*SP*' and '*TP*' denote the value for single phase and two-phase flows, respectively. The experimental data obtained by LDV shows 8 % and 11 % reduction of the wall shear stress at the inner and outer cylinders. The difference of the velocity gradient between the single and two-phase flow obtained by the hybrid analysis is small to be compared by naked eyes in FIG. 4-11 (a). The differences of the wall shear stress are 1.4 % and 3.5 % at the inner and outer cylinder walls, respectively. The wall shear stress is also lowered in the any parameter of hybrid simulation, the magnitude of reduction, however, differ from the experimental results. The difference is caused by the concept of this hybrid simulation combining the velocity data obtained from PTV and DNS without void fraction. The skin frictional drag is reduced by $O(10^{-2})$ because of the modifying

the vortex tubes due to the presence of microbubbles even with tiny void fraction of $O(10^{-4})$.

4.4.5 Contribution of weight function

In order to quantify the drag reduction ratio, the torque acting on the inner cylinder is estimated as well as the previous studies about the drag reduction by bubbles in Taylor–Couette flows [98] [110]. The dimensionless torque, G, is defined as

$$G = \frac{T}{\rho \nu^2 h}, \quad T = \frac{\rho\left(R_o^{\,2} - R_i^{\,2}\right) h \langle \varepsilon \rangle}{2R_i}, \tag{4-12}$$

where T, ρ, ν, h, R_o, R_i, and ε are the entire torque acting on the inner axis, density and kinematic viscosity of the test fluid, height of cylinders, radius of outer and inner cylinder, and energy dissipation rate, respectively. The energy dissipation rate is defined as

$$\langle \varepsilon \rangle = \nu \left\langle \left(\partial_i u_j\right)\left(\partial_i u_j\right) \right\rangle. \tag{4-13}$$

FIG. 4-12 compares the dimensionless torque obtained by (a) DNS in various case for number of azimuthal wave, m, and (b) hybrid simulation in the cases for the single phase (SP, black lines) and two-phase flows (TP, red lines). In the hybrid simulation, the time evolution of torque profiles for three different weight functions, cases A, E and H in TABLE 4-1, are also compared in FIG. 4-12. The right axis represents the torque ratio compared with the empirical dimensionless torque for single phase flows as a function of the Reynolds number given by Wendt [124] as

$$G_W = 1.45 \frac{\left(Re\,\eta\right)^{\frac{3}{2}}}{\left(1-\eta\right)^{\frac{7}{4}}}. \tag{4-14}$$

The arrow in the figure represents the torque for laminar flow given as

$$G_L = \frac{4\pi\eta\, Re}{\left(1+\eta\right)\left(1-\eta\right)^2}. \tag{4-15}$$

In the DNS for single phase flow (FIG. 4-12 (a)), the torque in statistically stable flow state depends on the number of azimuthal wave, m, as already reported by Eagles [153]. The experimentally obtained velocity distribution shows the waves with m = 6 or 7 as shown in FIG. 4-5 and FIG. 4-9 (a), the torque obtained by DNS is good agreement with

the empirical vale, G_W. In the hybrid simulation, the torques increase from that for the laminar flow and converge into stationary states, i.e. plateaus around $t\Omega = 8$ in FIG. 4-12 (b). When the weight on PIV is larger, the torque profile quickly reaches the stationary state in the both single and two-phase cases. The torques at the plateaus are the same value in any case for the weight function and the time step ratio of DNS and PIV. Further, the torque in the single phase condition is consistent with the empirical value [124]. The torques are reduced by 3 % in the two-phase condition compared to that in the single phase condition (listed in TABLE 4-1). The secondary flow field obtained by PIV is fed in hybrid velocity field, and the weight on PIV is less than $O(10^{-3})$. The drag reduction of $O(10^{-2})$ is achieved by the modification of wavy pattern by the addition of microbubbles of $O(10^{-4})$ in the void fraction.

The torques for the single phase flow decrease, after the torques are converged into the plateaus. These variations are caused by the destruction of modulation wave owing to the merge of the azimuthal waves disturbed by the modulation wave (mentioned in SECT. 4.4.2, and shown in FIG. 4-7 (b) and FIG. 4-9 (b)). The modulation waves have never appeared again, after the unsteady states appear. Further improvement in the process for the data combination in the hybrid simulation could be established for using high-order spatial differential or fractional time step scheme for a longer time observation of modulated waves.

4.4.6 Remark from findings

Through the investigation of both the velocity gradient and the torque acting on the inner cylinder, the reduction ratio of wall shear stress shows differences between the experiment and the hybrid simulation. This discrepancy might be from the modeling of hybrid simulation, which couples the radial and axial velocity components obtained by PIV and DNS. Local high void fraction region, which is the organized distribution of microbubbles shown in FIG. 4-4 (b), provides the modification of local effective viscosity, local buoyant force, and velocity disturbance of small length scale comparing to the grid size of the hybrid simulation due to the Stokeslets associated by the rising microbubbles. This hybrid simulation uses the velocity distribution of the secondary, radial and axial, flow with the weight function of less than $O(10^{-3})$. The trends of the decreases in wall shear stress due to the modification of velocity field by the addition of

microbubbles are successfully simulated in this hybrid analysis coupling the velocity field. The reductions of the wall shear stress of 1.4 % and 3.5 % at the inner and outer cylinder are attributed to the modification of the wavy pattern in the Taylor–Couette flows, therefore the modification of the flow contributes 30 % of the relaxation of the azimuthal shear. The rest of 70 % would be the contribution from the local buoyancy, the modification of the local buoyancy or velocity field smaller than PIV grid length scale.

4.4.7 Candidate for improvement

The hybrid simulation combining PIV and DNS which performed in this chapter achieved qualitative agreement of reconstructing modulation wave on azimuthal wave. The axial wave length of Taylor vortices and number of waves in azimuthal direction are good agreement with the experimentally obtained result, the traveling velocity of azimuthal wave, however, is not. The modulation on the azimuthal waves is reconstructed in limited temporal domain and then is disappeared when the calculation marches. The hybrid simulation is a convenient tool for reconstructing unique flow state in qualitative view. On the other hand, the quantitative agreement on the azimuthal waves has not been acquired yet. To achieve further improvement for capture the flow state, following candidates for improvement are able to be proposed: (i) extraction of experimental data in fine spatial and/or temporal domain, (ii) use of DNS grid which fined uniformly or refined in the near-wall regions in the radial direction, (iii) implementation of DNS using algorithm having highly conservation scheme for energy and momentum in finite differential method.

TABLE 4-1 Parameters for hybrid simulation and results obtained by hybrid simulations.

Case	ω	$\Delta t^{PIV} / \Delta t^{DNS}$	$\left.\frac{\tau_{SP}-\tau_{TP}}{\tau_{SP}}\right\|_{r=R_i}$	$\left.\frac{\tau_{SP}-\tau_{TP}}{\tau_{SP}}\right\|_{r=R_o}$	G_{SP} / G_W	G_{TP} / G_W	$\frac{G_{SP}-G_{TP}}{G_{SP}}$
Exp.	N/A	N/A	8 %	11 %	N/A	N/A	N/A
A	5×10^{-5}	16	1.4 %	3.5 %	0.9957	0.9582	3.2 %
B	5×10^{-5}	8	1.3 %	3.4 %	1.004	0.9720	3.2 %
C	1×10^{-4}	16	1.3 %	3.4 %	1.002	0.9706	3.6 %
D	1×10^{-4}	8	1.3 %	3.2 %	1.003	0.9718	3.1 %
E	2×10^{-4}	16	1.3 %	3.2 %	1.005	0.9722	3.1 %
F	2×10^{-4}	8	1.3 %	3.5 %	1.003	0.9711	3.2 %
G	5×10^{-4}	16	1.3 %	3.4 %	1.004	0.9677	3.2 %
H	1×10^{-3}	16	1.3 %	3.3 %	0.9983	0.9720	2.6 %
I	2×10^{-3}	16	1.5 %	3.4 %	1.003	0.9718	3.8 %

4.5 Conclusion

The effect of presence of microbubble with 60 μm in mean diameter on the wavy structure of a vertical Taylor-Couette flow was investigated. The iso-surface display of stream function calculated by the velocity of liquid phase obtained by PIV shows the diminishment of modulation wave by the addition of microbubble. The distribution of local high void-fraction region of microbubble shows the spatially organized distribution pattern in the wavy flow structure.

The hybrid simulations combining the velocity fields obtained by PIV and DNS, that satisfy the Navier-Stokes equation and the equation of continuity, are performed for the analyses of three-dimensional velocity field. The modulation of azimuthal wave, that is one of the difficult subjects to observe velocity fields obtained by DNS, is reconstructed by the hybrid simulation. In the case of the single phase condition, the torque acting on the rotating axis, which is estimated from the energy dissipation rate, is consistent with the empirical value. This attribute that the hybrid simulation provide correct velocity field. In contrast with the single phase condition, the modulation of velocity fluctuation is diminished, and the torque is reduced by 3% in the two-phase condition. The trend of skin frictional drag reduction is the same as that obtained by LDV. This can conclude that the modification of velocity field owing to the addition of microbubbles reduces the skin frictional drag by $O(10^{-2})$, even in the small void fraction of $O(10^{-4})$.

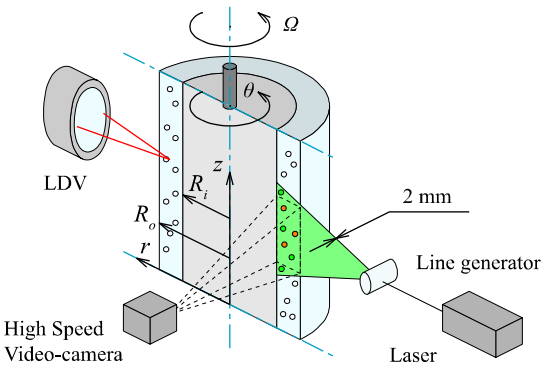


FIG. 4-1 Schematic outline of experimental setup

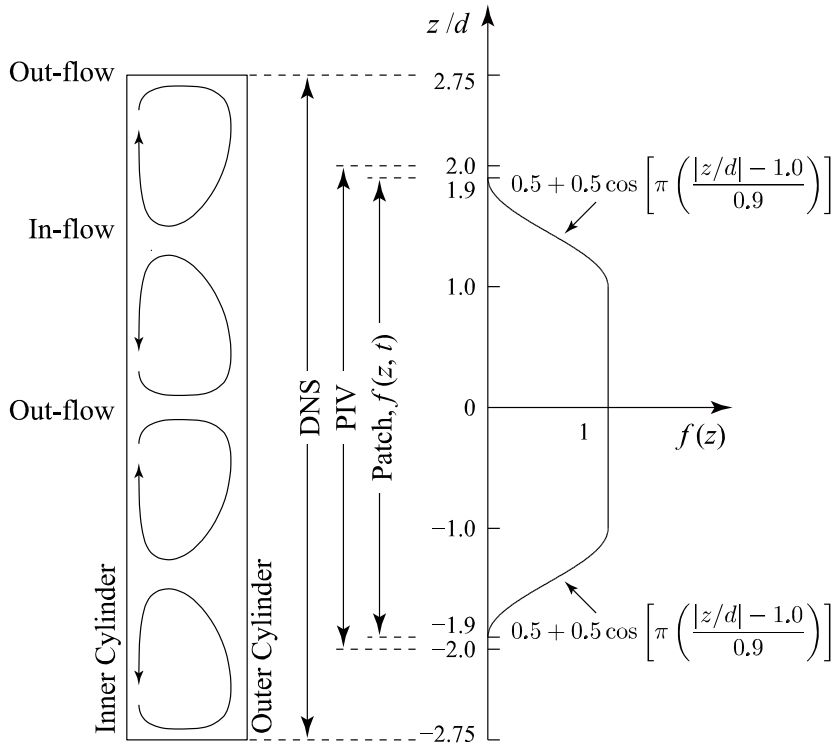


FIG. 4-2 Domain of DNS, PIV, and shape of patch function, *f*(*z*), in hybrid simulation

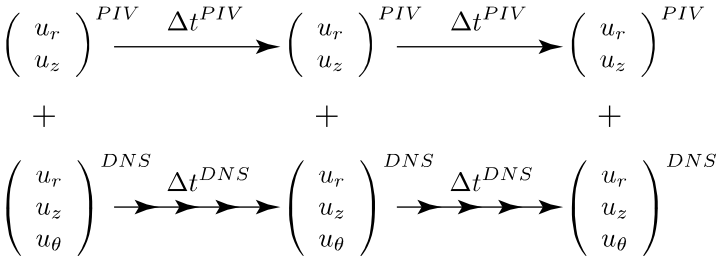


FIG. 4-3 Conceptual diagram of hybrid algorithm combining velocity datas of PIV and DNS

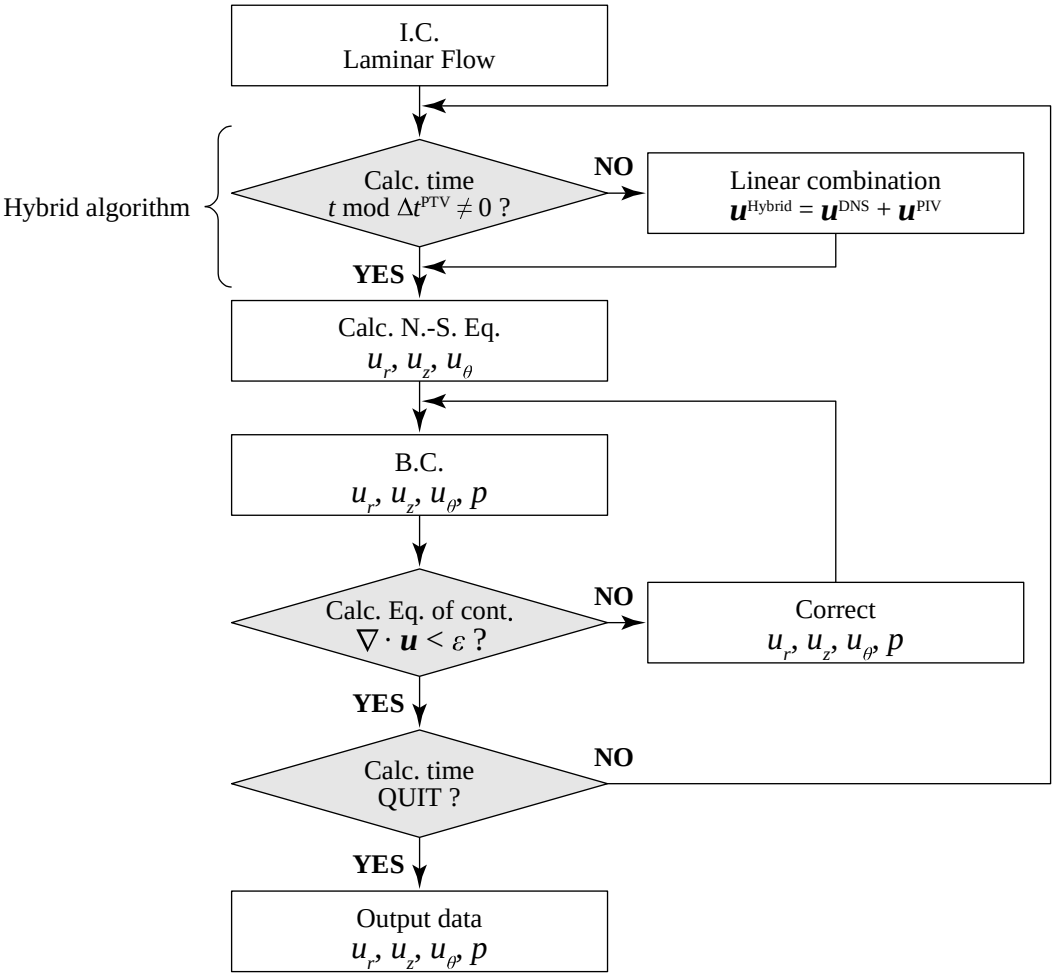


FIG. 4-4 Flow chart of the hybrid simulation combining PIV and DNS data

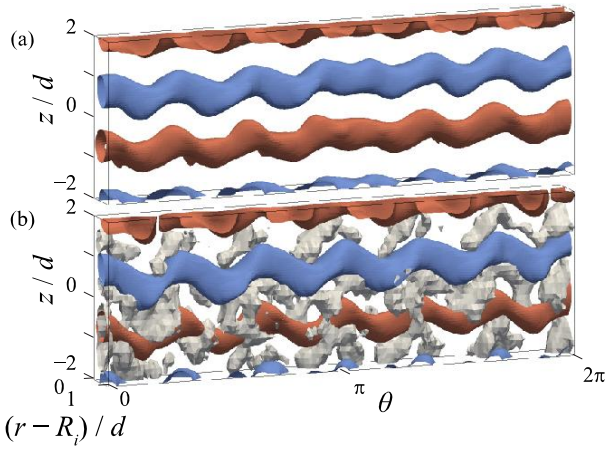


FIG. 4-5 Experimentally obtained iso-surface of stream function representing Taylor-vortex tube (red and blue) and local high void fraction region (gray) for (a) single phase and (b) two-phase flow

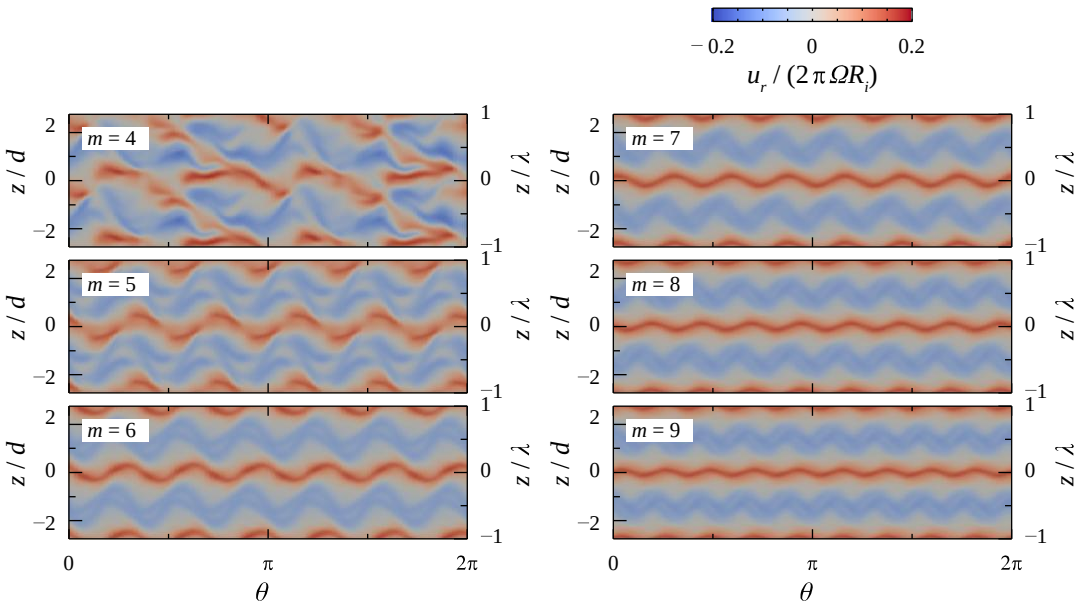


FIG. 4-6 Radial velocity distribution at $(r - R_i) / d = 0.5$ in single phase flow obtained by (a) PIV, and (b) hybrid simulation, where white arrows indicate modulation wave

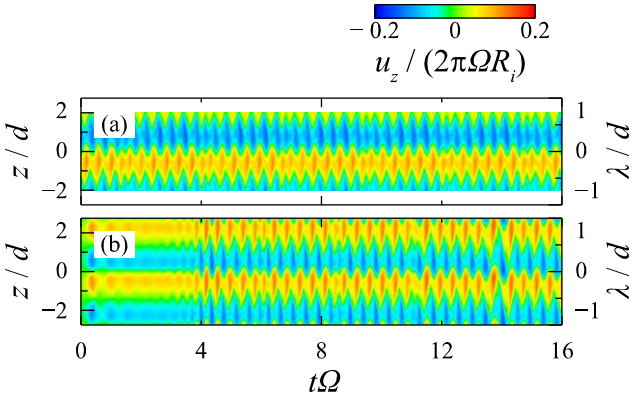


FIG. 4-7 Spatio-temporal distribution of axial velocity component at $(r - R_i) / d$ = 0.25 in single phase flow obtained by (a) PIV, and (c) hybrid simulation

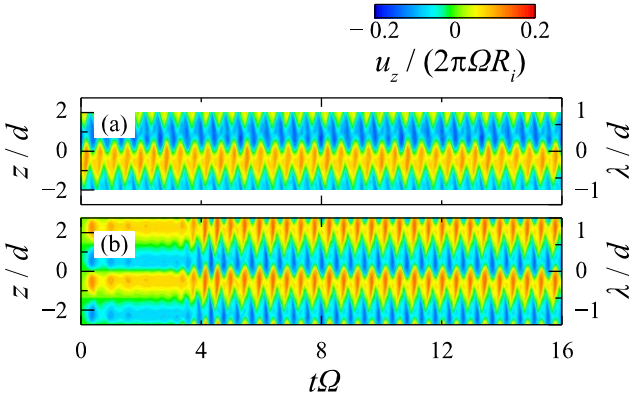


FIG. 4-8 Spatio-temporal distribution of axial velocity component at $(r - R_i) / d$ = 0.25 in two-phase flow obtained by (a) PIV, and (c) hybrid simulation

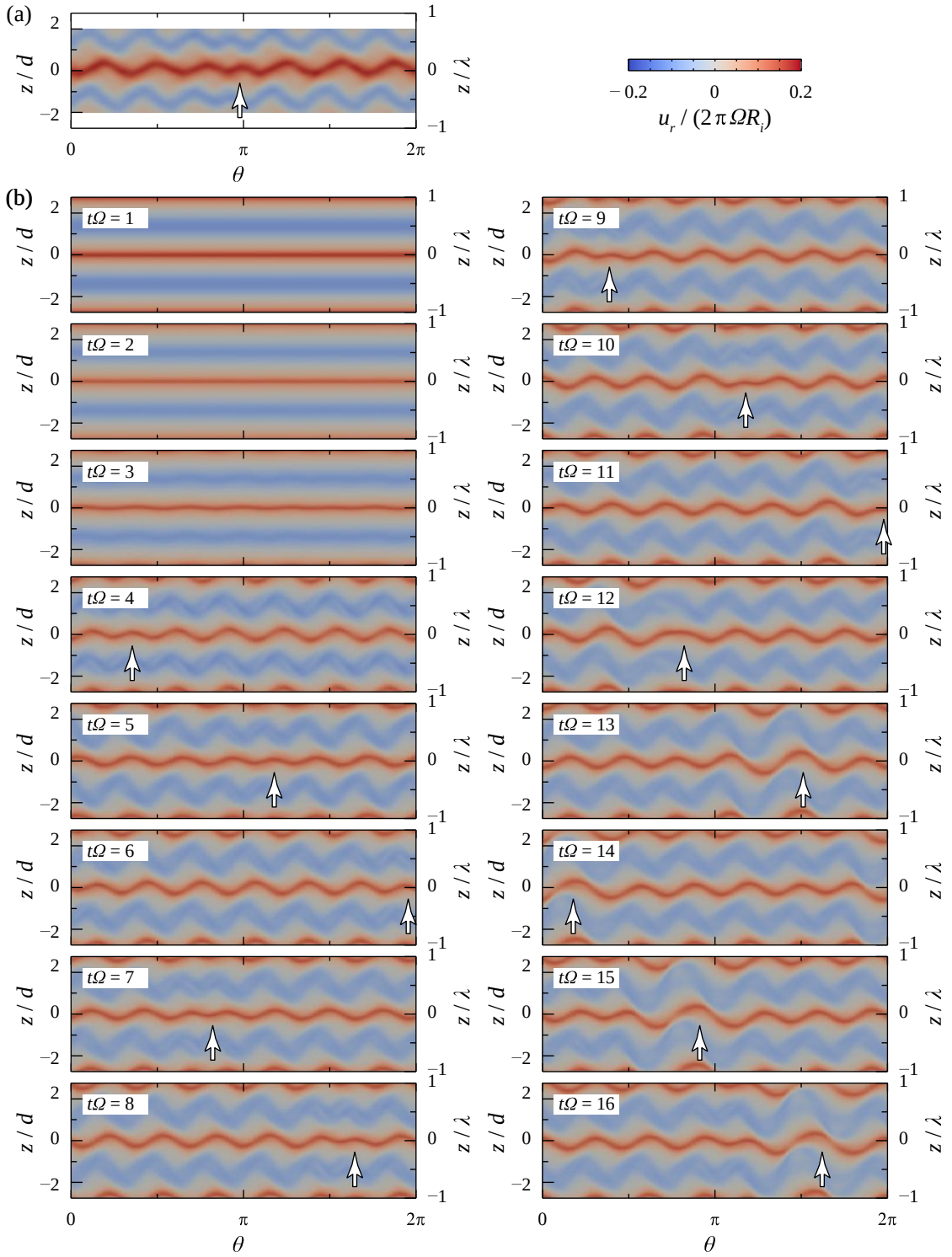


FIG. 4-9 Radial velocity distribution at $(r - R_i) / d = 0.5$ in single phase flow obtained by (a) PIV, and (b) hybrid simulation, where white arrows indicate modulation wave

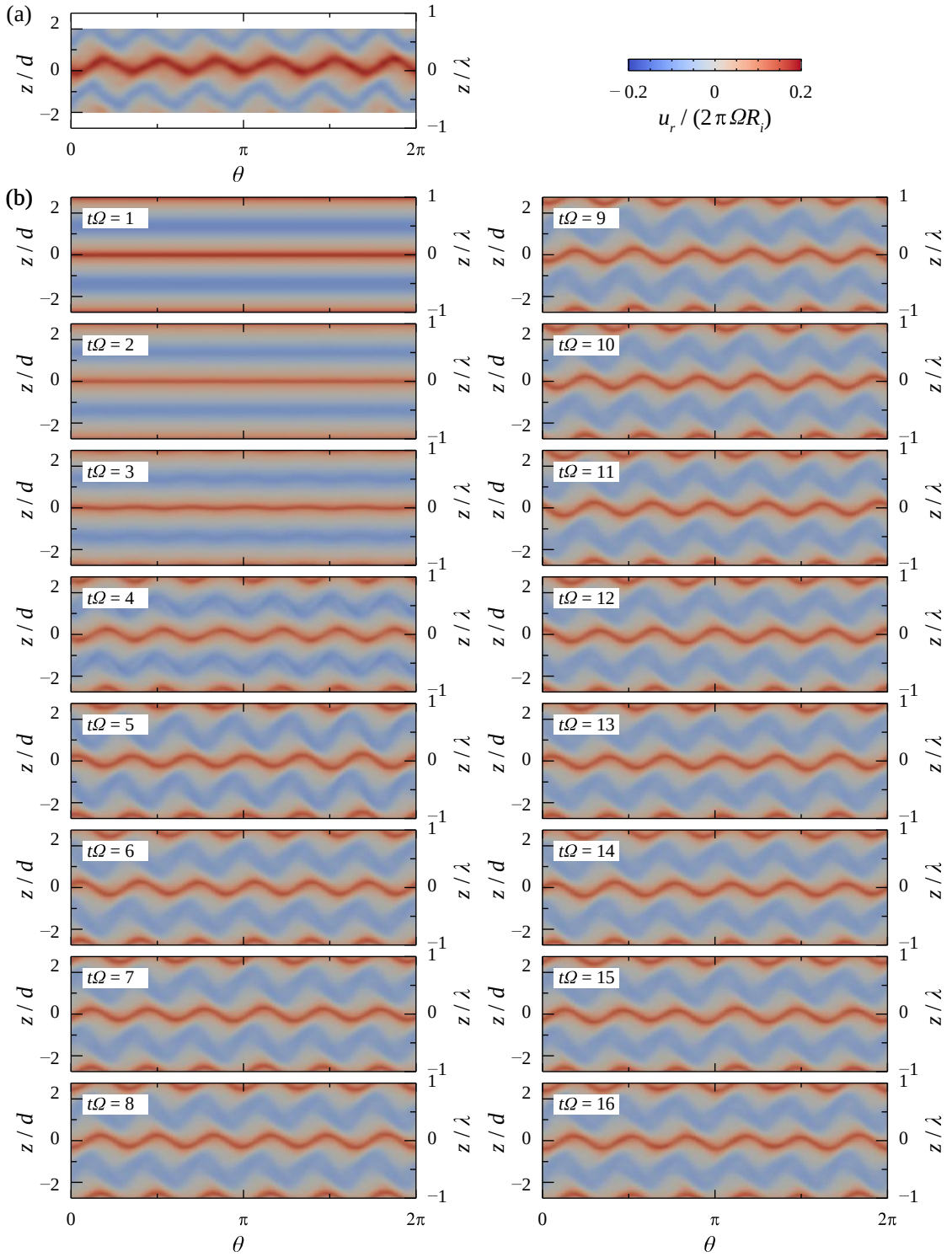


FIG. 4-10 Radial velocity distribution at $(r - R_i) / d = 0.5$ in single phase flow obtained by (a) PIV, and (b) hybrid simulation, where white arrows indicate modulation wave

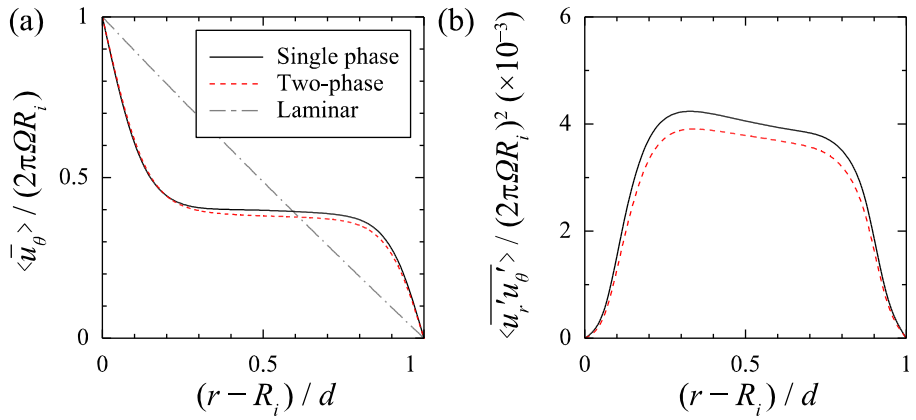


FIG. 4-11 Profiles of (a) mean azimuthal velocity and (b) Reynolds shear stress of single (solid line) and two-phase flow (dotted line), where 'Laminar' represents the analytic solution of the circular Couette flow (dashed-dotted line)

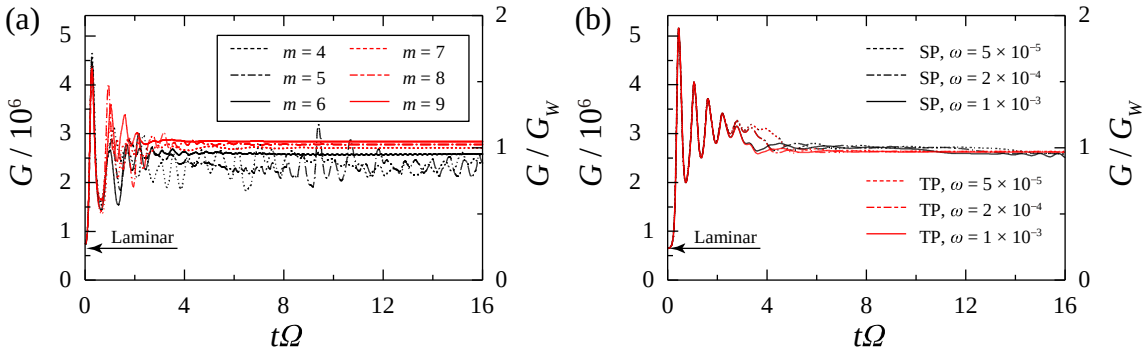


FIG. 4-12 Time-history of the dimensionless torque and that normalized by empirical value, G_W, obtained by (a) DNS for various number of azimuthal wave, m, and (b) hybrid simulation of single phase (SP, black) and two-phase flow (TP, red)

Chapter 5
Spatial development of microbubble clouds near a vertical plane wall

Abstract

To investigate the characteristic scale of spatio-temporal developing flow structures formed by ascending microbubbles, the distribution and motion of microbubbles near a vertical plane wall were experimentally investigated. Microbubbles with 40 μm in mean diameter were generated by water electrolysis in constant or pulsatile flow rate condition and were dispersed into the fluid layer from the bottom of the fluid container. The microbubble clouds (fluids blob with locally high void fraction) were visualized, and their velocities were measured by ultrasonic velocity profiling. The cloud transit time interval and cloud length are determined form velocity analysis based on wavelet transform of velocity profile. In the continuous bubble generation condition, enlargement of the microbubble clouds are caused by mergers of clouds, when clouds in different translation velocities contact with each other. The transit time intervals of microbubble clouds, therefore, increase with increasing the distance from the bottom of the fluid layer. In pulsatile bubble generation condition, the intervals of the clouds transit time were significantly modified comparing with continuous condition. The initial length of microbubble cloud in pulsatile bubble generation was comparable with the dominant wavelength for the onset of concentration interface modification of Rayleigh–Taylor instability. Furthermore, the cloud transit interval takes const value of 2 sec, because the cloud transit was locked-in the initial bubble generation period.

5.1 Introduction

Uses of bubbles are commonly encountered in industries such as chemical reactors, heat exchangers, erosion for interfacial cleaning of materials [154], and wastewater purification [155]. Bubbles are also used for reducing skin frictional drag as a purpose to increase fuel efficiencies of very large crude carrier [14]. Performances of these various industrial systems are consequently dominated by the flow structures in bubbly flows. A great number of investigations of bubbly flows revealed the motions of bubbles and surrounding liquid phase, and mentioned that phenomena in larger scales than single bubbles are essential for understating dynamics of bubbly flows. For instance, global motions, e.g. sinuous or swirling oscillation, of a bubble plume, are naturally induced by motions of liquid phase flow driven by dispersed bubbles ascending in the liquid. Generally, the global motions of plumes govern the spatial and temporal characteristics of transition in bubbly flows [156] [157] [158]. Clustering of bubbles is also important for understanding the effect of addition of bubbles on flows, because it causes modifications of Reynolds shear stress or re- laminarization in shear flows [159] [160]. The result of Proper Orthogonal Decomposition (POD) on velocity vector fields in bubbly flows conclude that bubble induced flow structures consist of various sizes of vortices [161]. Therefore, the flow structures induced by rising bubbles shows complexity of velocity structure as well as bubble distribution structure, namely, superposition of various modes in flow structures and its spatial developments.

A rise motion of bubble in quiescent fluid induces flow around bubble and vise versa. The separation distance between two bubbles rising up due to buoyancy is changed by the force from liquid phase acting on bubbles that is called as hydrodynamic interaction. The hydrodynamic interaction between two bubbles and the stable position for two-bubble alignment have been extensively studied in various bubble Reynolds number [162] [163] [164] [165] [166] [167] [168]. The motions of a large number of bubbles have also been investigated in various bubble Reynolds number [169] [170] [171] [172] [173] [174] [175] [176] [177]. The analytical studies reported that spherical two bubbles align vertically at low bubble Reynolds number (Stokes flow) [162] [163] [164] or horizontally at high bubble Reynolds number (potential flow) [165] [167] [168] [169] [170]. However, such bubble clustering is not observed in experiments [176] and numerical investigations [171] [172] [173] [175] in three-dimensional bubbly flow due

to the agitation produced by wake of a bubble. As in special case in a wall confinement or accumulation of bubbles in two-dimensional motion, the bubbles form horizontal clustering in finite length scale larger than bubble diameter [174] [177]. These experimental works suggest that the energy input by rising bubbles kinematic energy in low wavenumber mode [171] is limited in the length scale depending on the cluster size of bubble. In small particle Reynolds number case, on the other hand, particles show the collective motion when particle distribution has steep gradient, i.e. concentration interface [178] [179] [180]. These studies handled the small heavy particle of a very small Stokes number, the microbubbles having small diameter, slip velocity, and Stokes number, therefore, might behave as collective motion [94]: The coalescence, bulging, and breakup of particle/bubble concentrated cloud [178]; The deformation of concentration interface due to the Rayleigh–Taylor instability induced by the buoyant instability [179] [180]. The non-uniform spatial distribution of microbubbles appears naturally in those rising process because of different slip velocity depending on bubble diameter being polydisperse. The microbubble which slips in flow moves depending on flow around it, the concentration distribution, therefore, is modified due to flow which microbubbles induced. The presence of microbubbles and velocity field interact each other, so that the buoyant driven spatial developing flow contain essence for forming of unsteady buoyant convection driven by non-uniform buoyant force distribution due to the preferential concentration and motion of microbubble.

Kitagawa, *et al.*, (2013) [158] and (2011) [159] have used bubble injections near/in a thermal boundary layer of a natural convection due to a heated vertical plane wall, in order to enhance the heat transfer coefficient. The addition of bubbles with $O(10\ \mu m)$ in diameter (microbubble) provides much higher rate of increase in heat transfer coefficient to the power consumption of the bubble generation, comparing to bubbles with larger diameter. The careful investigations of bubble behaviors in flows indicate that the enhancement of the heat transfer coefficient by adding microbubbles is arisen by the wall normal mixing of eddies induced by the dynamic behavior of microbubbles, but for the less mixing in the wake of individual bubbles unlike larger ones in average diameter smaller than $O(0.1\ mm)$. Eddies of liquid phase driven by microbubbles and distributions of microbubbles show complex behaviors described as “intermittently-generated bubble cloud” even bubbles are continuously injected [158].

This suggests that the freely developing bubbles in the system can be actively controlled if motion and/or distribution of bubbles can be artificially controlled. In other words, the excitation or prevention of a particular flow mode naturally appearing in flows (i.e. control of microbubble cloud motion) would modify the efficiency of using bubbles in industries. For this reason, addition of the fluctuation in input gas flow rate, giving an oscillating driving force, is expected to be a method to enhance the one of modes in bubbly flows, following the knowledge on flow controls in single phase flows adopting external oscillating force, e.g. flow stabilization [166] or lock-in of vortex shedding frequency [182].

This study aims to elucidate the statics of vortex structure, whose length scale is larger than diameter of microbubble, induced by naturally appearing inhomogeneous distribution of microbubbles ascending near a vertical plane wall. The author has investigated the statistical quantities of transit time interval of bubble clouds from the vertical velocity profile measured by ultrasonic velocity profiling, to understand the nature in the spatial development of the bubbly flows. The characteristic length of developing flow structure driven by microbubbles is also examined from the cloud transit interval and time averaged velocity. Then, the author has compared its developing characteristics between continuous and pulsatile bubble generation conditions. Finally, the author mentioned the modification of bubble cloud due to the buoyant instability appearing microbubble concentration interface and lock-in of the flow structure in pulsatile period of microbubble generation under the pulsatile condition.

5.2 Experimental setup

The experiments were conducted in a rectangle open tank made of transparent Plexiglas to allow the flow visualization as shown in FIG. 5-1, where the height, width, and depth are 1600 mm, 150 mm, and 310 mm, respectively. The axes of x, y, and z are set along stream-wise (height), wall-normal (depth), and span-wise (width) directions, respectively. The origin of x direction is set at the bottom surface of the tank.

In order to quantify the flow pattern of ascending microbubbles, visualization of microbubbles in two configurations (on x-z and x-y plane) and ultrasonic velocity profiling (UVP) [126] are conducted. Microbubbles are illuminated by a metal halide white light sheet with 10 mm in thickness (Moritex, MHAB-150 W) or a diode-pulsed solid-state (DPSS) laser light sheet with 2 mm in thickness (Lasre quantum, Excel, 1 W). Scattering light from gas-liquid interface of microbubbbles is recorded by a CCD camera (Imperx, VGA210-L). These optical visualizations provide time series of the local void fraction distribution in the measurement plane, namely, $\alpha(x, y, t)$ or $\alpha(x, z, t)$ with the spatial resolution of 0.3 mm/pixel. Vertical velocity profile of microbubbles along the wall is obtained by UVP (Metflow, UVP-Duo). An ultrasonic transducer (US-TDX) for both emission of pulsed ultrasonic and receiving Doppler frequency from microbubbles is attached at the surface of the wall. Measurement line of UVP is located at 4 mm from the wall. Volume-averaged velocity of microbubbles in the measurement volume whose shape is a disk with 5 mm diameter and 0.7 mm thickness was measured, where the positive and negative sign of velocity indicate ascending and descending direction as shown in FIG. 5-1 (b). The UVP provides time series of the vertical velocity, $u_x(x, t)$ with the velocity resolution of 0.59 mm/s.

Tap water with saline with concentration of 0.3 wt % was used as the test fluid, and its temperature was maintained at 22 ± 1 °C. The modification of the physical properties of water is negligible small because of the small concentration of saline. The schematic of microbubble generator is shown in FIG. 5-1 (b). Hydrogen microbubbles were generated by water electrolysis from a Platinum wire with 100 μm in diameter used as a cathode. A Platinum hollow rod with 2 mm in diameter and 0.1 mm in thickness was used as an anode. The both electrodes were mounted at 20 mm below the bottom of the tank (x = − 20 mm). Hydrogen bubbles were dispersed into the test section of fluid layer, while oxygen bubbles were stored in the bubble generator to

prevent dispersion into the test section. The gas flow rate of microbubbles Q is theoretically estimated from Faraday's law and gas state equation, and is given as

$$Q = \frac{RTI}{2P}, \tag{5-1}$$

where R, T, I, and P are gas constant, temperature, electric current for water electrolysis, and atomic pressure, respectively. The gas flow rate of generated microbubbles is controlled by adjusting the electric current for electrolysis. FIG. 5-2 shows schematic of the variation of gas flow rate, which is set as (i) constant flow rate Q_c (= 30 mm^3/s) and (ii) pulsatile flow rate varying between 0.95 × Q_c (= 28.5 mm^3/s) and 1.05 × Q_c (= 31.5 mm^3/s) in time period of 1 second.

FIG. 5-3 (a) shows the probability distribution of microbubble diameter in various gas flow rate. The symbols indicate the experimental data obtained from 4 × 10^5 samples, while lines indicate the approximation line by Nukiyama & Tanasawa [183] [184] given as

$$p(d_b) = \frac{q\Gamma\left(\frac{4}{q}\right)^3}{D_b{}^3\Gamma\left(\frac{3}{q}\right)^4} d_b{}^2 \exp\left\{-\left[\frac{\Gamma\left(\frac{4}{q}\right)}{\Gamma\left(\frac{3}{q}\right)}\right]^q \left(\frac{d_b}{D_b}\right)^q\right\}, \tag{5-2}$$

where D_b, q and Γ are the mean diameter of microbubble defined as Eq. (5-3), valuable as a function of skewness, γ, given as Eq. (5-4) and gamma function, respectively.

$$D_b = \frac{\int_0^\infty d_b p(d_b) dd_b}{\int_0^\infty p(d_b) dd_b} \tag{5-3}$$

$$q = -0.67\gamma + 1.85 \tag{5-4}$$

The relationship between q and γ is empirical relationship obtained in the literature [184]. The experimentally obtained probability distributions of microbubble diameter are good agreement with the approximation model. The probability distribution also shows the increase of mean diameter and deviation with increasing the gas flow rate, Q. Mean diameter of microbubbles increases with increasing of gas flow rate as shown in FIG. 5-3 (b), where error bars indicate the standard deviation of the bubble diameter distribution. Thin vertical lines indicate the upper (1.05 × Q_c) and lower value of the gas flow rate (0.95 × Q_c) in the pulsatile condition. The variation of mean bubble diameter

with the gas flow rate is modified in the pulsatile condition, but the modification is small enough comparing with the standard deviation of bubble diameter distribution. The Stokes rising velocity, i.e. terminal velocity of a single microbubble in a Newtonian fluid, is given as

$$u_{St} = \frac{\rho g D_b^{\,2}}{12\mu}, \tag{5-5}$$

where ρ, μ, g, and D_b are the density and viscosity of the test fluid, gravitational acceleration, and mean bubble diameter, respectively. According to Eq. (5-5), u_{St} is estimated as 1.4 mm/s in this study. The bubble Reynolds number based on the bubble diameter, D_b, and bubble velocity, u_{St}, given as

$$Re_b = \frac{u_{St} D_b}{\nu}, \tag{5-6}$$

takes 0.06 assuming bubble slip velocity is approximated as Stokes terminal velocity, where ν is the viscosity of water.

FIG. 5-4 shows the probability distribution, p, and cumulative distribution, c, of microbubble distribution in the wall normal direction, y, with the vertical position at (a) x = 250 mm, (b) x = 500 mm, and (c) x = 750 mm, respectively. Most of the microbubbles distribute near the wall, because the peaks of the probability distribution locate the point nearest the wall in the any x position. The bubble layer thickness, δ_b, is defined as the position which cumulative distribution reaches 0.9. The void fraction, α, roughly estimated from the gas flow rate, Q, mean vertical velocity, U_x (see SECT. 5.3), and the cross-sectional area, A (= δ_b × 150 mm), is given as

$$\alpha = \frac{Q}{AU_x}. \tag{5-7}$$

The void fraction is estimated $\alpha \approx 3 \times 10^{-3}$ at x = 250 mm, $\alpha \approx 2 \times 10^{-3}$ at x = 500 mm and 450 mm, respectively. Again, this method for void fraction estimation is approximated value, however, is based on the physical quantities. The presence of microbubbles scatters the illumination light for optical visualization, the brightness in images, thereby, corresponds to the presence of microbubble. The void fraction profile is estimated from the brightness in images that are linearly calibrated with the theoretically estimated void fraction by Eq. (5-7).

5.3 Characteristic of microbubble cloud

5.3.1 Flow visualization

FIG. 5-5 shows typical bubble distributions of ascending microbubbles near the wall in the two different cross-sectional views; (a) *x*-*z* and (b) *x*-*y* plane obtained from different runs of experiments (not synchronized data). Gas-liquid interface of microbubbles scatters the illumination light. Hence, brightness in the figure shows the local void fraction, i.e. whiteness and blackness indicate high and low void fraction, respectively. Several microbubble clouds, namely, a fluid blobs with locally high void fraction region, are observed as distribution of spatially organized local void fraction. FIG. 5-4 (b) shows that the spatial development of the microbubble clouds; the length scale of microbubble clouds in both stream-wise and span-wise directions increases with increasing the distance from the bottom of the tank, *x*. A time series of photographs representing the typical motion of microbubble cloud in *x*-*y* plane is shown in FIG. 5-4 (b). The position of microbubble cloud is indicated by arrows in FIG. 5-4 (b).

Small microbubbles cloud which is available to be observed at x = 237 mm at t = 0 ascends and enlarges its size with increasing time t. Two small clouds are appeared at x = 242 mm and x = 252 mm in t = 1 s. The ascending translation velocity of the upper cloud was lower comparing to that of the lower one. Two clouds, therefore, collide each other at t = 2 s, and two clouds merge into a single large cloud shown at x = 260 mm in t = 3 s. Local void fraction increases in the cloud structure at $t < 3$ s, in merger process of clouds. However, local void fraction decreases for $t > 4$, because of the dispersion of bubbles far from the wall due to the wall normal velocity conducted by circulation in the plume-like motion in the structure of a microbubble cloud. Consecutive motions, collision and dispersion, of microbubbles are intermittently observed in any positions.

5.3.2 Statistic of local velocity and void fraction

In order to investigate the statistic motion of microbubbles induced by those inhomogeneous distributions, the velocity of the microbubbles was measured by UVP. The center of measurement volume with disk-like shape of 5 mm in diameter (y and z direction) and 0.7 mm in thickness (x direction) was located 5 mm from the wall. The time averaged vertical ,velocity, U_x, and RMS (root mean square) value of vertical velocity fluctuation, $u_{x,\,RMS}$, are measured in several runs of experiment and are shown

as a function of the distance, x, in FIG. 5-6. Circles indicate the values in the continuous bubble generation condition, while triangles indicate the values in the pulsatile bubble generation condition measured by UVP, respectively. Rectangles are values from the PTV in continuous case [183]. The vertical velocity increases at $0 < x < 50$ mm, since the bubbles are dispersed from the bottom boundary of the tank where the vertical flux of liquid being zero. On the other hand, the vertical velocity slightly deceases at $x > 50$ mm, due to the dispersion from a wall. In this experiments, the slip velocity between microbubble and surrounding liquid phase, estimated as 1.4 mm/s by Eq. (5-5), is much smaller than the time-averaged velocities, $U_x \sim 30$ mm/s at $x > 50$ mm, as $U_{St} / U_x \sim 5$ %. Assuming that the slip velocity of microbubbles is same order as the estimation by Eq. (5-5), the velocity obtained from UVP provides the velocity of the velocity of the fluid blob containing microbubbles, i.e. volume averaged velocity of microbubbles inside the disk shape (5 mm in diameter and 0.7 mm in thickness).

FIG. 5-7 shows spatio-temporal velocity distribution of (a) vertical velocity, u_x, and (b) local void fraction, α, at $200 < x < 300$ mm obtained from the UVP and optical visualization. The UVP and the camera are synchronized by a trigger signal from a pulse generator. The measurement volumes for the UVP and optical measurement were nearly same each other, i.e. a disk shape of 0.7 mm in thickness (x direction) and 5 mm in radius (y and z direction) for UVP, while a rectangle shape of 0.7 mm in x direction, 10 mm in y direction, and 5 mm in z direction. Both the velocity and void fraction show the stripe patterns from lower left to upper right. These indicate the locally high velocity fluid blobs and the locally high void fraction regions, i.e. microbubble clouds, translate from lower to upper position, respectively.

FIG. 5-8 shows the probability distribution of (a) vertical velocity $p(u_x)$ and (b) void fraction $p(\alpha)$ at the rage of $200 < x$ 300 mm and $0 < t < 200$ s respectively. The numbers of the data point are 4000 in spatial and 136 in temporal domains respectively, i.e. 5×10^5. The vertical dotted lines indicate averages, $u_{x,\,mean}$ and α_{mean}. The probability of the vertical velocity, $p(u_x)$, shows symmetric distribution about its average, $u_{x,\,mean}$. The probability of the void fraction, meanwhile, shows asymmetric distribution. Two-dimensional probability distribution $p(u_x, \alpha)$ describing the relationship between the temporal variation of the vertical velocity and void fraction is shown in FIG. 5-9. The data of velocity and void fraction shown in FIG. 5-7 are used in order to calculate

the value of $p(u_x, \alpha)$. Gray scale represents the probability $p(u_x, \alpha)$ and dotted lines indicate the mean (spatially and temporally averaged) velocity, u_x, and void fraction, α_{mean}, respectively. The red line indicates a typical trajectory of relationship between u_x, α at x = 275 mm in time period of 10 s. The starting position of the trajectory is indicated by an open symbol, end position, on the other hand, is indicated by the tip of the arrow. The numbers and dashed arrows also correspond to the order of variation and direction of the trajectory. The trajectory exhibits a series of the microbubble cloud motion. The local void fraction increases at first, then the velocity increase, finally, the void fraction is reduced due to the wall normal velocity induced by the vertical motion induced by the locally high velocity. The cross-correlation between the fluctuation of velocity and void fraction which gives

$$C = \frac{\int \left[u_x(t) - u_{x,\mathrm{mean}}\right]\left[\alpha(t) - \alpha_{\mathrm{mean}}\right] dt}{\left\{\int \left[u_x(t) - u_{x,\mathrm{mean}}\right]^2 dt\right\}^{1/2} \left\{\int \left[\alpha(t) - \alpha_{\mathrm{mean}}\right]^2 dt\right\}^{1/2}}, \tag{5-8}$$

is C = 0.47. Thus, the velocity of vertical motion in microbubbles and the increase of local void fraction have correlation, but not perfect correlation. The trajectory of instantaneous void fraction and vertical velocity draws the circle-like figures rotating in clockwise direction as shown in FIG. 5-9. This is a phase lag in the relationship between them. The phase lag, consequently, reduces the cross-correlation between the velocity and void fraction.

5.3.3 Characteristics of velocity profile

FIG. 5-10 shows the power spectra of the temporal variation of vertical velocity profile at x = 50 mm, 250 mm, and 450 mm. The spectra show that the accumulation of power in the low frequency domain, f < 0.1 Hz, and its quick decay in the high frequency domain, f > 0.1 Hz. The decrease of the power in the spectra is significant with increasing the distance from the bottom of the fluid layer. And its gradient follows the −5/3 at x = 450 mm. The energy spectra of velocity profiles show its dissipation following the energy cascade process with increase x.

The velocity fluctuation, generated by the collisions and merges of microbubble clouds, contains significant wide range of frequency. In order to identify the individual microbubble transit as a function of x, continuous wavelet transform [186] [187], which

gives instantaneous dominant frequency of fluctuations, was conducted. The wavelet coefficient of the vertical velocity fluctuation, u_x', is given as functions of both time, t, and frequency, f, as follows

$$W(t,f)=\int_{-\infty}^{\infty}u_x'(t')\psi(t,f)dt', \tag{5-9}$$

where ψ is the mother wavelet function given as

$$\psi(t,f)=\frac{2\pi}{\sigma}\exp\left\{-\frac{\left[2\pi f(t'-t)\right]^2}{2\sigma^2}\right\}\exp\left[2\pi i f(t'-t)\right], \tag{5-10}$$

In Eq. (5-9), σ is the width constant of the mother wavelet function. σ takes 0.5 in this time. The shapes of the real and imaginary part of the mother wavelet function are shown in FIG. 5-11. The reduced wavelet coefficient given is given as

$$W'(t,f)=\frac{\int_{-\infty}^{\infty}u_x'(t')\psi(t,f)dt'}{\left[\int_{-\infty}^{\infty}u_x'(t')^2dt'\right]^{1/2}\left[\int_{-\infty}^{\infty}\psi(t,f)^2dt'\right]^{1/2}}, \tag{5-11}$$

in order to compare the velocity fluctuation patterns as a view of correlation with the fluctuation pattern of mother wavelet function.

FIG. 5-12 shows (a) time series of the vertical velocity profile at x = 50 mm in continuous bubble generation condition; (b) real part of the wavelet coefficient, Re[W]; (c) real part of the normalized wavelet coefficient, Re[W']; (d) "modulus maxima lines" [187] [188] of the real part of the normalized wavelet coefficient; and (e) the timing of the microbubble cloud transit indicated as vertical lines, respectively. The horizontal lines in (d) and (e) represent f = 2 Hz and time averaged velocity, U_x, respectively. "Modulus maxima lines", which is Skelton of the wavelet coefficient, represent the local maxima of the wavelet coefficient in time direction, i.e., ∂Re[W] / ∂t = 0 and Re[W] > 0. The timings of the microbubble transit at an arbitrary position, x, are defined as time, t, which fulfills all the following terms: (i) instantaneous velocity larger than time averaged velocity; $u_x(t) > U_x$, (ii) cross point of modulus maxima line and f = 2 Hz, (iii) real part of the normalized wavelet coefficient; Re[W'] > 0.1. FIG. 5-13 and FIG. 5-14 show those for x = 250 mm, and x = 450 mm in the continuous microbubble generation condition. FIG. 5-15, FIG. 5-16, and FIG. 5-17, meanwhile, show those for x = 50 mm, x = 250 mm, and x = 450 mm in the pulsatile microbubble generation

condition, respectively. Velocity fluctuations are easily recognized in the raw velocity profiles (FIG. 5-12 (a), FIG. 5-13 (a), FIG. 5-14 (a), FIG. 5-15 (a), FIG. 5-16 (a), and FIG. 5-17 (a)) even with our naked eyes: high frequency at x = 50 mm and low frequency at x = 450 mm. The time series of the velocity fluctuations does not show clear periodicities as already mentioned above spectra analysis (shown in FIG. 5-10). The wavelet coefficients show the frequency domain having the most of the powers (FIG. 5-12 (b), FIG. 5-13 (b), FIG. 5-14 (b), FIG. 5-15 (b), FIG. 5-16 (b), and FIG. 5-17 (b)). The large magnitude of the wavelet coefficient does not show the unique peak frequency as expected in spectra analysis but id dispersed at wide range in the frequency domain. The most of the large magnitude of wavelet coefficient, however, shows the feature of accumulation at f ~ 1 Hz in x = 50 mm, f ~ 0.2 Hz in x = 250 mm, f = 0.1 Hz in x = 450 mm, respectively. The peak positions of the wavelet coefficients show fluctuations in the frequency domain as shown in figures. This is the phenomena so called frequency modulation. The normalized wavelet coefficient also exhibits the frequency modulation of the fluctuation pattern and emphasize the fluctuations of the vertical velocity fluctuations at the high frequency domain in (FIG. 5-12 (c), FIG. 5-13 (c), FIG. 5-14 (c), FIG. 5-15 (c), FIG. 5-16 (c), and FIG. 5-17 (c)). The curvature of the modulus maxima line is generated by the interaction of the wavelets having the different frequencies. Thus the straight lines also exhibit the most dominant mode of the frequency in the modulus maxima line displays (FIG. 5-12 (d), FIG. 5-13 (d), FIG. 5-14 (d), FIG. 5-15 (d), FIG. 5-16 (d), and FIG. 5-17 (d)). Most of the modulus maxima lines are shaped in straight line being parallel with vertical axis, so that it would be sufficient for the detection of the cloud transit timing. In both continuous and pulsatile bubble generation conditions, the bubble cloud transit is less frequently detected (FIG. 5-12 (e), FIG. 5-13 (e), FIG. 5-14 (e), FIG. 5-15 (e), FIG. 5-16 (e), and FIG. 5-17 (e)). This is due to the merger of cloud in translating process as visualized in FIG. 5-5 (b). The figures also shows that the intervals of the microbubble cloud transit timing display non-uniform intervals in any vertical positions.

5.3.4 Time interval of cloud transit

The translation velocities of vortex structures are the same as the time averaged velocity, because the time averaged velocity (FIG. 5-6) shows nearly same values with the

translation velocity of microbubble cloud that determined form the gradient of the stripe patterns corresponding to locally high velocity and locally high void fraction. Hence, the temporal velocity fluctuation indicates the transit of microbubble cloud at the measurement position. The period of the transit interval of microbubble cloud, τ, is determined from the time interval between the local maxima. FIG. 5-18 displays the probability density functions of the transit interval of microbubble clouds, p (τ), at the three different positions, x = 50 mm, 250 mm, and 600 mm, respectively. The experimental data indicated as symbols are in good agreement with the approximately obtained lognormal distribution indicated as continuous lines. The modes of the time intervals, τ_m, which are displayed as vertical dotted lines, increase with increasing x. The maximum value of $p(\tau)$ decreases with increasing x, on the other hand, its deviation widen as shown in FIG. 5-18. These results indicate the spatial development of microbubble cloud translation interval due to the mergers of clouds that observed in visualization in SECT. 5.3.1.

The relationship between the mode of transit interval of microbubble cloud, τ_m, and the position from the bottom of the fluid layer, x, is shown in FIG. 5-19 (a). In continuous bubble generation condition, the modes of transit intervals are determined from two different quantities, velocity of microbubbles u_x (open circle), and thickness of bubble layer δ_y, namely, the distance of the most distant bubble from the wall that is determined from a visualization of x-y view (same definition as Kitagawa & Murai [158]), (closed rectangle). τ_m from UVP and optical visualization are in very good agreement. The figure shows that τ_m depends on x at x > 100 mm. τ_m increases rapidly with increasing x, i.e., transit of clouds is observed less frequently. The growth rate of the cloud transit interval is given as $\tau_m = 0.33 \exp(2.5 \times 10^{-3} x)$ in continuous gas flow rate condition. The values of τ_m show differences between continuous and pulsatile flow rate conditions; τ_m is larger in pulsatile gas flow rate condition than in constant one at x < 500 mm, while the difference in τ_m between two conditions is smaller at x > 500 mm. The microbubble transit interval is given as $\tau_m = 0.59 \exp(2.1 \times 10^{-3} x)$ in the pulsatile bubble generation condition at x < 300 mm, therefore, the growth rate of τ_m in pulsatile bubble generation condition displays the same gradient as continuous one. Note that use of Taylor's frozen hypothesis as given by Eq. 5-12 and assumption in homogeneity of flow induced structures, the characteristic length scale, L, is determined as a function of

space, x (shown FIG. 5-19 (b)).

$$L = U_x \tau_m , \tag{5-12}$$

The characteristic length, L, increase with increasing distance because of bulging by merger of clouds. L increase rapidly in pulsatile bubble generation case. The collective motion of dispersed microbubble is induced by Rayleigh–Taylor instability at the concentration interface of dispersed phase, the concentration gradient generated by pulsatile generation of microbubbles may be a trigger for bubble cloud appearance. Assuming the following three conditions that are (i) the microbubbles are distributed in a quasi two-dimensional thin layer, (ii) the microbubbles have non-slip velocity relative to the surrounding liquid phase, and (iii) the concentration interface has non-diffusivity, the dominant wavelength for the onset of interface deformation in Rayleigh–Taylor instability [180] is given as.

$$\lambda_{RT} \left(= \frac{2\pi\delta_b}{\sqrt{6\left(\sqrt{5}-1\right)}} \right) = 2.31\delta_b , \tag{5-13}$$

where δ_b is the bubble layer thickness (see FIG. 5-4). The extrapolation of initial characteristic length of microbubble cloud $L|_{x=0}$ seems to be larger but comparable with λ_{RT} = 5.4 mm representing dashed-dotted line in FIG. 5-19 (b). Note that the dominant wavelength takes large value than λ_{RT} when the concentration interface has diffusivity [189]. The index for whether dispersed small dispersion phase behaves as collective liquid-like motion or individual particle-like motion is given as the ratio of the mean distance between small dispersion phase and the dominant wavelenght in flow by Harada [179] as

$$H = \frac{D_b}{\alpha^{1/3}\lambda_{RT}} . \tag{5-14}$$

According to the literature [179], the small dispersed phase shows collective motion called as fluid-like motion at $H < 4 \times 10^{-2}$, individual motion called as particle-like motion at $H > 3 \times 10^{-1}$, and mixed behavior of fluid-like and particle-like motion at 4×10^{-2} $H < 3 \times 10^{-1}$. The parameter H takes 6×10^{-2} in the pulsatile generation case. The microbubbles, therefore, might rise up in flow more likely to behave as collective than individual. The microbubble cloud develops as an initial bubble disturbance induced by Rayleigh–Taylor instability at the concentration interface, the pulsatile bubble injection

case. In continuous microbubble generation, the mechanism of generating initial characteristic length scale of microbubble cloud, however, is unclear but might be responsible to initial and/or self-inducing distribution of microbubbles moving with small and un-negligible slop velocity in flows.

These findings led us that the enlargement of microbubble clouds and lock-in of cloud structures in preferred scale were introduced by initial fluctuation of void fraction distribution. The clouds of microbubble, in general, naturally appear in flows (also mentioned by [158] [160]). The length scale of clouds grow due to mergers of neighboring ones because of the differences in translation velocity between clouds, and merger process depends on the bubble distributions. The initial distribution and arrangement of microbubble clouds are modified in the vertical direction, x, due to the spatial and temporal distribution of local void fraction resulting from pulsatile generation of microbubbles. The number of cloud mergers decrease in the early-stage of ascending behavior of microbubbles (x < 300 mm), because the clouds are enlarged in pulsatile microbubble generation condition. The wall normal motions of clouds modify the microbubble distribution. Further, the wall normal motion of liquid phase disperses microbubbles far from the wall. The enlarged clouds disperse microbubbles quicker and further far from wall in the pulsatile condition than the continuous one, because the size of microbubble clouds is enlarged in the pulsatile condition. The merging of microbubble clouds is naturally appeared in both microbubble generation cases, the growth rate in the pulsatile condition, therefore, keep same value as that in continuous case. The initially added distribution pattern of microbubble distribution in the period of 2 second still keeps its period even after undergoing merging process of microbubble clouds. For this reason, the gradient of the τ_m is modified at x > 300mm, and the τ_m in the pulsatile condition gradually close to τ = 2 s.

5.4 Conclusion

The spatial developments of the bubble cloud ascending near a vertical plane wall were investigated from the optical visualization of microbubble distribution corresponding local void fraction and ultrasonic velocity profiling of rising velocity of microbubbles. The flow rate of microbubbles generation is controlled in two conditions, continuous and pulsatile generation with 5 % fluctuation in gas flow rate.

In both bubble generation conditions, the visualization exhibits the behavior of microbubble clouds like thermal plumes. From the time series of microbubbles' vertical velocity fluctuation, the transit interval of microbubble clouds at a position was detected continuous wavelet transform. The modes of the cloud transit interval increase with increasing the distance from the bottom of the fluid layer, and the deviation of the interval widen. This is caused by merger of small microbubble clouds into larger ones, because of the differences in the translation velocity of clouds. Therefore, the size of clouds and distances between neighboring clouds were increased in their translation motion. In the pulsatile microbubble generation condition, the modes of the cloud transit interval were increased at $x < 300$ mm comparing with that in continuous condition. The characteristic length scale of microbubble cloud is estimated by the Taylor's frozen hypothesis using the mean velocity of microbubbles and transit interval of micobubble cloud. The initial length of microbubble cloud is comparable with the most dominant wavelength of Rayleigh–Taylor instability at the concentration interface of microbubbles generated by pulsatile microbubble generation. The mode in pulsatile condition shows nearly same value as that in the continuous condition $x > 300$ mm, however, is locked into the period of pulsatile bubble generation.

The mechanism of the naturally appearing microbubble cloud in the continuous bubble generation condition is still open problem, but might be responsible to the disturbance of non-uniform distance between microbubbles generated by hydrocyanic interaction or different rising velocity due to the polydisperse diameter of microbubbles. These results, however, suggest that the development of the microbubble cloud structure can be modified by giving the initial disturbance in the microbubble distributions. Further, the medication of microbubble cloud length depends on different mechanisms: Rayleigh–Taylor instability at the initial stage of the developing flow and lock-in of cloud interval at the developing stage.

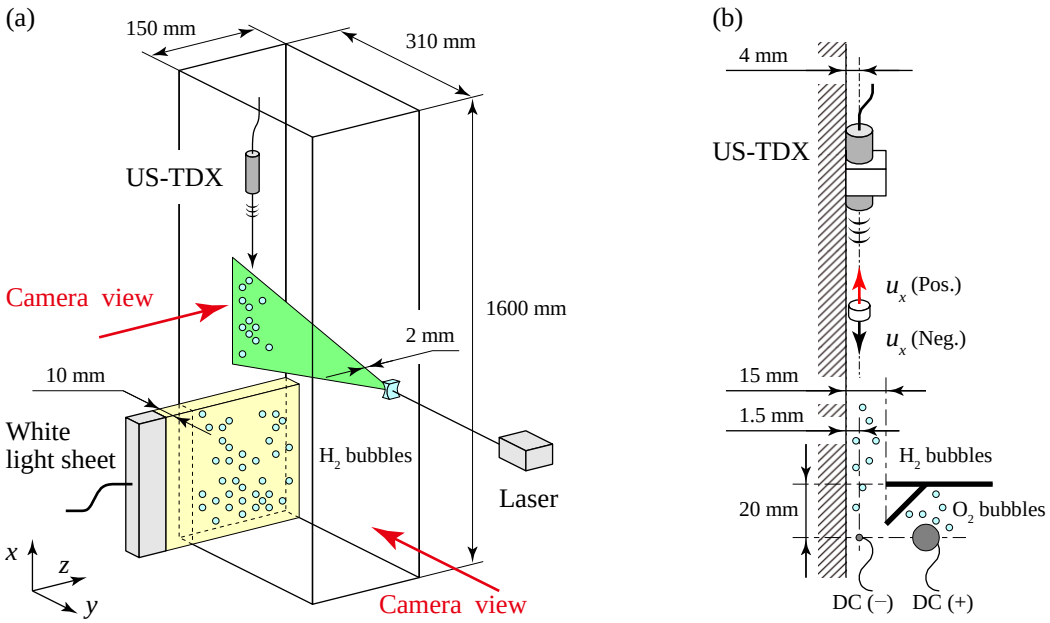


FIG. 5-1 (a) schematic outline and configuration of experimental setup. (b) The detailed outline of the microbubble generator and position of US-TDX attached at the surface of the wall. Red and black thicker arrows indicate the sign of the velocity obtained by UVP.

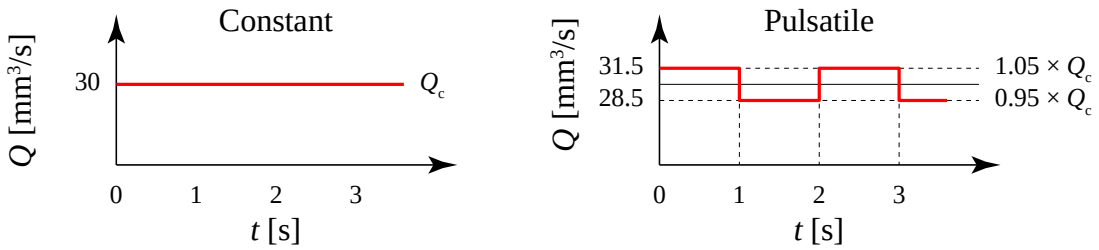


FIG. 5-2 Patterns of generating microbubbles in constant or pulsatile gas flow rate, where Q_c (= 30 mm^3/s) is the value for constant condition

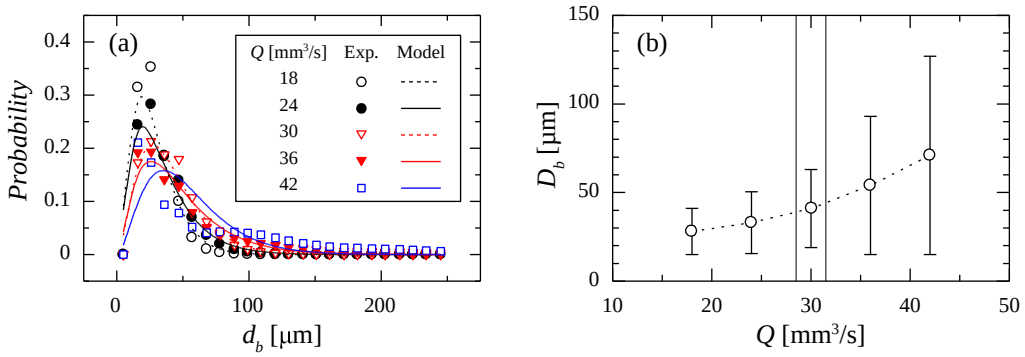


FIG. 5-3 (a) Probability distribution of microbubble diameter, d_b, where symbols and lines indicate the experimentally obtained data and approximation lines by Nukiyama & Tanasawa model [183] [184]. (b) Variation of mean microbubble diameter D_b, error bar represents standard deviation of microbubble diameter; thin vertical bar indicate upper and lower values for pulsatile gas flow rate in bubble generation.

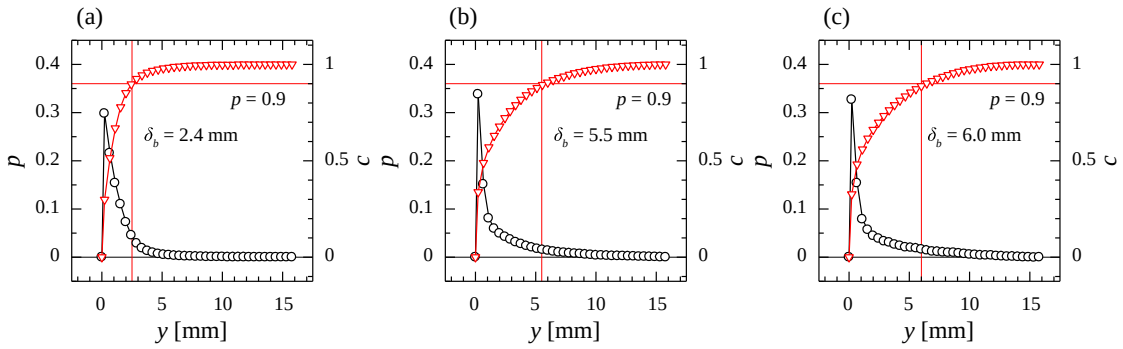


FIG. 5-4 Probability distribution, p, and cumulative distribution, c, of microbubble location in wall normal direction, y, at (a) x = 250 mm, (b) x = 250 mm, and (c) x = 750 mm, where bubble layer thickness, δ_b, is the position where cumulative distribution reaches 0.9

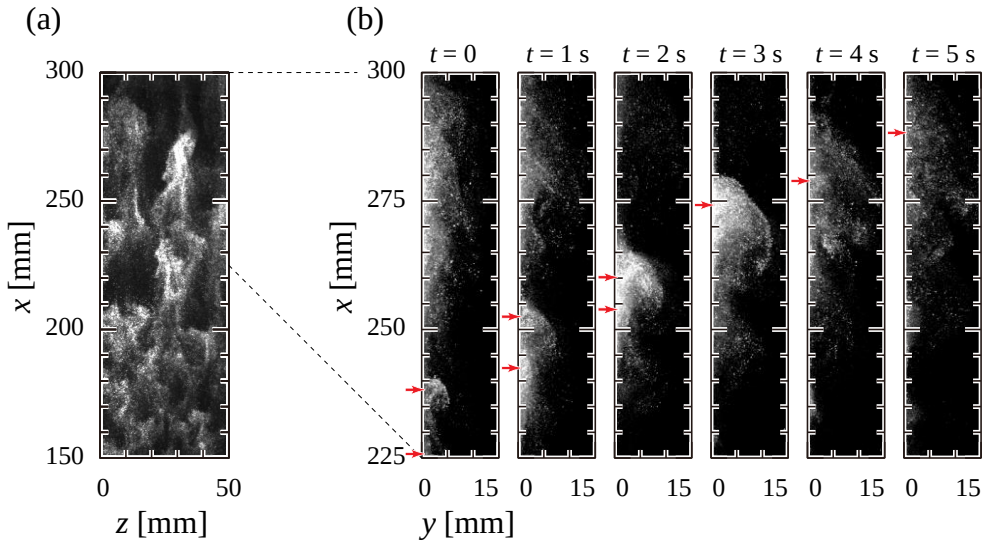


FIG. 5-5 Snap shot of bubble distribution pattern on (a) *x*-*z* and (b) *x*-*y* plane, where arrows indicate the locations of microbubble cloud in *x* direction

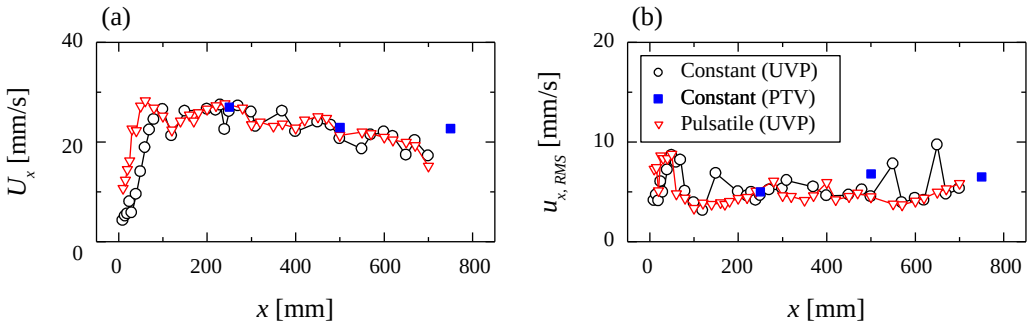


FIG. 5-6 Spatial-development of (a) time-averaged velocity and (b) RMS values of the vertical velocity fluctuation

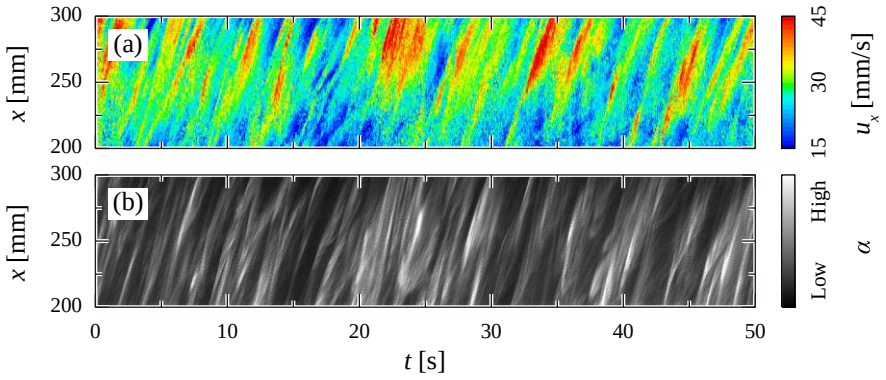


FIG. 5-7 Spatial-temporal distribution of (a) vertical velocity component and (b) local void fraction

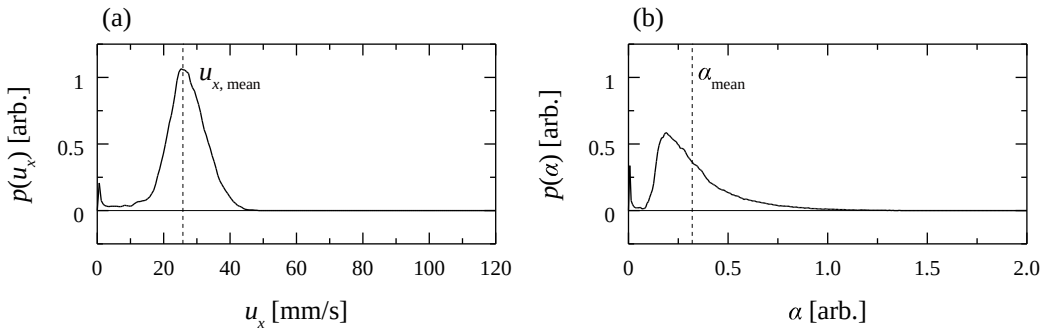


FIG. 5-8 Probability distribution of (a) vertical velocity, u_x, and (b) void fraction, α

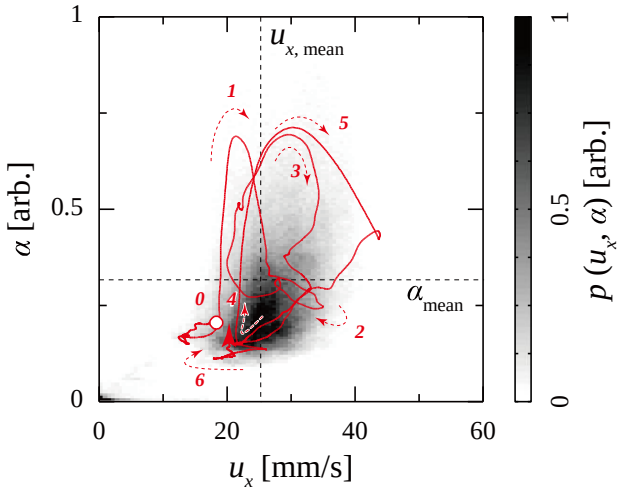


FIG. 5-9 Two-dimensional probability density distribution, trajectory of time variation of vertical velocity, u_x, and local void fraction, α

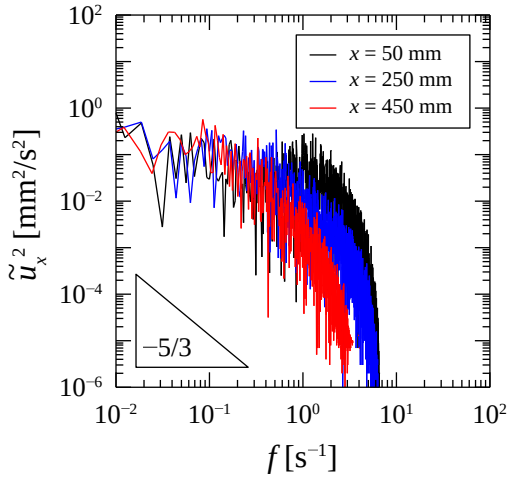


FIG. 5-10 Power spectra of vertical velocity fluctuation in various height, x, where the slope of the triangle in the bottom left of figures represents the gradient of −5/3

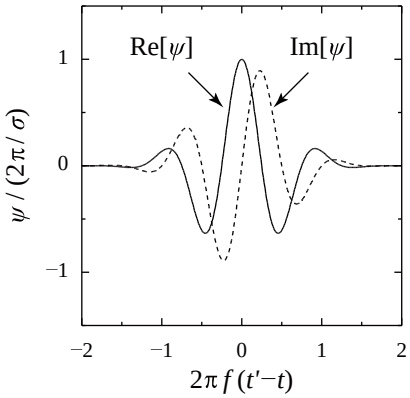


FIG. 5-11 Shape of the mother wavelet function for σ = 0.5

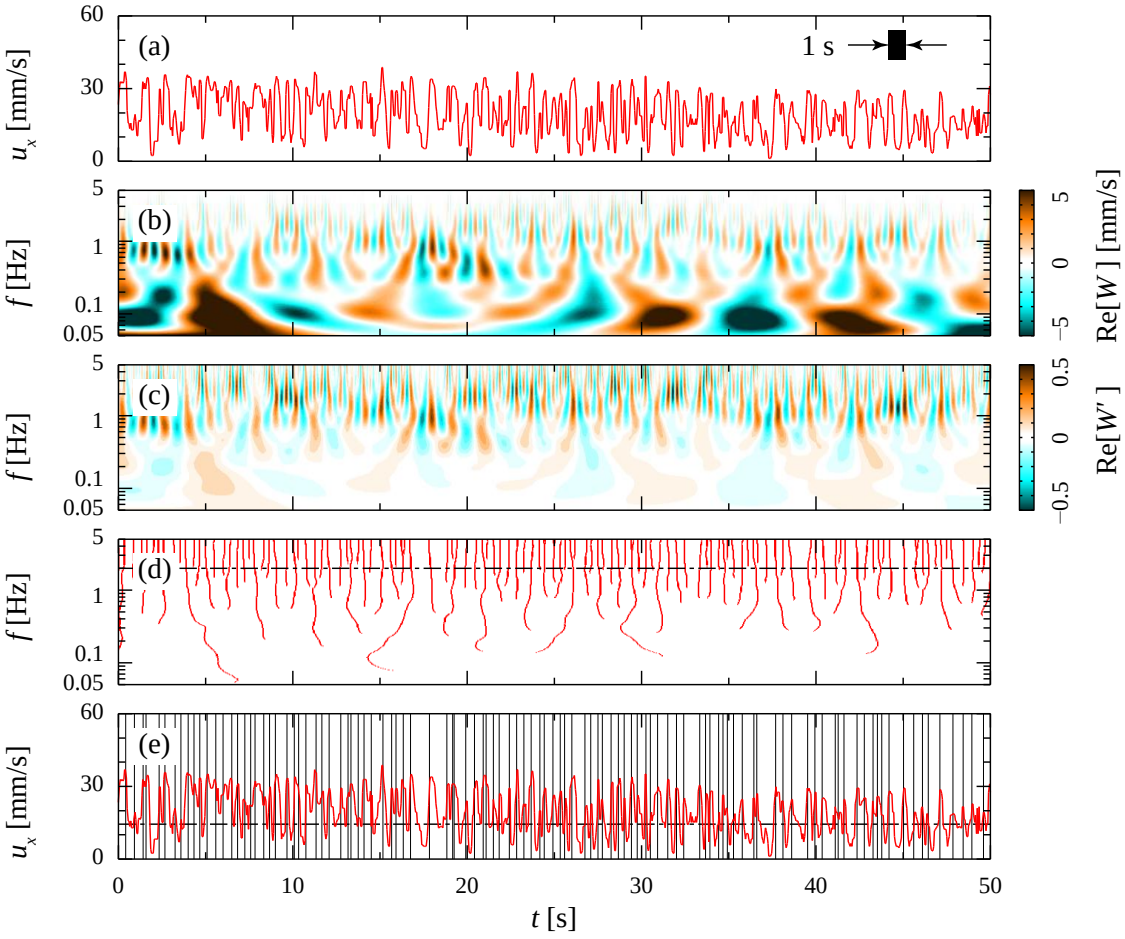


FIG. 5-12 (a) Temporal variation of vertical velocity at x = 50 mm in the continuous bubble generation; (b) real part of its wavelet coefficient, (c) real part of the normalized wavelet coefficient, (d) modulus maxima lines, and (e) extracted peak position of velocity fluctuation indicated as the vertical line

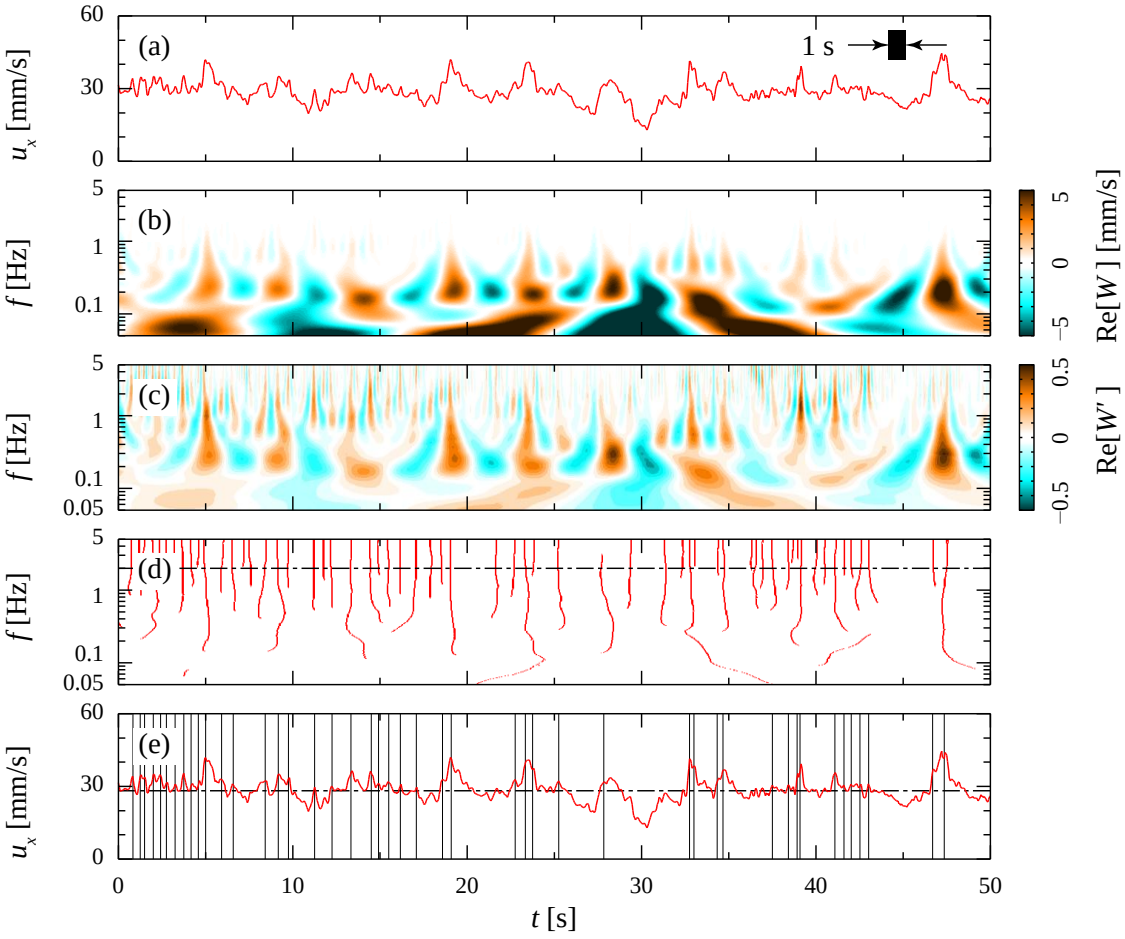


FIG. 5-13 (a) Temporal variation of vertical velocity at x = 250 mm in the continuous bubble generation; (b) real part of its wavelet coefficient, (c) real part of the normalized wavelet coefficient, (d) modulus maxima lines, and (e) extracted peak position of velocity fluctuation indicated as the vertical line

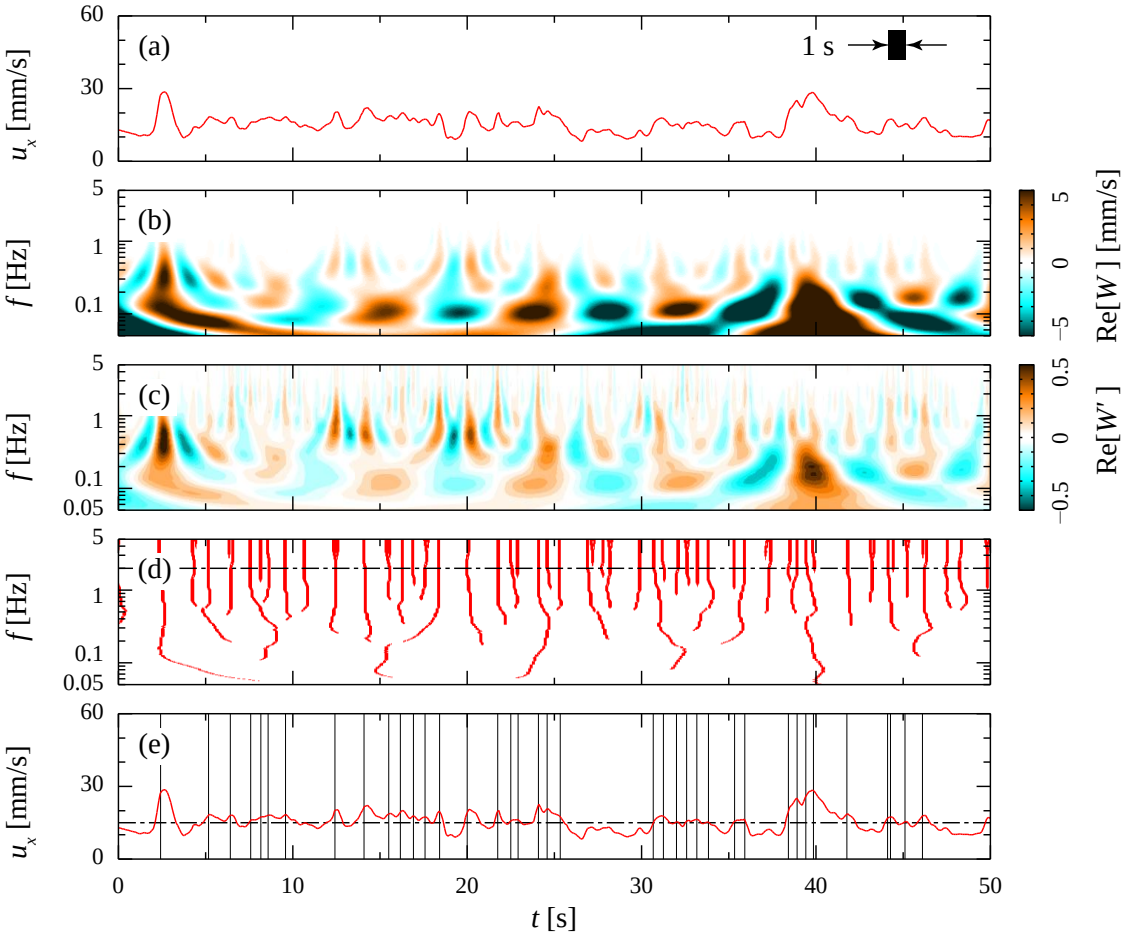


FIG. 5-14 (a) Temporal variation of vertical velocity at x = 450 mm in the continuous bubble generation; (b) real part of its wavelet coefficient, (c) real part of the normalized wavelet coefficient, (d) modulus maxima lines, and (e) extracted peak position of velocity fluctuation indicated as the vertical line

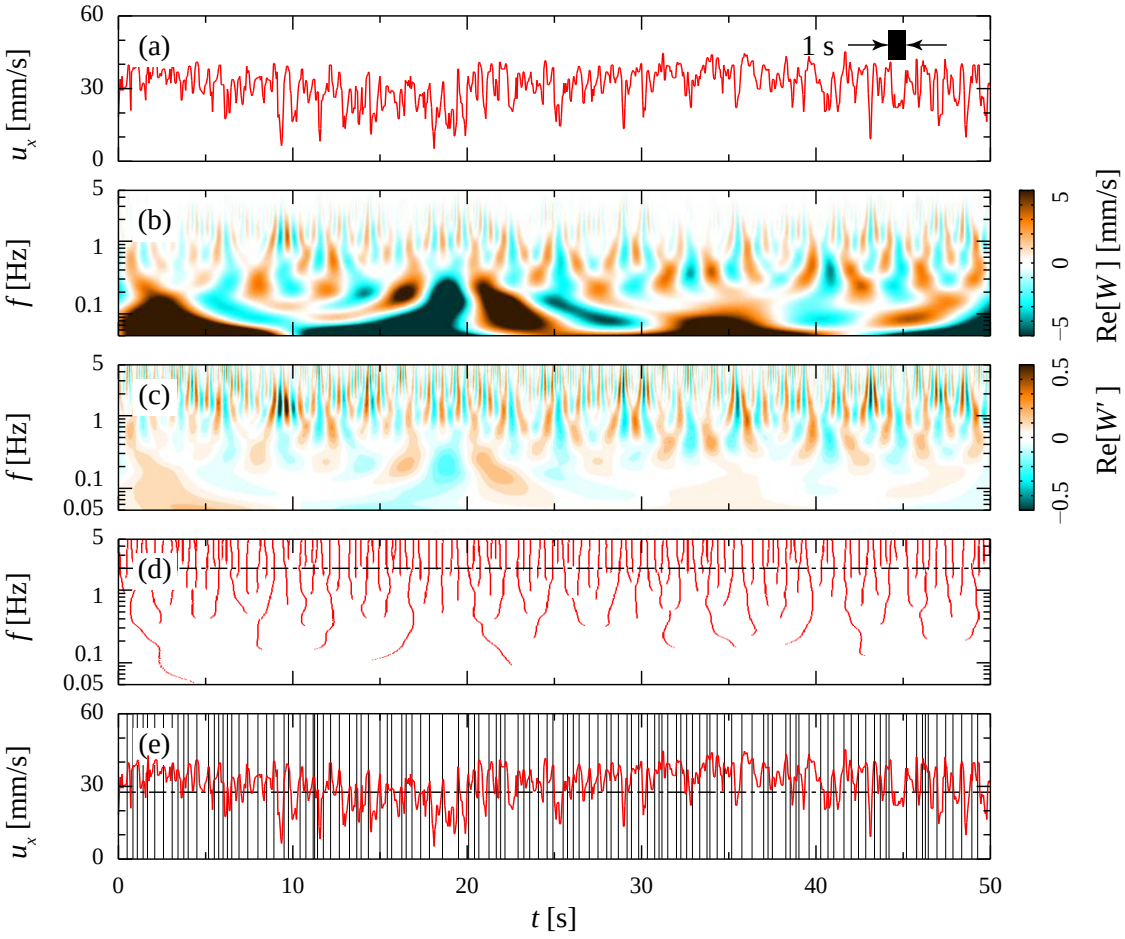


FIG. 5-15 (a) Temporal variation of vertical velocity at x = 50 mm in the pulsatile bubble generation of 5 % fluctuation; (b) real part of its wavelet coefficient, (c) real part of the normalized wavelet coefficient, (d) modulus maxima lines, and (e) extracted peak position of velocity fluctuation indicated as the vertical line

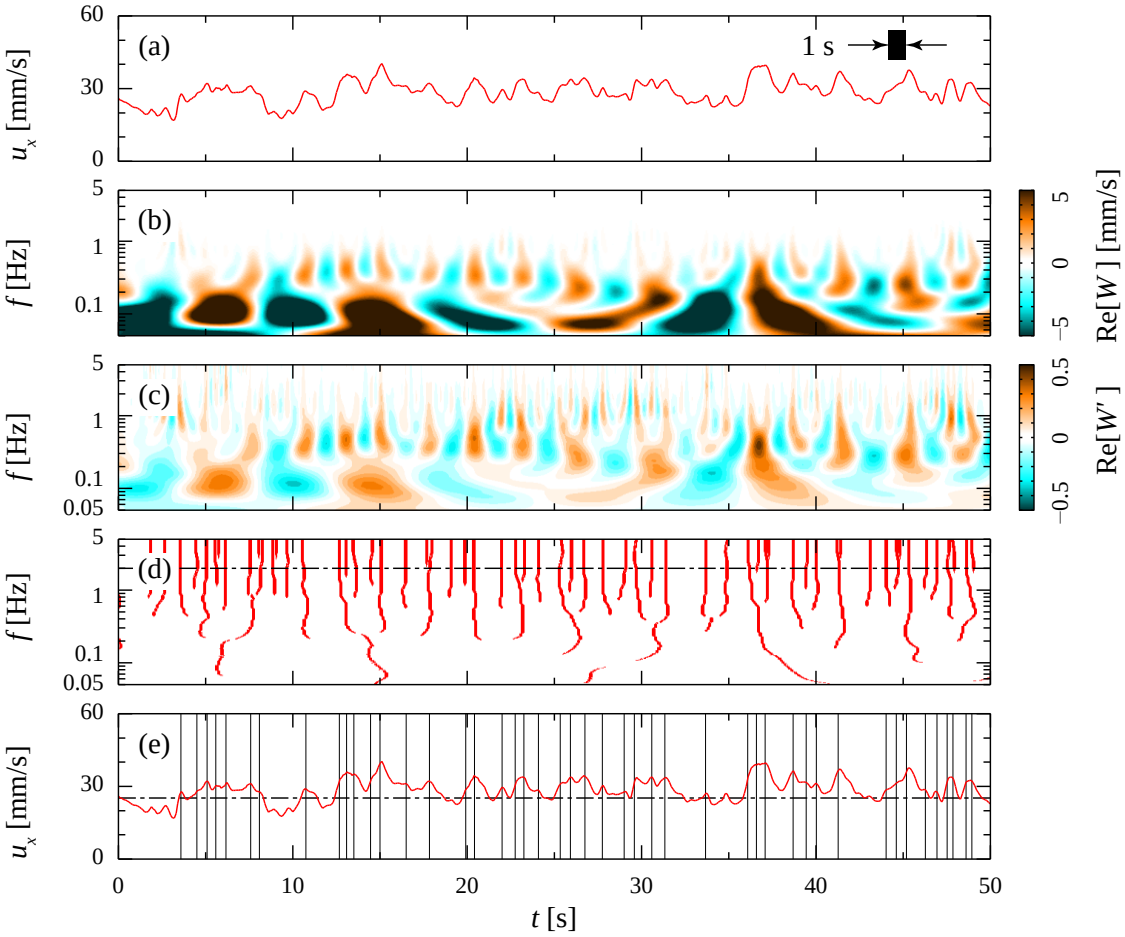


FIG. 5-16 (a) Temporal variation of vertical velocity at x = 250 mm in the pulsatile bubble generation of 5 % fluctuation; (b) real part of its wavelet coefficient, (c) real part of the normalized wavelet coefficient, (d) modulus maxima lines, and (e) extracted peak position of velocity fluctuation indicated as the vertical line

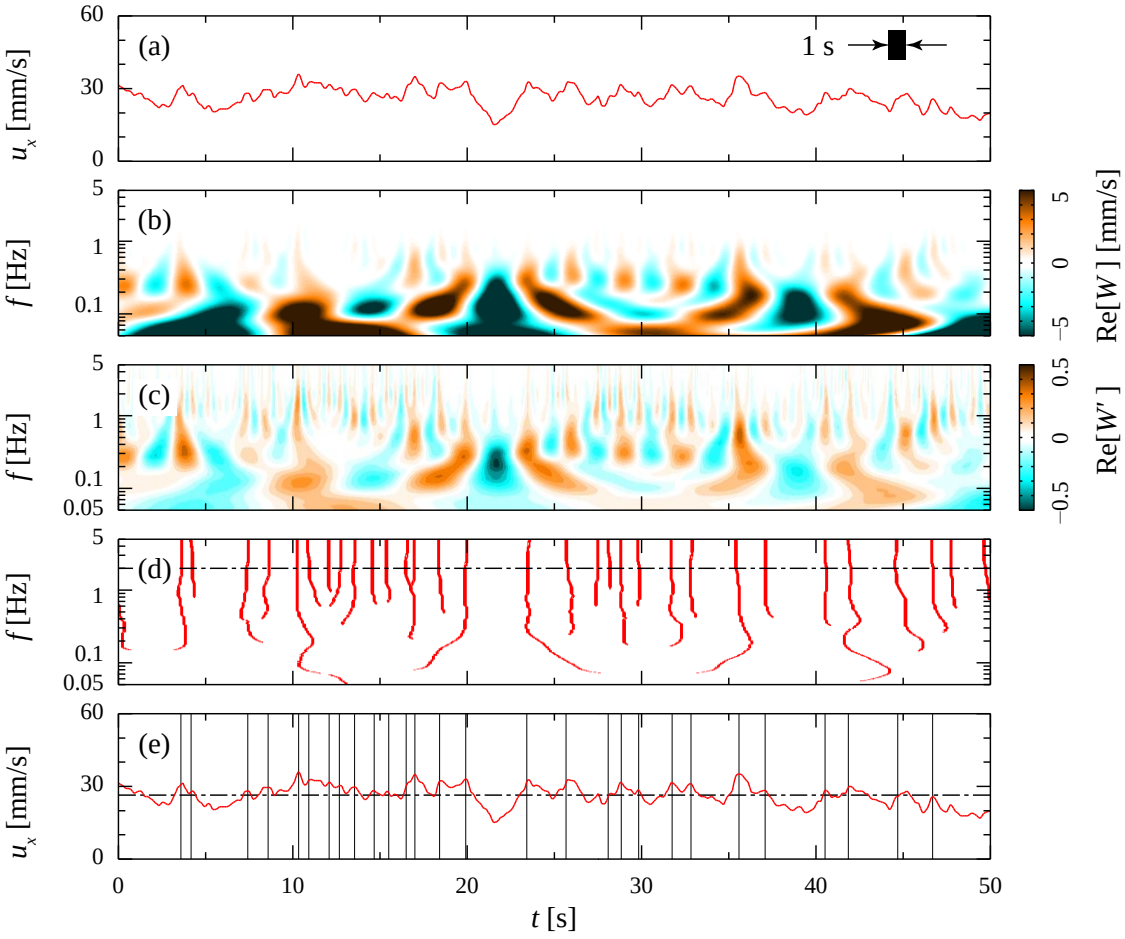


FIG. 5-17 (a) Temporal variation of vertical velocity at x = 450 mm in the pulsatile bubble generation of 5 % fluctuation; (b) real part of its wavelet coefficient, (c) real part of the normalized wavelet coefficient, (d) modulus maxima lines, and (e) extracted peak position of velocity fluctuation indicated as the vertical line

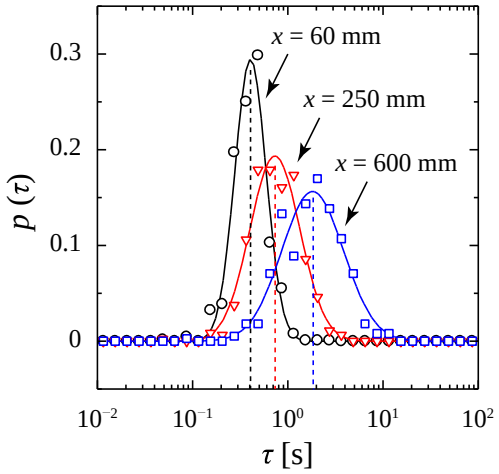


FIG. 5-18 PDF of transit time interval of bubble clouds τ, where symbols, continuous lines, and dotted lines indicate the experimental data, least mean approximated line by lognormal distribution curve, and modes of interval, τ_m

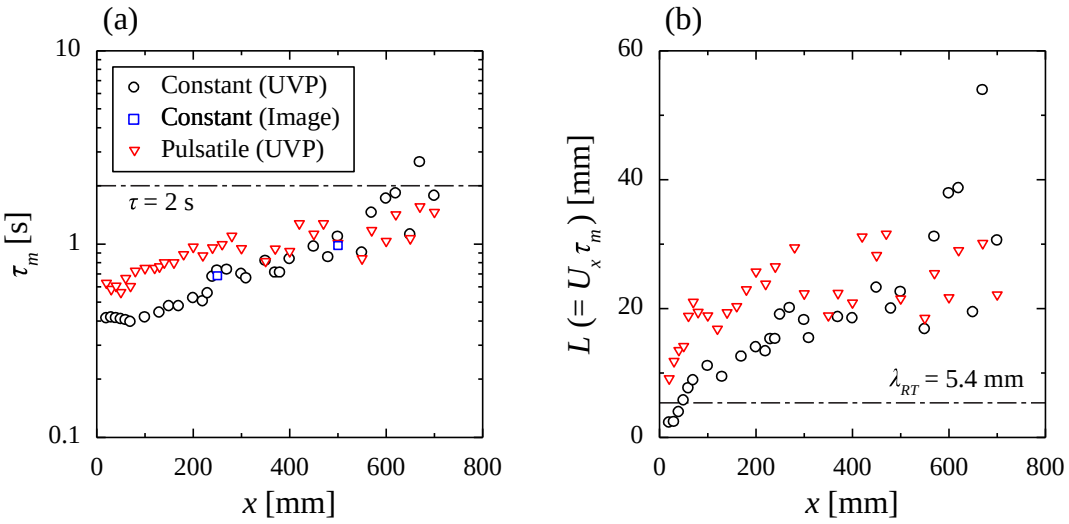


FIG. 5-19 Spatial development of (a) mode of time interval, τ_m, and (b) characteristic cloud length, L, determined form velocity data, u_x, obtained by UVP and bubble layer thickness, δ_y, obtained by image analysis

Chapter 6
Spectra modification of a mixing layer by introducing microbubbles

Abstract

In order to investigate the modification of spatial and temporal developing flows by the addition of microbubbles in *O*(10 μm) of diameter, flow structures appearing in shear flows of a horizontal mixing layer are visualized from velocity distributions obtained by (I) image analysis which combine particle tracking velocimetry (PTV) and laser induced fluorescence (LIF), and (II) ultrasound velocity profiling (UVP). As the result of the measurement, Reynolds shear stress increased by the addition of microbubbles at the early stage of the mixing layer. In the developing region, however, Reynolds shear stress decreases at the center of the mixing layer and is reduced in bulk. Energy spectra of the velocity fluctuations show that the energy of flow structure, whose length scale is as equivalent to the initial vortex layer thickness, is partially reduced. The size of vortex layer thickness is enlarged due to the local modification of the structure at the early stage of the mixing layer.

6.1 Introduction

Uses of bubbles in industries have been focused for engineering applications, because of the dispersibility, acoustic characteristics, or discriminating crush behavior. Many studies on bubbles in $O(10\ \mu m)$ of diameter called "microbubbules" have been conducted for as ultrasound contrast agents, drug delivery system in medicine [190], erosion for interfacial cleaning of materials [154], wastewater purification [155], heat exchange enhancement in natural convections [87] [158] [159] and drag reduction of hulls (submarine) or vessels (large ships) [14] [15], have conducted so far. Addition of microbubbles in flows achieves drag reduction of $O(10^{-1})$ even for the tiny void fraction of $O(10^{-4})$. To clarify the mechanism of such a great performance of drag reduction using microbubbles, velocity profiles in turbulent boundary layers have investigated as well as modification of wall shear stress by the addition of microbubbles in flows of pipe [36], channel [22] [23] [21] [34], or a parallel flat wall [24]. Velocity profiles in flows containing mirobubbles commonly show the enlargement of viscous sub-layer and modification of coherent turbulent flow structure above buffer layer.

The experimental observation of velocity profile in condition of drag reduction described the phenomenon as "the accumulation of microbubbles in a critical zone [22]" or "a complex and strongly nonhomogeneous concentration profiles [24]". The mechanisms for the modification of velocity profiles have been thought to be arisen from the interaction between the coherent vortex structure laden on the turbulent boundary layer and distributed of microbubbles. Modification or destruction of the coherent vortex structure [21] [23] [24] causes the reduction in momentum exchange due to decrease of eddy viscosity in turbulence. The modification of vortices in flows changes the transition from laminar to turbulent flows. The wall shear stress, therefore, is reduced by the prevention of transition so called Pseudo-Laminarization.

Investigations of wall shear stress in turbulent channel flows reported that the performance of drag reduction depends on the distance from the bubble injection point [15] [23] [34]. Both the distribution of bubbles and these motions in turbulent coherent vortex structures, however, have not discussed yet because of following issues: (a) difficulties in optical approaches in measurements (also mentioned by Jacob, *et al.*, [24]), (b) needs for the simultaneous measurement schemes for both microbubbles and surrounding liquid phase, which can provide spatial-temporal resolving data. The spatial

developing of flows like a pipe flow, or channel flow also makes difficulties mentioned above due to the non-periodicity or embedded vortex structure in cascade process. Hence, the investigation of the fundamental mechanisms of drag reduction in flows is still a challenging topic for its use and optimization in industries.

To investigate the influence of microbubbles on the spatial development of coherent vortex structure, horizontal mixing layers have been adopted as experimental platforms [191] [192] [193] [194] . Flow fields of the mixing layer are well understood and are recognized as flows display the fundamental vortex interactions from the investigations more than three decades ago [195] [196] [197]. The vortex layers in mixing layer shows the fluctuation of its position normal to the flow direction and spatial evolution of the vortex layer thickness. The instantaneous distribution and motion of bubbles in the spatially developing vortex layer is experimentally investigated in this section. Momentum exchange in the shear layer due to flow with two different velocities as well as the spatial development of vortex layer could be discussed from the statistic velocity distribution, i.e. mean and root means square (RMS) value of the velocity fluctuation. Following capability of individual small dispersed phase, such as a small solid particle, could be analytically predict for dilute (tiny volume) concentration cases in volume concentration $\alpha < 10^{-6}$, with considering the one-way coupling of force acting from fluid to particles [146]. The mechanisms on the generation of cloud or cluster (i.e. number density distribution), so called preferential concentration of dispersed phase and turbulent modulations (attenuation or enhancement) are still veiled yet [199] [147] [177].

For the understandings of bubble behaviors and modification of vortical flow structure suggested so far, instantaneous local velocity and void fraction distribution in a mixing layer are simultaneously resolved in experiments. Image analysis based on particle tracking velocimetry (PTV) and laser induced fluorescence (LIF), and ultrasound velocity profiling (UVP) are used for the measurement of velocity field in a mixing layer. We mentioned the modifications of the mixing layer thickness and turbulent spectrum due to the inhomogeneous distribution of microbubbles in a developing structure of the mixing layer.

6.2 Experimental system

6.2.1 Experimental setup

The experiments were conducted in a horizontal open channel tank made of transparent Plexiglas to allow the flow visualization as shown in FIG. 6-1 (a). The axes of x, y, and z are set along stream-wise (horizontal), gravity (vertical), and span-wise (width) directions, respectively. The width of the channel is 300 mm. The water level is 130 mm, and the splitter plate is arranged horizontally at 100 mm from the bottom of the channel. The origin of the coordinate is at the end of the flow splitter. The end of the splitter plate is tapered in order to reduce flow separations and vortex shedding as illustrated in FIG. 6-1 (b). A pump supplies tap water to the channel entrance. The velocities of upper and lower layer are varied by the different cross sectional area for the inlet to the two layers. Honeycomb placed at 50 mm upstream of the end of the splitter for the "straightened flow" in which turbulence is reduced comparing to "turbulent flow" without honeycomb. The schematic of vortex layer which appears in a shear flow is illustrated in FIG. 6-1 (c). The vortex layer thickness would be enlarged at the initial stage of the mixing layer, because the growth of the vortex layer thickness is motivated by fluctuation of vortex layer which induced by velocity disturbances.

The mean (time averaged) velocity, U, and the root mean square (RMS) value of velocity fluctuation, u_{rms}, are measured by particle tracking velocimetry (PTV) and ultrasound velocity profiling (UVP), and are shown in FIG. 6-2 and FIG. 6-3, respectively. The horizontal and vertical error bars indicate the spatial resolution, Δy, and velocity resolution, Δu_x. The mean velocity obtained from UVP shows larger scattering comparing with that from PTV. Stepper shaped distribution, however, could be seen in FIG. 6-2. The lower layer is maintained at a lower mean velocity, $U_1 \sim 10$ mm/s, than that of the upper layer, $U_2 \sim 50$ mm/s in both straightened and turbulent flow. The velocity resolutions are also indicated as horizontal dashed-dotted line as error bars, $\Delta u_{x,\,\mathrm{UVP}}$ in UVP and $\Delta u_{x,\,\mathrm{PTV}}$ in PTV as well as horizontal error bars in FIG. 6-2. In straightened flow, RMS value at $x < 0$ is small to resolve by PTV. The RMS value of the velocity fluctuations of the lower layer was $u_{1,\,\mathrm{rms}} = 2$ and 4 mm/s; and that of the upper layer was $u_{2,\,\mathrm{rms}} = 4$ and 6 mm/s in the straightened and turbulent flow, respectively. The basis of velocity profiles is highlighted in TABLE 6-1.

Hydrogen microbubbles were generated by water electrolysis from a Platinum

wire with 100 μm in diameter mounted at 30 mm upstream from the end of the splitter plate (x = − 30 mm) and used as a cathode. A cupper plate mounted at the upper layer was used as an anode. Hydrogen bubbles were dispersed into the channel from the lower fluid layer, while oxygen bubbles escaped to the atmosphere and not dispersed into the visualized area shown in FIG. 6-1 (a). The gas flow rate of microbubbles Q is theoretically estimated from Faraday's law and gas state equation, and is given as

$$Q = \frac{RTI}{2P}, \tag{6-1}$$

where R, T, I, and P are gas constant, temperature, electric current for water electrolysis, and atomic pressure, respectively. The void fraction of lower layer in the mixing layer estimated from the gas flow rate, Q, mean velocity of lower layer, U_1, and cross sectional area, A (= 100 × 300 mm^2), is given as

$$\alpha = \frac{Q}{AU_1}. \tag{6-2}$$

The maximum flow rate and void fraction of microbubble were Q = 56 mm^3/s and α = 1.9 × 10^{-4}, respectively. The distribution of microbubble diameter was measured from the object diameter in an image. The probability distribution of microbubble diameter is shown in FIG. 6-4. The mean diameter was 42 μm. The Stokes rising velocity, i.e. terminal velocity of a single microbubble in a Newtonian fluid, is given as

$$u_{St} = \frac{\rho g D_b^{\,2}}{12\mu}, \tag{6-3}$$

where ρ, μ, g, and D_b are the density and viscosity of the test fluid, gravitational acceleration, and mean bubble diameter, respectively. According to Eq. (6-2), u_{St} is estimated as 1.4 mm/s, and is smaller than U_1, U_2, $u_{1,\,\mathrm{rms}}$ and $u_{2,\,\mathrm{rms}}$ in this study.

In mixing layers, the vortex layer is generated by the shear of flows with Kelvin-Helmholtz instability. The vortex layer shows its positional fluctuation in y-direction because of velocity fluctuation. The fluctuations of vortex layer position translate to downstream, and these amplitudes evolve in translation process. Transverse vortices are generated in the mixing layer by the nonlinearity of flows. The vortices merge with neighboring ones (so called paring), the size of vortices, therefore, enlarged in mixing layers. We can observe the fluctuation of vortex layer and generation of vortices in the visualization section (see FIG. 6-1 (c)) in this chapter.

6.2.2 Measurement system

The two-dimensional velocity distribution of liquid phase, $\boldsymbol{u}$ [$u_x(x, y, t)$, $u_y(x, y, t)$], is obtained from the image analysis basis on particle tracking velocimetry (PTV) and laser induced fluorescence (LIF). This measurement provides the velocity of microbubbles, $\boldsymbol{u}_{\text{bubbles}}$ [$u_{x,\text{ bubbles}}(x, y, t)$, $u_{y,\text{ bubbles}}(x, y, t)$], and local void fraction, $\alpha(x, y, t)$, simultaneously with velocity distribution of liquid phase (mentioned in CHAPTER 3). The measurement section being the center of the channel width was illuminated by a blue laser (CNI Co. Ltd., wavelength: 473 nm) with 2 mm in thickness. Resin particles containing LIF dye (Thermo Co, Fluo-MAX, absorption wavelength: 465 nm, emission wavelength: 505 nm, specific gravity: 1.1, diameter: 50 μm) are used as tracer particles for PTV. Color information of fluorescent light from tracer particles and of scattering light from microbubbles' gas-liquid interface was used as criteria for the particle discrimination (see details in CAHPTER 2). The erroneous vectors are eliminated after obtaining the velocity vectors of liquid phase, and then the velocity vectors are rearranged on the grid point. As in the final post processing, the lacked velocity vectors on the grid points are interpolated by the spatio-temporal biquadratic ellipsoidal equation rearrangement (ST-BER) [74] in order to capture the detail of the unsteady advecting vortical structure in the mixing layer. The temporal resolution, grid size for vector rearrangement on grid points and velocity resolution were 8 ms, 3.1 mm and 2.4 mm/s, respectively.

The velocity profile of liquid phase was also obtained from ultrasound velocity profiling (UVP). UVP can provide only the spatial-temporal velocity distribution on the measurement line where ultrasound propagates, $u_x(x, t)$. Spatial resolution of UVP, however, is smaller comparing to that of grid size for PTV data rearrangement. The temporal resolution and velocity resolution were 55 ms and 0.47 mm/s, respectively. The measurement volume of UVP had the shape of a disk with 5 mm in diameter and 0.72 mm in thickness, thereby, the spatial resolutions were 0.72 mm in x direction, 5 mm in y and z direction, respectively. Porous resin particles with 100 μm in diameter (Mitsubishi HP 20SS, specific gravity: 1.1) were used for tracer particles for UVP.

TABLE 6-1 Mean velocity and RMS value of velocity fluctuation

Values	Straightened flow	Turbulent flow
U_1 [mm/s]	11	15
U_2 [mm/s]	50	50
$u_{1,\,rms}$ [mm/s]	1.4	4.7
$u_{2,\,rms}$ [mm/s]	3.8	6.1

6.3 Modification of developing mixing layer

6.3.1 Enlargement of vortex layer

FIG. 6-5 shows the y-direction gradient of time averaged horizontal velocity, U_x, noted as $\partial_y U_x$, in single phase ((a) and (b)) and two-phase ((c) and (d)) flow with α = 1.2 × 10^{-4}. The horizontal and vertical axes are the distance from the edge of the splitter plate, and the gradational color of the figures indicates the velocity gradient, $\partial_y U_x$. Since the vertical velocity component would be zero in the horizontal mixing layer at the initial condition, $\partial_y U_x$ is equivalent to the time averaged vorticity, Ω (= $\partial_y U_x - \partial_x U_y$). The velocity profile is obtained from PTV. The number of data for time averaging is 10,000 corresponding to 80 second. The characteristic time scale of the mixing layer estimated from the initial vorticity Ω_0 (= $\partial_y U_{x\,\max}$ at (x = 0)) is τ (= 4π / Ω_0) ~ 4 second, and is 1/20 of the measurement time. The left panels ((a) and (c)) are the results in the straightened flow, while the right panels ((b) and (c)) display the results in the turbulent flow, respectively. The y-direction locus indicating the maximum velocity gradient, $\partial_y U_{x\,\max}$, shows the displacement from higher to lower velocity section that is coincide with the literature [195]. The maximum value of velocity gradient, $\partial_y U_{x\,\max}$, decreases in turbulent two-phase flows (FIG. 6-5 (d)) comparing to turbulent single phase flow (FIG. 6-5 (b)). Furthermore, in the turbulent flow, the width of region showing certain value of velocity gradient stretches wider in the y direction in the two-phase condition than that in the single phase flow. In straightened flow, however, the maximum value of velocity gradient and the width of shear layer do not show any significant modifications.

To clarify the quantitative effect of presence of microbubbles on the mixing layer, the vortex layer thickness, δ_ω, is estimated from the velocity gradient, $\partial_y U_{x\,\max}$, and velocity ratio, ΔU (= $U_2 - U_1$), as

$$\delta_\omega = \frac{\Delta U}{\partial_y U_{x,\max}}. \tag{6-4}$$

The vortex layer thickness is also estimated from integral momentum thickness, θ (= δ_ω / 4), defined as

$$\theta = \frac{1}{\Delta U^2}\int_{-\infty}^{\infty}(U_2 - u_x)(u_x - U_1)\,dy. \tag{6-5}$$

We note that the grid size of vector position rearrangement for PTV data is 3 mm and the velocity resolution is 2.4 mm/s. So that, the velocity gradient obtained from Eq.

(6-4) is more likely to be estimated smaller and the integral momentum thickness obtained from Eq. (6-5) is likely to be estimated smaller than actual values. Thereby, the vortex layer thickness in this section is given as the averaged value obtained from Eq. (6-4) and Eq. (6-5). The spatial development of the vortex layer thickness is shown in FIG. 6-6. The circle symbols indicate the results in the straightened flow, while the triangles indicate that in the turbulent flow. The open and closed symbols are results in the single phase (SP) and the two-phase (TP) flow with the void fraction of α = 1.2 × 10^{-4}. The gradient of the hypotenuse placed at the bottom right of the figure indicates the growth rate of the vortex layer thickness reported in the literature [197], $\partial_x\delta_\omega$ = 0.17λ, where λ is the non-dimensional velocity ratio, (U_2 − U_1) / (U_1 + U_2). The initial vortex layer thicknesses defined as the minimum value were $\delta_{\omega,0}$ = 13 mm and 15 mm in the single phase and the two-phase flow in the straightened flow, while $\delta_{\omega,0}$ = 8 mm and 11 mm in the single phase and the two-phase flow in the turbulent flow. As expected in qualitative views in FIG. 6-6, the vortex layer thickness of two-phase flow is as same value as that for the single phase condition with straightened flow. By contrast, the vortex layer is enlarged by introducing microbubbles in the mixing layer. The grow rates gradually increase to the equivalent to that of the reference value regardless to the flow state or with/without microbubbles. The addition of microbubbles enlarges the vortex layer thickness by 25 % from the initial region of a turbulent mixing layer.

6.3.2 Modification of Reynolds shear stress

The modification of flow field, 25 % enlargement of the vortex layer thickness, was achieved even by microbubbles of $O(10^{-4})$ void fraction. The effective viscosity for the uniform dispersion of neutral buoyant small particles/bubbles in simple shear flows increase as a function of volume fraction of the disperse phase (1 + 5/2α), therefore it would be negligible in this condition. The modification of the coherent turbulent structure would be essential for the reduction of the vortex layer thickness like [21] [23]. The Reynolds shear stress is a key for the momentum exchange in the unsteady flows, and the Reynolds shear stress for two phase flow [21] is given as

$$\tau = \mu\frac{\partial U_x}{\partial y} + \rho\left\{-(1-\alpha)\overline{u_x' u_y'} + \overline{\alpha' u_y'}\,\overline{u_x} + \overline{\alpha' u_x' u_y'}\right\}, \qquad (6\text{-}6)$$

where U, u', “ ¯ ” indicate the time averaged velocity, velocity fluctuations (u' = (u −

U)), and time averages, respectively.

FIG. 6-7 shows the cross-correlation of velocity fluctuations, $\overline{u_x' u_y'} / \left(\overline{u_x'} \, \overline{u_y'} \right)$, in single phase flow ((a) and (b)); cross-correlations ((c) and (d)) $\overline{u_x' u_y'} / \left(\overline{u_x'} \, \overline{u_y'} \right)$, ((e) and (f)) $\overline{\alpha' u_y'} / \left(\overline{\alpha'} \, \overline{u_y'} \right)$, and ((g) and (h)) $\overline{\alpha' u_x' u_y'} / \left(\overline{\alpha'} \, \overline{u_x'} \, \overline{u_y'} \right)$, in two-phase flows with α = 1.2×10^{-4}, where prime " ' " an over-line " ¯ " indicate the fluctuation component and time average, respectively. In FIG. 6-7, left panels display results in straightened flow, while right panels represent those from turbulent flow. The upper layer of the fluid layer does not contain microbubbles as initial condition, cross-correlations as a function of void fraction, α' ((e) – (h)), would take zero, however, show non-zero values due to noises in identifying microbubble and tracer particle. Therefore, values of cross-correlation at the lower layer and inside of the mixing layer have meaningful in figures FIG. 6-7 (e) – (h). The distribution patterns in the cross-correlations of u_x' and u_y' are almost symmetric about the *x*-axis, however, the maximum position of the cross-correlation displace to the negative direction of *y*-axis due to the expansion of the jet [195]. The microubbles generate preferential distribution and motion in the mixing layer, because the cross-correlations as a function of void fraction, α' ((e) – (h)), shows the distribution pattern at the upper half part the inside of the mixing layer.

FIG. 6-8 shows the spatial development of Reynolds shear stress in single phase flow ((a) and (b)); Reynolds shear stress of two-phase flow which consist from ((c) and (d)) $-\left(1-\overline{\alpha}\right)\overline{u_x' u_y'}$, ((e) and (f)) $\overline{\alpha' u_y'} \, \overline{u_x}$, and ((g) and (h)) $\overline{\alpha' u_x' u_y'}$. The left panels show the results obtained in the straighten flow; the right panels show that in the turbulent flow. The figures signify that the magnitude of Reynolds shear stress in the single phase flow increases and its affection rage expands with increasing the distance *x*. The magnitude of Reynolds shear stress depends on the flow state, i.e. the straightened or the turbulent flow. The void fraction, α, and its fluctuation, α', in this study are both in $O(10^{-4})$, so that the decrease of medium density, $1 - \alpha$, is negligible small. Thereby the magnitude of $\overline{\alpha' u_y'} \, \overline{u_x}$ and $\overline{\alpha' u_x' u_y'}$ is negligible small, and $-\left(1-\overline{\alpha}\right)\overline{u_x' u_y'}$ component is dominant in the two-phase Reynolds shear stress. In the straightened flow, the magnitude of the Reynolds shear stress increases at x > 150 mm in two-phase flow (FIG. 6-8 (b)) comparing to that of the single phase flow (FIG. 6-8 (a)). In the turbulent flow, the magnitude of Reynolds shear stress also increases at x < 100 mm as well as the straightened flow, however, decreases at x > 100 mm by introducing microbubbles (see

FIG. 6-8 (c) and (d)). $\overline{\alpha' u_y'}$ (FIG. 6-8 (e) and (f)) and $\overline{\alpha' u_x' u_y'}$ (FIG. 6-8 (i) and (j)) showing the positive and negative ordered distribution patterns indicate that the velocity and the void fraction shows correlative motions in the mixing layer. $\overline{\alpha' u_y'}$ (FIG. 6-8 (e) and (f)) represents the increase of local void fraction and upward flow or decrease of local void fraction and downward flow. The maximum loci of $\overline{\alpha' u_y'}$ dose not correspond to that of $-\left(1-\overline{\alpha}\right)\overline{u_x' u_y'}$. The magnitude of $\overline{\alpha' u_x' u_y'}$ also shows asymmetric distribution about the center line of the mixing layer. This is that the preferential motion of distribution of microbubbles in the fluid structure of the mixing layer could be well observed in the upper part of the vortex layer.

Probability distributions of time series of the velocity fluctuation and the void fraction in the turbulent flow are shown in FIG. 6-9 for the upper layer at (x, y) = (170 mm, 13 mm) and in FIG. 6-10 for the lower layer at (x, y) = (170 mm, − 13 mm). The gray scale indicates the linear scale of the probability normalized by the maximum value in each panel. Whiteness and blackness indicate high and low value in probability. The fluctuations of vortex layer position provide the Reynolds shear stress in both the single and two-phase flow (as shown in FIG. 6-8), the time series of u_x' and u_y', therefore, shows negative correlations at the positions. As shown in FIG. 6-9 (a) and FIG. 6-10 (a) in the upper side of the mixing layer, the introducing of microbubbles stretches the probability distribution in the direction of u_y'. The maximum probability is located $\alpha' < 0$ and $u_x' > 0$ in FIG. 6-9 (c), and is also located $\alpha' < 0$ and $u_x' > 0$ in FIG. 6-9 (d). In the upper layer of the mixing layer, the fluctuation having $u_x' < 0$, $u_y' > 0$, $\alpha' > 0$ component exist as a rare but characteristic motion in the flow. In the lower layer of the mixing layer, the characteristic patterns of the probability are less significant to be recognized in both FIG. 6-10 (c) and FIG. 6-0 (d). FIG. 6-11 shows the iso-surface of the probability distribution in the velocity and local void fraction at (a) upper (x, y) = (170 mm, 13 mm) and (b) lower layer (x, y) = (170 mm, − 13 mm) in the mixing layer. The iso-surface of the probability distribution also displays the characteristic shapes of the fluctuation of the velocity u_x', u_y' and local void fraction α'. There is an aculeate hump at $u_x' < 0$, $u_y' > 0$, $\alpha' > 0$ in FIG. 6-11 (a). Increasing of the local void fraction is observed, when a ascending fluid blob having slower horizontal velocity in the upper high velocity layer. In the lower layer (FIG. 6-11 (b)), on the other hand, the decreasing of the local void fraction in descending fluid blob having high horizontal velocity is less significant to

observe comparing to a ascending fluid blob having slower horizontal velocity, despite the correlation term $\overline{\alpha' u_x' u_y'}$ shows negative value in FIG. 6-8 (j).

FIG. 6-12 shows schematic of velocity and void fraction fluctuation patterns in the two-phase mixing layer that obtained from fluctuation correlation shown in FIG. 6-8. The flowing phenomena are classified in four separated section (S1, S2, S3, and S4). As shown in FIG. 6-8 (e) and (f), the term $\overline{\alpha' u_y'}$ is larger at the upper half part of the mixing layer (S1 and S2) than that in lower half part (S3 and S4). On the other hand, the term $\overline{\alpha' u_x' u_y'}$ shows the negative value at the upper half part but shows the positive at the lower half of the mixing layer. The increase of local void fraction, $\alpha' > 0$, and ascending flow, $u_y' > 0$, in slower horizontal velocity region, $u_x' < 0$, (S1 and S4 in FIG. 6-12) proves negative value of $\overline{\alpha' u_x' u_y'}$, while the decrease of local void fraction, $\alpha' < 0$, and descending flow, $u_y' < 0$, in high speed region, $u_x' > 0$, (S2 and S3) provides positive value of $\overline{\alpha' u_x' u_y'}$. The negative $\overline{\alpha' u_x' u_y'}$ shows the larger magnitude comparing to that of positive $\overline{\alpha' u_x' u_y'}$. The fluctuations giving $\overline{\alpha' u_x' u_y'}$ are larger in S1 and S2 than that in S2 and S3. Summarizing the fluctuations, the most dominant fluctuations in this mixing layer happens in S1; the phenomena that the ascending motion of fluid having high void fraction from slower to higher velocity layer in mixing layer.

FIG. 6-13 shows Reynolds shear stress distribution in the single phase (SP) and the two-phase (TP) turbulent flows. The circles represent the Reynolds sheer stress at x = 17 mm (~ 2 $\delta_{\omega, 0}$), and triangles represents that at x = 170 mm (~ 20 $\delta_{\omega, 0}$), respectively. The Reynolds shear stress increases by 60 % at x ~ 2 $\delta_{\omega, 0}$ in the two-phase condition, on the other hand it decreases by 30 % at x ~ 20 $\delta_{\omega, 0}$. The presence of microbubbles in the mixing layer enhances the momentum exchange due to the unsteady motion in flows at the early stage of the turbulent mixing layer. However, it reduces the momentum exchange at the developing region. The momentum exchange is also enhanced at x ~ 13 $\delta_{\omega, 0}$ in the straightened flow. These common phenomena suggest that the modification of flow field by the motions of microbubbles appears when the background velocity fluctuation increases. The comparison of the Reynolds shear stress and correlation between the fluctuations of fluid velocity and void fraction lead the hypothesis that the criteria of the flow field modification by the dilute microbubble flow would be the strength of the velocity fluctuation.

6.3.3 Modification of instantaneous velocity field

FIG. 6-14 and FIG. 6-15 show the spatio-temporal distribution of horizontal velocity component, u_x, obtained from UVP in single phase and (b) two-phase flow with void fraction of $\alpha = 1.2 \times 10^{-4}$, and (c) local void fraction obtained from image analysis at the straightened (FIG. 6-14) and turbulent flow (FIG. 6-15). The gradient of the hypotenuse placed in (a) indicates the velocity, U_1, U_2 and $\overline{U}$ (= (U_1 + U_2) / 2), respectively. The velocity fluctuation shows the diagonal stripe pattern in both the single phase and the two-phase flow. The diagonal patterns near the splitting plate with a slower translating velocity than mean velocity of the lower layer in the mixing layer indicate the wake structure due to the end shape of the splitting plate. The translating (advection) velocity of the large amplitude in diagonal pattern representing the mean velocity, $\overline{U}$, appear in in all spatio-temporal velocity display. The fine diagonal stokes, whose translating velocity are comparable with U_1 or U_2, could be identified in the straightened single phase flow (FIG. 6-14 (a)), straightened two-phase phase flow (FIG. 6-14 (b)), and turbulent single phase flow (FIG. 6-15 (a)). The diagonal pattern indicating men velocity of the mixing layer, $\overline{U}$, could be observed in the turbulent two-phase flow (FIG. 6-15 (b)), the fine diagonal patterns whose translating velocity correspond U_1 or U_2, however, are disappeared. Addition of microbubble immediately modifies the velocity fluctuations in the turbulent mixing layer.

The diagonal fluctuation patterns also appear in spatio-temporal distribution of local void fraction as shown in FIG. 6-14 (c) and FIG. 6-15 (c). The local void fraction in the turbulent two-phase flow shows thinner diagonal pattern comparing to that in the straightened flow. This fluctuation pattern represents the advection of locally high void fraction region, called void wave or preferential concentration. In turbulent flow case, the advection velocity of bubble distribution is comparable with the vortical structures advecting in the mixing layer. Furthermore, the fluctuations of the velocity of liquid phase flow and the local void fraction shows the positive cross-correlations in the turbulent two-phase flow case as shown in FIG. 6-7 (f) and FIG. 6-7 (h). Hence, these relationships between the translating motion of microbubble distributions and translating vortical structures suggest that the microbubbles are captured and preferentially dispersed in the turbulent mixing layer. In the straightened flow, on the other hand, the diagonal patterns of the local void fraction shows that the translating

velocity is comparable with U_1 at $x < 100$ mm and gradually reaches $\overline{U}$ at $x > 100$ mm. Hence, the microbubbles are captured into neither the wake of splitting plate nor spatial fluctuation pattern of velocity fluctuations, appear in FIG. 6-14 (c) due to the velocity fluctuation of the lower layer.

FIG. 6-16 shows the probability distribution of neighboring distance between local maxima of void fraction distribution, l, obtained from the spatao-temporal void fraction distribution in straightened flow as shown in FIG. 6-14 (c) and the turbulent flow as shown in FIG. 6-15 (c), respectively. The probability $p(l)$ distributes widely in the special domain l, $p(l)$, however, shows the unique maximum peak in both cases. The curved lines are the second-order polynomial approximation line connecting the maximum and its neighboring data points (closed symbols). The vertical dashed-dotted lines indicate the local maximal position approximately obtained. The maximal position p indicate l = 15 mm in the straightened flow and l = 10 mm in the turbulent flow, respectively. This distance between the microbubble clouds are comparable with the initial vortex layer thickness as mentioned in SECT. 6.3.1. The RMS value of the fluctuating local void fraction takes $\alpha_{\mathrm{rms}} = 0.95 \times 10^{-4}$ in the turbulent flow and $\alpha_{\mathrm{rms}} = 1.1 \times 10^{-4}$ in the turbulent flow case with mean void fraction of $\alpha_{\mathrm{rms}} = 1.2 \times 10^{-4}$ estimated by Eq. (6-3). Therefore, the microbubbles are seemed to be much captured by 15 % in the vortical structure of the turbulent mixing layer.

FIG. 6-17 shows power spectrum of horizontal velocity fluctuation at $y = 0$, $\overline{\hat{u}_x^{\,2}}$, obtained from (a) PTV and (b) UVP. The hat '^' and over line '¯' indicate power of spatial velocity fluctuation and time average, respectively. The horizontal axes are wavenumber, k, and that normalized by the initial vortex layer thickness, $k / \delta_{\omega,\,0}{}^{-1}$, where the hatching at the top axis represents the error range in the wavenumber normalization. The vertical axes are the power of velocity fluctuation, $\overline{\hat{u}_x^{\,2}}$, and that normalized by the mean velocity of the mixing layer, $\overline{U}$. The arrow at the bottom of the figure indicate the wavenumber corresponding the characteristic length scale of void fraction, k_α (= l^{-1}). The Kolmogorov length scale, ℓ_{d}, estimated by kinematic viscosity of the test fluid, ν, initial vortex layer thickness, $\delta_{\omega,\,0}$, and velocity ratio, ΔU (= $U_1 - U_2$), are, given as

$$\ell_{\mathrm{d}} = \left(\frac{\nu^3 \delta_{\omega,0}}{\Delta U^3} \right)^{\frac{1}{4}}, \tag{6-7}$$

takes ℓ_{d} = 0.13 mm in turbulent single phase flow case. Therefore, the wavelength representing the Kolmogorov length scale is k_{d} (= $\ell_{\mathrm{d}}{}^{-1}$) = 7.6 mm^{-1}. In this study, the spatial resolution for the velocity measurement is not sufficient to resolve the Kolmogorov length scale (out of the range in FIG. 6-17), however, is acceptable to resolve the inverse energy cascade process in mixing layer, i.e. smaller wavelength than initial vortex layer thickness, $\delta_{\omega,\,0}$. The powers obtained PTV and UVP shows the difference in values because of the both velocity and spatial resolutions, the wavenumber dependency of the power spectra shows same decreasing feature and show lower powers in two-phase flows comparing to that in single phase flows at the wavelength scale $k \sim \delta_{\omega,\,0}{}^{-1}$. Further, in this study, the energy spectrum is obtained from Fourier transform the velocity profile in the spatial direction without using Taylor's frozen hypothesis, the tilt of the center line of the mixing layer as shown in FIG. 6-7 and FIG. 6-8 significantly modify the spectra in low wavenumber domain. Therefore, we would focus on the modifications at the center of the spectra.

The most of the power of velocity fluctuation consist from k < 0.03 mm^{-1} the wavenumber domain. Spectra power of 0.03 < k < 0.3 mm^{-1} of which occupy 50 % of the total power in the single phase flow decreases in the two-phase flows. In the two-phase flow α = 1.8 × 10^{-4} in the void fraction, the power at that frequency domain declines to 25 % of that in the single phase condition, at the maximum modification case. The bubbles generate the preferential concentration [140] [141] correlating with the velocity fluctuation in the mixing layer as shown in FIG. 6-15 (c) and FIG. 6-16. The spatial distribution pattern of the buoyant force due to the preferential concentration of microbubbles stretches and enlarges the vortices corresponding to the preferential scale of microbubbles, l. The Froude number, Fr, the ratio of inertia force to buoyant force is given as

$$Fr = \frac{\overline{u_{rms}}}{\sqrt{\alpha_{rms} \delta_{\omega,0} g}}, \tag{6-8}$$

where $\overline{u_{rms}}$, α_{rms}, $\delta_{\omega,\,0}{}^{-1}$, and g are the average of the RMS value for upper and lower layer (($u_{1,\,\mathrm{rms}}$ + $u_{2,\,\mathrm{rms}}$) / 2), spatial average of RMS value of void fraction at y = 0, initial

vortex layer thickness, and gravitational acceleration, respectively. The Froude number takes Fr = 0.57 and 1.6 in the straightened and turbulent flow cases, respectively. The spatial distribution pattern of microbubbles is more likely to be modified and be captured into the spatial fluctuation pattern of the mixing layer in the turbulent than straightened condition. The captured microbubbles in the coherent vortical structure stretch the vortices in the gravity direction due to buoyant force. Consequently, the Reynolds shear stress increase at the early stage of the turbulent mixing layer and the vortex layer thickness is enlarged by introducing microbubbles. The velocity fluctuation in flow field, therefore, is modified in the limited length domain in which microbubbles generating preferential concentration distribution.

TABLE 6-2 Variations in typical quantities in straightened and turbulent mixing layers at single and two-phase flow

	Straightened flow		Turbulent flow	
Values	Single phase	Two-phase	Single phase	Two-phase
α [-]	0	1.2×10^{-4}	0	1.2×10^{-4}
α_{rms} [-]	N/A	1.1×10^{-4}	N/A	0.95×10^{-4}
l [mm]	N/A	15	N/A	10
$\delta_{\omega, 0}$ [mm]	13	15	8	11
ℓ_d [mm]	0.14	0.14	0.12	0.13
Fr [-]	N/A	0.57	N/A	1.6

6.4 Conclusion

The modification of spatially developing turbulent spectra by introducing microbubbles of 40 μm in diameter was experimentally investigated in the horizontal mixing layer with different disturbance, i.e. straightened and turbulent inlet flows. The presence of microbubbles would be negligible in the general theory in the uniform dispersion of neutral buoyant particles. The fluctuation of velocity distribution in shear flow is modified in certain frequency domain, and the shear of the mixing layer is relaxed by introducing microbubbles with void fraction $\alpha = 1.2 \times 10^{-4}$.

The microbubbles in the mixing layer generate distribution of the local void fraction. The correlation between velocity fluctuations and local void fraction shows the preferential motion and distribution of microbubbles in upward flows of the mixing layer. The inhomogeneous microbubble distribution generates external forcing by its buoyancy. Therefore, the power spectra, in which wavenumber corresponding to the distance between local maxima of void fraction distribution, was locally declined to 10 % of that in the single phase flow. The fluctuation of vortex layer location appearing due to the shear instability or the disturbance of flow is enlarged into larger structure in the developing region of mixing layer. The buoyant force generated by the preferential distribution of microbubbles enhances the turbulent mixing and accelerates the growth of the vortex size. The Reynolds shear stress at the initial part of mixing layer increased and the vortex layer thickness was enlarged. As space and time development, the inhomogeneous distribution pattern of microbubbles becomes unclear and makes into homogenous distribution. After that, the enhancement of mixing by microbubbles is no longer observed. And the vortex layer thickness still develops into larger, following with the mixing nature in single phase flows.

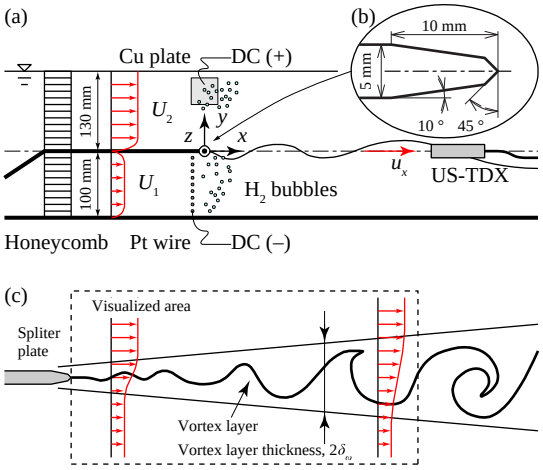


FIG. 6-1 Schematic outline of (a) experimental setup, (b) edge shape of the splitting plate, and (c) spatial developing of vortex layer thickness

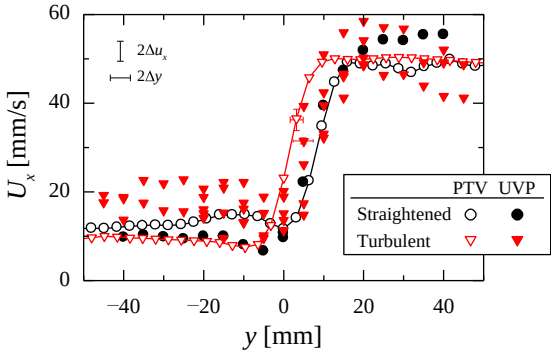


FIG. 6-2 Time averaged horizontal velocity component in single phase flow, where the horizontal and vertical error bars indicate the spatial and velocity resolutions

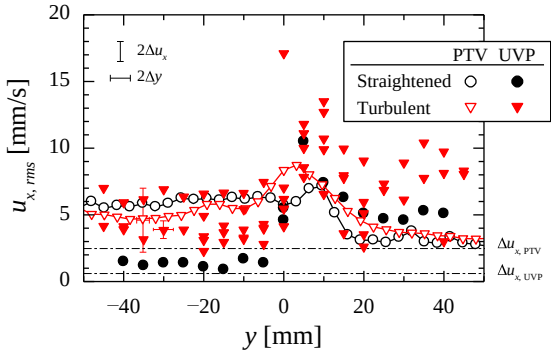


FIG. 6-3 RMS value of horizontal velocity fluctuation in single phase flow, where the horizontal and vertical error bars indicate the spatial and velocity resolutions

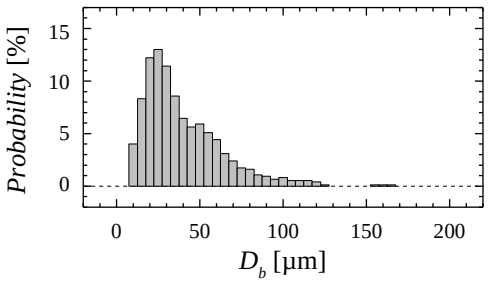


FIG. 6-4 Distribution of microbubble diameter

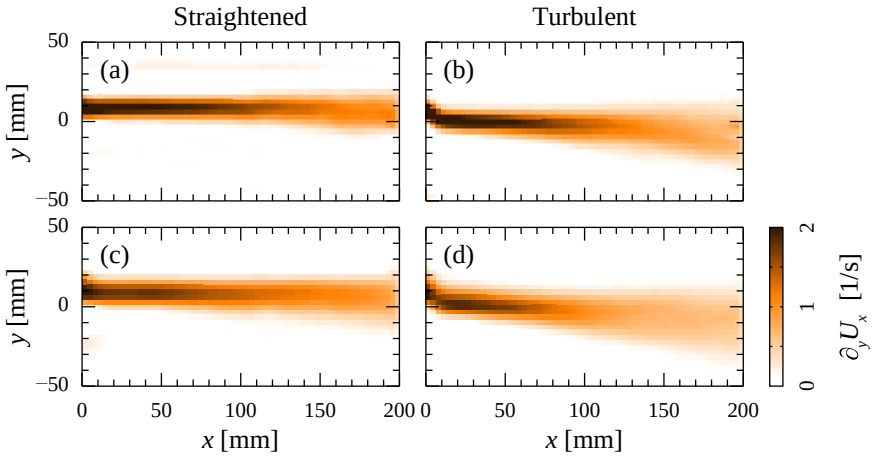


FIG. 6-5 Vertical gradient of time averaged velocity field in (a) single phase and (b) two-phase flow (α = 1.2 × 10^{-4}). The left panels display results in straightened flow, while right panels represent those from turbulent flow.

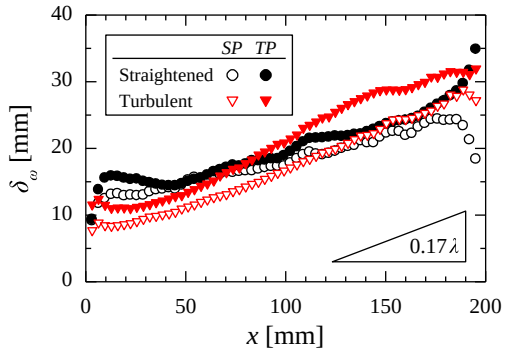


FIG. 6-6 Development of vortex layer thickness in single phase (SP) and two-phase (TP) condition with α = 1.2 × 10^{-4}. The slope of triangle indicates the growth rate of vortex layer thickness, $\partial_x\delta_\omega$ = 0.17 λ (Browand & Troutt, 1985), where λ is non-dimensional velocity ratio, $(U_2 - U_1) / (U_2 + U_1)$.

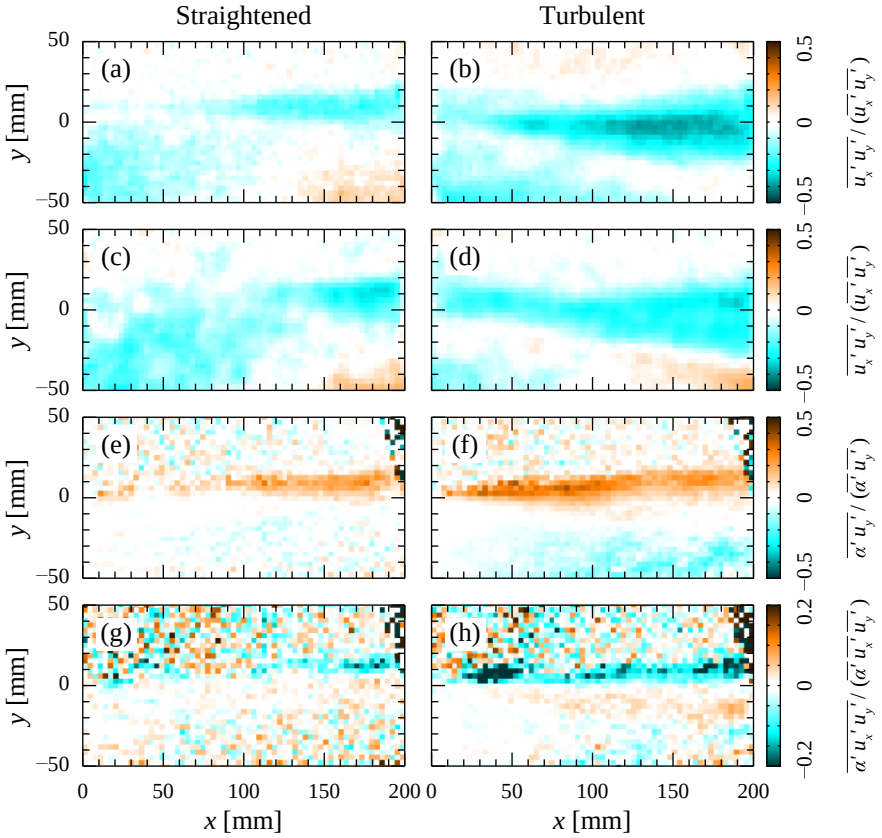


FIG. 6-7 Spatial development of cross-correlation of velocity component (a) (b) $\overline{u_x' u_y'}/\left(\overline{u_x'}\,\overline{u_y'}\right)$ in single phase flow; cross-correlations in two-phase flows with α = 1.2 × 10^{-4}: (c) (d) $\overline{u_x' u_y'}/\left(\overline{u_x'}\,\overline{u_y'}\right)$, (e) (f) $\overline{\alpha' u_y'}/\left(\overline{\alpha'}\,\overline{u_y'}\right)$, and (g) (h) $\overline{\alpha' u_x' u_y'}/\left(\overline{\alpha'}\,\overline{u_x'}\,\overline{u_y'}\right)$ components, where left panels display results in straightened flow, while right panels represent those from turbulent flow

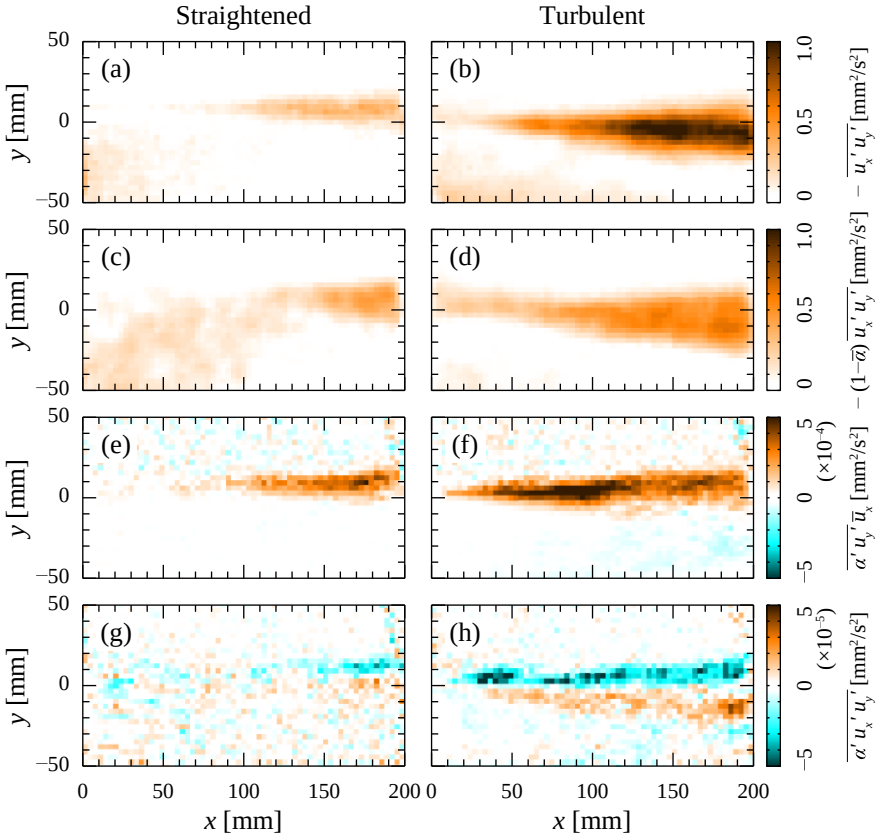


FIG. 6-8 Spatial development of Reynolds shear stress in (a) (b) single phase flow; Components of Reynolds shear stress in two-phase flows with α = 1.2 × 10^{-4}: (c) (d) $-\left(1-\bar{\alpha}\right)\overline{u_x'u_y'}$, (e) (f) $\overline{\alpha' u_y'}\,\overline{u_x}$, and (g) (h) $\overline{\alpha' u_x' u_y'}$ components, where left panels display results in straightened flow, while right panels represent those from turbulent flow

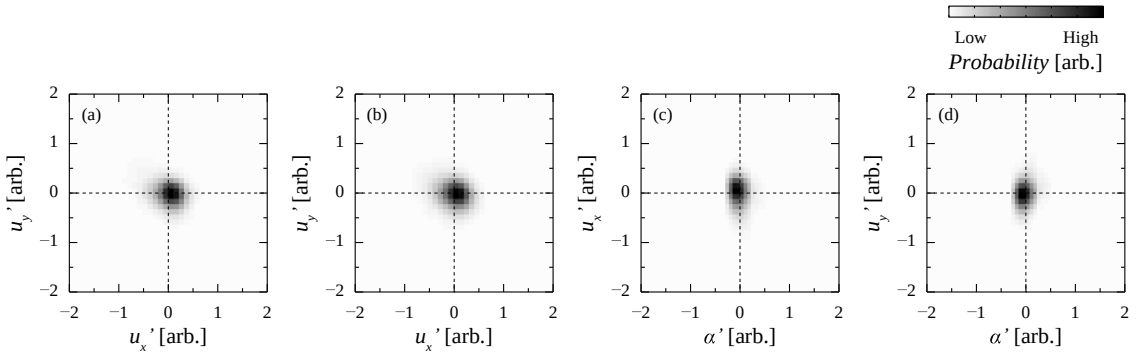


FIG. 6-9 Probability distribution of time series of (a) u_x' and u_y' in single phase flow; (b) u_x' and u_y', (c) α' and u_x', (d) α' and u_y' in two-phase flow at upper layer (x , y) = (170 mm, 13 mm)

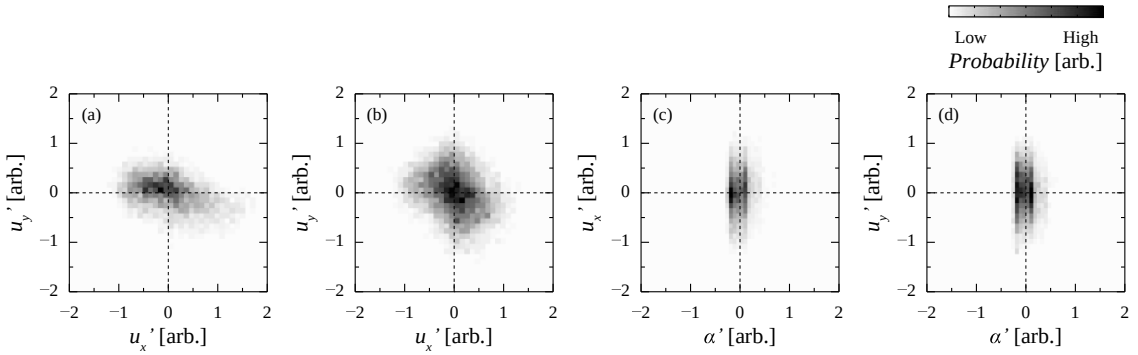


FIG. 6-10 Probability distribution of time series of (a) u_x' and u_y' in single phase flow; (b) u_x' and u_y', (c) α' and u_x', (d) α' and u_y' in two-phase flow at lower layer (x , y) = (170 mm, − 13 mm)

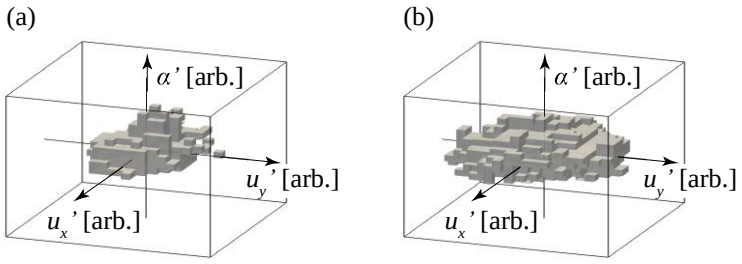


FIG. 6-11 Iso-surface of probability distribution at (a) upper (x, y) = (70 mm, 13 mm) and (b) lower layer (x , y) = (170 mm, − 13 mm)

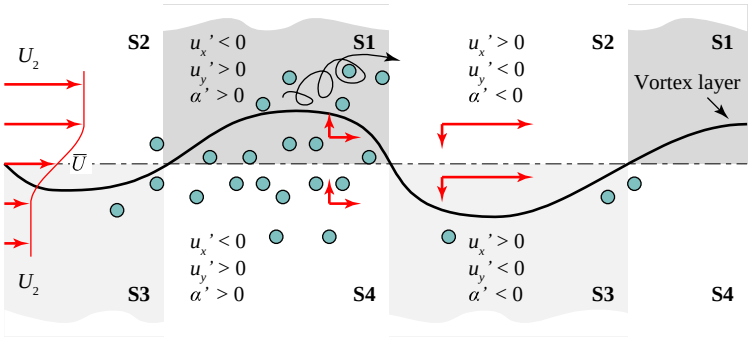


FIG. 6-12 Schematic of fluctuation of velocity and void fraction in vortex layer

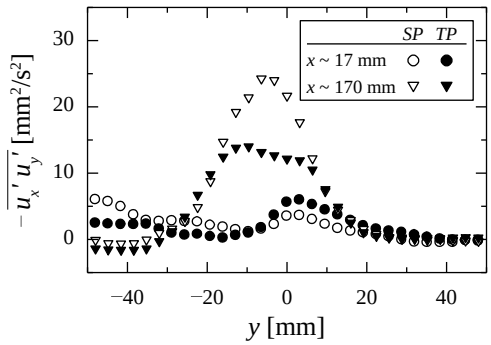


FIG. 6-13 Reynolds shear stress at y ~ 17 and 170 mm in single phase (*SP*) and two-phase (*TP*) flow with $\alpha = 1.2 \times 10^{-4}$

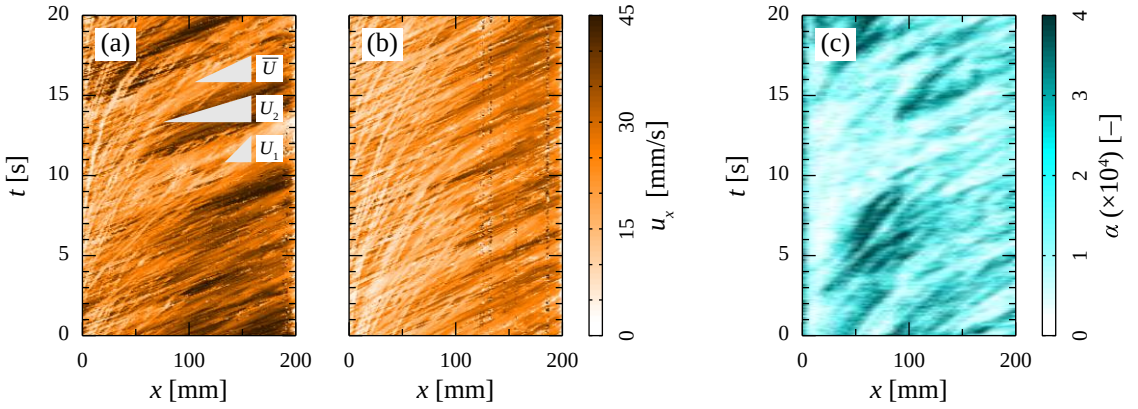


FIG. 6-14 Spatio-temporal distribution of horizontal velocity component at the center of mixing layer in straightened flow at (a) single phase and (b) two-phase flow with $\alpha = 1.2 \times 10^{-4}$, and (c) local void fraction, where slope of the triangles in (a) represent the velocity for U_1, U_2, and $\overline{U}$ (= $(U_1 + U_2) / 2$), respectively

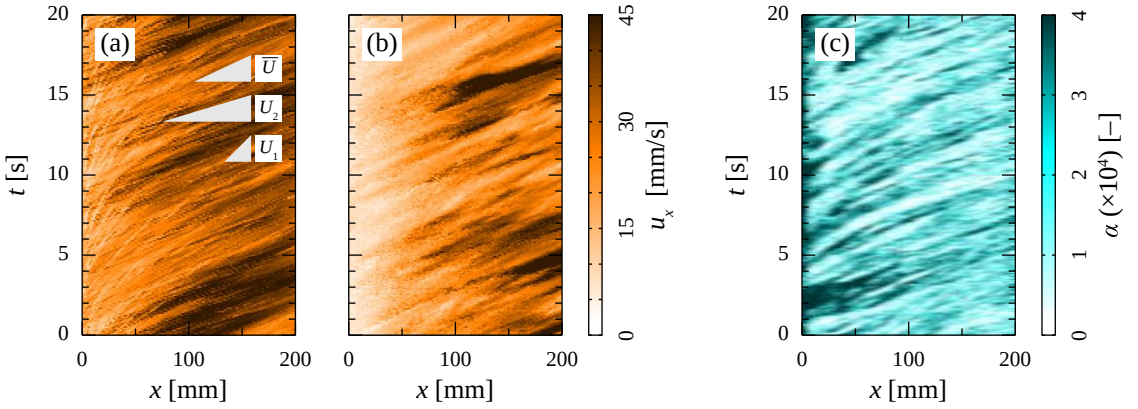


FIG. 6-15 Spatio-temporal distribution of horizontal velocity component at the center of mixing layer in turbulent flow at (a) single phase and (b) two-phase flow with $\alpha = 1.2 \times 10^{-4}$, and (c) local void fraction, where slope of the triangles in (a) represent the velocity for U_1, U_2, and $\overline{U}$ (= $(U_1 + U_2) / 2$), respectively

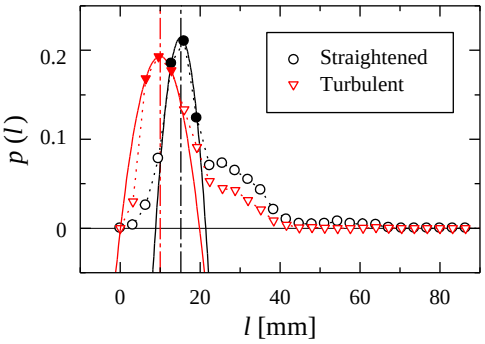


FIG. 6-16 Probability distribution of the neighboring distance of microbubble clouds in straightened (circle) and turbulent (triangle) flows, where the curvature lines and vertical dashed-dotted lines are the second-order polynomial approximation line of the maximum and its neighboring data points (closed symbols) and centers of the approximated line

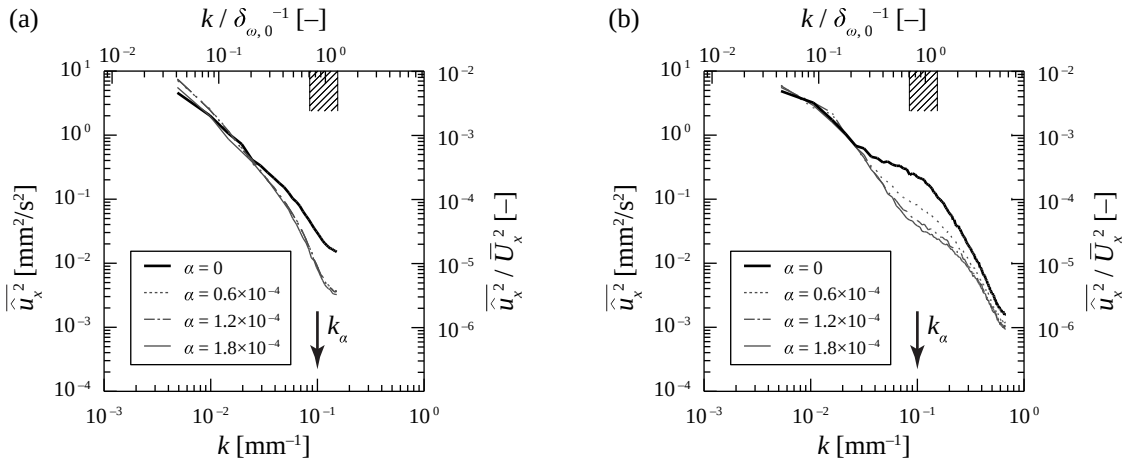


FIG. 6-17 Energy spectrum of the velocity fluctuation obtained from (a) PTV and (b) UVP, where the hatching at the top axis represents the error in normalized wavenumber, $k / \delta_{\omega,0}{}^{-1}$; Arrow at the bottom of figure indicates the wave number of fluctuation in local void fraction k_α.

Chapter 7
Conclusion

7.1 Review of chapters

In this work, the influence of the addition of mcirobubbles in diameter of *O*(10 μm) on the flow field of time dependent flows in a laminar-turbulent transient region were studied. In chapter 2, particle tracking velocimetry (PTV) utilizing color information was developed for three dimensional PTV and PTV for microbubbly flows. In chapter 3, modification waves in Taylor–Couette flow by the addition of microbubbles was experimentally investigated in order to examine the pseudo-decrease in effective Reynolds number. In chapter 4, the drag reduction due to the modification of secondary flow structure corresponding to azimuthally propagating waves on Taylor vortices was investigated by hybrid simulations combining PTV and direct numerical simulation (DNS). In chapter 5, spatially developing process of microbubble clouds were investigated by ultrasonic velocity profiling (UVP) and image analysis. In chapter 6, the influence of microbubbles on spatially developing horizontal mixing layers was experimentally investigated. The results obtained in each chapter have already summarized as individual conclusions, the conclusion is again recited as the conclusion of this thesis.

The accuracy of PTV utilizing color information was improved in order to achieve (a) three-dimensional (3D) three-component PTV using a single camera and a liquid crystal display (LCD) projector as a simplified system, and (b) discrimination of tracer particles in microbubbly flows with applying laser induced fluorescence (LIF). In order to estimate the particle position in the depth direction on an image, the tracer particle in a measurement volume were illuminated by the gradation-color-coded light whose hue changes as a function of depth position applying a LCD projector. To minimize the uncertainties in identifying reprehensive scattering colored light, the hue in HSV color coordinate is used to convert RGB color information of tracer particles. The presented algorithm of saturation-weighted averaged-hue in polar coordinate (SWAH-P) successfully reduced the uncertainties in the color identification. The proposed algorithm SWAH-P yielded the uncertainties of standard deviation of 1.4 % in

the hue and 2.0 % in the position estimated from the hue.

The improvement of identification of color information guaranteed the accuracy in position and velocity determined in 3D-3C PTV. The vortex structures generated behind a rotating impeller enable to be successfully displayed by the physical quantities, streamlines, vorticities, and enstrophy density. Discrimination of tracer particles in flows containing microbubbles whose diameter is of same order as that of tracer particles was achieved by giving a criteria for particle color in an image consisting of RBG color information.

The influence of the presence of microbubbles with 60 μm on the coherent vortical structures and flow transitions were experimentally investigated in a vertically arranged Taylor–Couette flow in a laminar-transition regime. Velocity profiles of the liquid phase were measured by PTV applying LIF developed in Chapter 2, ultrasonic velocity profiling (UVP), and laser Doppler velocimetry (LDV). The bubble distribution and motion in the fluid layer were measured by PTV applying LIF simultaneously with the liquid phase velocity. The void fraction in bulk was estimated as $O(10^{-4})$ at the maximum case. The distribution of microbubbles measured by LIF based image analysis indicated that the microbubbles form voidage wave, i.e. number density distribution, in the azimuthally traveling wave of Taylor vortices. The number density of microbubbles increases at the crest of waves and decreases at the trough. The highly concentrated microbubbles migrate in the axial streams connecting successive counter-rotating Taylor vortices. The measurements of liquid phase velocity showed that the critical Reynolds number for the Taylor vortex flow (having axially arranged torus vortices, so called Taylor vortices) to wavy vortex flow (having azimuthal wave superimposed on Taylor vortices), and wavy vortex flow to modulated wavy vortex flow (having modulation of azimuthal wave) were both increased by the addition of microbubbles. The azimuthal velocity gradient was also decreased by the addition of microbubbles. The skin frictional drag was reduced by 10 %, and the effective Reynolds number corresponding to the flow state was reduced by 20 %. The modification of secondary flow pattern reaches the modification of main flow even though the buoyant force act on perpendicular to the main flow direction.

The influence of modification of wavy pattern on the skin frictional drag was investigated by hybrid simulation combining the PTV and DNS that satisfy the

Navier-Stokes equation and equation of continuity. The spatio-temporal velocity dataset obtained in Chapter 3 was fed as experimental data into DNS. In single phase conditions, modulation of the azimuthal wave, that is the one of the difficult subjects to observe in velocity fields obtained by DNS, was successfully reconstructed by the hybrid simulation. The torque acting on the axis, which is estimated from the energy dissipation rate, was consistent with the empirical value. In two-phase flow conditions, the modulation on azimuthal wave was diminished, and torque is reduced by 3 % comparing to that in the single phase case. The velocity fields obtained from this hybrid simulation provide the conclusion that the modification of velocity field owing to the addition of microbubbles reduces the skin frictional drag by $O(10^{-2})$ even in the tiny void fraction of $O(10^{-4})$.

The ascending motions of microbubbles near a vertical plane wall were experimentally investigated for clarifying bubble induced flow structures and bubble motions in the flows. The microbubbles with 40 μm in diameter were generated and were dispersed into stationary fluid layer from the bottom. The microbubbles generate inhomogeneous distributions of local void fraction called microbubble cloud. The simultaneous measurement of local velocity and void fraction shows their correlative relationship. The local void fraction increase at first, then the velocity increases. The wavelet coefficient of the velocity fluctuation displayed the non-periodic motion of ascending microbubble clouds as frequency modulation of cloud transit intervals. The transit interval of microbubble cloud was evaluated from the time interval of modulus maxima lines of wavelet coefficient, and its probability distribution showed the spatial development of mode of probability. The spatially developing process of microbubble cloud was quantitatively evaluated and compared in various boundary conditions of microbubble generations.

The influence of presence of microbubbles with 40 μm in diameter on spatially developing flow was investigated in a horizontal mixing layer. The intensity of background disturbance in the inlet was controlled by a flow straightener consisting of honeycombs placed upstream of the measurement section of mixing layer, straightened or turbulent flow. The velocity field of liquid phase was measured by PTV applying LIF and UVP. The motion and distribution of microbubbles were also measured by PTV applying LIF simultaneously with liquid phase velocity. The time averaged velocity

field shows that the vortex layer thickness was enlarged by the addition of microbubbles in the turbulent flows, while the vortex layer thickness of two-phase flow remains same as that of the single phase flow in the straightened flow. The Reynolds shear stress in two-phase flow increased at the initial stage of the mixing layer, while decreased in the developing stage. The correlation between fluctuations of velocity and local void fraction shows the preferential concentration of microbubbles in the upward flow of the unsteady motion in mixing layer. Further, the spectra of velocity fluctuation indicated that the addition of microbubbles reduces the power of fluctuations in the certain range of length scale. The modified length scale is comparable with the distance of local maxima of high void fraction distribution and the initial vortex layer thickness. The results obtained in this chapter can be summarized as follows: The background velocity fluctuation is an important factor for generating inhomogeneous distribution; the length scale of void distribution is comparable with initial length scale of vortex layer thickness; the distribution of microbubbles reduce the velocity fluctuation due to the enhancement of development of vortex into larger scale. Therefore the vortex layer thickness was increased by introducing microbubbles.

7.2 Organizing parameters

Since the microbubbles in flows generate preferential concentration behaving as collective, we assume local high void fraction region as a bubble. FIG. 7-1 is the schema of microbubble behavior in flows. The microbubbles preferentially distributed in flow with rising velocity generate local high void fraction with the length ℓ, and align in horizontal with the distance L. u' and α' are the fluctuation component of velocity and void fraction. The Reynolds number, which is the ratio of the inertia force to the viscous force, and Froude number, which is the ratio of the inertia force to the buoyant force, for the collective motion of microbubbles are employed as below as candidates for the index of modification of flow

$$Re_{\Lambda} = \frac{u_{rms}\ell}{\nu}, \tag{7-1}$$

$$Fr_{\Lambda} = \frac{u_{rms}}{\sqrt{\alpha_{rms} Lg}}. \tag{7-2}$$

The Reynolds number, Re_{Λ}, is the index for the bubble-bubble interaction for bubbles

rising side-by-side (aligned horizontally), i.e. bubbles yield a repulsive force at $Re < 10^1$ while an attractive force at $Re > 10^2$ [167]. The Froude number for collective motion of microbubbles, Fr_Λ, is the index for whether or not velocity fluctuations in flows modify rise motion of inhomogeneously distributed microbubbles. The characteristic length, velocity and void fraction for Re_Λ and Fr_Λ in each configuration are listed on TABLE 7-1, where TCF, BCC and HML represent Taylor–Couette flow (CHAPTER 3), bubble cloud convection (CHAPTER 5), and horizontal mixing layer (CHAPTER 6), respectively. The parameter given by Hosokawa [134]: the ratio of the bubble induced eddy viscosity, ϕ, the parameter given by Harada [179]: the ratio of the mean distance between particles to the most dominant length of disturbance in flow, H, and the cross correlation between the local void fraction and vertical velocity $\overline{\alpha' u_y'}/\alpha_{rms} u_{y,rms}$ are also listed in TABLE 7-1. The motion of microbubbles in flow unable to modify turbulent flow structure because of significant small value of $\phi \sim O(10^{-3})$. The microbubble behaves more likely to behave collective as swarm-like motion than individual as particle-like motion because of small value of $H \sim O(10^{-2})$. These parameters also support the modeling of modification of flow by the collective motion of preferentially concentrated microbubbles.

The relationship between Re_Λ and Fr_Λ is plotted on FIG. 7-2, where symbols indicate the configurations: TCF, BCC, and HML. Small arrows indicate the developing way of flows.The characteristic velocity scale in TCF is lowered because of (a) the measurement volume of UVP measuring axial velocity component near the inner cylinder wall; and (b) power of velocity fluctuation are scattered in harmonics and linear combinations of primary and modulation wave. Even for these under estimations, the data from TCF are scattered around $Fr_\Lambda^2 \sim 1$. The motion of collective behavior of microbubbles interacts with the velocity fluctuation in flow and vise versa. The preferential concentration distribution of microbubbles, therefore, is generated in the primary wave and intensifies the wave due to those ascending motion. The Froude number Fr_Λ^2 also distribute around 1 in HML. Fr_Λ^2 are higher in the turbulent flow comparing to those in he straightened. The intensity of velocity fluctuation is more interactive to generate preferential distribution of microbubbles correlative with the velocity fluctuation. The vortex layer thickness is enlarged due to the preferential distribution and motion of preferentially distributed microbubbles in the turbulent

mixing layer. The data from BCC distribute Fr_Λ^2 ~ 0.1 lower than those in TCF and HML. The buoyant force of microbubbles is much larger than the inertial force. The order of Fr_Λ^2 keeps 1 in HML and 0.1 in BCC, respectively. Hence the ratio of inertia force and buoyant force balance even the Reynolds number increase in spatially developing flows. Re_Λ increases from 5 to ~ 50 in BCC with continuous bubble generation case, while takes Re_Λ ~ 50 from the initial stage of flow developing at the pulsatile bubble generation case. The interactive force on bubbles rising up side by side yield a neutral at $Re_\Lambda \approx 50$, i.e. a repulsive at $Re_\Lambda < 1$ and a attractive at $Re_\Lambda e > 10^2$ [167]. Preferentially distributed microbubbles takes stable state with modifying those length, rising velocity, and flow field around them. According to the pulsatile generation of microbubbles, the initial disturbance of microbubble distribution leads quick convergence of the stable state preferred by microbubbles. Re_Λ also takes around 50 in TCF and BCC, the existence of microbubbles, therefore, do not make great modification of flow field unlike re-laminarization or destruction of coherent structure.

In summary, this thesis dealt with the influence of microbubbles in unsteady time depending flow in laminar-transition regions. The modification of flow field was brought by the inhomogeneous microbubble distribution correlative with velocity fluctuations introduced by the coherent vortical structures. The interaction between bubble distribution and coherent structure in shear flows changes momentum exchanges due to the dynamics of the convective term, i.e. Reynolds shear stress. The elements in velocity fluctuations are simpler and more limited in laminar-transition flow regime compared to turbulent flows, the addition of microbubbles, therefore, generate the preferential distribution in particular scale achieves the modifications of coherent structures and flow transitions.

TABLE 7-1 Characteristic scales and dimensionless quantities in each configuration

Values	TCF	BCC	HML
D_b [μm]	60	40	40
L [mm]	$\pi(R_i + R_o)/m \sim 100$	~ 20	$\delta_\omega \sim 10$
ℓ [mm]	$d\ (=R_o - R_i) = 10$	$L / 2 \sim 10$	$L / 2 \sim 5$
u_{rms} [mm/s]	$\langle u_z \rangle \sim 1$	$u_{x,rms} \sim 5$	$((u_{x,rms}^2 + u_{y,rms}^2)/2)^{1/2} \sim 5$
α_{mean} [-]	6×10^{-5}	3×10^{-3}	1×10^{-4}
α_{rms} [-]	2×10^{-5}	3×10^{-3}	1×10^{-4}
D_b / ℓ [-]	6×10^{-3}	4×10^{-3}	4×10^{-3}
u_{St} / u_{rms} [-]	0.5	0.3	0.3
$\phi\ (= u_{St} D_b / u_{rms} \ell)$ [-]	3×10^{-3}	1×10^{-3}	1×10^{-3}
$H\ (= D_b / \alpha_{mean}^{1/3} L)$	2×10^{-2}	5×10^{-2}	8×10^{-2}
$\overline{\alpha' u_y'} / \alpha_{rms} u_{y,rms}$ [-]	0.5	0.5	0.4

TCF, BCC, and HML represent Taylor–Couette flow, bubble cloud convection, and horizontal mixing layer, respectively.

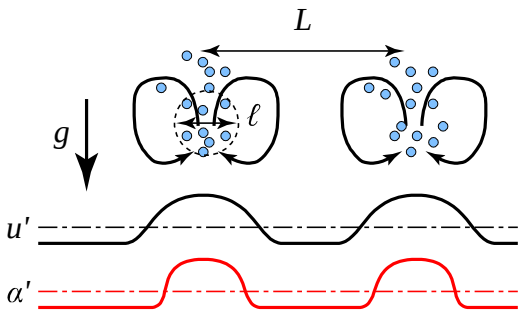


FIG. 7-1 Schematic outline of collective arrangement and motion of microbubbles

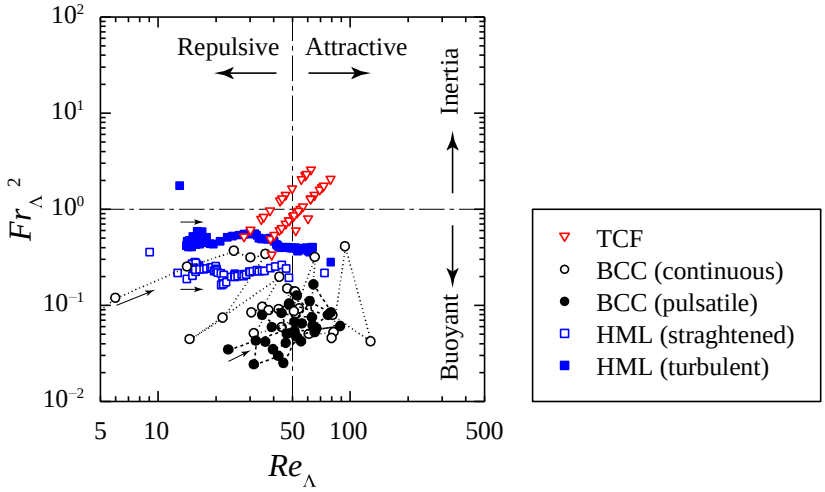


FIG. 7-2 Relationship between Reynolds number Re_Λ and Froude number Fr_Λ of collective microbubble motion

Appendix 1:
Estimation of hydrogen microbubble generation rate

Water electrolysis is a conventional method in microbubble generation as used [15] [20] [21] [22] [23] [24] [85] [86] [87] [94]. In general, the gas flow rate for hydrogen microbubble generation by water electrolysis is estimated by Faraday's law given as

$$Q = \frac{nRTI}{P}, \tag{A1-1}$$

where n, R, T, I and P are constant for gas generation: 1/2 for hydrogen bubble; 3/4 for hydrogen and oxygen bubble generation, gas constant, temperature, electric current for water electrolysis, and atomic pressure, respectively. Most of the literature does not take account the Ohmic loss [15] [20] [21] [22] [24] [85] [86] [87] [94]. Hara, *et al.*, (2011) [23] estimated the efficiency of water electrolysis as 0.8 by measuring the increase of equivalent bubble volume to compare the theoretical gas flow rate given by Eq. (A2-1). The gas flow rate of hydrogen bubble is smaller than theoretical value. The gas flow rate, however, is the same order as the theoretical estimation.

The solubility [200] [201]and diffusivity [201] of hydrogen, nitrogen, and oxygen gases in water at 20 °C and 0.1 M Pa are listed in TABLE A1-1. Decrease of the diameter of microbubble consist of air is smaller than 5 % per 100 mm when microbubble rises up in turbulent flow of water [202]. The solubility and diffusivity of hydrogen gas are same order as that of nitrogen and oxygen, the decrease of hydrogen microbubble diameter would be same order as the literature expected as smaller than 5 %. The dissolution effect on bubble diameter is neglected in this study.

TABLE A1-1 Physical properties of hydrogen, nitrogen and oxygen gases in water

Valuables	Hydrogen, H_2	Nitrogen, N_2	Oxygen, O_2
Solubility [m^3/kg]	1.8×10^{-5}	1.6×10^{-5}	3.1×10^{-5}
Diffusivity [m^2/s]	4.0×10^{-9}	1.7×10^{-9}	2.1×10^{-9}

Appendix 2:
Kinematic viscosity of silicone oil, KF96-10cs

In this section, the kinematic viscosity of the silicone-oil (Shin-etsu chemical co., KF96-10cs) used as the test fluid, ν, is measured as a function of temperature, T. Specification of the temperature depending viscosity of the test fluid in its catalogue is shown in TABLE A2-1 as the reference. The detail of temperature dependency, however, is still unclear and has large ambiguity for the determination of the critical Reynolds number for a Taylor-Couette apparatus. A capillary-type kinematic viscometer (Shibata chemical app. mfg. co., SU-78170) is used as the measurement equipment (FIG. A2-1 (a)). The time for which the level of the test fluid passes through the distance between the two marks on the capillary tube, t, is measured by a digital stopwatch in various temperature, T, kept particular values by controlling the room temperature. Temperature is also monitored by a handy-type digital thermometer. The kinematic viscosity is obtained from the following equation

$$\nu = c\,t\,, \qquad \text{(A2-1)}$$

where c is the conversion factor taking c = 0.0452 [mm^2/s^2] for this viscometer (see the specification sheet, shown in FIG. A2-1 (b)). The resolution for measuring the time, t, is 1 seconds, therefore the resolution in kinematic viscosity is $\Delta\nu$ = 0.0452 mm^2/s. The resolution for measuring the temperature by the thermometer is ΔT = 0.1 °C in this case.

FIG. A2-2 shows the relationship between the measured kinematic viscosity, ν, and temperature, T. The symbols represented ensemble averaged values of 10 runs of measurement for each temperature. The line in the figure represents the least square approximation line (ν = 14.46 − 0.2069 T). The square at the top right of the figure indicates the size of the temperature (width) and viscosity (height) resolution ($2\Delta T$ × $2\Delta\nu$). The approximation line well follows the measured points. The extrapolating value gives 9.46 mm^2/s at 25 °C. The values of kinematic viscosity determined from the measurements and its catalogue are in very good agreement, representing measured kinematic viscosity, 9.46 mm^2/s, shows 5.3 % lower value than that of catalogue value, 10 mm^2/s, at 25 °C (see TABLE A2-1).

TABLE A2-1 Kinematic viscosity of silicone-oil, FK96-10cs, in catalogue specification

Temperature, T [°C]	− 20	0	**25**	50	100
Kinematic viscosity, ν [mm^2/s (= cS)]	28	17	**10.0**	6.3	3.0

(a) (b)



FIG. A2-1 Photograph of (a) capillary-type kinematic viscometer, and (b) its specification sheet

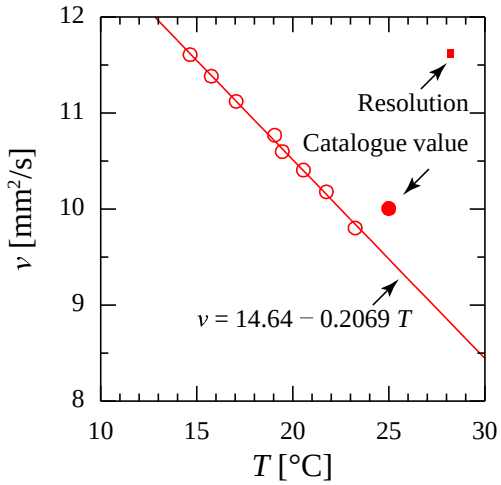


FIG. A2-2 Temperature depending kinematic viscosity of silicone-oil, KF96-10cs, measured by capillary type viscometer (open symbols), where closed symbol indicates viscosity in its catalogue, the line represents the least square approximation line, and the square at the top right of figure indicates the size of the resolution in temperature (width) and viscosity (height), respectively

Appendix 3:
Definition of variable locations in collocated and staggered grid arrangement

In this section, the conversion of the velocity defined by collocated and staggered grid arrangement is defined. In general, al three-dimensional vector has three variables for each direction, e.g. $\boldsymbol{x} = [x, y, z]$. The valuables in each component are located at the same locations. On a staggered grid arrangement, however, the scalar variables are located at the face centers of the control volume. The variables describing a scalar distribution, e.g. pressure, are located at the body centers of the control volume. FIG. A3-1 shows the velocity vector component for a collocated and staggered grid arrangement on a control volume. The x, y, and z are the axes. Δx, Δy, and Δz are the spatial resolutions in each direction. u, v, and w are the velocity components in the x, y, and z axes, respectively. p is the pressure. Suffixes i, j, and k are the designations of x, y, and z, respectively. Superscripts c and s note variables in collocated and staggered grid arrangement.

The conversions of variable between the collocated and staggered grid arrangement are given as following equations,

$$\begin{cases} u^s_{i,j,k} = \dfrac{1}{4}\left(u^c_{i,j,k} + u^c_{i,j+1,k} + u^c_{i,j,k+1} + u^c_{i,j+1,k+1}\right) \\ u^s_{i,j,k} = \dfrac{1}{4}\left(v^c_{i,j,k} + v^c_{i+1,j,k} + v^c_{i,j,k+1} + v^c_{i+1,j,k+1}\right) \\ u^s_{i,j,k} = \dfrac{1}{4}\left(w^c_{i,j,k} + w^c_{i+1,j,k} + w^c_{i,j+1,k} + w^c_{i+1,j+1,k}\right) \end{cases}, \tag{A3-1}$$

$$\begin{cases} u^c_{i,j,k} = \dfrac{1}{4}\left(u^s_{i,j,k} + u^s_{i,j-1,k} + u^s_{i,j,k-1} + u^s_{i,j-1,k-1}\right) \\ u^c_{i,j,k} = \dfrac{1}{4}\left(v^s_{i,j,k} + v^s_{i-1,j,k} + v^s_{i,j,k-1} + v^s_{i-1,j,k-1}\right) \\ u^c_{i,j,k} = \dfrac{1}{4}\left(w^s_{i,j,k} + w^s_{i-1,j,k} + w^s_{i,j-1,k} + w^s_{i-1,j-1,k}\right) \end{cases}. \tag{A3-2}$$

Divergence is described as

$$div. = \frac{\partial u}{\partial x} + \frac{\partial v}{\partial y} + \frac{\partial w}{\partial z}. \tag{A3-3}$$

The discretized divergence of the control volume, $D_{i,j,k}$, which is located at the same location as the pressure in FIG. A3-1, is given as

$$D_{i,j,k} = \frac{u^s_{i+1,j,k} - u^s_{i,j,k}}{\Delta x} + \frac{v^s_{i,j+1,k} - v^s_{i,j,k}}{\Delta y} + \frac{w^s_{i,j,k+1} - w^s_{i,j,k}}{\Delta z}. \qquad \text{(A2-4)}$$

FIG. A3-2 shows the divergence of the divergence in the iteration process of VCP [74] which is one of the post-processing for PIV data. In the visualization of three-dimensional velocity vector field using color PTV in CHAPTER 2 and hybrid analysis combining PTV and HSMAC method in CHAPTER 4, the conversions of velocity data between collocated and staggered grid arrangement are followed these manners.

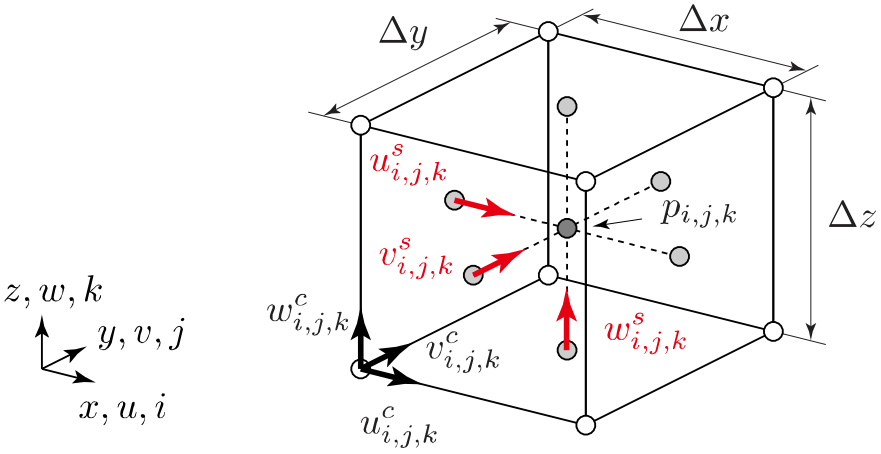


FIG. A3-1 Definition of variable location in collocated and staggered arrangements

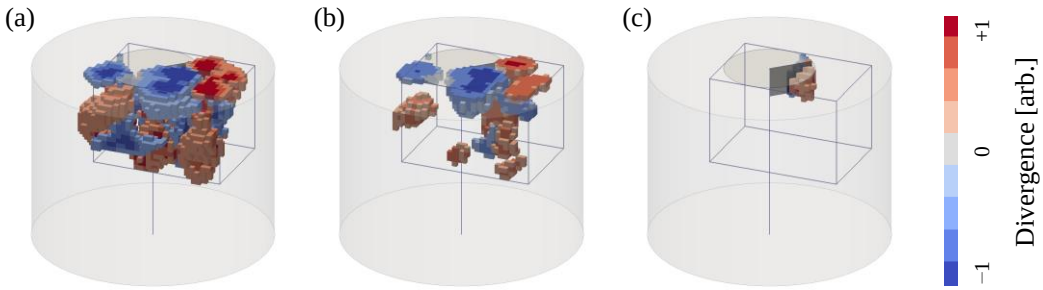


FIG. A3-2 Distribution of divergence (a) before, (b) after 5 and (c) 100 iterations of VCP treatment

Appendix 4:
Derivation of the Kolmogorov length scale in a Taylor-Couette flow

In Taylor-Couette flow systems having a rotating inner cylinder and a fixed outer one, the empirical relation of the dimensionless torque, G, as a function of the Reynolds number, Re, is given by Wendt [124] as

$$G=\frac{T}{\rho\nu^2 h}=\begin{cases}4\pi\dfrac{\eta}{(1+\eta)(1-\eta)^2}Re & \left(\text{for } Re<Re_c\right)\\ 1.45\dfrac{\eta^{\frac{3}{2}}}{(1-\eta)^{\frac{7}{4}}}Re^{1.5} & \left(\text{for } 4\times10^2<Re<10^4\right),\\ 0.23\dfrac{\eta^{\frac{3}{2}}}{(1-\eta)^{\frac{7}{4}}}Re^{1.7} & \left(\text{for } 10^4<Re<10^5\right)\end{cases} \qquad \text{(A3-1)}$$

where T, ρ, ν, h ,η, and Re_c are the torque acting on the inner axis, the density and kinematic viscosity of the test fluid, height of the cylinders, the radius ratio of the cylinders, and the critical Reynolds number for the onset of instability, respectively. Herein, the Reynolds number, Re, and the radius ratio, η, are defined as in bellows.

$$Re=\frac{U_{wall}d}{\nu}, \qquad \text{(A4-2)}$$

$$\eta=\frac{R_i}{R_o}, \qquad \text{(A4-3)}$$

where U_{wall}, R_i, R_o, and d are the velocity of the inner cylinder wall surface, inner and outer cylinder radii, and the gap distance, d (= R_o − R_i), respectively. The torque acting on the inner cylinder is related to the spatio-temporal averaged energy dissipation rate, $\langle\bar{\varepsilon}\rangle$, as follows

$$\langle\bar{\varepsilon}\rangle=\frac{TU_{wall}}{\pi\rho\left(R_o^{\,2}-R_i^{\,2}\right)h}. \qquad \text{(A4-4)}$$

The energy dissipation, $\langle\bar{\varepsilon}\rangle$ is also related to the Kolmogorov length scale, ℓ, with the relationship given as

$$\left\langle \bar{\varepsilon} \right\rangle = \frac{\nu^3}{\ell^4}. \qquad \text{(A4-5)}$$

Substituting Eq. (A3-1), (A3-4), and (A4-5), for Re 4×10^2, the Kolmogorov length scale normalized by the gap distance, ℓ / d, is given as

$$\frac{\ell}{d} = \begin{cases} \left[\dfrac{\pi\left(R_o + R_i\right)}{1.45{R_o}^2} \dfrac{\left(1-\eta\right)^{-\frac{1}{4}}}{\eta^{\frac{3}{2}}} \right]^{\frac{1}{4}} Re^{-\frac{5}{8}} & \left(\text{for } 4\times10^2 < Re < 10^4\right) \\ \left[\dfrac{\pi\left(R_o + R_i\right)}{0.23{R_o}^2} \dfrac{\left(1-\eta\right)^{-\frac{1}{4}}}{\eta^{\frac{3}{2}}} \right]^{\frac{1}{4}} Re^{-\frac{2.7}{4}} & \left(\text{for } 10^4 < Re < 10^5\right) \end{cases}. \qquad \text{(A4-6)}$$

FIG. A4-1 shows the relationship between the normalized Kolmogorov length and Reynolds number for a Taylor-Couette configuration for the radius ratio η = 0.905. Solid and dotted lines are for $4 \times 10^2 < Re < 10^4$ and $10^4 < Re < 10^5$, respectively. The Kolmogorov length scale monotonically decreases with increasing the Reynolds number, e.g. ℓ / d takes 0.07 and 0.04 at Re = 400 and 1200 (Re / Re_c = 3 and 9).

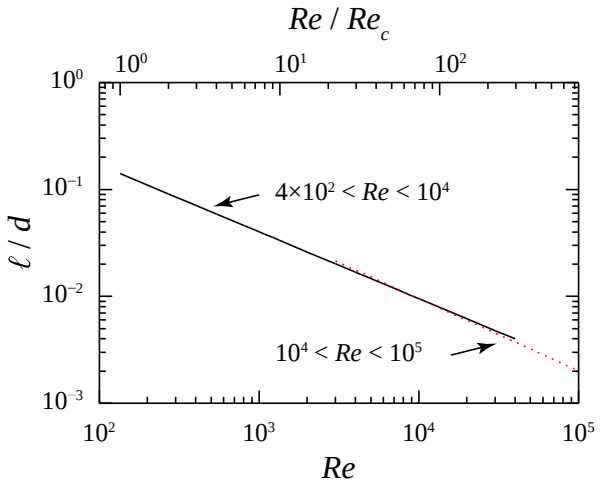


FIG. A4-1 Normalized Kolmogorv length scale, ℓ / d for the radius ratio η = 0.905, where d is the gap distance between the inner and outer cylinders. Re_c is the critical Reynolds number for the onset instability taking Re_c = 134 in this radius ratio.

Appendix 5:
Oscillation frequency of a deformable bubble

Oscillations of a bubble are classified into some modes as shown in FIG. A5-1. This section handles the oscillatory motion of a bubble which consists of compressible gas in incompressible viscous liquid. The density and viscosity of the gas are small enough to be neglected. Mode 0 of the bubble oscillation shows expansion and contraction of volume of the bubble. Mode 1 shows parallel translation of bubble center in direction of π rad without changes of shape and volume of the bubble. In $n \geq 2$ of mode n, a bubble surface deforms in 2π / n rad of expansion and contraction. The center of mass of bubble is steady, and the volume of a bubble is kept constant.

The bubble radius, R, having initial radius of R_0 (= D / 2) obeys following Reyleigh-Plesseet equation [203] as

$$R\frac{\partial^2 R}{\partial t^2}+\frac{3}{2}\left(\frac{\partial R}{\partial t}\right)^2=\frac{1}{\rho}\left[p_G\left(\frac{R_0}{R}\right)^{3\gamma}-p_\infty-\frac{2\sigma}{R}-\frac{4\mu}{R}\frac{\partial R}{\partial t}\right], \tag{A5-1}$$

where t, ρ, p_G, p_∞, γ, σ, and μ are time, the density of the liquid phase, pressure inside of the bubble, pressure in the liquid at a large distance from the bubble, specific heat ratio of the gas inside of the bubble, surface tension, and viscosity of the liquid phase, respectively. Pressure inside the bubble, p_G, is given as

$$p_G=P_\infty+\frac{2\sigma}{R_0}. \tag{A5-2}$$

Eq. (A5-1) yield the frequency of mode 0 as

$$f_0=\frac{1}{2\pi R_0}\sqrt{\frac{1}{\rho}\left(3\gamma p_G-\frac{2\sigma}{R_0}\right)-\left(\frac{2\mu}{\rho R_0}\right)^2}. \tag{A5-3}$$

If the surface tension and viscosity of the liquid phase are neglected, Eq. (A5-3) coincide with the result of obtained by Minnaert (1993) [204] as

$$f_0=\frac{1}{2\pi R_0}\sqrt{\frac{3\gamma p_G}{\rho}}. \tag{A5-4}$$

The eigen frequency of mode n with surface deformations in the radial direction

given by Plesset & Prosperetti (1997) [203] is expressed as

$$f_n = \frac{1}{2\pi R_0}\sqrt{\frac{(n^2-1)(n+2)\sigma}{\rho R_0}}. \qquad \text{(A5-5)}$$

We note that the mode 1 does not shows oscillation but translation in the motion. Eq. (A5-5), therefore, is applicable in $n \geq 2$ of oscillation mode n. In FIG. A5-2, the oscillation frequencies of a hydrogen bubble in water are displayed as a function of bubble diameter, D. The gradient of mode 0 frequency follows $f_0 \sim D^{-1}$, while that of the others' frequency follows $f_n \sim D^{-3/2}$. Microbubbles with diameter of O(10 μm) have eigen frequencies of less than f = 1 MHz, translation of ultrasound in UVP with MHz frequency, therefore, thought not to affect on oscillations of bubbles in diameter of O(10 μm).

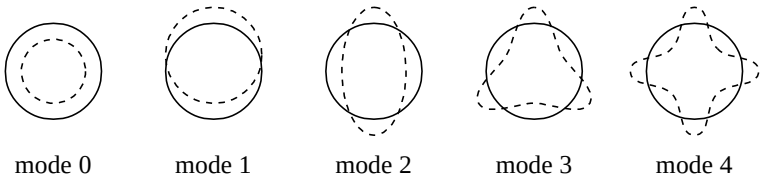


FIG. A5-1 Oscillations mode of bubbles

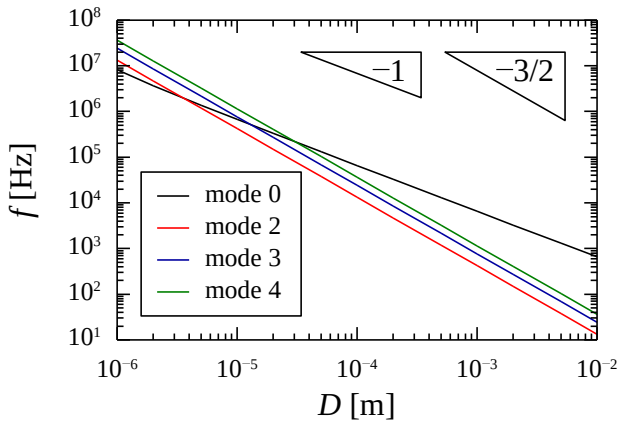


FIG. A5-2 Eigen frequency of bubbles in oscillations, where the hypotenuse of the triangles placed upper right of figure indicate the gradient of −1 and −3/2, color of lines indicate f_0 (mode 0, black), f_2 (mode 2, red) , f_3 (mode 3, blue) , f_4 (mode 4, green), respectively

Appendix 6:
Validation of PIV/PTV performance

In this chapter, the performace of particle image velocimetry (PIV) and particle tracking velocimatry (PTV) are varidated by using PIV standared images [205]. PIV/PTV programs are written in c language, are compiled by microsoft visual studio 2010, and are excuted on window 7 OS. FIG. A6-1 shows (a) a snapshot and (b) particle pathline generated by 4 images in time seriese of "PIVstandard image 01". The images consist of 256 × 256 pixels of 8 bit data for the blightness. 4000 of particle are inuclded, the maximum and mean particle displacement between the images are 15 pixel/frame and 7.5 pixel/frame, respectively. The details are described in [205]. FIG. A6-1 (c) shows the particle position extracted by particle mask correlation (PMC) [95] in images, where the color indicates the order in the images (1st: black, 2nd: red, 3rd: blue, 4th: green). The streaming pattern of particle trajectories in FIG. A6-1 (c) is in good agreement with particle pathline shown in FIG. A6-1 (b). This particle positions are used in PTV conducted in this chpter. FIG. A6-2 shows the displacement vector obtained by (a) direct cross-correlation PIV, (b) binary image cross-correlation PTV, (c) tripple pattern matching PTV, and (d) four-time-step PTV, respetively. The side length of the search window in PIV takes N_s = 33 pixel, and the search radius in PTV takes R_s = 16 pixel. So that the maximum values of the displacement vector takes 16 pixel. Other paramter of PIV/PTV are listed in TABLE A6-1. The erronuous vectors appear in the all results, any post processing for removeing erronuous vectors, however, dose not treated for the comfirmation of the performaces in each PIV/PTV algorithm. The flow patterns are in good agreement with the literatures [71] [205] and that indicated by the particle pathline an trajectiries shown in FIG. A6-1 (b) and (c). The maximum and mean paritcle displacement are about 15.5 pixel/frame and 7.3 pixel/frame, in the palgorithms. For these reasons, the PIV/PTV programes are acceptable to be used.

The processing times of PIV/PTV are also investigated in this section. The clock frequency of central conputin unit (CPU) has already reached plateu at 3 GHz in 2005. The computational performance still being improved by employing multiple core processor core in on a CPU die [206]. In order to use the maximum computational

reasources, the PIV/PTV programes were tuned for parallel processing in multi-core CPU or for general-purpose computing on graphics processing units (GPGPU) utilizing graphic processing unit (GPU) as well as a way for accelaration of CFD [207]. OpenMP and the compiler optimization of visual studio 2010 were used for multi-core processing in CUP. Compute unified device architecture (CUDA) was used for the GPU platform. The processing performace were evaluated in several comuting environments using different CUPs and GPUs as listed in following TABLE A6-2. The default of parameters of direct cross-correlation PIV are: the number of vector n_v = 961, the side length of interrogation window N_i = 33, and the side length of search region N_s = 33, respectively. When one parameter is varied, other two parameters are fixed in the default values. In the parallel processing using GPU, two different type of processing (type A and B) are tested to be compared. In type A, each thread of GPU calculate each cross-correlation coefficient, while in type B, each thread of GPU calculate a set of cross-correlation coefficient for each vector. FIG. A6-3 shows the processing time on different CPUs and GPUs as a function of the PIV parameter, n_v, N_i, and N_s, where "opt." corresponds the optimization for parallel processing using OpenMP and compiler optimization of visual studio 2010. The slope of the triangle in the figures indicates the expected gradient of the processing time. The optimization of the PIV using CUP reduces the processing time in all the cases. The reduction of the processing time of PIV using GPU depends on the algorithm for the parallel processing. The processing time using GPU, however, is reduced comparing to that using single core of CPU, neither parallel processing nor optimization of CPU. The processing time of four-time-step PTV and PMC are also investigated on different CPUs and GPUs. FIG. A6-4 shows the processing time of (a) four-time-step PTV as a function of the mean number of particle in the images and (b) PMC as a function of the side length of the mask window, N_m, respectively. A 8 bit image in 1280 × 1024 pixel of sizes are used for the investigation of PMC performance. GPUs can calculate branching (e.g. if-then-else), but usually with a performance penalty. Many if-then-else statements are used for particle matching in the algorithm of the four-time-step PTV. Therefore, the processing time is not successfully reduced by using GPU. The processing time of the PMC, on the other hand, is significantly reduced by using GPU, because PMC code less includes branching segmentations.

TABLE A6-1 Parameters for PIV/PTV

Parameter	Value
Direct corss-correlation PIV	
Side length of search window	33 [pixel]
Side length of intterogation window	33 [pixel]
Number of vectors	961 (= 31 × 31)
Binary image corss-correlation PTV	
Radius of search area	16 [pixel]
Side length of intterogation window	33 [pixel]
Triple pattern matching PTV	
Radius of 1st search area	16 [pixel]
Radius of 2nd search area	8 [pixel]
Side length of intterogation window	33 [pixel]
Angle of vectors in frams	15 [deg.]
Four-time-step PTV	
Radius of 1st search area	16 [pixel]
Radius of 2nd and 3rd search area	8 [pixel]
Angle of vectors in frams	15 [deg.]

TABLE A6-2 Specification list of processing units

Processor name	Processor type	Clock freq. [GHz]	Number of core
Core i5 750	CPU	2.7	4
Core i5 3317U	CPU	1.7	4
Core i7 2600K	CPU	3.7	8
Core i7 3960X	CPU	3.3	12
GTX 550 Ti	GPU	1.8	192
GTX 580	GPU	1.5	512

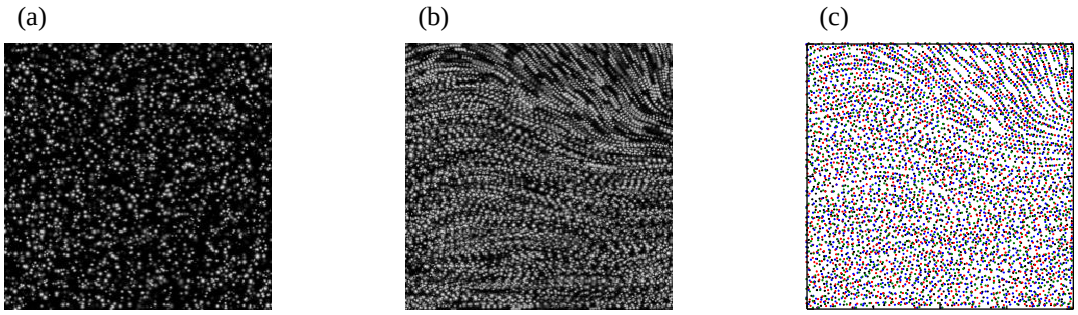


FIG. A6-1 (a) Snapshot, (b) particle pathline, and (c) particle position extracted from PIV standard image 01 by particle mask correlation (PMC), where color of particle represent order in the images (1st: black, 2nd: red, 3rd: blue, 4th: green)

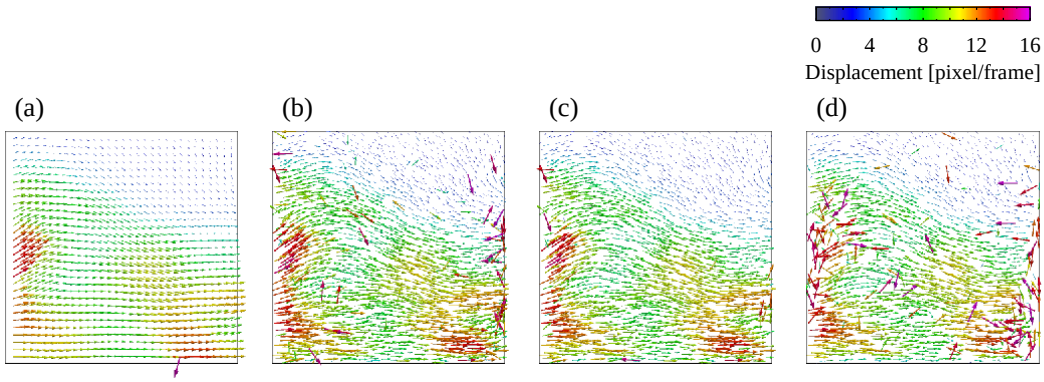


FIG. A6-2 Particle displacement vectors obtained by (a) direct cross-correlation PIV, (b) binary image cross-correlation PTV, (c) triple pattern matching PTV, and (c) four-time-steps PTV, respectively

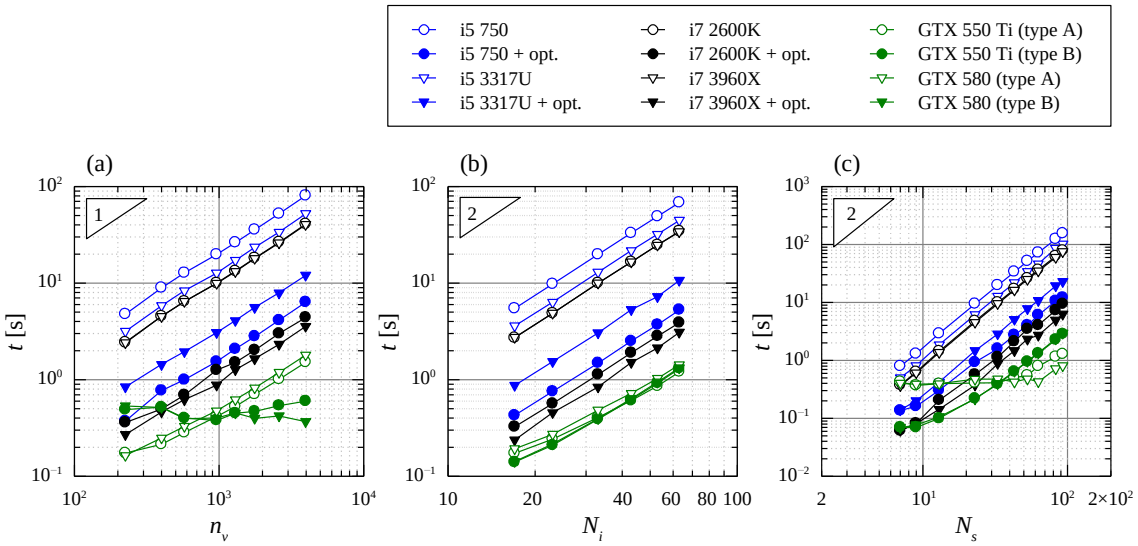


FIG. A6-3 Processing time, t, of direct cross-correlation PIV as a function of (a) number of vectors, n_v, (b) side length of interrogation window, N_i, and (c) side length of search window, N_s

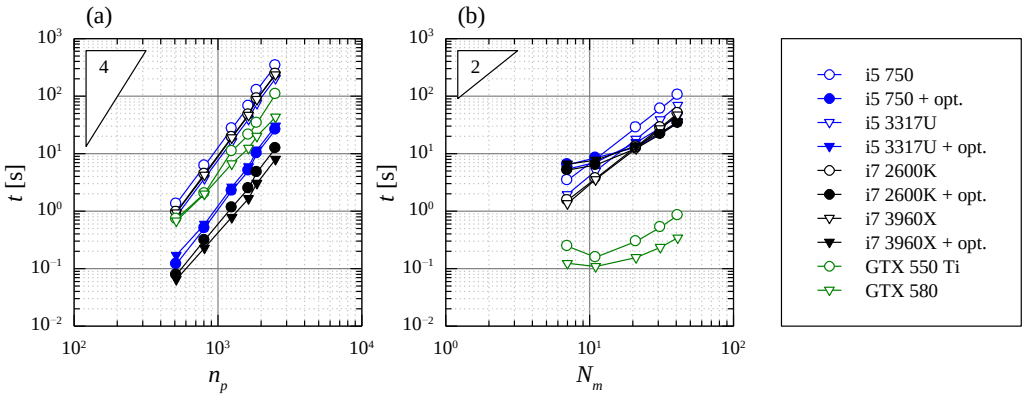


FIG. A6-4 Processing time, t, of (a) four-time-steps PTV as a function of mean number of particles in images, n_p, and (b) particle mask correlation as a function of side length of mask window, N_m

References

[1] Corbett, J., J., Koehler, H. W., "Updated emissions from ocean shipping", *J. Geo. Res.* **108** (2003), 4650-4664.

[2] Kim, J., "Physics and control of wall turbulence for drag reduction", *Phil. Trans. R. Soc. A* **369** (2011), 1396-1411.

[3] Gad-el-Hak, M.,"Modern Developments in Flow Control", *App. Mech. Rev.* **49** (1996), 365-379.

[4] Bushnell, D. M., McGinley, C. B., "Turbulence control in wall flows", *Annu. Rev. Fluid Mech.* **21** (1989), 81–96.

[5] Bushnell, D., M., Moore, K. J., "Drag reduction in nature", *Annu. Rev. Fluid Mech.* **23** (1991), 65–79.

[6] Yabe, A., Mori, Y., Hijikata, K., "Active heat transfer enhancement by utilizing electric fields", *Annu. Rev. Heat Transfer* **7** (1996), 1–55.

[7] McManus, K. R., Poinsot, T., Candel, S. M., "A review of active control of combustion instabilities", *Prog. Energy Combus. Sci.* **19** (1993), 1–29.

[8] Ho, C. M., Huerre, P., "Perturbed free shear layers", *Annu. Rev. Fluid Mech.* **16** (1984), 365–424.

[9] Reynolds, W. C., Parekh, D. E., Juvet, P. J. D., Lee, M. J. D., "Bifurcating and blooming jets", *Annu. Rev. Fluid Mech.* 35 (2003), 295–315.

[10] Choi, H., Jeon, W. P., Kim, J., "Control of flow over a bluff body", *Annu. Rev. Fluid Mech.* **40** (2008), 113–139.

[11] Lumley, J., Blossey, P., "Control of turbulence", *Annu. Rev. Fluid Mech.* **30** (1998) 311–327.

[12] Zakin, J. L., Lu, B., Bewersdorff, H. V., "Surfactant drag reduction", *Rev. Chem. Eng.* **14** (1998), 255–320.

[13] Kasagi, N., Suzuki, Y., Fukagata, K., "Microelectromechanical systems-based feedback control of turbulence for skin friction reduction", *Annu. Rev. Fluid Mech.* **41** (2009), 231-251.

[14] Cessio, S. L., "Frictional Drag reduction of external flow with bubble and gas injection", *Annu. Rev. Fluid Mech.* **42** (2010), 183–203.

[15] McCormick, M. E., Bhattacharyya, R., "Drag reduction of a submersible hull by electrolysis", *Nav. Eng. J.* **85** (1973), 11-16.

[16] Sanders, W. C., Winkel, E. S., Dowing, D. R., Perlin, M., Cessio, S. L., "Bubble friction drag reduction in a high-Reynolds number flat plate turbulent boundary layer", *J. Fluid Mech.* **552** (2006), 353-380.

[17] Elbing, B. R., Winkel, E. S., Lay, K A., Cessio, S. L., Dowing, D. R., Perlin, M., "Bubble-induced skin-friction drag reduction and abrupt transition to air-layer drag reduction", *J. Fluid Mech.* **612** (2008), 201-223.

[18] Shen, X., Ceccio, S. L., Perlin, M., "Influence of bubble size on micro-bubble drag recution", *Exp. Fluids* **41** (2006), 415-424.

[19] Murai, Y., Oishi, Y., Sasaki, T., Kodama, T., Yamamoto, F., "Turbulent shear stress profile in horizontal bubbly channel flow", *Proc. 6th Int. Symp. Smart Control of Turbulence*, Tokyo (2005), 289-295.

[20] Hassan, Y. A., Gutierrez-Torres, C. C., Jimenez-Bernal, J. A., "Temporal correlation modification by microbubbles injection in a channel flow", *Int. Commun. Heat Mass Transf.* **32** (2005), 1009–1015.

[21] Murai, Y., Oishi, Y., Takeda, Y., Yamamoto, F., "Turbulent shear stress profiling in a bubbly channel flow assessed by particle tracking velocimetry", *Exp. Fluids* **41** (2006), 343-352.

[22] Ortiz-Villafuerte, J., Hassan, Y. A., "Investigation of Microbubble Boundary Layer Using Particle Tracking Velocimetry", *J. Fluid Eng.* **128** (2005), 507519.

[23] Hara, K., Suzuki, T., Yamamoto, F., "Image analysis applied to study on frictional-drag reduction by electrolytic microbubbles in a turbulent channel flow", *Exp. Fluids* **50** (2011), 715-727.

[24] Jacob, B., Olivieri, A., Miozzi, M., Campana, E. F., Piva, R., "Drag reduction by microbubbles in a turbulent boundary layer", *Phys. Fluids* **22** (2010), 115104.

[25] Legner, H. H., "A simple model for gas bubble drag reduction", *Phys. Fluids* **27** (1984), 2788-2790.

[26] Taylor, G. I., "The viscosity of a fluid containing small drops of another fluid", *Proc. R. Soc. London Ser A* **146** (1932), 41-48.

[27] Batchelor, G. K., "An introduction to fluid dyanamics", Cambridge University Press, Cambridge (1967).

[28] L'vov, V. S., Pomyalov, A., Procaccoia, I., Tiberkevich, V., "Drag Reduction by Microbubbles in Turbulent Flows: The Limit of Minute Bubbles", *Phys. Rev. Lett.* **94** (2005) 174502.

[29] Schlichting, H. "Boundary layer theory", *New York Press* (1979), 102-107.

[30] Dean, R. B., "Reynolds Number Dependence of Skin Friction and Other Bulk Flow Variables in Two-Dimensional Rectangular Duct Flow", *J. Fluid Eng.* **100** (1978) 215-225.

[31] Ferrante, A., Elghobashi, S., "On the physical mechanisms of drag reduction in a spatially developing turbulent boundary layer laden with microbubbles", *J. Fluid Mech.* **503** (2004), 345-355.

[32] Ferrante, A., Elghobashi, S., "Reynolds number effect on drag reduction in a microbubble-laden spatially developing turbulent boundary layer", *J. Fluid Mech.* **543** (2005), 93-106.

[33] Ferrante, A., Elghobashi, S. E., "A robust method for generating inflow conditions for direct simulations of spatially-developing turbulent boundary layers", *J. Comp. Phys.* **198** (2004), 72-387.

[34] Madavan, N. K., Deutsch, S., Merkle, C. L., "Measurement of local skin friction in a microbubble-modified turbulent boundary layer", *J. Fluid Mech.* **156** (1985), 237-256.

[35] Kodama, Y., Kakukawa, A., Takahashi, T., Kawashima, H., "Experimental study on miceobubble ans their applicability to ships for skin friction reduction", Int. J Heat Fluid Flow 21 (2000), 582-588.

[36] Serizawa, A., Inui, T., Eguchi, T., "Flow characteristics and Pseudo-Laminarization of Vertically Up-ward Air-Water Milky Bubbly Flow with Micro Bubble in a Pipe", *Konsoryu, J. Japan Soc. Multiphase Flow (in Japanese)* **19** (2005), 335-343.

[37] Adrian, R. J., "Particle-image techniques for experiment fluid mechanics", *Ann. Rev. Fluid Mech.* **23** (1991), 261-304.

[38] Adrian, R. J., "Twenty years of particle image velocimetry", *Exp. Fluids* **39** (2005) 159-169.

[39] Nedderman, R. M., "The use of stereoscopic photography for the measurement of velocities in liquids", *Chemical Eng. Sci.* **16** (1961), 113-119.

[40] Mass, H. G., Grunen, A., Papantoniou, D., "Particle tracking velocimetry in three-dimensional flows, Part I: Photogrammetric determination of particle coordinates" *Exp. Fluids* **15** (1993), 133-146.

[41] Malik,N. A., Dracos, Th., Papantoniou, D. A., "Particle tracking velocimetry in three-dimensional flows, Part II: Particle tracking", *Exp. Fluids* **15** (1993), 279-294.

[42] Arroyo, M. P., Greated, C. A., "Stereoscopic particle image velocimetry" *Measurement Sci. Technol.* **2** (1991), 1181-1186.

[43] Brücker, C., Althaus, W., "Study of vortex breakdown by particle tracking velocimentry (PTV), Part 1: Bubble-type vortex breakdown", *Exp. Fluids* **13** (1992), 339-349.

[44] Hori, T., Sakakibara, J., "High Speed Scanning Stereoscopic PIV for 3D Vorticity Measurement in Liquids", Measurement Science and Technology, **15** (2004), 1067-1078.

[45] Meng, H., Hussain, F., "Holographic particle velocimetry: A 3D measurement technique for vortex interactions, coherent structure", *Fluid Dynamics Research* **8** (1991), 33-52.

[46] Stolz, W., Köhler, J., "In-plane determination of 3D-velocity vectors using particle tracking anemometry (PTA)", *Exp. Fluids* **17** (1994), 105-109.

[47] Willert, C. E., Gharib, M., "Three-dimensional particle imaging with a single camera", *Exp. Fluids* **12** (1992), 353-358.

[48] Cierpka, C., Segura, R., Hain, R., Kahler, C. J., "A simple single camera 3C3D velocity measurement technique without errors due to depth of correlation and spatial averaging for microfluids", *Measurement Sci. Technol.* **21** (2010),

045401.

[49] Elsinga,G. E., Scarano, F., Wieneke, B., van Oudheusden, B. W., "Tomographic particle image velocimetry", *Exp. Fluids* **41** (2006), 933-947.

[50] Casey, T.A., Sakakibara, J., Thoroddsen, S. T., "Scanning tomographic particle image velocimetry applied to a turbulent jet", *Phys. of Fluids* **25** (2013), 025102.

[51] Cenedess, A., Paglialunga, A., "A new technique for the determination of the third velocity component with PIV", *Exp. Fluids* **8** (1989), 228-230.

[52] Kimura, I., Kohno, Y., Ogasawara, T., Takamori, T., "Measurement of Three Dimensional Velocity Vectors in a Flow Field Using a Color Spectrum", *Trans. Society Instrument and Control Eng.*, **27** (1991), 755-761 (in Japanese).

[53] Brücker, Ch., "3-D PIV via spatial correlation in a color-coded light-sheet", *Exp. Fluids* **21** (1996), 312-314.

[54] Kähler, C. J., Kompenhans, J., "Fundamentals of multiple plane stereo particle image velocimetry", *Exp. Fluids* **29** (2000), S70-S77.

[55] Hirahara, H., Kawahashi, M., Kadono, H., "A new technique of three-dimensional particle image detection by using color encoded illumination system", *Proc. ASME FEDSM'00 (ASME 2000 Fluids Engineering Division Summer Meeting June 11-15, 2000, Boston, Massachusetts),* Paper ID FEDSM2000-11097 (2000), 1-5.

[56] Ido, T., Shimizu, H., Nakajima, Y., Ishikawa, M., Murai, Y., Yamamoto, F., "Single-camera 3-D particle tracking velocimetry using liquid crystal image projector", *Proc. ASME/JSME Joint Fluids Eng. Conf.* (2003), 2 C, 2257-2263.

[57] Iio, S., Tasaka, H., "Examination of Air Flow Velocity Measurement by Three-Dimensional PTV Using a Color Layer", *J. Visualization Society of Japan* **24** (2004), 43-48 (*in Japanese*).

[58] Prenel,J. P., Bailly,Y., "Recent evolution of imagery in fluid mechanics: From standard tomographic visualization to 3D volumic velocimetry", *Optics and Lasers in Eng.* **44** (2006), 321-334.

[59] McGregor, T. J., Spence, D. J., Coutts, D. W., "Laser-based volumetric colour-coded three-dimensional particle velocimetry", *Optics and Lasers in Eng.* **45** (2007), 882-889.

[60] Pick, S., Lehmann, F-O., "Stereoscopic PIV on multiple color-coded light sheets and its application to axial flow in flapping robotic insect wings", *Exp. Fluds* **47** (2009), 1009-1023.

[61] Ruck, B. "Colour-coded tomography in fluid mechanics", *Optics and Lasers Tech.* **43** (2011), 375-380.

[62] Munsell, A. H., "A Color Notation. 7 th Ed.", Munsell Color (1926).

[63] Munsell, A. H., "Book of color. Pocket Ed.", Munsell Color (1965).

[64] Economikos, L., Shoemarker, C., Russ, E., Brodkey, R. S., "Toward Full-Field Measurement of Instantaneous Visualization of Coherent Structures in Turbulent

Shear Flows", *Exp. Therm. Fluid Sci.* **3** (1990), 74-86.

[65] Bendicks, C., Tarlet, D., Roloff, C., Bordás, R., Wunderlich, W., Michaelis, B., Thévenin, R., "Improved 3-D Particle Tracking Velocimetry with Colored Particles", *J. Signal and Info. Process.* **2** (2011), 59-71.

[66] Smith, A. R., "Color gamut transform pairs", *SIGGRAPH '78 Proceedings of the 5th ann. Conf. on Computer graphics and interactive tech.* (1978), 12-19.

[67] Joblove, G. H., Greenberg, D., "Color spaces for computer graphics", *SIGGRAPH '78 Proc. the 5th Ann. Conf. on Computer graphics and interactive tech.* (1978), 20-25.

[68] Kimura, I., Takamori, T., Ozawa, M., Takenaka, N., Manabe, Y., "Quantitative thermal flow visualization using color image process (application to a natural convection visualized by liquid crystals) ", *Flow visualization, ASME-FED (ed. Khalighi B, Brown M J, Foreitas C J)* **85** (1989), 261-269.

[69] Mahan, R. P., "Circular statistical methods: Applications in spatial and temporal performance analysis", *US Army Res. Inst., Spec. Rep. 16*, (1991).

[70] Fisher, N. I. "Statistical Analysis of Circular Data", *Cambridge University Press*, (1993).

[71] Visualization Society of Japan, "Handbook of Particle Image Velocimetry", *Morikita Publishing* (2002), (*in Japanese*).

[72] Mezaki, R., Mochizuki, M., Ogawa, K., "Engineering data on mixing", *Elsevier* (2000).

[73] Alvarez, M. M., Zalc, J. M., Shinbrot, T., Arratia, P. E., Mussio, F. J., "Mechanism of mixing and creation of structure in laminar stirred tanks", *AIChE J.* **48** (2002), 2135-2148.

[74] Ido, T., Murai, Y., Yamamoto, F., "Postprocessing algorithm for particle-tracking velocimetry based on ellipsoidal equations", *Exp. Fluids* **32** (2002), 326-336.

[75] Van't Riet, K., Smith, J. M., "The trailing vortex system produced by rushton turbine agitators", *Chem. Eng. Sci.* **30** (1975), 1093-1105.

[76] Schäfer, M., Yianneskis, M., Wächer, P., Durst, F., "Trailing vortices around a 45° pitched-blade impeller", *AIChE J.* **44** (1998), 1233-1246.

[77] Bernard, P. S., Thomas, J. M., Handler, R. A., "Vortex dynamics and the production of Reynolds stress", *J. Fluid Mech.* **253** (1993), 385-419.

[78] Porter, D. H., Pouquest, A., Woodward, P. R., "Kolmogorov-like spectra in decaying three-dimensional supersonic flows", *Phys. Fluids* **6** (1994), 2133-2141.

[79] Tanaka, M., Kida, S., "Characterization of vortex tube and sheets", *Phys. Fluids A* **5** (1993), 2079-2082.

[80] Murai, Y., Nakada, T., Suzuki, T., Yamamoto, F., "Particle tracking velocimetry applied to estimate the pressure field around a Savonius turbine", *Measurement*

Sci. Technol. **18** (2007), 2491-2503.

[81] Broder, D., and M. Sommerfeld. "An advanced LIF-PLV system for analysing the hydrodynamics in a laboratory bubble column at higher void fractions", *Exp. Fluids* **33** (2002), 826-837.

[82] Lindken, R., and W. Merzkirch. "A novel PIV technique for measurements in multiphase flows and its application to two-phase bubbly flows", *Exp. Fluids* **33** (2002), 814-825.

[83] Khalitov, D. A. and Longmire, E. K. "Simultaneous two-phase PIV by two-parameter phase discrimination", *Exp. Fluids* **32** (2002), 252-268.

[84] Fujiwara, A., Danmoto, Y., Hishida, K., Maeda, M., "Bubble deformation and flow structure measured by double shadow images and PIV/LIF", *Exp. Fluids* **36** (2004), 157-165.

[85] Kitagawa, A., Hishida, K., Kodama, Y., "Flow structure of microbubble-laden turbulent channel flow measured by PIV combined with the shadow image technique", *Exp. Fluids* **38** (2005), 466-475.

[86] Kitagawa, A., Hagiwara, Y., Kouda, T., "PTV investigation of phase interaction in dispersed liquid-liquid two-phase turbulent swirling flow", *Exp. Fluids* **42** (2007), 871-880.

[87] Kitagawa, A., Kosuge, K., Uchida, K., Hagiwara, Y., "Heat transfer enhancement for laminar natural convection along a vertical plate due to sub-millimeter-bubble injection", *Exp. Fluids* **45** (2008), 473-484.

[88] Tanaka, T., Eaton, J. K., "Sub-Kolmogorov resolution partical image velocimetry measurements of particle-laden forced turbulence", *J. Fluid Mech.* **643** (2010), 177.

[89] Sathe, M. J., Thaker, I. H., Strand, T. E., Joshi, J. B., "Advanced PIV/LIF and shadowgraphy system to visualize flow structure in two-phase bubbly flows", *Chem. Eng. Sci.* **65** (2013), 2431-2442.

[90] Cheng, Y., Pothos, S. and Diez, F. J., "Phase discrimination method for simultaneous two-phase separation in time-resolve stereo PIV measurements", *Exp. Fluids* **49** (2010), 1375-1391.

[91] Jacob, B., Olivieri, A., Miozzi, M., Campana, E. F. and Piva R., "Drag reduction by microbubbles in a turbulent boundary layer", *Phys. Fluid* **22** (2010), 115104.

[92] Ishikawa, M., "Flow Visualization and Image Measurement on a Bubble Jet Flow and Its Post-Processing by Using POD", *Trans. JSME B* **78** (2012), 263-275.

[93] Hosokawa, S., Tomiyama, A, "Bubble-induced pseudo turbulence in laminar pipe flows", *Int. J. Heat and Fluid Flow* **40** (2013), 97-105

[94] Kitagawa, A., Mimura, T., Ishikawa, M. Murai, Y., "Visualization of counter-current convection induced by microbubbles and small particles", *J. Vis.* **16** (2013), 313-321.

[95] Takehara, K., Etoh, T., "A study on Particle Identification in PTV -Particle Mask Correlation Method-", *J. Vis.* **1** (1999), 313-323.

[96] Liao, P. S., "A fast algorithm for multilevel thresholding", *J. Info. Sci. Eng.* **17** (2001), 713-727.

[97] Otsu, N., "A threshold selection method from gray-level histogram", *IEEE Trans. on systems, man, and cybernetics* **9** (1979), 62-66.

[98] Sugiyama, K., Calzavarini E. and Lohse, D., "Microbubbly drag reduction in Taylor–Couette flow in wavy vortex regime", *J. Fluid Mech.* **608** (2008), 21-41.

[99] Xu, J., Maxey, M. R., Karniadakis, G. E., "Numerical simulation of turbulent drag reduction using micro-bubbles", *J. Fluid Mech.* **468** (2002), 271-281.

[100] Couette, M., "Etude sur le frottement des liquides", *Ann. Chim. Phys.* **21** (1890), 433.

[101] Taylor, G. I., "Stability of a viscous liquid contained between two rotating cylinders", *Phil. Trans. Roy. Soc. London A* **223** (1923), 289-343.

[102] Andereck, C. D., Liu, S. S. and Swinney, H. L., "Flow regimes in a circular Couette system with independently rotating cylinders", *J. Fluid Mech.* **164** (1986), 155-183.

[103] Koschmieder, E. L., "Bénard Cells and Taylor Vortices", Cambridge Univrsity Press, New York, (1993).

[104] Shiomi, Y., Kutsuna, H., Akagawa, K. and Ozawa, M. "Two-phase flow in an annulus with a rotating inner cylinder (flow pattern in bubbly flow region)" *Nucl. Engng Design* **141** (1993), 27-34.

[105] Djeridi, H., Gabillet, C. and Billard, Y., "Two-phase Couette–Taylor flow: arrangement of the dispersed phase and effect on the flow structure", *Phys. Fluids* **16** (2004), 128-139.

[106] Mehel, A., Gabillet, C., Djeridi, H., "Analysis of the flow pattern modifications in a bubbly Couette–Taylor flow", *Phys. Fluids* **19** (2007), 118101.

[107] van den Berg, T. H., Luther, S, Lathrop, D. and Lohse, D., "Bubbly Turbulent Drag Reduction Is a Boundary Effect", *Phys. Rev. Lett.* **98** (2007), 084501.

[108] Climent, E., Simonnet, M., Magnaudet, J., "Preferential accumulation of bubbles in Couette-Taylor flow patterns", *Phys. Fluids* **19** (2007), 083301.

[109] van den Berg, T. H., Luther, S., Lathrop, D. P. and Lohse, D., "Drag Reduction in Bubbly Taylor–Couette Turbulence", *Phys. Rev. Lett.* **94** (2005), 044501.

[110] Murai, Y., Oiwa, H., Takeda, Y., "Frictional drag reduction in bubbly Taylor–Couette flow", *Phys. Fluids* **20** (2008), 034101.

[111] Yoshida, K., Tasaka, Y., Murai, Y., Takeda, Y., "Mode transition in Bubbly Taylor–Couette flow measured by PTV", *J. Phys. Conf. Ser.* **147** (2009), 012013.

[112] van Gils, D. P. M., Guzman, D. N., Sun, C., Lohse, D., "The importance of bubble deformability for strong drag reduction in bubbly turbulent Taylor–Couette flow", *J. Fluid Mech.* **722** (2013), 317-347.

[113] Lu, J., Fernández, A., Tryggvason, G., "The effect of bubbles on the wall drag in a turbulent channel flow", *Phys Fluids* **17** (2005) 095102.

[114] Lo, T., S., L'vov, V. S., Procaccia, I., "Drag reduction by compressible bubbles", *Phys. Rev. E* **73** (2006), 036308.

[115] Di Prima R. C. and Swinney, H. L., "Instabilities and Transition in Flow between Concentric Rotating Cylinders", *Topic in Applied Phys.* **45** (1979), 139-180.

[116] Dutcher, C. S., Muller, S. J., "Explicit analytic formulas for Newtonian Taylor–Couette primary instabilities", *Phys. Rev. E* **75** (2007), 047301.

[117] Esser, A., Grossmann, S., "Analytic expression for Taylor–Couette stability boundary", *Phys. Fluids* **8** (1996) 184-1819.

[118] Coughlin, K. T., Marcus, P. S., Tagg, R. P., Swinney, H. L., "Distinct quasiperiodic modes with like symmetry in a rotating fluid", *Phys. Rev. Lett.* **66** (1991), 1161-1164.

[119] Gorman, M, Swinney, H. L., "Spatial and temporal characteristics of modulated waves in the circular Couette system", *J. Fluid Mech.* **117** (1982), 123-142.

[120] Zhang, L. H., Swinney, H. L., "Nonpropagating oscillatory modes in Couette–Taylor flow", *Phys. Rev. A* **31** (1985), 1006-1009.

[121] Coughlin, K. T., Marcus, P. S., "Modulated waves in Taylor–Couette flow Part 1. Analysis", *J Fluid Mech.* **234** (1992), 1-18.

[122] Coughlin, K. T., Marcus, P. S., "Modulated waves in Taylor–Couette flow Part 2. Numerical simulation", *J Fluid Mech.* **234** (1992), 19-46.

[123] Takeda, Y., "Quasi-periodic state and transition to turbulence in a rotating Couette system", *J. Fluid Mech.* **389** (1999), 81-99.

[124] Wendt, F, "Turbulente Strömungen zwischen zwei rotierenden konaxialen", *Zylindern. Ing.-Arch.* **4** (1933), 577–595.

[125] Takeda, Y., "Velocity profile measurement by ultrasound Doppler shift method", *Int. J. Heat Fluid Flow* **7** (1986), 313-318.

[126] Takeda, Y., ed., "Ultrasonic Doppler Velocity Profiler for Fluid Flow", *Springer* (2012).

[127] Takeda, Y., Fischer, W. E., Kobashi, K., Takada, T., "Spatial characteristics of dynamic properties of modulated wavy vortex flow in a rotating Couette system", *Exp. Fluids* **19** (1992) 199-207.

[128] Landau, L., D., Lifshitz, E. M., "Fluid Mechanics - course of the theoretical physics", Pergamon Press, Bristol (1959), 102-107.

[129] Neitzel, G. P., "Numerical comparison of time-dependent Taylor-vortex flows in finite-length geometries", *J. Fluid Mech.* **141** (1984), 51-66.

[130] Marcus, M., "Simulation of Taylor–Couette flow. Part 2. Numerical results for wavy-vortex flow with one travelling wave", *J. Fluid Mech.* **146** (1984), 65-113.

[131] Jones, C. A., "Transition to wavy Taylor vortices", *J. Fluid Mech.* **157** (1985),

135-162.

[132] Akonur, A., Lueptow, R. M., "Three-dimensional velocity field for wavy Taylor–Couette flow", *Phys. Fluids* **15** (2003), 947-960.

[133] Gore, R. A., Crowe, C. T., "Effect of particle size on modulating turbulent intensity", *Int. J. Multiphase Flow* **15** (1989), 279-285.

[134] Hosokawa, S., Tomiyama, A., "Turbulence modification in gas-liquid and solid-liquid dispersed two-phase pipe flows", *Int. J. Heat Fluid Flow* **25** (2004), 489-498.

[135] Wereley, S. T., Lueptow, R. M., "Spatio-temporal character of non-wavy and wavy Taylor–Couette flow", *J. Fluid Mech.* **364** (1998), 59-80.

[136] Ashwin, P., King, G. P., "A study of paths in non-axisymmetric Taylor–Couette flows", *J. Fluid Mech.* **338** (1997), 341-362.

[137] Wereley, S. T., Lueptow, R. M., "Azimuthal velocity in supercritical circular Couette flow", *Exp. Fluids* **18** (1994), 1-9.

[138] Walsh, T. J, Wagner, W. T., Donnelly, R. J., "Stability of Modulated Couette Flow", *Phys. Rev. Lett.* **58** (1987), 2546-2546.

[139] Takeda, Y., Morinaga, M., Tasaka, Y., "Oscillating Taylor–Couette Flow (Azimuthal motion)", *J. Phys.: Conf. Ser.* **137** (2008), 012002.

[140] Bosse, T., Kleiser, l., "Small particles in homogeneous turbulence: Settling velocity enhancement by two-way coupling", *Phys. Fluids* **18** (2006), 027102.

[141] Yeo, K., Dong, S., Climent, E., Maxey, M. R., "Modulation of homogenous turbulence with finiute size bubbles or particles", *Int. J. Multiphase Flow* **36** (2010), 221-233.

[142] Choi, H., Moin, P., Kim, J., "Active turbulence control for drag reduction in wall-bounded flows", *J. Fluid Mech.* **262** (1994), 75-110.

[143] Kim, J., Lim, J., "A linear process in wall-bounded turbulent shear flows", *Phys. Fluids* **12** (2000) 1885-1888.

[144] Coles, D., Transition in circular Couette flow, *J. Fluid Mech.* **21** (1965), 385-425.

[145] Benjamin, T. B., Mullin, T., "Notes on the multiplicity of flows in the Taylor experiment", *J. Fluid Mech.* **121** (1982), 219-230.

[146] Elghobashi, S., "On Preditiing Particle-Laden Turbulent Flow", *Applied Sci. Res.* **52** (1994), 309-329.

[147] Balachandar, S., Eaton, J., "Turbulent Dispersed Multiphase Flow", *Annu. Rev. Fluid Mech.* **42** (2010), 111-133.

[148] Suzuki, T., Ji, H., Yamamoto, F., Unsteady PTV velocity field past an airfoil solved with DNS: Part 1. Algorithm of hybrid simulation and hybrid velocity field, *Exp. Fluids* **47** (2009), 957-976.

[149] Suzuki, T., Reduced-order Kalman-filtered hybrid simulation combining particle tracking velocimetry and direct numerical simulation, *J. Fluid Mech.* **706** (2012),

4-40.

[150] Tennekes, H., Lumley, J. L., A First Course in Turbulence, *The Massachusetts Institute of Technology* (1972), 253.

[151] Hirt, C. W., Cook, J. L., Calculating Three-dimensional Flows Around Structures and over Rough Terrain, *J. Computational Phys.* **10**, (1972), 324-340.

[152] van Leer, B., Towards the ultimate conservative difference scheme II. Monotonicity and conservation combined in a second order scheme, *J. Computational Phys.* **14**, (1974), 361–370

[153] Eagles, "On the torque of wavy vortices", *J. Fluid Mech.* **62** (1974), 1-9.

[154] Lindau, O., Lauterborn, W., "Cinematographic observation of the collapse and rebound of a laser-produced cavitation bubble near a wall", *J. Fluid Mech.* **479** (2003) , 327-348.

[155] Terasaka, K., Hirabayashi, A., Nishino, T., Fujioka, S., Kobayashi, D., "Development of microbubble aerator for waste water treatment using aerobic activated sludge", *Chem. Eng. Sci.* **66** (2011), 3172-3179.

[156] Alam, M., Alakeri, V. H., "Observatios on transition in plane bubble plumes", *J. Fluid Mech.* **254** (1993) 363-374.

[157] Murai, Y., Matsumoto, Y., "Numerical Study of the Three-dimensional structure of a bubble plume", *J. Fluid Eng.* **122** (2000), 754-760.

[158] Kitagawa, A., Murai, Y., "Natural convection heat transfer from a vertical heated plate in water with micobubble injection", *Chem. Eng. Sci.* **99** (2013), 215-224.

[159] Kitagawa, A., Endo, H., Hagiwara, Y., "Effects of sub-millimeter-bubble injection of transition to turbulence in natural convection boundary layer along a vertical plane in water", *Exp. Fluids* **51** (2011) 701-711.

[160] So, S., Morita, H., Takagi, S., Matsumoto, Y., "Laser Doppler velocimetry measurement of turbulent bubbly channel flow", *Exp. Fluids* **33** (2002), 135-142.

[161] Ishikawa, M., Irabu, K., Teruya, I., Nitta, M., "Spatiotemporal structure analysis on a bubbly jet flow using POD", *AIP Conf. Proc., the 7th Int. Symp. Meas. Tech. Multiphase Flows* **1428** (2011), 18-25.

[162] Stimson, M., Jeffery, G., "The motion of two spheres in a viscous fluid", *Proc. R. Soc. London, Ser. A* **111**, (1926) 110-116.

[163] Happen, J., Brenner, H., "Low Reynolds number hydrodynamics", *Prentice-Hall, Englewood Cliffs*, (1965).

[164] Narayan, S., Goossense, L. H. J., Kossen, N. W. F., "Coalescence of two bubbles rising in line at low Reynolds numbers", *Chem. Eng. Sci.* **29** (1974), 2071-2082.

[165] van Wijngaarden, "The mean rise velocity of pairwise-interacting bubbles in liquid", *J. Fluid Mech.* **251** (1993) 55-78

[166] Yuan, H., Prosperetti, A., "on the in-line motion of two spherical bubbles in a viscous fluid", *J. Fluid Mech*. **278** (1994), 325-349.

[167] Legendre, D., Magnaudet, J., Mougin, G., "Hydrodynamic interactions between twp-spherical bubbles side by side in a viscous liquid", *J. Fluid Mech.* **497** (2003) 133-166.

[168] Hallez, Y., Legendre, D., "Interaction between two spherical bubbles rising in a viscous liquid", *J. Fluid Mech.* **673** (2011) 406-431.

[169] Sangani, A. S., Didwania, A. K., "dynamic simulation of flows of bubbly liquids at large Reynolds number" *J. Fluid Mech.* **250** (1993) 307-337.

[170] Yurkovetsky, Y., J. F. Brady, "Statistical mechanics of bubbly liquids", *Phys. Fluids* **8** (1996) 881-893.

[171] Esmaeeli, A., Tryggvason, G., "An inverse energy cascade in two-dimensional low Reynolds number bubbly flows" *J. Fluid Mech.* **314** (1996) 315-330.

[172] Esmaeeli, A., Tryggvason, G., "Direct numerical simulations of bubbly flows. Part 1. Low Reynolds number" *J. Fluid Mech.* **377** (1998) 313-345.

[173] Esmaeeli, A., Tryggvason, G., "Direct numerical simulations of bubbly flows. Part 1. Moderate Reynolds number" *J. Fluid Mech.* **385** (1999) 325-358.

[174] Zenit, R., Koch, D. L., Sangani, A., "Measurements of the average properties of a suspension of bubbles rising in a vertical channel" *J. Fluid Mech.* **429** (2001) 307-341.

[175] Bunner, B., Tryggvason, G., "Dynamics of homogeneous bubbly flows Part 1. Rise velocity and microstructure of the bubbles" *J. Fluid Mech.* **466** (2002) 313-345.

[176] Riboux, G., Risso, F., Legendre, D., "Experimental charaterization of the agitation generated by bubbles rising at high Reynolds number " *J. Fluid Mech.* **643** (2010) 509-539.

[177] Takagi, S., Matsumoto, Y., "Surfactant Effects on Bubble Motion and Bubbly Flows", *Ann. Rev. Fluid. Mech.* **43** (2011), 615-636.

[178] Machu, G., Meile, W., Niche L. C., Schaflinger U., "Coalescence, torus formation and breakup of sedimenting drops: experiments and computer simulations", *J. Fluid Mech.* **447** (2001), 299-336.

[179] Harada, S., Mitsui, T., Sato, K., "Particle-like and fluid-like settling of a stratified suspension", *Eur. Phys. J. E* **35** (2012), 1-6.

[180] Harada, S., Kondo, S., Watanabe, K., Shitani, T., Saito, K., "Collective settling of fine particles in a narrow channel with arbitrary cross-section", *Chem. Eng. Sci.* **93** (2013), 307-312.

[181] von Kerczek, C. H., "The instabillity of oscillating plane Poiseuille flow", *J. Fluid Mech.* **116** (1982), 91-114.

[182] Olinger, D. J., Sreenivasan, K. R., "Nonlinear dynamics of the wake of an oscillating cylinder", *Phys. Rev. Lett.* **60** (1988), 797-800.

[183] Nukiyama, S., Tanasawa, Y., "Experiments on the Atomization of liquids in a Air Stream Report 3; On the Drop-size Distribution in an Atomized Jet", *Trans.*

JSME **5** (1939), 62-67.

[184] Taya, C., Maeda, Y., Hosokawa, S., Tomiyama, A., Ito, Y., Shibata, N., "Size Distribution of Micro-bubbles Generated by a Pressurized Dissolution Method", *Konsoryu, J. Japan Soc. Multiphase Flow (in Japanese)* **25** (2012), 407-414.

[185] Kitagawa, A., Ozato, T., Murai, Y., "Motion Characteristics of Microbubbles Rising near a Vertical Plane wall", *Tras. JSME B* **79** (2013), 701-711 (in Japanese).

[186] Farge, M., "Wavelet transforms and their applications to turbulence", *Ann. Rev. Fluid Mech.* **24** (1992), 395-458.

[187] Tropea, C., Yarin, A. L., Foss, J, Eds., "Handbook of Experimental Fluid Mechanics", *Springer* (2007).

[188] Mallat, S., "A wavelet tours of signal processing, third ed.", *Academic press* (2008), 179.

[189] Fernandez, J., Kurowski, L., Petitjeans, P., "Wavelenght selection of fingering instability inside Hele-Shaw cells", *Phys. Fluids* **13** (2001), 3120-3125.

[190] Hoff, L., "Acoustic Characterization of Contrast Agents for Medical Ultrasound Imaging", *Springer* (2002).

[191] Rightley, P. M., Lasheras, J. C., "Bubble dispersion and interphase coupling in a free-shear flow", *J. Fluid Mech.* **412** (2000), 21-59.

[192] Yang, X., Huang, X., Rielly, C., Zouaoui, Z., Guo, L., "The modification of a plane mixing layer by condensed bubbles", *Chem. Eng. Sci.* **60** (2005), 6876-6886.

[193] Aeschlimann, V., Barre, S., Djeridi, H., "Velocity field analysis in an experimental cavitating mixing layer", *Phys. Fluids* **23** (2011), 055105.

[194] Aeschlimann, V., Prothin, S., Barre, S., Djeridi, H., "High speed visualizations of the cavitating vortices of 2D mixing layer", *Euro. J. Mech. B/Fluids* **31** (2013), 171-180.

[195] Browand, F., Latigo, K., "Growth of the two-dimensional mixing layer from a turbulent and nonturbulent boundary layer", *Phys. Fluids* **22** (1979), 1011-1019.

[196] Monkewits, P. A., Huerre, P., "Influence of the velocity ratio on the spatial instability of mixing layers", *Phys. Fluids* **25** (1982), 1137-1143.

[197] Browand, F. K., Troutt, T. R., "The turbulent mixing layer: geometry of large vortices", *J. Fluid Mech.* **158** (1985), 489-509.

[198] Elghobashi, S., "On Predicting Particle-Laden Turbulent Flows", *Appl. Sci. Res.* **52** (1994), 309-329.

[199] Crowe, C. T., Troutt, T. R., Chung, J. N., "Particle interactions with vortices", in: Green, S. I. (ed.), Fluid Vortices, *Kluwer Academic Publishers* (1995), 829-861.

[200] Baranenko, V. I., and Kirov, V. S., "Solubility of hydrogen in water a broad temperature and pressure range", *Soviet Atomic Energy* **66** (1989), 30-34.

[201] Broecker, W. S., Peng, T. H., "Gas exchange rates between air and sea", *Tellus*

26 (1974), 121-35.

[202] Sugiyama, K., Kawashima, H., Fujiwara, A., Hishida, K., Nadeda, T., Kameda, M., Kodama, Y., "On relevance of turbulence to microbubble dissolution process", *Paper of National Maritime Research Institute* **6** (2006), 139-154.

[203] Plesset, M. S., Prosperetti, A., "Bubble dynamics and cavitation", *Ann. Rev. Fluid. Mech.* **9** (1977), 145-185.

[204] Minnaert, M., "On musical air-bubbles and sound of running water", *Phil. Mag.* **16** (1933), 235-248.

[205] Okamoto, K., Nishino, K., Saga, T., Kobayashi, T., "Standard images for particle-image velocimetry", *Meas. Sci. Technol.* **11** (2000), 685-691.

[206] Danowitz, A., Kelley, K., Man, J., Stevenson, J. P., Horowitz, M., "CPU DB: Recording Microprocessor History", *Communication ACM* **55** (2013), 55-63.

[207] Brandvik, T., Pullan, G., "Acceleration of a two-dimensional Euler flow solver using commodity graphic hardware", *Proc. Inst. Mech. Eng. C: J. Mech. Eng. Sci.* **221** (2007), 1745-1748.

Publication & Presentation

Chapter 2

· **Tomoaki WATAMURA**, Yuji TASAKA, Yuichi MURAI, "LCD-projector-based 3D color PTV", *Experimental Thermal and Fluid Science*, Vol. 47, pp.68-80 (2013.05).

Chapter 3

· **Tomoaki WATAMURA**, Yuji TASAKA, Yuichi MURAI, "Intensified and attenuated waves in a microbubble Taylor–Couette flow", *Physics of Fluids*, Vol. 25, 054107 (2013.05).

· **Tomoaki WATAMURA**, Yuji TASAKA, Yuichi MURAI, "Quantitative visualization of microbubble streams in Taylor vortices", *Theoretical and Applied Mechanics Japan*, Vol. 61, pp. 123-131 (2013.01).

· **Tomoaki WATAMURA**, Yuji TASAKA, Yuichi MURAI, Yasushi TAKEDA, "Suppression of the Flow Transition By microbubble in a Taylor–Couette flow", *Transaction of Japan Society of Mechanical Engineering B*, Vol. 76, pp. 2160-2167 (2010.12). (in Japanese)

Chapter 4

· **Tomoaki WATAMURA**, Yuji TASAKA, Yuichi MURAI, "Wavy bubble distribution in an azimuthal wave of Taylor–Couette flows", *Proceedings of International Conference on Multiphase Flow 2013*, (2013.05).

Chapter 5

· **Tomoaki WATAMURA**, Atsuhide KITAGAWA, Toakuya OZATO, Yuji TASAKA, Yuichi MURAI, "Spatio-temporal characterization of ascending microbubbls near a vertical plane wall", *The 12th International Symposium on Fluid Control, Measurement and Visualization* (2013.11).

· Yoshihito MIYAGISHIMA, **Tomoaki WATAMURA**, Yuji TASAKA, Yuichi MURAI, "Self organized structure of microbubble plume in a thin fluid layer", *Proceedings of ASME-JSME-KSME Joint Fluid Engineering Conference,*

AJK2011-11006, pp.2669-2675 (2011.07).

· Yoshihito MIYAGISHIMA, **Tomoaki WATAMURA**, Yuji TASAKA, Ichiro KUMAGAI, Yuichi MURAI, "Quantitative Visualization of Buoyant Rise Process in a Swarm of Microbubble Plumes", *Transaction of Japan Society of Mechanical Engineering B*, Vol. 77, pp. 2306-2315 (2010.12). (in Japanese)

Chapter 6

· **Tomoaki WATAMURA**, Yuji TASAKA, Yuichi MURAI, "Localized Modification of turbulent spectra in a horizontal mixing-layer", *Transaction of Japan Society of Multiphase Flow*, (Accepted). (in Japanese)

Curriculum Vitae

Tomoaki WATAMURA

Education

2011 - 2014 Ph.D. (Engineering)
"Study on modulation of flow transition by microbubble injection"
Hokkaido University

2010 - 2011 Master's Degree (Engineering)
"Delay of flow transition by preferential interaction between microbubbles and wavy motion in Taylor–Couette flow"
Hokkaido University

2006 - 2010 Bachelor's Degree (Engineering)
"Flow controllability of microbubbles in Taylor–Couette flow"
Hokkaido University

Honor & Award

2012 - 2014 Research Fellow (DC2), *JSPS (Japan Society for the Promotion of Science)*

2013.10 Excellent Presentation Award, *Japan Soc. Multiphase Flow*
2011.03 Miura Award, *Japan Soc. Mech. Eng.*
2010.03 Best Presentation Award, *Japan Soc. Mech. Eng. Hokkaido Branch Student Meeting*

Special Skills

Experience in C, CUDA, ImageJ, LaTEX, LabVIEW, OpenMP, ParaView, and Windows
Extensive experience in machining with metals and Plexiglas